# ABSTRACT

HOU, LIQIANG. Dark Matter Annihilation in Small Scales. (Under the direction of Katherine Mack).

This dissertation explores the impact of dark matter on the early universe and cosmological observables, with a focus on dark matter annihilation effects on thermal history and dark matter annihilation at the small scales, including the formation of the first stars and galaxies. Dark matter annihilation, enhanced by cosmic inhomogeneities, reshapes the gas temperature and ionization history of the early universe. Annihilation injects energy into the IGM, raising the gas temperature and ionization fraction. This process can either suppress or accelerate the star formation.

This study examines the effects of dark matter annihilation on the minimum cooling mass of halos at different redshifts. Notably, this work presents the first combined calculation of dark matter annihilation and dark matter baryon velocity offsets, which have previously been treated separately. Our detailed calculations reveal the non-trivial effects of interplay between dark matter annihilation and dark matter baryon velocity offsets affects the evolution of structure formation. To explore these effects further, we extend existing models to include both molecular and atomic cooling halos, allowing star formation to occur in lower-mass halos and offering insights into how dark matter annihilation, streaming velocity, and cooling mechanisms shape early observable signals.

Our study calculates the sky-averaged brightness temperature of the high-redshift 21cm absorption signal against the cosmic microwave background, also known as the “global 21cm signal”, including the effects of both dark matter annihilation and velocity offsets. These factors create distinct features in the 21cm signal, providing potential observational signatures of dark matter properties.

We also examine energy transfer processes within dark matter halos, including inverse Compton scattering, photoionization, and pair production. By applying a refined Monte Carlo energy-transfer calculation code, we link single-particle simulations to energy deposition fractions. These developments will be crucial for connecting small-scale effects with large-scale galaxy formation models and ultimately interpreting observational data from the early universe.

Dark Matter Annihilation in Small Scales

by
Liqiang Hou

A dissertation submitted to the Graduate Faculty of
North Carolina State University
in partial fulfillment of the
requirements for the Degree of
Doctor of Philosophy

Physics

Raleigh, North Carolina
2025

APPROVED BY:

| | |
|---|---|
| Rongmon Bordoloi | James Kneller |
| James Martin | Stephen Reynolds |

Katherine Mack
Chair of Advisory Committee

# BIOGRAPHY

The author was born in Huaibei, China, a small city nestled in the mountainous region. From a young age, the author developed a keen interest in the sciences which was further nurtured through his early education. He enrolled at North Carolina State University to pursue a PhD in astrophysics. In 2018, he joined the research group led by Dr. Katie Mack, focusing on exploring the effects of dark matter annihilation.

# ACKNOWLEDGEMENTS

First, I want to thank my advisor, Dr. Katie Mack, for her unwavering support and guidance. Her mentorship has allowed me to explore the fascinating topics that fuel my passion for science. Her encouragement and enthusiasm have been a constant source of inspiration, influencing both my academic pursuits and my personal growth.

I am deeply grateful to Weikang Lin, who provided immense support during his postdoctoral tenure. His help has been invaluable for my academic work.

I must also thank my NCSU peers: Akhlak Mahmood, Sherwood Richers, and Tongjie Chen. They are the best people I have ever met, offering invaluable help in both my studies and life.

To those who have supported me behind the scenes, I owe my deepest gratitude. My parents, who have always believed in me without hesitation, and my friends, whose encouragement has been a constant source of strength, especially during overwhelming moments. Additionally, I extend my thanks to the kind individuals from online communities who have made a meaningful difference in my journey.

Finally, I would like to thank those who read this dissertation. Your reading and feedback are invaluable; they breathe life into these pages and bestow value upon my work. I must confess that this document may harbor numerous inconsistencies. My entire Ph.D. journey has been an effort to reconcile these inconsistencies to ensure they are compatible with each other. Even so, you may still encounter some peculiarities, whether typos or unresolved mysteries. Your patience and understanding are deeply appreciated.

With the end of my dissertation, which also marks the end of my Ph.D. career, I implore you to believe me that choosing the right moment to conclude this journey is no easy feat. However, Dr. Steven Weinberg said, "I managed to get a quick PhD – though when I got it I knew almost nothing about physics." (Weinberg 2003). Approaching the finale of my Ph.D., I find myself truly knowing nothing about physics. Therefore, it seems this is indeed the perfect time to wrap up my Ph.D. journey.

# TABLE OF CONTENTS

# LIST OF TABLES

# LIST OF FIGURES

CHAPTER

# 1

# INTRODUCTION

## 1.1 Structure Formation in ΛCDM

### 1.1.1 Overview

The Lambda cold dark matter (ΛCDM) model is the leading cosmological framework for understanding the structure and evolution of the Universe. It combines the cosmological constant (Λ), representing dark energy, with CDM. The ΛCDM model offers a unified explanation for key astronomical phenomena, including the cosmic microwave background (CMB) radiation, large-scale structure of the cosmos, and accelerating expansion of the Universe.

The origins of the ΛCDM model trace back to the early 20th century. When applying field equations from General Relativity to the Universe, Einstein observed that the resulting model of the Universe was either expanding or contracting, which conflicted with the prevailing notion of a static Universe at the time. To resolve this, Einstein introduced the cosmological constant (Λ) to achieve a stable, static model of the Universe. However, after Edwin Hubble's study of distant galaxies in the late 1920s (Nussbaumer and Bieri 2011), which revealed that the Universe is expanding (now known as Hubble's law), Einstein abandoned the cosmological constant, famously calling it his "greatest blunder."

Despite this, the cosmological constant (Λ) was revived following a groundbreaking dis-

covery in the late 20th century. Two independent research teams studying "standard candles" (Type Ia supernovae) discovered that the Universe is expanding at an accelerating rate (Riess et al. 1998; Perlmutter et al. 1999). This discovery led to a revision of the standard model of the Universe, reintroducing the cosmological constant ($\Lambda$) as a description of the observed acceleration, thereby shaping the modern $\Lambda$CDM framework.

CDM refers to hypothetical particles that move at low velocities relative to the speed of light. In 1932, Jan Oort analyzed the rotation curves of stars in the Milky Way and observed that stars in the outer regions were moving faster than expected based on their visible mass, suggesting the presence of DM. In 1933, Fritz Zwicky investigated the Coma cluster of galaxies and discovered a substantially greater mass-to-light ratio than that observed in our local neighborhood. This discrepancy indicated missing mass and prompted Zwicky to propose the existence of "dunkle Materie" or DM.

In 1951, Harold Ewen and Edward Purcell detected the 21-cm line, representing the spin-flip transition of neutral hydrogen. This line demonstrated potential for measuring the rotation of the outer parts of galaxies. Later, in 1970, Ken Freeman analyzed photometric data, along with observed rotation curves from 21-cm radio observations, assuming an exponential disk model. Freeman discovered that in galaxies such as NGC 300 and M33, the observed rotation curves peaked at larger radii than those predicted by visible matter alone, suggesting that additional mass was required in the outer parts of galaxies.

The rotational velocity of a spherically symmetric galaxy can be expressed as

$$v_{\mathrm{circ}}(R) = \sqrt{\frac{GM(R)}{R}}\,, \tag{1.1}$$

where $M(R)$ denotes the mass enclosed within radius $R$, and $G$ represents the gravitational constant. This equation provides information regarding the mass distribution within a galaxy. A comparison of the mass distribution derived from the observed rotational velocity with the distribution of observed luminous matter can help identify the presence of unseen mass components.

In the 1970s, astronomers Vera Rubin and Kent Ford conducted detailed observations of galaxy rotation curves using sensitive spectrographs (Rubin et al. 1980). Their measurements of the rotational velocities of gases and stars at various distances from galactic centers revealed that, contrary to expectations, the rotational velocities did not decrease with increasing distance from the center. Instead, they remained nearly constant. This provided compelling evidence regarding the existence of a substantial amount of unseen mass within galaxies.

The $\Lambda$CDM framework has made significant strides in explaining and predicting various cosmological phenomena.

In 1965, Arno Penzias and Robert Wilson first discovered cosmic microwave background (CMB) radiation, providing strong evidence supporting the Big Bang theory and indicating that the Universe had a hot and dense phase. The ΛCDM model predicts anisotropies in CMB—specifically, the statistical properties of temperature fluctuations across different regions. In the 2000s, the Wilkinson Microwave Anisotropy Probe was used to conduct a detailed full-sky survey of CMB anisotropies, confirming the predictions of the ΛCDM model (Bennett et al. 2013). This conclusion was further corroborated by the Planck satellite, launched by the European Space Agency in 2009. Planck's observation provided more detailed data on CMB and demonstrated excellent agreement with the predictions of the ΛCDM model.

Another major achievement of the ΛCDM model is its successful replication of the large-scale structure formation history of the Universe. Based on this model, the structure of the Universe originates from primordial fluctuations, which have grown over time. Within this framework, small structures are assumed to form first and progressively merge into large structures, a bottom-up scheme known as the hierarchical model.

Numerous simulations based on the ΛCDM model have been conducted to reproduce this structure formation. These simulations have accurately replicated the large-scale distribution of DM halos and galaxies, matching observations.

The theoretical framework of the ΛCDM model relies on the assumption of a homogeneous and isotropic Universe on large scales, as described by the Friedmann–Lemaître–Robertson–Walker metric.

$$ds^2 = c^2 dt^2 - a^2(t)\left[\frac{dr^2}{1-kr^2} + r^2(d\theta^2 + \sin^2\theta\, d\phi^2)\right]. \tag{1.2}$$

This metric provides an analytical solution to Einstein's field equations, yielding the Friedmann equations:

$$\begin{aligned} \left(\frac{\dot{a}}{a}\right)^2 + \frac{k}{a^2} &= \frac{8\pi G}{3}\rho + \frac{\Lambda}{3} \\ 2\frac{\ddot{a}}{a} + \frac{\dot{a}^2 + k}{a^2} &= -8\pi G p + \Lambda \end{aligned}, \tag{1.3}$$

where $a$ denotes the scale factor, $p$ represents pressure, $\rho$ denotes total energy density, and $k$ represents spatial curvature. These equations were derived before Hubble's discovery of the expanding Universe. Later, the expansion rate was quantified using Hubble's law, where $H \equiv \frac{\dot{a}}{a}$ denotes the Hubble constant. A positive value of $\Lambda$, the cosmological constant, indicates the presence of a negative pressure accelerating the expansion of the Universe. Scientists often express $\Lambda$ in terms of energy density, as indicated in the following equation:

$$\Lambda \equiv 8\pi G \rho_{\rm vac} \,, \tag{1.4}$$

where $\rho_{\rm vac}$ denotes the vacuum energy density.

The critical density, $\rho_{\rm crit} = 3H^2/8\pi G$, is the total density required for a spatially flat universe. The ratio of each energy density component to the critical density is denoted as $\Omega_i = \rho_i/\rho_{\rm crit}$, where

$$\Omega_\Lambda + \Omega_m + \Omega_r + \Omega_k = 1 \,. \tag{1.5}$$

In the above equation, $\Omega_\Lambda$ represents the dark energy density parameter, $\Omega_m$ denotes the matter density parameter (including both DM r and baryonic matter), $\Omega_r$ denotes the radiation density parameter, and $\Omega_k$ represents the curvature density parameter. Notably, in flat space, $\Omega_k = 0$.

Recent measurements of these parameters were reported by the Planck 2018 collaboration (Aghanim et al. 2020). The study determined the Hubble constant to be $H_0 = 67.66 \pm 0.42$ km s$^{-1}$ Mpc$^{-1}$, along with the current values of the density parameters: $\Omega_\Lambda = 0.6889$, $\Omega_m = 0.3111$, and $\Omega_r = 9.139 \times 10^{-5}$. This indicates that dark energy constitutes about 69% of the Universe's total energy density. The matter density, $\Omega_m$, accounts for 31% of the total density and is composed of baryonic matter, $\Omega_b = 0.049$, and cold dark matter (CDM), $\Omega_{\rm DM} = 0.2616$.

Despite the notable achievements of the ΛCDM model in explaining and predicting large-scale cosmic phenomena in the Universe, some challenges remain at smaller scales.

1. **Small-Scale Challenges**

Although the ΛCDM model accurately simulates large-scale structures, discrepancies arise when comparing its predictions with small-scale observations. Notable examples of these discrepancies include the core-cusp problem, missing satellites problem, and too-big-to-fail (TBTF) problem:

- **The core-cusp problem**: The core-cusp problem refers to the discrepancy between the predicted and observed DM density profiles at the centers of galaxies. Simulations based on the ΛCDM model predict the presence of a "cusp" wherein the CDM mass density increases steeply toward the galaxy center. Specifically, these simulations suggest a density profile described by $\rho_{\rm DM} \propto r^{-\beta}$, where $\beta \approx 1$ (Navarro et al. 1997). As the radius $r$ approaches zero, the model predicts a steep increase in DM density $\rho \to \infty$, leading to a divergent profile at the core. However, observations of galactic rotation curves suggest a constant-density core instead, which contradicts this "cusp" scenario (McGaugh et al. 2001). This discrepancy highlights the need for further investigations into

the assumptions of the ΛCDM model or potential modifications to its framework to better align its predictions with observational data. Some studies propose that baryonic physics, which is often not entirely included in simulations, could account for the flattening of the central cusps of halos (Navarro et al. 1996). To resolve this issue, several alternative models have been suggested by researchers studying DM physics. One such model is the warm DM (WDM) framework, wherein DM particles are assumed to move at greater velocities compared to those in the CDM paradigm. Such higher velocities lead to a flatter density profile. However, the WDM framework is still debated, as it cannot explain certain observations, such as the behavior of galactic rotation curves (Wu and Kroupa 2014), structure of subhalos (Schneider et al. 2014), and configuration of the Lyman-$\alpha$ forest (Narayanan et al. 2000; Kuzio de Naray et al. 2010).

- **The missing satellites problem**: The missing satellites problem represents the discrepancy between the predicted and observed number of subhalos in Milky-Way-like DM halos. High-resolution N-body simulations predict a much steeper stellar mass function at low masses compared to the corresponding observations (Klypin et al. 1999; Moore et al. 1999). This discrepancy suggests that star formation may be suppressed owing to reionization and feedback effects in smaller masses and the minimum mass for atomic cooling in the early Universe (Bullock and Boylan-Kolchin 2017). Previous studies considering the principles of baryonic physics have predicted a low number of satellites, accounting for feedback and reionization mechanisms (Brooks et al. 2013; Wetzel et al. 2016; Buck et al. 2019). Moreover, a study by Kim et al. (2018) revealed that observational biases may directly contribute to this problem, which could potentially be resolved with future surveys. However, addressing this bias may lead to the "too many satellites problem."

- **The too-big-to-fail (TBTF) problem**: The TBTF problem refers to the discrepancy between the circular velocities predicted by ΛCDM simulations and the observed velocities of dwarf galaxies. Dissipationless ΛCDM simulations predict that most highly massive subhaloes in the Milky Way are too dense to host any of its bright satellites (Boylan-Kolchin et al. 2011). The TBTF problem is also prevalent in the M31 system and across the Local Group. Several studies have proposed solutions to the TBTF problem by incorporating the effects of baryonic physics, such as supernovae feedbacks and tidal disruption (Zolotov et al. 2012; Brooks and Zolotov 2014; Garrison-Kimmel et al. 2019).

2. **Challenges in the First Light**

Cosmic Dawn marks the onset of the first star formation processes and the end of the "Dark Ages." The formation of the first stars and galaxies not only illuminated the Universe but also

played a crucial role in reionizing the intergalactic medium (IGM). While the ΛCDM model accurately predicts the large-scale structures that set the stage for early galaxy formation, the specific mechanisms underlying the formation of the first stars and the reionization of the IGM remain unclear, necessitating further investigation.

- **Gas Cooling**: During the Cosmic Dawn phase, the first stars, known as Population III (Pop III) stars, formed in small DM halos. However, gas cooling processes, deemed essential to trigger the formation of these stars, were unlikely because the metal-free primordial gas lacked efficient cooling channels. Here, cooling predominantly occurred through molecular hydrogen, which is known to be sensitive to the gas temperature and density. Additionally, feedback from the first stars, such as ultraviolet (UV) radiation, supernova explosions, and stellar winds, could either suppress or accelerate further star formation processes (Greif et al. 2007). These complex phenomena, including cooling limitations and feedback effects, require detailed modeling to comprehensively understand the formation processes of the first stars. Researchers have begun examining early observational data from the James Webb Space Telescope (JWST), offering insights into the properties of the first galaxies. However, a comprehensive understanding is still forthcoming.

- **reionization**: Following recombination, the Universe entered the "Dark Ages," a period characterized by the absence of luminous sources and the predominance of neutral gas. The formation processes of the first stars, primarily comprising hydrogen and helium, produced ionizing photons that initiated the reionization of the IGM. While star-forming galaxies are widely regarded as the primary drivers of reionization, several uncertainties remain (Ellis and Silk 2008), particularly regarding their ionizing efficiencies and the escape fraction of ionizing photons. These uncertainties suggest the possibility of alternative or additional influencing ionizing sources. Determining the relative contributions of these sources is essential for acquiring a comprehensive understanding of the reionization era.

- **21-cm Line Observations**: The 21-cm line, arising from the hyperfine transition of neutral hydrogen, serves as a unique observational probe for studying the early Universe. Observations of this line offer insights into the thermal history and spatial distribution of neutral hydrogen during the Cosmic Dawn and reionization epochs. The Experiment to Detect the Global Epoch of Reionization Signature (EDGES) yielded a brightness temperature of $T = -500 \pm 200$ mK at a redshift of $z = 17.2$ (Bowman et al. 2018). However, this strong absorption signal cannot be explained by the standard cosmological model and remains a subject of active debate. For example, even under extreme assumptions, such as those that disregard astrophysical heating, assume negligible reionization, and

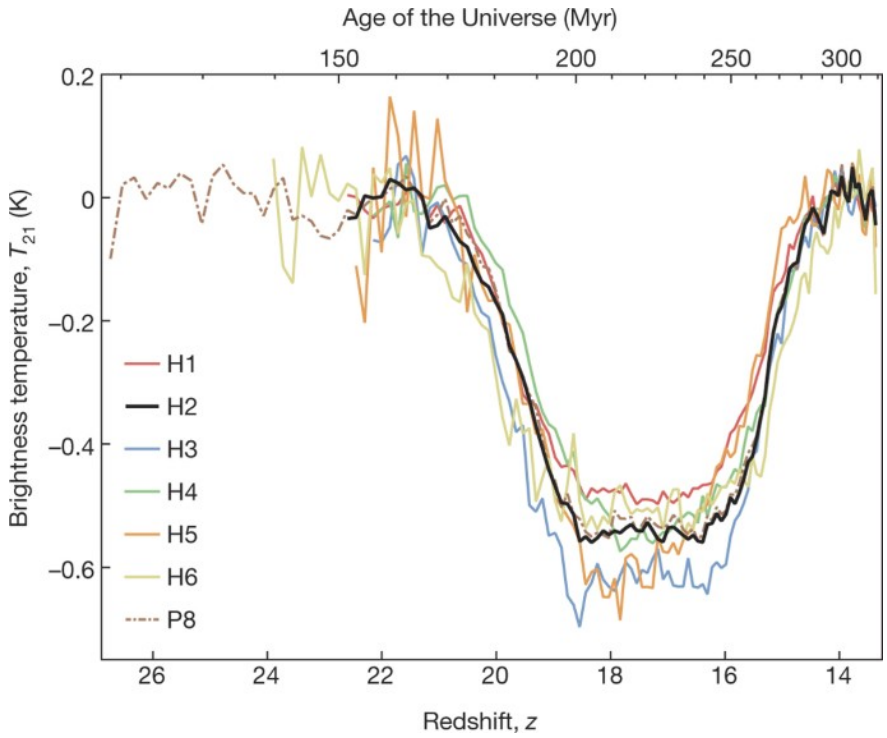


Figure 1.1: EDGES sky measurement of brightness temperature, displaying a strong absorption signal at $z = 17.2$ with an amplitude of $-500$ mK. Adapted from the work of Bowman et al. (2018).

consider saturated coupling, the strongest predicted absorption signal is $T \approx -209$ mK at $\nu = 78$ MHz (Barkana 2018). Thus, the result of the EDGES, which is still far beyond this value, suggests a colder IGM than that predicted by the standard cosmological model. If confirmed, this observation could imply the need to consider new physics in the ΛCDM model, such as DM–baryon interactions or previously disregarded cooling mechanisms prevalent in the early Universe.

3. **Mystery of Dark Matter**

Although the ΛCDM model attributes approximately 26% of the total density of the Universe to CDM, the nature of this DM remains unknown. Experimental endeavors, such as PandaX-4T, LUX-ZEPLIN, and XENONnT, are yet to successfully detect DM particles, casting doubts on the existence of prominent DM candidates, such as weakly interacting massive particles (WIMPs). Explorations of alternative candidates, including axions and sterile neutrinos, are underway, yielding different implications for particle physics and cosmology.

Some existing models suggest that DM particles may self-interact and annihilate into Standard Model particles, altering observable aspects of the Universe. For instance, these interactions can heat and ionize the primordial gas, leaving detectable signatures in astrophysical

phenomena. Certain studies suggest that self-interacting DM models may help resolve small-scale structure problems. However, the effects such interactions remain poorly understood and require further investigation.

4. **Hubble Tension**

The Hubble tension refers to the significant discrepancy observed between values of the Hubble constant derived from different observational methods. Measurements derived from observations of the early Universe, including the CMB observations of the Planck satellite, yield a lower value of the Hubble constant ($H_0 = 67.66\,\mathrm{km\,s^{-1}\,Mpc^{-1}}$). Conversely, measurements derived from Type Ia supernovae calibrated against Cepheid variables suggest a higher value ($H_0 \approx 74\,\mathrm{km\,s^{-1}\,Mpc^{-1}}$) (Riess et al. 2019, 2022). The Hubble tension has been confirmed at a high significance level ($> 5\sigma$), making it one of the most pressing challenges in the context of the ΛCDM model.

**Constraints in the $H_0 - \Omega_m$ Plane**

The Hubble tension is typically analyzed by analyzing the constraints on $H_0$ alone. However, post-recombination cosmic evolution in the ΛCDM model is governed by two parameters: the Hubble constant ($H_0$) and the matter-energy density fraction ($\Omega_m$). The analysis of constraints based on different observations from the parameter space $H_0$–$\Omega_m$ offers several advantages: (1) This approach allows constraints derived from different observations to be treated as independently as possible. (2) It simplifies the consideration of single-sided constraints. (3) It enables a more robust analysis of the compatibility between different constraints. (4) It clarifies the model dependence of individual constraints. (5) It provides a more effective framework for testing whether nonstandard models can resolve inconsistencies between conflicting constraints.

A systematic outlier analysis of Hubble tension in the $H_0$-$\Omega_m$ parameter space was reported in Lin et al. (2020), as presented in Fig. 1.2. Lin's study highlighted several key findings. Constraints derived from various observations, despite differing in their degeneracy directions, converge in a common region centered around $H_0 \approx 68.5$ km/s/Mpc and $\Omega_m \approx 0.3$. The existence of this region is supported by measurements such as baryon acoustic oscillations, galaxy clustering, and the cosmic chronometer method. The local measurement of $H_0$ from Cepheid-calibrated Type Ia supernovae represents the most significant outlier, as it does not overlap with the common region suggested by other constraints. Similarly, time-delay strong-lensing measurements exhibit only marginal overlap, making them the next most significant outliers.

### 1.1.2 Halo Mass Function

The Universe follows a hierarchical structure formation process, wherein smaller structures form first and progressively merge to create larger ones. The distribution of these structures is

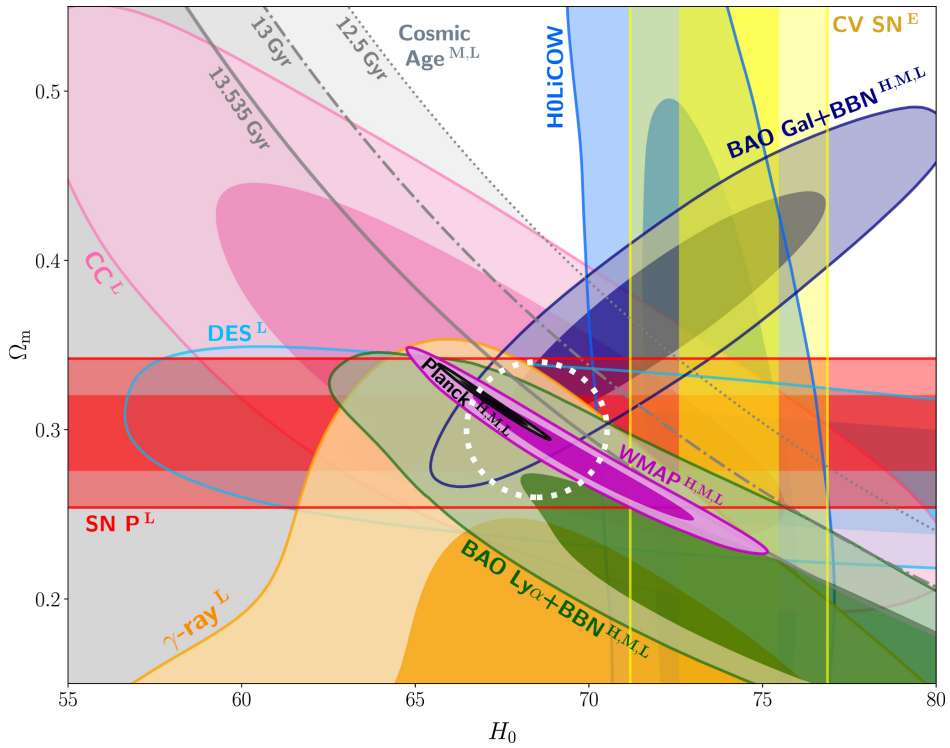


Figure 1.2: Different constraints in the $H_0$–$\Omega_m$ parameter space derived using the flat ΛCDM model. The dark and light contours denote the 68% and 95% confidence regions of each posterior, respectively, except for the cosmic-age bounds. Adapted from the work of Lin et al. (2020).

described by the halo mass function (HMF), which represents the number density of halos as a function of their mass. The HMF offers a crucial tool for understanding the formation and evolution of cosmic structures.

The theoretical prediction of the HMF is often derived from the Press–Schechter (PS) formalism (Press and Schechter 1974). According to this formalism, a collapse occurs when the overdensity $\rho/\bar{\rho}$ exceeds a critical value, $\delta_c$, which is determined based on the spherical collapse model. The PS mass function is defined as

$$\frac{dn}{dM} = \sqrt{\frac{2}{\pi}} \frac{\bar{\rho}}{M} \frac{\delta_c}{\sigma^2(M)} \frac{d\sigma(M)}{dM} \exp\left(-\frac{\delta_c^2}{2\sigma^2(M)}\right), \tag{1.6}$$

where $\bar{\rho}$ denotes the mean density of the Universe, and $\sigma(M)$ represents the variance of the density field, smoothed using a top-hat filter of mass $M$. The variance of the density field is defined as

$$\sigma^2(M) = \int_0^\infty \frac{1}{k} \Delta^2(k) W^2(kR) dk, \tag{1.7}$$

where $\Delta^2(k)$ denotes the power spectrum of the density field, and $W(kR)$ represents the Fourier transform of the top-hat filter.

The Sheth–Tormen (ST) mass function (Sheth et al. 2001) builds upon the PS formalism by incorporating a correction for the ellipsoidal collapse model. This modification results in a more accurate representation. Consequently, the ST mass function better fits the results derived from numerical simulations. The ST mass function is expressed as

$$\frac{dn}{dM} = A\sqrt{\frac{2a}{\pi}} \frac{\bar{\rho}}{M} \frac{\delta_c}{\sigma^2(M)} \left[1 + \left(\frac{\sigma^2(M)}{a\delta_c^2}\right)^p\right] \exp\left(-\frac{a\delta_c^2}{2\sigma^2(M)}\right), \tag{1.8}$$

where $A = 0.3222$, $a = 0.707$, and $p = 0.3$.

Fig. 1.3 illustrates the HMFs calculated using the PS (black line) and ST (blue line) formalisms at a redshift of $z = 20$. To improve the accuracy of HMF calculations, several alternative models have been proposed. For comparison, the above figure also includes HMFs derived from the models proposed by Reed et al. (2003) (orange line), Tinker et al. (2008) (red line), and Watson et al. (2013) (green line). As illustrated, the PS mass function predicts steeper slopes at the high-mass end, whereas the ST mass function produces a shallower slope.

The HMF serves as an important probe for studying the nature of DM, as the abundance of halos is sensitive to the properties of DM, particularly on small scales.

For instance, if DM retains residual thermal energy, the collapse process is modified by free-streaming effects. This phenomenon has been studied in the context of WDM (Schneider

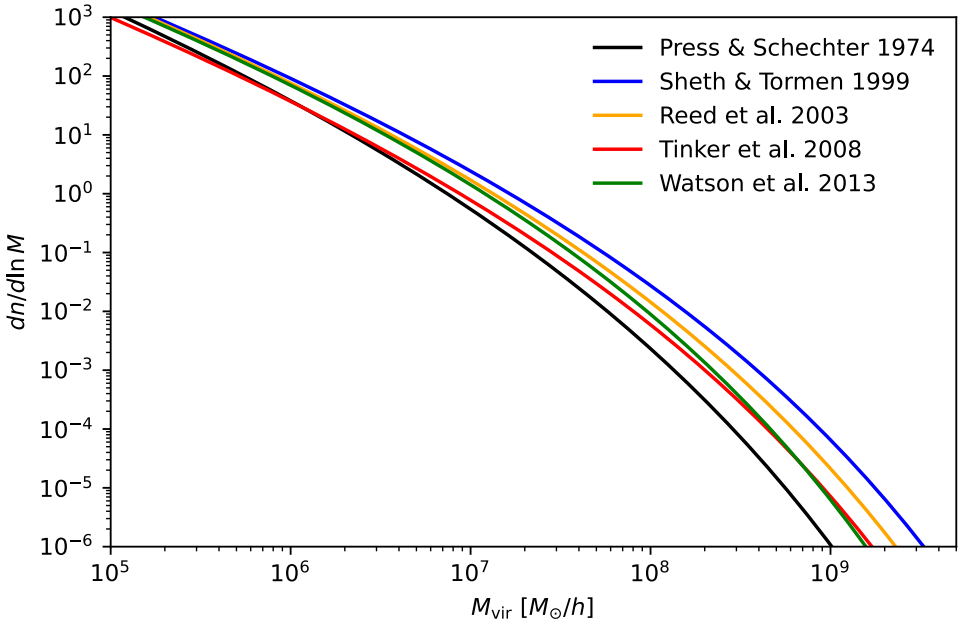


Figure 1.3: HMFs derived from different models at a redshift of $z = 20$, represented by various colors.

et al. 2013; Lovell et al. 2014), revealing that the HMF is suppressed on small scales compared to the predictions of the CDM model, depending on the mass of WDM particles. Consequently, the HMF can constrain the mass of WDM particles. A semi-analytical model of hidden DM (HiDM) has been developed by Lin et al. (2023). This model is more general and predicts a suppression of the HMF on small scales, similar to the WDM model. Hence, the HMF constrains the characteristic parameters of the HiDM model. Similarly, fuzzy DM (FDM) modifies the HMF through quantum pressure effects. Marsh and Silk (2014) demonstrated that the linear power spectrum of structure formation is suppressed below a characteristic scale in the FDM model. Furthermore, Schive et al. (2016) conducted collisionless N-body simulations with FDM initial conditions, while Kulkarni and Ostriker (2022) used an analytical model and observed fewer halos when employing sharp-k windows. Fully resolved FDM dynamics simulations have revealed that the HMF is sensitive to both initial conditions and the nonlinear dynamics of FDM (May and Springel 2023).

The direct impact of DM annihilation and decay on the structure of DM halos is generally expected to be minimal. This is because according to perturbation theory, the density of baryonic matter is much lower than that of DM. However, the influence of the structure of DM halos on energy injection from DM annihilation can be substantial (Mack 2014a). This topic will be covered in detail in the following section.

### 1.1.3 Alternative DM Histories

Efforts to understand the nature of DM have led to the exploration of alternative models that deviate from the conventional CDM paradigm, including those considering WIMPs. These alternative models often involve modifications to the thermal coupling of DM particles to baryons, which can substantially alter structure formation in the Universe. This section delves into the dynamics of the single-species HiDM model as a representative example.

The HiDM model represents a generalized hypothesis of DM, initially proposed in 2006 by Chen and Tye (2006) and was further developed by Lin et al. (2023). Unlike the standard assumption that DM was initially in thermal equilibrium with Standard Model particles in a hot "soup" HiDM exhibits an entirely different thermal history from Standard Model particles. The dynamic evolution of HiDM is governed by the following properties:

1. Given that HiDM is hidden from the Standard Model sector, its *entropy per unit comoving volume remains constant.*

2. Given the existence of only a single DM species, *the particle number per unit comoving volume also remains constant.*

Numerical solutions for the background evolution of HiDM have been derived for both thermal equilibrium and free-streaming cases. The results reveal minimal differences between the two scenarios, further indicating that both cases can be well approximated by a universal parameterized function of the scale factor $a$. This function is determined by the scale factor at the relativistic-to-nonrelativistic transition of DM particles, denoted by $\hat{a}$. Notably, the background evolution of HiDM is particularly sensitive to the transition time, which depends on the initial temperature-to-mass ratio. However, the evolution is relatively insensitive to other particle properties such as mass, intrinsic degrees of freedom, or initial chemical potential.

The fluctuation dynamics of HiDM differ from those in the standard CDM scenario. Specifically, when HiDM is relativistic, overdensities oscillate. If the relativistic-to-nonrelativistic transition occurs late enough, these oscillations can visibly suppress the formation of small-scale structures.

The suppressed mass scale in the presence of HiDM is expressed as

$$M_{\rm sup} \simeq \frac{4\pi}{3}\left(\frac{\pi}{k_{\rm sup}}\right)^3 \rho_m^0 = 1.6\times 10^{11} h^2 M_\odot \left(\frac{R_{\rm eq}^T}{0.001}\right)^{2.5}, \tag{1.9}$$

where $R_{\rm eq}^T$ denotes the characteristic parameter associated with the relativistic-to-nonrelativistic transition of DM particles, $\hat{a}$, which is defined as

$$R_{\rm eq}^T = \frac{\hat{a}}{a_{\rm eq}}. \tag{1.10}$$

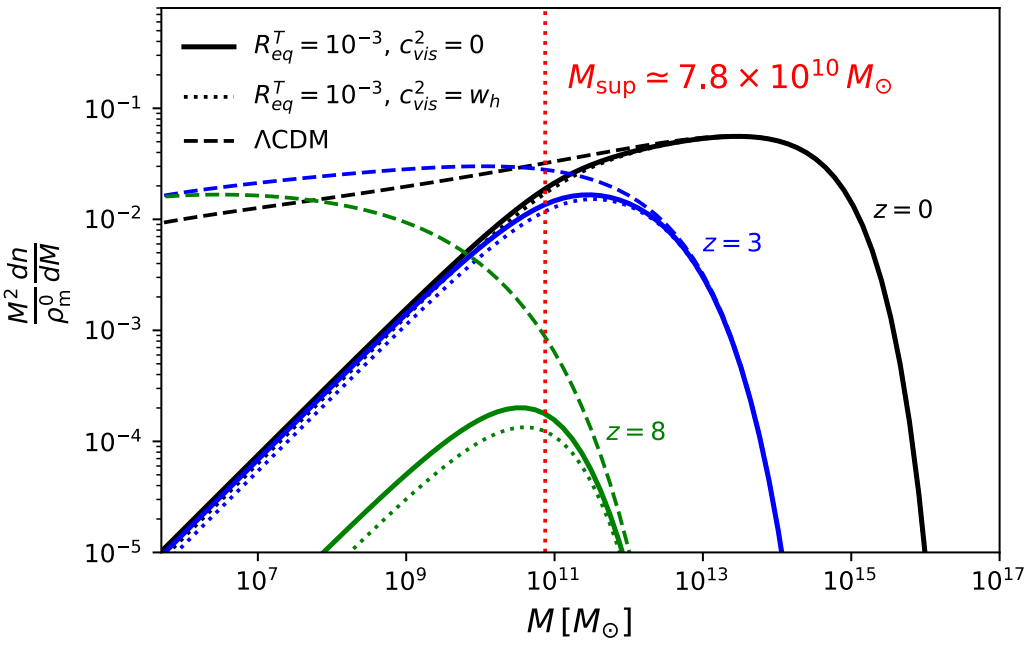


Figure 1.4: HMFs calculated using the extended PS formalism with HiDM. A suppressed mass scale, $M_{\rm sup}$, exists, below which the number of halos is reduced compared to the ΛCDM case at all times. Adapted from the work of Lin et al. (2023).

In the above equation, $a_{\rm eq} = 4.15\times10^{-5}/\Omega_m h^2$ represents the scale factor at matter–radiation equality in the standard CDM model. Furthermore, a value of $R_{\rm eq}^T < 1$ indicates that the transition occurred before the standard matter–radiation equality.

Fig. 1.4 illustrates the impact of the extended PS formalism on nonlinear structure formation, focusing on for calculating the HMF. The number of low-mass halos is substantially suppressed for masses below $M_{\rm sup}$ across all redshifts. This mass scale, $M_{\rm sup}$, remains independent of redshift owing to the suppression of the initial linear power spectrum. Such suppression influences the abundance of dwarf galaxies and other small-scale structures, potentially addressing some small-scale structure problems in the CDM model.

### 1.1.4 Streaming Velocity

In the early Universe, baryons remained coupled to the photon field until recombination, whereas DM had decoupled much earlier. This resulted in a relative velocity between DM and baryonic matter, known as the streaming velocity. At recombination, the root-mean-squared value of the streaming velocity was approximately 30 km/s (Tseliakhovich and Hirata 2010). This bulk relative motion substantially influenced early structure formation in the Universe on scales of a few comoving megaparsecs.

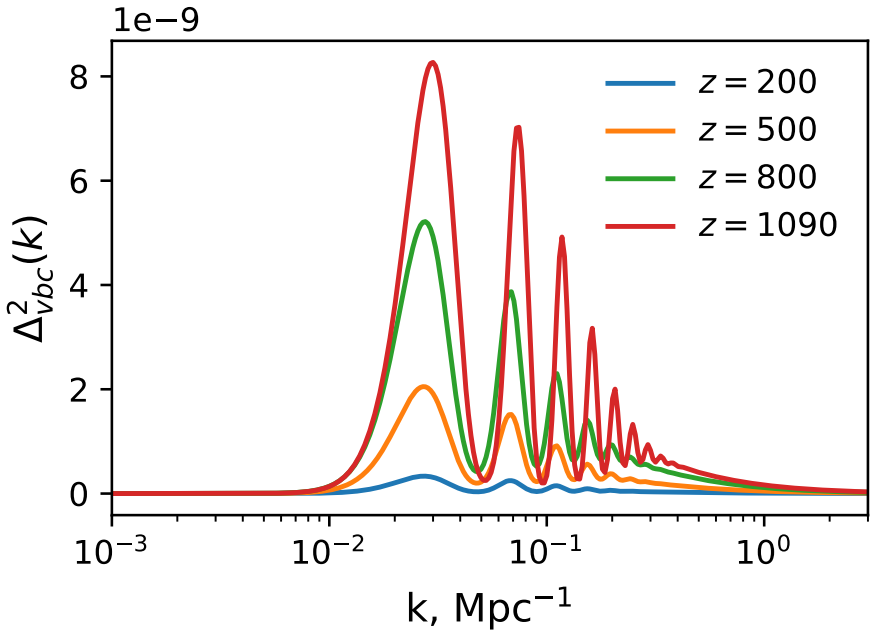


Figure 1.5: Variance in the relative velocity perturbation, $\Delta^2_{vbc}$, per log $k$ at different redshifts, recalculated using CAMB.

Tseliakhovich and Hirata (2010) demonstrated that streaming velocity fundamentally influenced the formation and evolution of small-scale structures in the early Universe. Their analysis revealed that streaming velocity suppressed the formation of small-scale structures, diminishing the small-scale power spectrum. Specifically, they observed a $\sim 15\%$ reduction in the power spectrum around the Jeans scale ($k_{\rm J} \sim 200\,{\rm Mpc}^{-1}$) at a redshift of $z = 40$. This suppression reduced the number of early halos and altered their spatial distribution, introducing a scale-dependent bias and stochasticity in the first halos. Further research by Dalal et al. (2010) revealed that streaming velocity potentially influences gas density and star formation, thereby impacting observable signatures.

The variance of streaming velocity is defined as

$$\Delta^2_{vbc}(k,z) = \frac{1}{2\pi^2} k^3 P_{vbc}(k,z)\,, \tag{1.11}$$

where $P_{vbc}(k,z)$ denotes the power spectrum of the relative velocity perturbation. The root-mean-square of the relative velocity is expressed as

$$v^2_{\rm rms}(z) = \int_0^\infty \frac{1}{k} \Delta^2_{vbc}(k,z) d\,k\,. \tag{1.12}$$

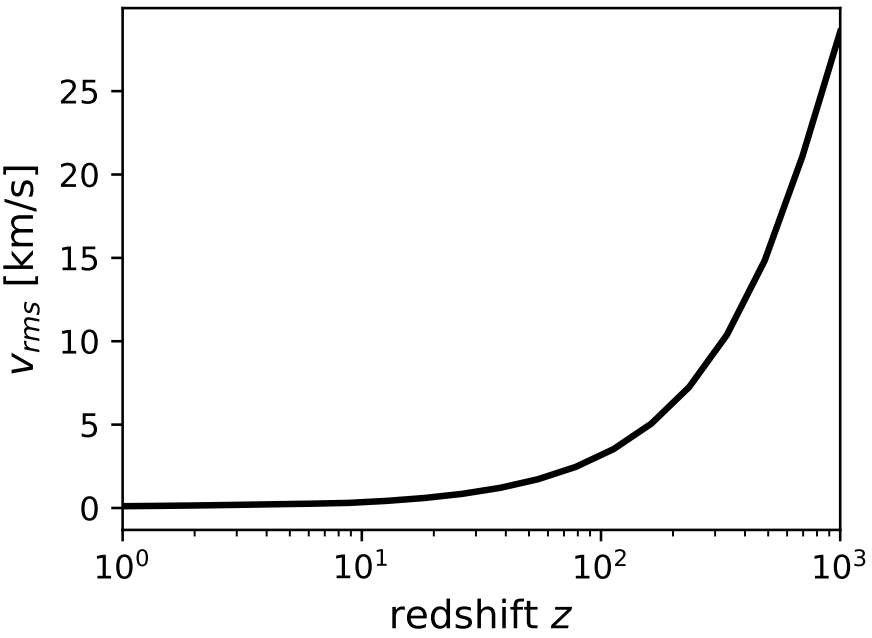


Figure 1.6: Root-mean-square value of the relative velocity as a function of the redshift.

Fig. 1.5 illustrates the variance in relative velocity perturbation, $\Delta^2_{vbc}$, as a function of the scale $k$. The plot was created using the cosmological code `CAMB` (Lewis and Challinor 2011), with the latest parameters derived from Planck observations. As depicted, the power spectrum of the relative velocity declines rapidly for $k > 0.5\,\mathrm{Mpc}^{-1}$, indicating that relative velocity effects are negligible on large scales.

Fig. 1.6 shows the root-mean-square (rms) of the relative velocity as a function of redshift given by Equation. 1.12. The relative velocity is largest at high redshifts and decreases as $(1+z)$ with the Universe evolves. At recombination redshift $z \approx 1000$, the relative velocity is about 30 km/s.

Numerical simulations conducted by Stacy et al. (2011) and Greif et al. (2011) confirm this effect, demonstrating that streaming velocity reduced gas fractions, which in turn suppressed star formation in the early Universe. Regions with higher streaming velocities formed stars later and with low efficiency. Further, in a theoretical study, Fialkov et al. (2012) developed a semi-analytical model to capture the impact of streaming velocities on the minimum cooling mass required for gas cooling and star formation. Notably, this model relates the value of streaming velocity to the minimum circular velocity, as follows:

$$V^2_{\mathrm{cool}} = V^2_{\mathrm{cool},0} + (\alpha v_{\mathrm{bc}})^2\,, \tag{1.13}$$

where $V_{\rm cool,0} = 3.714$ km/s represents the circular velocity of a halo in the absence of streaming velocity, and $\alpha = 4.015$ denotes the scale of the streaming velocity. Both parameters are derived from previous simulations. The above relationship suggests the suppression of star formation in low-mass halos.

Recent studies have extended the concept of streaming velocity to various contexts. For instance, Muñoz (2019) performed calculations of the 21-cm signal while considering streaming velocity to examine its effect. Their results revealed that considerations of streaming velocity during 21-cm signal calculations are essential. Moreover, Kulkarni et al. (2021) and Schauer et al. (2019b, 2021) developed comprehensive numerical simulations of early star formation. These simulations incorporated the effects of streaming velocity. Their results indicated that streaming velocity increases the required minimal cooling mass and leads to stronger suppression of star formation.

The impact of streaming velocity on structure formation can be quantified using the PS formalism as follows:

The number density of halos with mass $M$ at redshift $z$ is expressed as

$$n(M,z) = \sqrt{\frac{2}{\pi}} \frac{\bar{\rho}}{M} \frac{\delta_c}{\sigma^2(M,z)} \frac{d\sigma(M,z)}{dM} \exp\left(-\frac{\delta_c^2}{2\sigma^2(M,z)}\right), \tag{1.14}$$

where $\sigma(M,z)$ denotes the variance in the density field smoothed with a top-hat filter of mass $M$.

$$\sigma^2(M,z) = \int_0^\infty \frac{1}{k} \Delta^2_{vbc}(k,z) W^2(kR) dk, \tag{1.15}$$

where $W(kR)$ denotes the Fourier transform of the top-hat filter.

## 1.2 First Stars

The first stars, also known as Pop III stars, represent the earliest generation of stars formed in the Universe. The formation of these stars marked the end of the cosmic dark ages and the beginning of a transformative era in cosmic history. The first stars played a crucial role in shaping the reionization history of the Universe(Gnedin and Ostriker 1997; Loeb and Barkana 2001; Kitayama et al. 2004) and the production of heavy elements (Furlanetto and Loeb 2005; Wise et al. 2011), which led to the subsequent evolution of galaxies (Barkana and Loeb 2001a). Thus, investigating the first stars is important for understanding structure formation in the early Universe, which ultimately influenced the development of the present-day Universe.

High-redshift studies (Bromm et al. 2002; Bromm 2013a; Hirano et al. 2015) have demon-

strated that first stars formed within low-mass halos, with typical masses ranging from $10^5 \sim 10^6 M_\odot$, known as minihalos, at redshifts of $z \sim 10-30$. The formation of these stars was governed by structure formation and the rise in fluctuations. Consequently, their formation was directly influenced by small-scale physics, including parameters such as streaming velocity (Greif et al. 2011). In turn, the first stars exerted feedback on their surrounding gas, significantly affecting subsequent star formation and galaxy formation in various ways (Greif et al. 2010). Thus, understanding the formation of the first stars is vital for unraveling the complexities of small-scale physics, which remain uncertain in current cosmological research.

Simulations and theoretical studies have significantly advanced our understanding of the formation of the first stars. However, direct observations of these stars remain elusive. The JWST is expected to detect objects at very high redshifts. However, at present, its sensitivity is far below that required for observing individual first stars (Schauer et al. 2020). Gravitational lensing can magnify the light emitted from first stars, increasing the likelihood of their detection. However, the scarcity of sufficiently massive Pop III stars makes this method extremely challenging (Rydberg et al. 2013). Furthermore, distinguishing high-redshift Pop III galaxies from non-Pop III stellar populations is difficult. This process requires careful analysis of observational data (Trussler et al. 2023; Katz et al. 2023).

An alternative method for studying the first stars involves the analysis of the 21-cm signal of neutral hydrogen, arising from the spin-flip transition. This signal depends on the spin temperature, which is influenced by the formation of the first stars. When the first stars formed in the early Universe, they emitted abundant Lyman-$\alpha$ photons, which coupled the spin temperature of neutral hydrogen with the gas temperature through the Wouthuysen–Field effect, thereby altering the 21-cm signal. Furthermore, the X-ray radiation emitted by the first stars heated the IGM via photoionizations, causing the 21-cm signal to transition from absorption to emission. Previous studies have examined various other factors influencing the 21-cm signal, such as the initial mass function of the first stars (Gessey-Jones et al. 2022) and stellar feedback processes, such as the Lyman–Werner (LW) feedback (Fialkov et al. 2013a). Recent studies have further examined the influence of DM–baryon relative velocities on the 21-cm signal (Barkana 2016; Schauer et al. 2019a), highlighting its critical role in understanding the early universe. Observations of the 21-cm signal, therefore, provide rich information to constrain the formation processes of the first stars.

This section focuses on the current understanding of the formation processes of first stars. We begin by discussing the first-star formation mechanisms, including gas infall and cooling. We also outline the impact of streaming velocity on first-star formation. Additionally, we explore the feedback effects of the first stars. For more comprehensive discussions on these topics, readers are referred to reviews by (Loeb et al. 2008; Bromm 2013b; Klessen and Glover 2023).

### 1.2.1 Gas Infall and Cooling

#### Jeans Mass

In 1902, Sir James Hopwood Jeans assessed the stability of a gas cloud under its self-gravity and derived a criterion for its collapse, now known as Jeans instability. This instability describes the interplay between the thermal pressure of the gas and gravitational force. When the mass of the gas cloud exceeds the Jeans mass, its self-gravity overcomes the internal pressure, leading to gravitational collapse of the cloud.

On cosmological scales, the Jeans length scale, $\lambda_J$, is defined by two characteristic timescales: the free-fall timescale, $t_{\rm ff} = \sqrt{3\pi/32G\rho_0}$, and the pressure timescale, which represents the time required by sound waves to transverse the gas, $t_s = \lambda_J/c_s$. Gas collapse occurs when the gravitational free-fall timescale is shorter than the pressure timescale $t_{\rm ff} < t_s$.

Following recombination in the early Universe, the primordial gas was thermally coupled to CMB photons via Compton scattering. At this time, the pressure of the primordial gas was adequately to resist gravitational forces. However, at redshifts $z \lesssim 150$, the kinetic temperature of the gas decoupled from the CMB temperature. As the Universe expanded, the gas cooled nearly adiabatically, with its temperature scaling as $T_{\rm K} \propto a^{-2}$. In regions where the gas pressure became insufficient to counteract gravitational contraction, gas clouds collapsed into structured DM halos.

For a system comprising both DM particles and baryons, the total density is expressed as $\rho = \rho_B + \rho_{\rm DM}$. Based on linear perturbation theory, we can derive the following:

$$\frac{d^2\delta_X}{dt^2} + 2H\frac{d\delta_X}{dt} = 4\pi G\rho(\Omega_X\delta_X + \Omega_B\delta_B) \tag{1.16}$$

$$\frac{d^2\delta_B}{dt^2} + 2H\frac{d\delta_B}{dt} = 4\pi G\rho(\Omega_X\delta_X + \Omega_B\delta_B) - c_s^2\frac{k^2}{a^2}\delta_B\,, \tag{1.17}$$

where $\delta_X$ and $\delta_B$ denote the overdensities of DM particles and baryons, respectively, and $c_s$ represents the speed of sound in the gas which depends on the temperature of the gas.

When the gas temperature scales as $T \propto 1/a$, we have the following:

$$\frac{\delta_B}{\delta_X} \approx \frac{1}{1 + k^2/k_J^2}, \tag{1.18}$$

where $k_J = a\sqrt{4\pi G\rho}/c_s$ denotes the Jeans scale. At very high redshifts of $z > 150$, when the gas temperature is coupled to the radiation temperature via Compton scattering, the Jeans scale remains constant because $\sqrt{\rho/c_s^2} \propto a^{-1}$. Thus, at these epochs, the Jeans scale becomes independent of the redshift.

For calculations of the Jeans scale, the speed of sound in an ideal gas can be expressed as

$$c_s = \sqrt{\frac{5k_B T}{3\mu m_N}}, \tag{1.19}$$

where $k_B$ denotes the Boltzmann constant, and $\mu = 1.22$ represents the mean molecular weight of neutral primordial gas.

The Jeans wavelength is defined as

$$\lambda_J = c_s \sqrt{\frac{3\pi}{32G\rho_0}}. \tag{1.20}$$

Further, the Jeans mass, defined as the total mass in the Jeans scale, is

$$M_J = \frac{4}{3}\pi\rho_0 \left(\frac{\lambda_J}{2}\right)^3. \tag{1.21}$$

At redshifts of $z \lesssim 150$, the electron population in the gas becomes insufficient to sustain Compton scattering. Consequently, the gas temperature decouples from the CMB photons and decreases faster than the radiation temperature.

The filtering scale, introduced in Gnedin (2000), provides a general solution for the baryonic fraction. This solution matches the numerical solution at high $k$ values, even though it is derived for small $k$.

The relationship between the overdensities of DM particles and baryons is expressed as

$$\frac{\delta_B}{\delta_X} = 1 - \frac{k^2}{k_F^2} + \mathcal{O}(k^4). \tag{1.22}$$

The filtering scale, $k_F$, is defined as

$$\frac{1}{k_F^2} = \frac{1}{D_+(t)} \int_0^t dt' a^2(t) \frac{\ddot{D}_+(t') + 2H(t')\dot{D}_+(t')}{k_J^2(t')} \int_{t'}^t \frac{dt''}{a^2(t'')}. \tag{1.23}$$

Under the assumption of a flat universe, where the growth factor $D_+(t) = a(t)$, this equation simplifies to

$$\frac{1}{k_F^2} = \frac{3}{a} \int_0^a \frac{da'}{k_J^2(a')} \left[1 - \left(\frac{a'}{a}\right)^{\frac{1}{2}}\right]. \tag{1.24}$$

For gas in a halo with mass $M_h$ at redshift $z$, the total density is approximated as $\rho = \rho_{\rm DM} + \rho_{\rm B} \approx \rho_{\rm DM}$ because the baryonic density was negligible compared to the DM density in the early Universe. The speed of sound, $c_s$, in this gas is expressed as

$$c_s(z,M) = \sqrt{\frac{5k_B T_g(z,M)}{3\mu m_N}}, \tag{1.25}$$

where $T_g(z,M)$ denotes the gas temperature in a halo of mass $M$ at redshift $z$, $\mu = 1.22$ represents the mean molecular weight of neutral primordial gas, $m_N$ denotes the proton mass, and $k_B$ represents the Boltzmann constant.

The Jeans mass, $M_{\rm J}$, is defined as the mass enclosed within the Jeans scale:

$$M_{\rm J} = \frac{4}{3}\pi\rho\left(\frac{\lambda_{\rm J}}{2}\right)^3, \tag{1.26}$$

where $\lambda_{\rm J} = 2\pi/k_{\rm J}$ represents the Jeans wavelength.

To estimate the gas fraction within DM halos, computing the time-averaged Jeans mass (Gnedin 2000; Naoz and Barkana 2007; Barkana and Loeb 2011), also known as the filtering mass $M_{\rm F}$, is essential. The filtering mass is defined as

$$M_{\rm F}^{3/2}(a) = \frac{3}{a}\int_0^a M_{\rm J}^{3/2}(a)\,da'\left(1-\sqrt{\frac{a'}{a}}\right), \tag{1.27}$$

where $a$ denotes the scale factor, and $M_{\rm J}$ represents the Jeans mass at a given redshift.

The gas fraction inside halos, denoted as $f_{\rm gas}$, follows the equation (Gnedin 2000; Naoz and Barkana 2007) below:

$$f_{\rm gas}(z,M) = f_{\rm b,0}\left[1+\left(2^{\alpha/3}-1\right)\left(\frac{M_{\rm F}}{M}\right)^{\alpha}\right]^{-3/\alpha}, \tag{1.28}$$

where $M_{\rm F}$ denotes the filtering mass at redshift $z$ (Equation 1.27), and $\alpha = 0.7$, as recommended by Tseliakhovich et al. (2011). The cosmic baryon fraction, $f_{\rm b,0}(z)$, is expressed as

$$f_{\rm b,0}(z) = \frac{\Omega_b(z)}{\Omega_m(z)}(1+3.2\,r_{\rm LSS}), \tag{1.29}$$

where $\Omega_b(z)$ and $\Omega_m(z)$ denote the density parameters for baryons and DM particles, respectively, at redshift $z$, and $r_{\rm LSS}$ represents a redshift-dependent function defined in Naoz and Barkana (2007).

**Cooling Mass**

As the baryonic gas in the surrounding environment falls into the halo, the gas collides with itself. These collisions and rapid compression lead to the formation of shocks. DM halo shock-heated primordial gas within virial halos to high temperatures which is determined by the mass

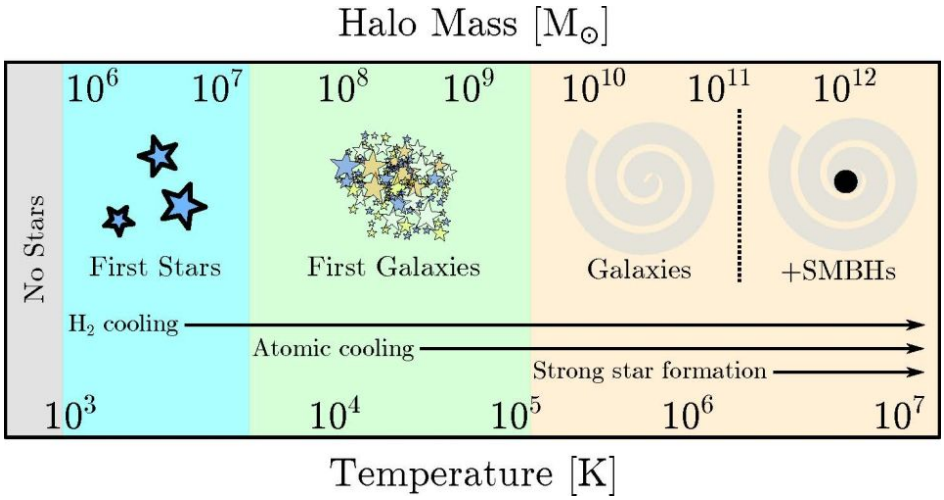


Figure 1.7: Gas cooling within halos. Small halos with $M \lesssim 10^5$ solar mass cannot support gas cooling and star formation. Conversely, halos with $10^6$ to $10^7$ solar mass support efficient $H_2$ cooling and the formation of first stars. Meanwhile, massive halos such as those forming supermassive black holes support the formation of massive objects. Adapted from Wise (2019).

of the halo. This gas, primarily comprising hydrogen and helium, required further cooling to enable star formation. This gas cooling occurred through various processes, including atomic line cooling and molecular line cooling.

**Atomic cooling** becomes significant at high temperatures ($T > 10^4$ K). At these temperatures, gas cools by emitting radiation at specific wavelengths, such as the Lyman-$\alpha$ line of hydrogen. This cooling mechanism is efficient in massive halos with virial masses $M_{\rm vir} > 10^8 M_\odot$. However, in lower-mass halos, atomic processes are not sufficient to cool the gas effectively.

**Molecular cooling** dominates at lower temperatures, where the gas cools by emitting radiation through the rotational and vibrational transitions of molecules. This process is effective in halos with $M_{\rm vir} \lesssim 10^7 M_\odot$ and supports the formation of the first stars.

In low-mass halos, gas cooling is predominantly driven by molecular cooling, with $H_2$ serving as the primary coolant. Generally, the cooling rate must be sufficient to lower the gas temperature, thereby enabling gravitational gas collapse and star formation. In this scenario, multiple factors influencing the cooling process, including the abundance of key elements (e.g., hydrogen, helium, and electrons) involved in $H_2$ production and cooling, as well as the reaction and cooling rates, which depend on the gas temperature $T_g$.

The minimum cooling mass, $M_{\rm cool}$, corresponds to the lowest mass of star-forming halos below which the gas is unable to cool efficiently and form stars.

The minimum cooling mass, $M_{\rm cool}$, corresponds to the critical virial temperature, $T_{\rm crit}$, at which cooling proceeds effectively. The relationship between halo mass and virial temperature

has been established by (Barkana and Loeb 2001b), as follows:

$$T_{\rm vir} = 1.98 \times 10^4 \left(\frac{\mu}{0.6}\right)\left(\frac{M}{10^8 h^{-1} M_\odot}\right)^{2/3}\left[\frac{\Omega_{m,0}}{\Omega_m}\right]^{1/3}\left(\frac{1+z}{10}\right) \mathrm{K}\,, \tag{1.30}$$

where $\mu$ denotes the mean molecular weight of fully neutral primordial gas, which has a value of approximately $\mu \approx 1.22$. By setting the virial temperature to $T_{\rm vir} = 10^4$ K, the atomic cooling threshold can be derived as

$$M_{\rm atom} \approx 1.83 \times 10^7 \left[\frac{\Omega_{m,0}}{\Omega_m}\right]^{-1/2}\left(\frac{1+z}{10}\right)^{-3/2} \mathrm{M}_\odot\,. \tag{1.31}$$

where $\Omega_{m,0}$ denotes the cosmic matter density today, and $\Omega_m$ is the cosmic matter density at redshift $z$.

### 1.2.2 Radiative Feedback

#### Lyman-Werner Feedback

When the first stars formed, they emitted abundant Lyman-Werner (LW) photons within the energy range of 11.2–13.6 eV. These photons dissociated molecular hydrogen within the primordial gas, suppressing further star formation.

In practice, LW photons increase the minimum cooling mass (O'Shea and Norman 2008; Safranek-Shrader et al. 2012; Schauer et al. 2021), thereby suppressing star formation in low-mass halos. Previous studies have incorporated the effects of LW feedback in simulations using fixed intensities (Machacek et al. 2001; Wise and Abel 2008) and derived the following relationship between cooling mass and the intensity of LW feedback:

$$M_{\rm cool}(z, F_{\rm LW}) = M_{\rm cool,0}(z)\left[1 + 6.96(F_{\rm LW})^{0.47}\right]\,, \tag{1.32}$$

where $M_{\rm cool,0}$ represents the cooling mass in the absence of LW feedback, and $F_{\rm LW} = 4\pi J_{\rm LW}$ denotes the LW flux, measured in units of $10^{-21}$ ergs s$^{-1}$ cm$^{-2}$ sr$^{-1}$ Hz$^{-1}$.

Recent high-resolution simulations have demonstrated the effect of LW feedback. For instance, Schauer et al. (2021) employed the `AREPO` moving-mesh cosmological hydrodynamics code to simulate the effects of LW photons at a redshift of $z \sim 17$ with intensities $0 \leq J_{\rm LW} \leq 0.1$. For these photons, their model accounted for self-shielding using the `TREECOL` algorithm proposed by Clark et al. (2011) and computed the effective self-shielding factor following the methodology proposed by Draine and Bertoldi (1996). Their results revealed minor differences under a weak background $J_{\rm LW} = 0.01$ and significant differences under a stronger background $J_{\rm LW} = 0.1$. These researchers examined two characteristic masses: the minimum mass threshold

($M_{\rm min}$) and average mass threshold ($M_{\rm ave}$). Both masses scale with the square root of the LW background intensity, expressed as

$$\begin{aligned} \log M_{\rm ave} &= 6.0174 \times (1 + 0.166 \times \sqrt{J_{\rm LW}}) \\ \log M_{\rm min} &= 5.562 \times (1 + 0.279 \times \sqrt{J_{\rm LW}}) \end{aligned} . \tag{1.33}$$

Similarly, Kulkarni et al. (2021) examined the formation processes of the first stars under UV (LW) radiation using the adaptive mesh refinement code ENZO. Their model incorporated the updated self-shielding prescription outlined by Wolcott-Green and Haiman (2019) and reaction rates detailed by Glover (2015). Their findings revealed that the minimum cooling mass increases as redshift decreases, following a power law relationship, $(1+z)^{-1.58}$, when $J_{\rm LW} = 0$. For non-zero LW backgrounds, the cooling mass is defined as

$$M_{\rm cool}(J_{\rm LW}) = M_0 (1 + J_{\rm LW})^{\beta_1} \left( \frac{1+z}{21} \right)^{\alpha(J_{\rm LW})} , \tag{1.34}$$

where $M_0 = 1.96 \times 10^5 M_\odot$, $\beta_1 = 0.80$ and $\alpha(J_{\rm LW}) = 1.64(1 + J_{\rm LW})^{0.36}$.

**X-ray Feedback**

X-ray feedback exerted two distinct effects on molecular cooling in the early Universe: 1. Positive Feedback through Ionization: X-ray photons ionized the IGM, increasing the electron fraction. The resulting free electrons catalyzed the formation of molecular hydrogen via the $H^-$ channel. Ultimately, the abundance of $H_2$ enhanced cooling efficiency and promoted star formation in low-mass halos. 2. Negative Feedback through Heating: X-ray heating raised the temperature of the IGM, increasing the Jeans mass and inhibiting gas cloud collapse into halos. Overall, elevated temperatures complicated the gravitational collapse of gas clouds, thereby suppressing star formation.

Ricotti (2016) conducted an analytical study on the combined effects of LW feedback and X-ray radiation. During their analysis, they identified a global feedback loop wherein positive feedback dominates at low X-ray intensities, whereas negative feedback dominates at high X-ray intensities. The X-ray background radiation emitted by Pop III stars indirectly influences their formation rates. Notably, Ricotti (2016) identified a critical X-ray background intensity relative to the LW background.

Park et al. (2021) further explored these effects through simulations considering varying LW and X-ray radiation intensities. Their results confirmed the critical X-ray background intensity identified by Ricotti (2016). They also observed that X-rays reduce the critical mass more substantially under strong LW backgrounds. Additionally, the effects of X-ray self-shielding were found to be negligible in most cases. They also demonstrated that X-ray irradiation

enhanced cooling within collapsing protostellar cores by increasing the $H_2$ fraction, ultimately reducing the speed of sound in gas and accretion rates and consequently lowering the final masses of Pop III stars.

Recent simulations conducted by Hegde and Furlanetto (2023) examined the effects of X-ray feedback on the minimum halo mass required for star formation. Their findings highlighted the importance of X-ray feedback at redshifts $z \lesssim 15$. Specifically, at low X-ray intensities, their simulations demonstrated that positive feedback from photoionization dominates, lowering the minimum mass threshold for star formation. However, as the X-ray intensity increases, heating effects take precedence, raising the minimum mass threshold for star formation. This demonstrates a clear transition from positive to negative feedback with increasing X-ray background intensity.

**Streaming Velocity**

Previous studies have examined the impact of streaming velocity on the formation of first stars using high-resolution simulations (Greif et al. 2011; Stacy et al. 2011). Their findings indicate that streaming velocity increases the minimum cooling mass threshold for star formation, thereby suppressing star formation. Fialkov et al. (2012) expressed the cooling threshold in terms of the halo circular velocity, $V_{\rm cool}$, which depends on the minimum circular velocity, $V_{\rm cool,0}$, and streaming velocity, $v_{\rm bc}$. This relationship is expressed as

$$V_{\rm cool}^2 = V_{\rm cool,0}^2 + (\alpha v_{\rm bc})^2.\,, \tag{1.35}$$

where $V_{\rm cool,0}$ denotes the minimum circular velocity without streaming velocity effects.

Recent simulations (Kulkarni et al. 2021; Schauer et al. 2019b, 2022) have further explored Pop III star formation by considering the effects of both streaming velocity and LW radiation feedback. In particular, Schauer et al. (2021) derived the relationship between the cooling mass and streaming velocity as follows:

$$\begin{aligned} \log M_{\rm ave} &= \log M_0 + 0.4159 \times \frac{v_{\rm bc}}{\sigma_{\rm rms}} \\ \log M_{\rm min} &= \log M_0 + s \times \frac{v_{\rm bc}}{\sigma_{\rm rms}} \end{aligned}, \tag{1.36}$$

where $M_0$ denotes the cooling mass without streaming velocity effects, $\sigma_{\rm rms}$ represents the root-mean-square value of the streaming velocity, and $s = 0.614(1-0.560\sqrt{J_{\rm LW}})$ accounts for the LW feedback effect.

Meanwhile, Kulkarni et al. (2021) observed that the minimum cooling mass increased with streaming velocity. Notably, the cooling mass found to be

$$
\begin{aligned}
M_{\rm cool}(J_{\rm LW}, v_{\rm bc}) &= M_0 (1+J_{\rm LW})^{\beta_1} (1+v_{\rm bc}/30)^{\beta_2} \\
&\quad \times (1+J_{\rm LW} v_{\rm bc}/3)^{\beta_3} \left(\frac{1+z}{21}\right)^{\alpha(J_{\rm LW}, v_{bc})} \\
\alpha(J_{\rm LW}, v_{bc}) &= 1.64(1+J_{\rm LW})^{0.36}(1+v_{bc}/30)^{-0.62} \\
&\quad \times (1+J_{\rm LW} v_{bc}/3)^{0.13}
\end{aligned}
, \tag{1.37}
$$

where $M_0 = 1.96 \times 10^5 M_\odot$, $\beta_1 = 0.80$, $\beta_2 = 1.83$, $\beta_3 = -0.06$.

## 1.3 DM Constraints

### 1.3.1 Overview

Fritz Zwicky's study of the Coma cluster of galaxies in 1933 provided the first notable evidence for the existence of DM. Applying the virial theorem to the Coma cluster, Zwicky calculated a substantially higher mass-to-light ratio compared to that observed in the local solar neighborhood, suggesting the presence of unseen mass. Around the same time, in 1932, Jan Oort studied the rotational curves of stars in the Milky Way, finding evidence supporting DM. Specifically, Oort observed that the rotational speeds of stars in the outer regions of the galaxy were much higher than expected based on the visible mass. Recently, with advancements in cosmology from both theoretical and observational perspectives, strong evidence supporting the existence of DM has been obtained from various sources. Consequently, DM has become a cornerstone of the standard cosmological framework. One of the most recent evidence for DM is provided by the high-precision CMB data recorded by the Planck satellite.

Despite extensive evidence supporting the existence of DM, its nature remains unclear. DM generally interacts very weakly with light, making it invisible to telescopes and other instruments that rely on electromagnetic radiation for detection. This lack of direct DM detection has resulted in a wide range of theoretical DM candidates. An alternative explanation to the existence of DM is provided by a modification of gravitational theory, such as modified Newtonian dynamics (MOND) (McGaugh 2015). While MOND successfully explains the rotational curves of galaxies without invoking DM particles, it has been ruled out by observations such as the Bullet Cluster (Clowe et al. 2004) and the CMB structure (Dodelson 2011).

Massive compact halo objects (MACHOs), such as black holes, brown dwarfs, and neutron stars, were once considered plausible DM candidates. These objects emit little to no light. However, searches for MACHOs have revealed that they cannot account for the observed amount of DM in the Universe.

Currently, the prevailing hypothesis is that DM comprises a new type of particle that in-

teracts very weakly with ordinary matter. This idea is supported by the failure of the Standard Model of particle physics to offer a viable candidate for the primary component of DM. Considerable theoretical efforts have been devoted to the proposition of new particles as DM constituents. However, stringent observational constraints limit the plausible properties of these candidates (Taoso et al. 2008).

The most popular DM candidates include WIMPs, axions, and sterile neutrinos. Among these, WIMP are particularly compelling as they naturally explain the observed DM abundance.

Ultralight DM (ULDM), also known as FDM, is an intriguing DM candidate, characterized by extremely light bosons with masses in the range of $10^{-22}$ to $10^{-20}$ eV/$c^2$. ULDM effectively addresses the core-cusp problem as the quantum pressure of its particles smooths out the density distribution of DM halos. Additionally, ULDM provides the minimum DM halo mass threshold for star formation, offering a solution to the missing satellites problem (Khlopov et al. 1985). ULDM signals lie far below current detection thresholds, making direct detection challenging. On cosmological scales, ULDM suppresses small-scale mass fluctuations relative to CDM, which alters galaxy formation processes and can be probed in a Lyman-$\alpha$ forest (Hui et al. 2017). Moreover, if ULDM suppresses mass fluctuations on minihalo scales, which are beyond the limits of current Lyman-$\alpha$ forest observations, ULDM detection based on the 21-cm signal may become feasible in the future (Kadota et al. 2014; Shimabukuro et al. 2020).

This section outlines the current constraints on the direct and indirect detection of DM, along with prospects for future experiments aimed at DM detection.

### 1.3.2 Direct Detection

The direct detection of DM relies on the measurement of nuclear recoils induced by the scattering of DM particles from nuclei. Given that DM particles are expected to be electrically neutral, their interactions with electrons are negligible. However, they can transfer energy to nuclei, producing quantifiable nuclear recoils. Major experimental efforts toward the direct detection of DM have focused on massive DM candidates, such as WIMPs. Lighter DM particles such as axions can also be considered. However, compared to WIMPs, axions are substantially lighter and hence cannot transfer adequate energy to nuclei to generate detectable signals.

The expected number of events in a direct DM detection experiment with a live time $T$ and detection efficiency $\epsilon$ is expressed as

$$N = T \int_{E_{low}}^{E_{high}} dE_R \epsilon(E_R) \frac{dR}{dE_R}, \tag{1.38}$$

where $E_R$ denotes the energy of nuclear recoil, and $dR/dE_R$ represents the differential

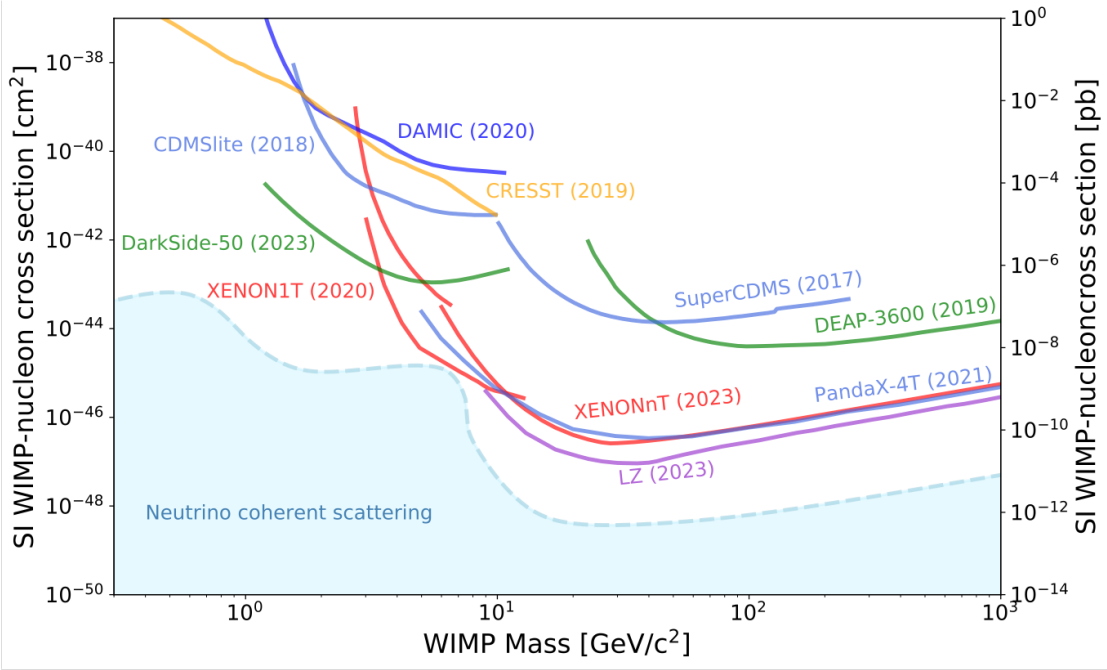


Figure 1.8: Most recent results of spin-independent WIMP–nucleus scattering cross-sections, derived from direct detection experiments. Adapted from Navas et al. (2024).

scattering rate, which depends on the WIMP–nucleus scattering cross-section.

The energy range of detectable events is determined by the energy threshold of the experiment. WIMPs with masses $m_{DM} < 1$ GeV/$c^2$ fail to produce detectable nuclear recoils, complicating direct DM detection in this region of parameter space.

Figure 1.8 illustrates the latest results of spin-independent WIMP–nucleus scattering cross-sections obtained from direct detection experiments, imposing the most stringent constraints in the 10–100 GeV range. The DAMA experiment (Bernabei et al. 2010, 2018), using NaI scintillators for model-independent observations of annual modulation, has reported a 12.9$\sigma$ detection in the 2–6 kVee (electron-equivalent energy) energy range, based on 20 years of data. However, this result is inconsistent with those of other experiments. For instance, although COSINE-100 (Adhikari et al. 2019) and ANAIS-112 (Amaré et al. 2021) used similar detection tools, COSINE-100 reported a potential null result, whereas ANAIS-112 confirmed a null result at the 99% level.

The detection of massive DM particles above 10GeV/$c^2$ primarily relies on noble gas detectors, particularly xenon-based detectors such as PandaX-4T (Meng et al. 2021), LUX-ZEPLIN (LZ) (Aalbers et al. 2023), and XENONnT (Aprile et al. 2023) and argon-based detectors such as DEAP-3600 (Ajaj et al. 2019) and DarkSide-50 (Agnes et al. 2023). Conversely, for the detection of lighter DM candidates ($m_{\mathrm{DM}} \lesssim 5$ GeV/$c^2$), cryogenic detectors, such as EDELWEISS using

Ge (Hehn et al. 2016), SuperCDMS using Si/Ge (Agnese et al. 2018), and CRESST-III using $CaWO_4$ (Abdelhameed et al. 2019), prove more sensitive. Meanwhile, ionization detectors, such as CDEX (Liu et al. 2019), NEWS-G (Arnaud et al. 2018), SENSEI (Abramoff et al. 2019), and DAMIC (Aguilar-Arevalo et al. 2020), can detect energy thresholds down to single-electron levels, enabling the search for sub-gigaelectronvolt DM. Directional detectors, such as MIMAC (Santos et al. 2011) and DRIFT (Battat et al. 2017), focus on the directional information of nuclear recoils. These detectors have the potential to probe cross-sections below the neutrino floor, even under low exposure.

### 1.3.3 Indirect Detection

Indirect detection offers an alternative approach for probing the properties of DM. Its primary advantage lies in its potential to complement direct detection methods. For instance, while direct DM detection techniques are effective in the gigaelectronvolt to teraelectronvolt energy range, they suffer from poor sensitivity in the kiloelectronvolt to gigaelectronvolt range (Undagoitia and Rauch 2015). Unlike direct DM detection, indirect DM detection seeks the byproducts of DM annihilation or decay, such as gamma rays, cosmic rays, and positrons. The observable signals emitted by these byproducts are closely linked to astrophysical processes, which can both simulate and help the interpretation of potential DM signatures.

The rate of DM decay is mathematically expressed as

$$\Gamma_{\text{decay}} = \frac{\rho_{\text{DM}}}{m_{\text{DM}}} \frac{1}{\tau_{\text{DM}}}, . \tag{1.39}$$

Meanwhile, the rate of DM annihilation is defined as

$$\Gamma_{\text{anni}} = s \frac{\rho_{\text{DM}}^2}{m_{\text{DM}}^2} \langle \sigma v \rangle, \tag{1.40}$$

where $\tau_{\text{DM}}$ denotes the DM particle lifetime before decaying, $\rho_{\text{DM}}$ denotes the DM density, $m_{\text{DM}}$ represents the DM mass, $\langle \sigma v \rangle$ signifies the thermally averaged annihilation cross-section of DM, and $s$ is a factor that assumes a value of 1/2 if a DM particle annihilates with its antiparticle or 1/4 if the DM particle is a Majorana particle (i.e., the DM particle is its own antiparticle).

Generally, the successful detection of DM annihilation or decay signals requires a DM density that is sufficiently high to produce quantifiable effects. Given that DM annihilation signals scale with $\rho^2$, high-density regions, such as the centers of galaxies, are anticipated to yield strong signals. Dwarf spheroidal galaxies (dSphs) also represent popular targets for indirect DM detection owing to their high DM content and low gas concentration. Consequently,

the gamma-ray and X-ray emissions of dSphs include distinct baryonic backgrounds. Although DM signals emitted from dSphs are anticipated to be substantially weaker than those from the Galactic Center (GC) (Daylan et al. 2016), dSphs still serve as independent and reliable DM probes.

Gamma rays are among the most promising signatures of DM annihilation. The spectra of the resulting photons depend on the annihilation channel. When DM particles directly annihilate into photons, they typically produce monoenergetic photons with energies near the rest mass of the DM particles. For massive DM particles in the gigaelectronvolt to teraelectronvolt energy range, very-high-energy gamma rays serve as compelling signatures. This is because only limited known astrophysical processes generate gamma rays with energies above the gigaelectronvolt scale.

To date, numerous experiments have focused on detecting gamma rays originating from DM annihilation near the GC. These include Fermi-LAT (Foster et al. 2023), MAGIC (Abe et al. 2023), HESS (Abdallah et al. 2018), and VERITAS (Ryan 2023). These experiments offer high energy resolutions and sensitivities across the ten gigaelectronvolt to hundreds of teraelectronvolt range. The findings of these experiments have capped the upper limits of the DM annihilation cross-section at $\langle \sigma v \rangle \lesssim 10^{-28} \sim 10^{-30}$ cm$^3$/s.

As detailed before, dSphs also represent critical targets for experiments aimed at detecting gamma rays emitted from DM annihilation. Initially identified in surveys such as the Sloan Digital Sky Survey and the Dark Energy Survey, these galaxies have been extensively analyzed using gamma-ray telescopes, such as Fermi-LAT (Di Mauro et al. 2023), HAWC (Albert et al. 2018), VERITAS (Acharyya et al. 2024), and MAGIC (Acciari et al. 2022). Depending on the assumed DM density profiles, the DM annihilation cross-section limits in dSphs can reach $\langle \sigma v \rangle \sim 10^{-23} \sim 10^{-24}$ cm$^3$/s (Hiroshima et al. 2019).

When DM particles annihilate into neutrinos, the resulting signals can be detected using neutrino telescopes. Generally, DM annihilation within high-density regions such as the Earth's core, the Sun, or the galactic halo can produce detectable neutrinos (Pérez de los Heros 2017). IceCube, a ground-based telescope, detects neutrinos through Cherenkov radiation. This telescope is sensitive to neutrinos with energies greater than 10 GeV, making it suitable for detecting DM particles with masses ranging from teraelectronvolts to petaelectronvolts. While such DM signals are yet to be detected, IceCube has constrained the velocity-averaged annihilation cross-section into neutrinos to $\langle \sigma v \rangle \lesssim 10^{-23}$ cm$^3$/s for petaelectronvolt-scale DM particles (Abbasi et al. 2023). Similar results have been obtained from ANTARES (Bouta et al. 2021), and further improvements are anticipated from next-generation neutrino telescopes such as KM3NeT (Šaina et al. 2023), P-ONE (Agostini et al. 2020), and IceCube-Gen2 (Aartsen et al. 2021).

Positrons or antiprotons that cannot be accounted for by standard astrophysical processes may originate from DM annihilation or decay. These particles can be detected using charged-particle detectors such as PAMELA (Donato et al. 2009) and AMS-02 (Cui et al. 2017; Krommydas and Cholis 2023). Experiments using these detectors are particularly sensitive to DM particles with masses $m_{\rm DM} > 10$ GeV and impose stringent conditions on DM particles with masses $m_{\rm DM} \gtrsim 80$ GeV. These constraints are more restrictive than those derived from the gamma-ray analysis of dSphs. The above experiments have constrained cross-section limits to $\langle \sigma v \rangle \lesssim 10^{-26}$ cm$^3$/s for the $b\bar{b}$ annihilation channel, with slightly weaker limits for channels such as $e^+e^-$ and $\mu^+\mu^-$.

The 21-cm signal provides a unique observational window into the reionization history of the Universe and is also regarded an important probe in the field of particle physics. Telescopes such as SARAS (Singh et al. 2017, 2022) and LEDA (Bernardi et al. 2016) offer high-resolution measurements of the global redshifted brightness temperature and are anticipated to play pivotal roles in the observation of the 21-cm signal from the early Universe. Similarly, radio telescopes such as LOFAR (Patil et al. 2017), HERA (DeBoer et al. 2017), and the upcoming SKA (Ciardi et al. 2015) are capable of setting stringent upper limits on the 21-cm power spectrum at high redshifts, thereby aiding in constraining models of reionization and uncovering the properties of the early Universe.

The EDGES collaboration reported the detection of a global 21-cm absorption feature at a redshift of $z \approx 17$, corresponding to a frequency of around 78 MHz Bowman et al. (2018). This unexpectedly deep signal suggests that the IGM may be colder than that predicted by standard cosmological models. If confirmed, this finding could provide insights into critical constraints on interactions among DM particles and baryons (Barkana 2018; Liu et al. 2019).

Certain DM candidates, such as WDM, exhibit a suppressed power spectrum on small scales, which delays the formation of galaxies. While these effects are observable using cosmological probes such as the Lyman-$\alpha$ forest, they can be easily detected using the 21-cm signal when spectral suppression extends down to the scale of minihalos. Theoretical analyses predict that future observations of 21-cm line fluctuations will help identify constraints on the properties of DM candidates, such as WDM (Sekiguchi and Tashiro 2014; Sitwell et al. 2014) and FDM (Kadota et al. 2014; Shimabukuro et al. 2020). Recent studies, based on the EDGES result, have reported a value of $m_{\rm TH} > 6.1$ keV for the WDM mass and a value of $m_a > 8 \times 10^{-21}$ eV for the ultralight axion mass (Schneider 2018). Primordial black holes emit UV photons, which ionize neutral hydrogen and potentially alter the globally averaged signal, influencing the reionization process (Hektor et al. 2018; Mena et al. 2019). Furthermore, the 21-cm signal is sensitive to the annihilation of DM particles. Such DM annihilation can deposit energy into the IGM, raise the medium's temperature, affect the ionization fraction, and produce Ly-$\alpha$ photons. However, the

specific effects of DM annihilation depend on the types of DM particles and can be probed using the 21-cm signal (Furlanetto et al. 2006; Valdes et al. 2007a). This topic will be reviewed in Chapter 4.

CHAPTER

# 2

# DARK MATTER ANNIHILATION AND COSMIC STRUCTURE

## 2.1 DM Annihilation Models

This section briefly introduces the fundamental assumptions underlying DM annihilation and offers insights into energy deposition in the primordial gas.

DM annihilation proceeds under the premise that DM particles (denoted by $\chi$) interact with one another and annihilate into Standard Model particles such as photons, neutrinos, or electrons, depending on the annihilation channel. The particles produced by annihilation subsequently interact with the IGM. In scenarios where DM particles annihilate into photons or electrons, these secondary particles interact with the IGM primarily through ionization, excitation, or other physical processes, depositing energy that heats the gas and ionizes neutral hydrogen. This energy deposition alters the thermal and ionization history of the primordial gas.

Energy deposition from DM annihilation influences both the IGM and other cosmological phenomena. For instance, the heating and ionization of the IGM can delay the formation of the first stars and galaxies, thereby shifting the timeline of cosmic reionization. These processes also leave observable imprints on the CMB power spectrum and the global 21-cm signal,

offering new avenues to test and constrain DM models.

The process of DM annihilation can be mathematically expressed as

$$\chi\chi \rightarrow b\bar{b}\,, \tag{2.1}$$

where $b, \bar{b}$ denotes the resulting Standard Model particles.

The DM annihilation rate per unit volume and time, $p$, is defined as the product of the annihilation cross-section, $\sigma$, and the number densities of the two DM particles:

$$p = \langle\sigma v\rangle n_1 n_2\,, \tag{2.2}$$

where $n_1$ and $n_2$ denote the number densities of two distinguishable DM particles, and $\langle\sigma v\rangle$ represents the average-velocity-weighted annihilation cross-section.

For identical DM particles, such as Majorana particles (which are their own antiparticles), the annihilation rate depends on the square of the number density, $n$, of the DM particles:

$$p = \frac{1}{2}\langle\sigma v\rangle n^2\,. \tag{2.3}$$

Here, the factor $\frac{1}{2}$ accounts for the double counting of particle pairs during annihilation.

### 2.1.1 Cross Section

Despite significant efforts toward the examination of the properties of DM, its fundamental nature remains elusive. The annihilation of DM is possible.

The annihilation rate of DM is proportional to the average-velocity-weighted cross-section, $\langle\sigma v\rangle$, which depends on the DM mass ($m_{\mathrm{DM}}$) and temperature ($T$). In most cases, the above cross-section can be expanded as a power series of velocity $v$:

$$\langle\sigma v\rangle = \sigma_0 + \sigma_2 v^2 + \sigma_4 v^4 + \cdots\,, \tag{2.4}$$

where $\sigma_i$ denote model-dependent coefficients. In the CDM paradigm, where the average velocity $v \ll 1$, the cross-section is dominated by the first term $\sigma_0$, which is independent of velocity. This phenomenon is referred to as s-wave annihilation. The second term, proportional to $v^2$, corresponds to p-wave annihilation, while the third term, proportional to $v^4$, corresponds to d-wave annihilation. Owing to the low velocities involved, these higher-order terms are difficult to constrain using current data. Consequently, this dissertation exclusively focuses on s-wave annihilation. The cross-section of DM annihilation is determined solely by the type of DM.

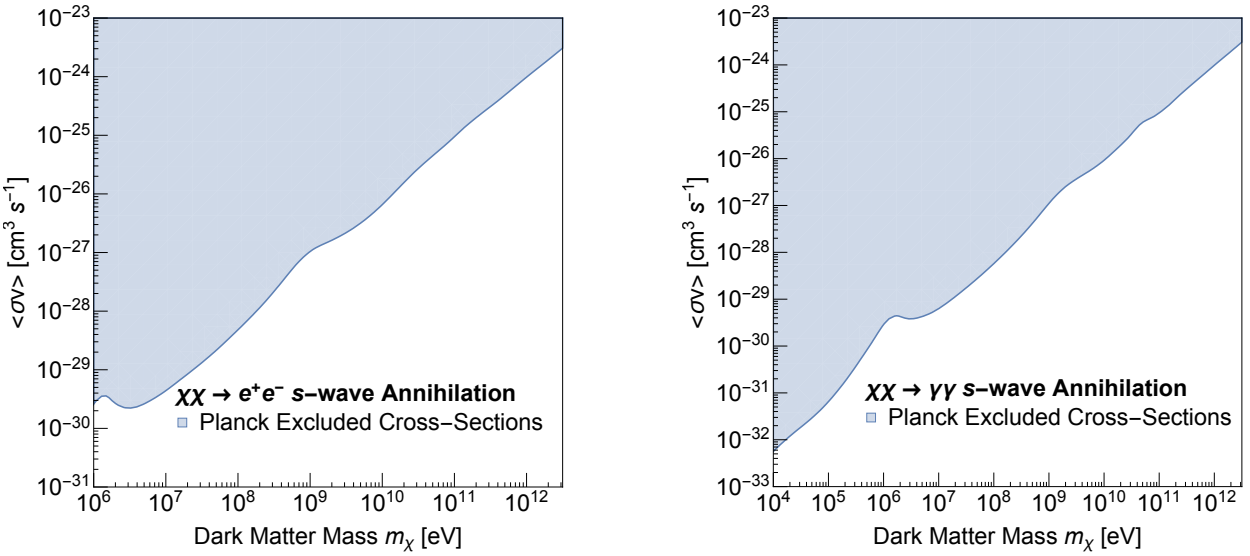


Figure 2.1: 95% excluded cross-section based on Planck's upper limit, using the TT, TE, EE+lowP Planck likelihood. The left panel shows the constraints on s-wave annihilation into $e^+e^-$; the Right panel shows the constraints on s-wave annihilation into $\gamma\gamma$. Adapted from Liu et al. (2016).

Given the average-velocity-weighted cross-section, $\langle\sigma v\rangle$, the DM annihilation rate can be derived as

$$p_{\rm ann} = \frac{\langle\sigma v\rangle}{m_{\rm DM}}\rho^2_{\rm DM}\,, \tag{2.5}$$

where $\rho_{\rm DM}$ denotes the DM density.

Fig. 2.1 illustrates the relationship between the annihilation cross-section and DM mass for s-wave annihilation. The power associated with DM annihilation is described as

$$p_{\rm ann} \leq 4.1\times10^{-28}\,{\rm cm^3\,s^{-1}\,GeV^{-1}}\,, \tag{2.6}$$

where $p_{\rm ann} = f_{\rm eff}\langle\sigma v\rangle/m_{\rm DM}$ (Collaboration et al. 2014; Liu et al. 2016). Furthermore, $f_{\rm eff}$ represents a constant that approximates the deposited energy fraction, which depends on the properties of the DM particles and cosmological parameters.

### 2.1.2 Energy Deposition

According to current experimental constraints, the interactions between DM particles and baryons are extremely weak. However, DM annihilation is regarded as one of the primary mechanisms through which DM particles interact with Standard Model particles and deposit

energy into the IGM.

When DM particles annihilate into Standard Model particles, such as electrons, positrons, or gamma rays, these primary particles either decay or interact with the surrounding matter and radiation. These interactions produce secondary products, such as lower-energy photons, which further interact with their environment. Overall, the interactions of these primary and secondary particles with their environment influence the energy deposition profile of each annihilation channel.

The primary processes for energy deposition vary by particle type:

- **Electrons and Positrons**: Depending on their energy, electrons and positrons interact with baryons through mechanisms such as Compton scattering, electron ionization, Coulomb scattering, or inverse Compton scattering (ICS) with background radiation.
- **Gamma Rays**: Leveraging their speed and low cross-section, high-energy gamma photons traverse long distances without significant absorption. However, they can engage in processes such as pair production and photoionization under certain conditions.
- **Neutrinos**: Owing to their extremely weak interactions with Standard Model particles, neutrinos contribute minimally to local energy deposition. However, they may leave imprints in dense environments such as stellar cores or become detectable through high-resolution experiments.

The mechanisms of energy deposition from DM annihilation in primordial gas can be categorized as heating, which represents the primary channel for such energy deposition, and ionization and excitation. When DM particles annihilate into particles such as electrons and positrons, these primary particles interact with the surrounding medium, transferring kinetic energy and thus raising the gas temperature. Meanwhile, high-energy electrons can also ionize or excite hydrogen and helium atoms in the primordial gas. Moreover, photons produced during annihilation can ionize atoms via photoionization. Additionally, DM annihilation can produce Ly-$\alpha$ photons that can subsequently photodissociate $H^-$. LW photons within the 11.2–13.6 eV energy range can photodissociate $H_2$ molecules, which are critical for early gas cooling.

Early numerical models (Shull and van Steenberg 1985; Chen and Kamionkowski 2004) investigating energy deposition by 3 keV electrons through heating and ionization in gas clouds are referred to as SSCK. These models provide estimates of the fraction of the electrons' energy deposited through ionization:

$$f_{\text{ion}} = \frac{1 - x_e}{3}\,, \tag{2.7}$$

where $x_e$ denotes the electron fraction in the gas cloud.

Although the SSCK model has been widely used and validated by recent calculations, discrepancies arise at higher electron energies. Specifically, for electron energies exceeding the megaelectronvolt range, ICS becomes dominant. Consequently, the process enters the relativistic regime rather than the classical Thomson regime. To address this, Slatyer (2016) recomputed the energy deposition profiles of injected particles with energies ranging from the kiloelectronvolt to the multi-teraelectronvolt scale. Their most recent numerical results suggest higher deposit efficiency of DM annihilation in the early universe (Lopez-Honorez et al. 2016).

## 2.2 21cm Cosmology

### 2.2.1 Overview

The spin-flip transition of neutral hydrogen (HI) emits radiation with a frequency of 1.42 GHz, corresponding to a wavelength of 21-cm. The 21-cm line, first predicted by H. van de Hulst in 1944 and detected by Ewen and Purcell in 1951, provides a unique observational window into the Dark Ages and is recognized as one of the most critical probes for examining the thermal and ionization states of the IGM.

The 21-cm line remains visible at high redshifts exceeding six as long as the IGM remains neutral (Carilli et al. 2002). Observations of the 21-cm signal can offer valuable insights into various aspects of cosmology, including the initial condition of inflation (Loeb and Zaldarriaga 2004), nature of dark energy (Wyithe et al. 2008), formation of the first stars and galaxies (Furlanetto et al. 2006), reionization history (Pritchard and Loeb 2008), and properties of DM (Valdes et al. 2007a; Loeb and Wyithe 2008; Natarajan and Schwarz 2009).

The intensity of the 21-cm signal is determined by the ratio of hydrogen atoms in the singlet state to those in the triplet state, described by the spin temperature $T_S$:

$$\frac{n_1}{n_0} = \frac{g_1}{g_0} \exp\left(-\frac{T_*}{T_S}\right), \tag{2.8}$$

where $g_1 = 3$ and $g_0 = 1$ denotes the spin degeneracy factors of the triplet and singlet states, respectively, and $T_* = 0.068$ K corresponds to the energy of the 21-cm transition.

At very high redshifts ($z > 300$), collisional coupling dominated owing to the high gas density. Hydrogen–hydrogen, hydrogen–electron, and hydrogen–proton collisions constituted the primary types of interactions. The total collision rate is defined as

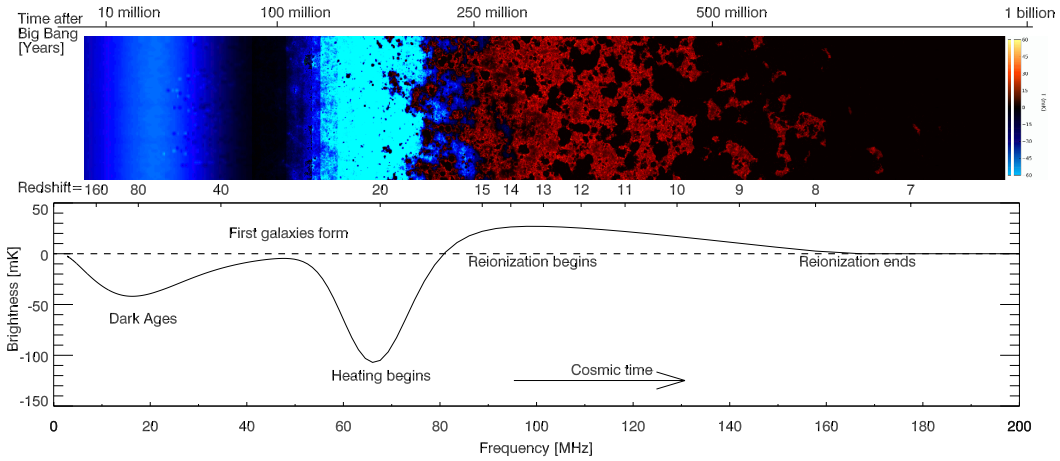


Figure 2.2: 21-cm cosmic signal. Adapted from Pritchard and Loeb (2012).

$$
\begin{aligned}
x_{\rm c} &= x_{\rm c}^{\rm HH} + x_{\rm c}^{\rm eH} + x_{\rm c}^{\rm pH} \\
&= \frac{T_\star}{A_{10}\,T_\gamma}\left[\kappa_{1-0}^{\rm HH}(T_{\rm k})\,n_{\rm H} + \kappa_{1-0}^{\rm eH}(T_{\rm k})\,n_{\rm e} + \kappa_{1-0}^{\rm pH}(T_{\rm k})\,n_{\rm p}\right],
\end{aligned}
\tag{2.9}
$$

where $\kappa$ denotes the scattering rate as a function of the kinetic temperature ($T_K$), as detailed in previous studies (Liszt 2001; Kuhlen et al. 2006; Pritchard and Loeb 2012). During this time, the kinetic temperature was coupled to the CMB temperature through Compton scattering. Hence, the spin temperature was also indirectly coupled to the CMB temperature, resulting in temperature $T_S \approx T_K \approx T_\gamma$ and no detectable 21-cm signal.

Once the kinetic temperature decoupled from the CMB temperature, the gas cooled adiabatically. Thus, the kinetic temperature dropped faster than the CMB temperature, leading to $T_K < T_\gamma$. The spin temperature also dropped below the CMB temperature, producing the 21-cm signal as an absorption line. Over time, the expansion of the Universe reduced the gas density, weakening collisional coupling. Consequently, the spin temperature gradually recoupled with the CMB temperature, causing the 21-cm signal to fade around $z \sim 30$.

The period of Cosmic Dawn ($z \lesssim 30$) was characterized by the formation of the first stars and galaxies. These stars and galaxies produced numerous Ly-$\alpha$ photons, which enabled the spin temperature to recouple with the kinetic temperature through the Wouthuysen–Field effect (Wouthuysen 1952; Field 1958). During this period, the spin temperature was lower than the CMB temperature, indicating $T_S \approx T_K < T_\gamma$. This led to the appearance of absorption lines. As stars continued to form, the kinetic temperature of the gas rose above the CMB temperature causing the spin temperature to exceed the CMB temperature, $T_S \approx T_K > T_\gamma$. At this stage, emission lines appeared.

The Lyman-$\alpha$ coupling coefficient ($x_\alpha$), related to the Wouthuysen–Field effect, is defined as

$$x_\alpha = \frac{16\pi^2 T_\star e^2 f_\alpha}{27 A_{10} T_\gamma m_e c} S_\alpha J_\alpha \,, \tag{2.10}$$

where $A_{10} = 2.85 \times 10^{-15} s^{-1}$ denotes the spontaneous emission coefficient, $f_\alpha = 0.4162$ denotes the oscillator strength of the Lyman-$\alpha$ transition, and $S_\alpha$ represents the correction factor of order unity.

As the Universe underwent reionization ($z < 6$), the 21-cm line disappeared entirely.

Throughout cosmic history, the spin temperature of the gas was influenced by several factors: First, it was coupled to the CMB temperature $T_{\rm CMB} = T_0(1+z)$ through Compton scattering, where $T_0 = 2.725$ K, denotes the present-day CMB temperature. Next, it was coupled to the kinetic temperature $T_{\rm K}$ through collisional coupling. Finally, it was coupled to the Lyman-$\alpha$ radiation field through the Wouthuysen–Field effect. Thus, overall, the spin temperature is determined by the interplay between the CMB temperature, kinetic temperature, and the coupling mechanisms that connect these temperatures to the spin temperature. The spin temperature can be expressed as

$$T_S^{-1} = \frac{T_\gamma^{-1} + x_\alpha T_\alpha^{-1} + x_c T_K^{-1}}{1 + x_\alpha + x_c} \,, \tag{2.11}$$

where $T_\alpha$ represents the color temperature of the Lyman-$\alpha$ radiation field, which is coupled to the kinetic temperature $T_\alpha = T_K$ in the current context. $x_c$ denotes the collisional coupling coefficient, which depends on the kinetic temperature $T_K$.

Fig. 2.2 illustrates an example of the 21-cm signal, as presented by Pritchard and Loeb (2012). During the Dark Ages (until a redshift of $z \approx 30$), early absorption lines were produced. Subsequently, the spin temperature was coupled to the kinetic temperature through the Wouthuysen–Field effect, resulting in a deep absorption feature near $z = 20$. Subsequently, the gas was reheated by X-ray radiation emitted by the first stars and galaxies, leading to the appearance of emission lines at redshift $z \approx 15$. Finally, the 21-cm signal disappeared owing to the reionization of the Universe.

The optical depth of a gas cloud can be expressed as

$$\tau_\nu = \int ds \left(1 - \exp\left(-\frac{E}{k_B T_S}\right)\right) \frac{3c^3 h A_{10}}{32\pi k_B \nu_0^2} \phi(\nu) \,, \tag{2.12}$$

where $\nu_0 = 1420.4$ MHz represents the frequency of the 21-cm signal, and $\phi(\nu)$ denotes the line profile.

To observe the 21-cm signal in practice, the difference between the CMB temperature and

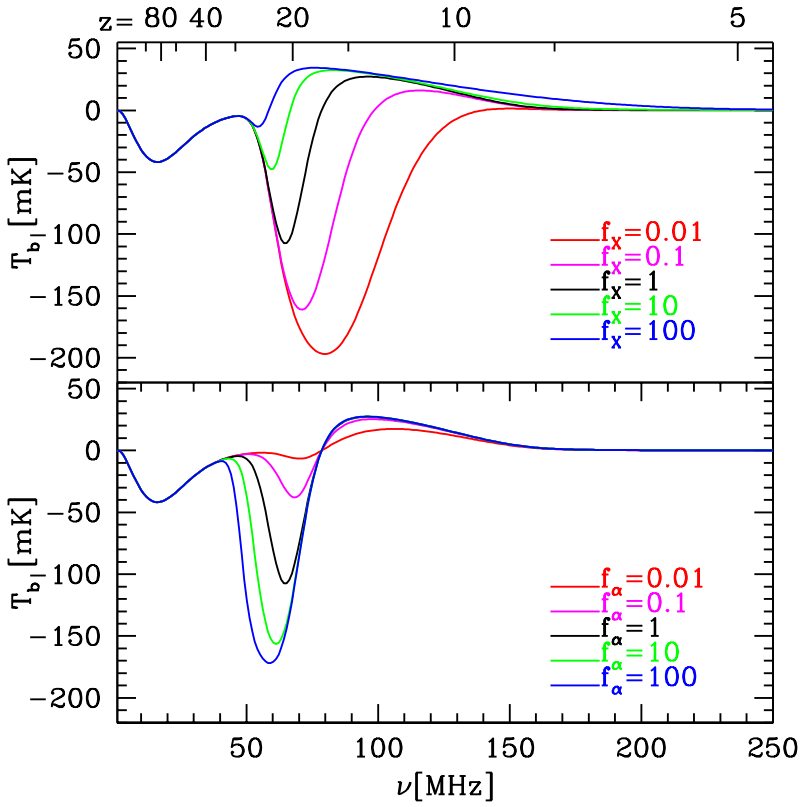


Figure 2.3: Dependence of the 21-cm signal on X-ray and Lyman-$\alpha$ emissivity. Adapted from Pritchard and Loeb (2012).

the spin temperature of neutral hydrogen ($T_S$) is determined. The observable quantity is the differential brightness temperature, $\delta T_b$, which represents the contrast between the CMB and 21-cm signal. For small optical depths, ($\tau_\gamma$), $\delta T_b$ can be approximated as follows:

$$\begin{aligned}\delta T_b &= \frac{T_S - T_{\rm CMB}}{1+z}\left(1+e^{-\tau_\gamma}\right) \\ &= 27 x_{\rm HI}(1+\delta_b)\left(1-\frac{T_{CMB}}{T_S}\right)\left(\frac{1}{1+H^{-1}\frac{\partial v_r}{\partial r}}\right)\left(\frac{1+z}{10}\right)^{-\frac{1}{2}}\left(\frac{0.15}{\Omega_m h^2}\right)^{\frac{1}{2}}\left(\frac{\Omega_b h^2}{0.023}\right)\text{mK}\end{aligned}, \tag{2.13}$$

where $x_{\rm HI}$ denotes the neutral fraction of hydrogen, and $\delta_b$ represents the baryon overdensity.

### 2.2.2 DM Impacts

Previous studies have extensively investigated the impact of DM annihilation on the 21-cm signal. For instance, Natarajan and Schwarz (2009) reported that DM annihilation could leave

a distinctive detectable signature in the 21-cm signal. Building on this, Evoli et al. (2014) calculated the 21-cm brightness temperature during the Cosmic Dawn phase, specifically utilizing the 21cmFAST code to explore the effects of $\chi\chi \rightarrow \mu^+\mu^-$ annihilation. LH16 developed a comprehensive history of brightness temperature for the $\chi\chi \rightarrow e^+e^-$ annihilation, demonstrating that certain DM mass ranges could leave notable signatures on the 21-cm signal. Cheung et al. (2019) utilized spin temperature data derived from the EDGES experiment to simulate the 21-cm signal for various DM models. Basu et al. (2020) examined the combined impacts of DM annihilation with DM–baryon scattering on the 21cm signal, observing that these interactions could substantially modify the expected signal. Cang et al. (2023) examined the inhomogeneous effects of DM annihilation, demonstrating that these effects could enhance the amplitude of fluctuation in 21-cm power spectrum by some orders of magnitude, providing a potential method for distinguishing between various DM models. Finally, Qin et al. (2023) utilized the DarkHistory code to investigate the impact of DM annihilation on molecular hydrogen ($H_2$) generation for star formation. Their findings revealed that exotic energy transfers from DM annihilation could either accelerate or delay the formation of the first stars, highlighting the complex interplay between DM annihilation and early star formation.

Lopez-Honorez et al. (2016) (thereafter LH16) investigated the annihilation of DM particles with masses in the megaelectronvolt to gigaelectronvolt range into electron–positron pairs. They employed the energy deposition fraction calculation method proposed by Liu et al. (2016) and observed enhancements in both the temperature and ionization fractions during the epoch of reionization. The contribution of DM annihilation to the thermal history was computed using the `Comsorec` code for the early Universe, while `21cmFAST` was used for the corresponding calculations during the period from Cosmic Dawn to reionization. Several parameters such as the HMF, X-ray efficiency, and DM particle mass influenced the calculated spin temperature. Among the models analyzed in LH16, those with $m_{\rm DM} \sim 100$ MeV demonstrated the most pronounced effects.

While these previous studies have preliminarily examined the 21-cm signal, comprehensive study of this spectral feature, combined with the formation of the first stars, requires a more detailed treatment. Although some studies have accounted for the effects of the stellar LW feedback, the properties of molecular cooling halos, which play notable roles in the formation of the first stars, are often omitted in simulations using `21cmFAST`. Omissions of molecular cooling halos may delay the onset of star formation during simulations (e.g., Evoli et al. (2014); Lopez-Honorez et al. (2016)). Furthermore, DM annihilation may impact the star formation rate in such low-mass halos, altering early stellar feedback mechanisms. The energy deposition fraction, which varies with both the redshift and DM mass, also demands careful consideration. Previous studies (Basu et al. 2020; Cang et al. 2023) have relied on energy deposition fractions

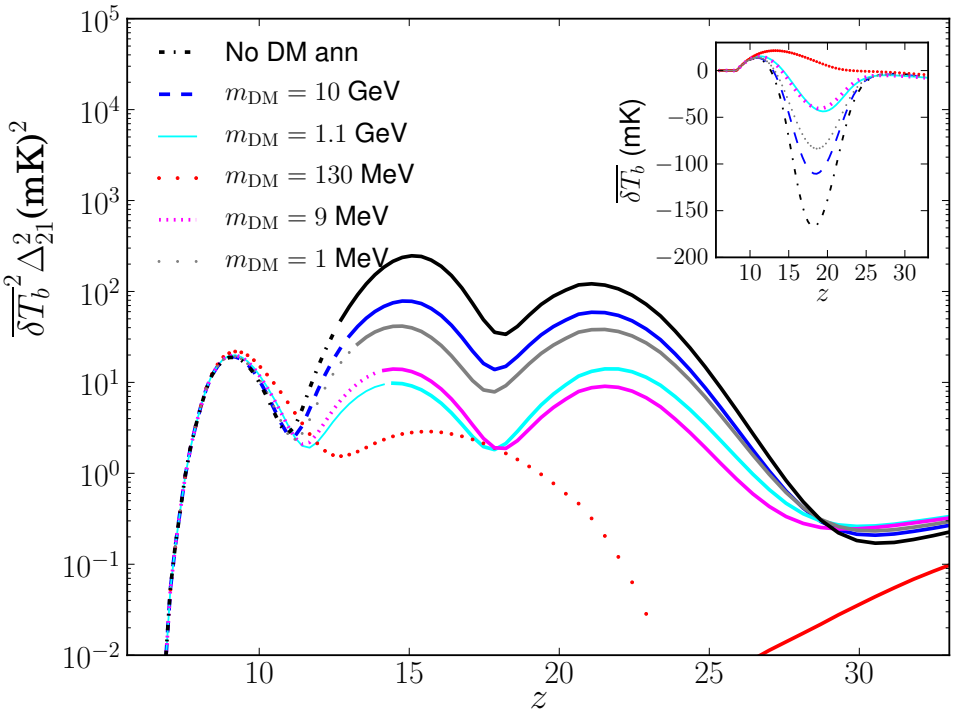


Figure 2.4: Global 21-cm signal and the power spectrum of fluctuations at a scale of 0.1 Mpc$^{-1}$, plotted for five different DM masses, with DM annihilation cross-sections saturating the Planck CMB limits. Adapted from Lopez-Honorez et al. (2016).

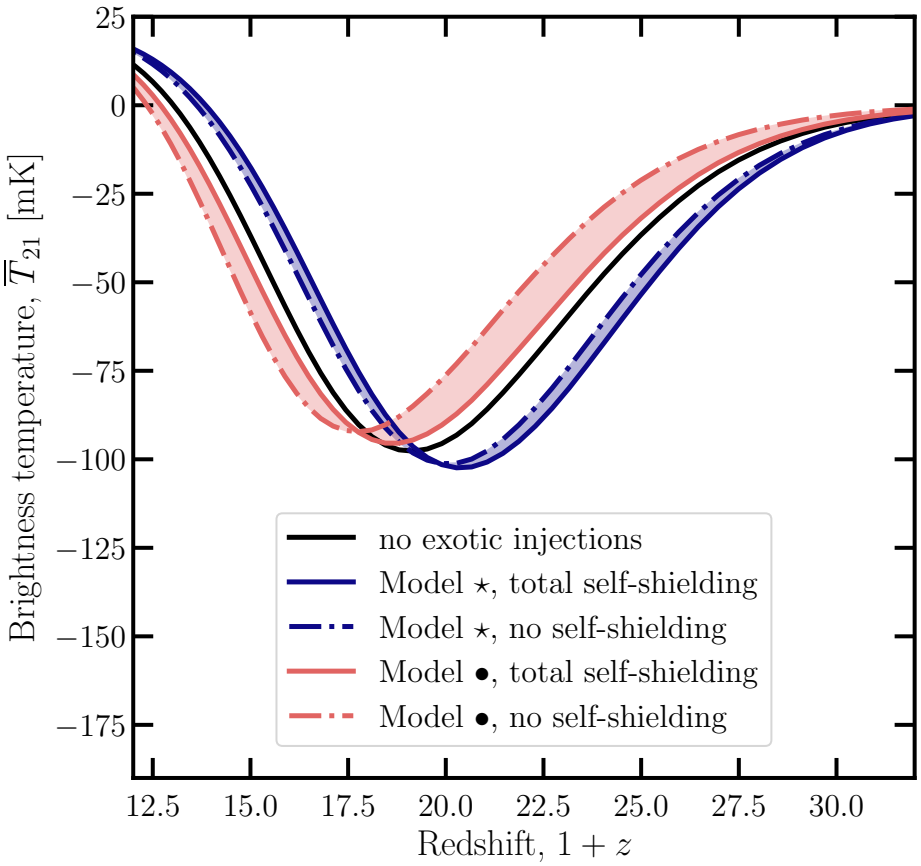


Figure 2.5: The 21cm global signal as a function of redshift, with dark matter decay for two fiducial dark matter models. The shaded contours bracket the effect of $H_2$ self-shielding. Adapted from Qin et al. (2023).

derived from numerical models (Shull and van Steenberg 1985; Chen and Kamionkowski 2004), commonly referred to as the SSCK model). While these models have been widely adopted and validated by recent calculations, they are based on 3 keV electrons, and discrepancies emerge with increasing electron energy. Hence, an improved modeling method is crucial for accurately understanding and constraining the effects of DM annihilation (Slatyer 2016). Furthermore, the inclusion of DM–baryon velocity offsets is essential for self-consistency. These offsets suppress structure formation on small scales and alter the impact of DM annihilation.

Fig. 2.4 represents the global 21-cm signal and the power spectrum of fluctuations as a function of redshift. Dark matter annihilation modify the 21-cm signal by altering the thermal history of the universe. Fig. 2.5 represents the impact of different models of dark matter decay on the 21cm global signal as a function of redshift.

CHAPTER

# 3

# MODELING ANNIHILATION IN DARK MATTER HALOS

## 3.1 Model

The energy from dark matter (DM) annihilation events arises not only from a smooth background but is also significantly amplified in regions with structured DM distributions. Because the DM annihilation rate is proportional to the square of the DM density, annihilation events are substantially more intense in dense regions and become further enhanced by the presence of inhomogeneities, as expressed by the relation $\bar{\rho_\chi^2} \geq (\bar{\rho_\chi})^2$.

The energy released through DM annihilation is deposited into the primordial gas, altering the thermal history of the intergalactic medium (IGM) through both heating and ionization processes. Moreover, the properties of gas within dark matter halos are shaped by this energy deposition, which can either suppress or accelerate early gas cooling required for Population III (Pop III) star formation. On one hand, DM annihilation increases the ionization of the primordial gas, thereby raising the electron fraction and catalyzing molecular hydrogen production. On the other hand, the heating from DM annihilation elevates the temperature of the IGM, leading to an increase in the Jeans mass, which inhibits gas collapse into halos. Consequently, gas cooling is suppressed because of exotic energy injection in thermal energy, and the star

formation become less efficient due to the low-density environments.

In this study, I investigate the energy deposition from dark matter annihilation in dark matter halos and evaluate their impact on early star formations. In order to obtain potential power in calculating observable signals, such as the luminosity function and the global 21cm signal, which can be compared with future observations, I include a comprehensive discussion of related processes, such as Lyman-Werner (LW) feedback and streaming velocity effects.

### 3.1.1 Dark Matter Annihilation Power

For self-annihilating dark matter (DM), the annihilation power per unit volume is described by the equation

$$\frac{dE}{dVdt} = \frac{\langle\sigma v\rangle}{m_{\rm DM}}\rho_{\rm DM}^2, \tag{3.1}$$

where $\langle\sigma v\rangle$ represents the thermally averaged annihilation cross-section, $\rho_{\rm DM}$ is the DM density, and $m_{\rm DM}$ denotes the mass of the DM particle.

For the case of s-wave dark matter annihilation, the cosmic microwave background (CMB) spectrum provides an upper limit on the cross-section, as reported by the Planck collaboration: $p_{\rm ann} \leq 4.1\times10^{-28}\,{\rm cm^3\,s^{-1}\,GeV^{-1}}$, where $p_{\rm ann} = f_{\rm eff}\langle\sigma v\rangle/m_{\rm DM}$ (Collaboration et al. 2014; Liu et al. 2016). Here, $f_{\rm eff}$ is a constant proxy for the deposited fraction, which depends on the dark matter particles and cosmological parameters. Given the value of $f_{\rm eff}$, one can derive constraints on the dark matter annihilation cross-section.

In this study, I employ a constant mass-weighted cross-section,

$$\langle\sigma v\rangle/m_{\rm DM} = 10^{-27}\,{\rm cm^3\,s^{-1}\,GeV^{-1}}.$$

This value is allowed for $f_{\rm eff}\lesssim 0.1$ and serves as a useful benchmark to check against current limits. Additionally, I assume annihilation occurs through the channel $\chi\chi\rightarrow e^+e^-$.

Since the annihilation rate depends on the squared density of dark matter, the formation of collapsed halos results in a boost in the cosmic dark matter annihilation power. I separate the power of dark matter annihilation into two parts: $\frac{dE}{dt} = (\frac{dE}{dt})_{\rm smooth} + (\frac{dE}{dt})_{\rm struct}$. The former comes from the smooth dark matter background, and the latter comes from collapsed dark matter structures. In terms of the boost factor $B(z)$, accounting for this structure effect, the annihilation power at redshift $z$ can be written as

$$\left.\frac{dE}{dVdt}\right|_{\rm injected} = \left.\frac{dE}{dVdt}\right|_{\rm smooth} + \left.\frac{dE}{dVdt}\right|_{\rm struct} = \frac{\langle\sigma v\rangle}{m_{\rm DM}}\rho^2_{\rm DM,0}(1+z)^6(1+B(z))\,, \tag{3.2}$$

where $\rho_{\rm DM,0}$ indicates the average DM density in the current time. The component of annihilation power from structure is related to the smooth component by

$$\left.\frac{dE}{dVdt}\right|_{\rm struct} = B(z)\left.\frac{dE}{dVdt}\right|_{\rm smooth}. \tag{3.3}$$

The boost factor depends on the halo mass function and halo profile, written in Cirelli et al. (2009) as

$$B(z) = \frac{1}{\rho^2_{\rm DM,0}(1+z)^3}\int_{M_{\rm h}^{\rm min}}^{\infty}\frac{dN}{dM}dM\int_0^{R_{\rm vir}}\rho^2_{\rm DM}(r)4\pi r^2 dr, \tag{3.4}$$

where $\frac{dN}{dM}$ is the comoving halo mass function (HMF), and $\rho_{\rm DM}(r)$ is the dark matter halo density profile. The minimum halo mass, $M_{\rm h}^{\rm min}$, representing the smallest mass of halos, depends on the model of dark matter particle. As noted in Evoli et al. (2014); Lopez-Honorez et al. (2016) and Mack (2014b), this value affects the intensity of the structured boost factor of the dark matter annihilation signal, altering the 21cm signal. I use the value $M_{\rm h}^{\rm min} = 10^{-9}{\rm M}_\odot$ in this paper.

For the halo mass function, I use the Sheth-Tormen model with parameters $a' = 0.75$ and $p' = 0.3$, identified as optimal fits (Sheth et al. 2001). I also employ the mass-concentration relation from Diemer and Joyce (2019) and use the Navarro-Frenk-White (NFW) profile to characterize dark matter halos, which provides the total dark matter annihilation for a given halo.

Note that the deposited energy is highly dependent on the chosen cosmological and DM models. These dependencies include the density profile, mass concentration relation, and halo mass function, as detailed in Mack (2014b); Schon et al. (2014). Additionally, our model assumes DM annihilates entirely into $e^+e^-$ pairs and lies in the approximate 10 MeV to GeV mass range.

The DM energy deposition into gas is modelled as follows: the deposited fraction $f_c(z)$ assumes that power deposition is proportional to the injected power at the same redshift, going into each channel $c$ for heating, HI and HeI ionization, and Ly-$\alpha$ photons. Thus, the deposited energy in channel $c$ per unit time per baryon is given as

$$\epsilon_c^{\rm DM}(z) = \frac{1}{n_{\rm B}} f_c(z) \left.\frac{dE}{dV\,dt}\right|_{\rm injected}, \tag{3.5}$$

where $n_{\rm B}$ is the mean baryon number density at redshift $z$.

The deposited energy in Equation 3.5 represents the energy deposited into the background IGM. For gas in overdense regions, such as dark matter halos, the energy deposit rate is given by the total DM energy from both local DM and the global DM background: $\epsilon_c^{\rm DM} = \epsilon_{\rm c,local}^{\rm DM} + \epsilon_{\rm c,BG}^{\rm DM}$. The local deposit rate originates from local dark matter annihilation, which could heat and ionize the surrounding gas (Schön et al. 2017; Clark et al. 2017). However, the local effect depends heavily on the interaction between annihilation products and baryonic particles in the gas environment, which remains poorly understood. In this study, I focus on the global DM energy deposition. For the global annihilation background, I assume the energy deposit rate per baryon in halos is the same as that in the IGM. Therefore, I consistently use $\epsilon_c^{\rm DM}(z)$ from Equation 3.5 throughout this work.

### 3.1.2 Structure of Dark Matter Halos

For halo mass function, I utilize the Sheth-Tormen model with parameters $a' = 0.75$ and $p' = 0.3$, identified as optimal fits (Sheth et al. 2001). This section addresses two primary profiles, Navarro-Frenk-White (NFW) profile and the Einasto profile.

The NFW profile, suggest by Navarro et al. (1996), is a universal profile based on large-scale N-body simulations. The density of dark matter $\rho(r)$ as a function of radius from the center of halo, is defined as

$$\rho(r) = \frac{\rho_s}{\frac{r}{r_s}\left(1+\frac{r}{r_s}\right)^2}, \tag{3.6}$$

where $\rho_s$ is the characteristic density, and $r_s$ is the scale radius. The NFW profile predicts a cusp core with slope $r^{-1}$ at small radii $r \ll r_s$, and slope $r^{-3}$ at outer regions.

The Einasto profile proposed by Einasto (1965) generalized the inner density profile of NFW as an additional free parameter. As a result, the Einasto profile does not have a sharp cusp as the NFW profile. The density profile $\rho(r)$ is written as

$$\rho(r) = \rho_s e^{-\frac{2}{\alpha}\left[\left(\frac{r}{r_s}\right)^\alpha - 1\right]}, \tag{3.7}$$

where $\rho_s$ is the characteristic density, and $r_s$ is the scale radius. $\alpha$ is the free parameter in Einasto profile, depending on halo mass (Gao et al. 2008).

The scale radius $r_s$ is determined by the concentration of dark matter halos, as defined by

$$r_s = \frac{R_{\rm vir}}{c}\,, \tag{3.8}$$

where $R_{\rm vir}$ is the virial radius of the dark matter halo, and $c$ is the concentration parameter.

With the development of numerical simulations, the concentration-mass relation has studied and evolved over the past two decades. Various models offer different perspectives on the concentration-mass relations for different mass range and redshift. In the work, I adopt the relation from Diemer and Joyce (2019), and compute using python toolkit `COLOSSUS`.

Diemer and Joyce (2019) demonstrate high accuracy semi-analytical fitting function based on simulation result. The relation is in good agreement with their previous model, DK15 (Diemer and Kravtsov 2015) at lower redshift ($z < 6$), but improved due to better fit to scale-free cosmologies and accurate power spectrum at high redshift ($z > 6$). This result reveals systematic deviations ($\sim 20\%$) from other models (eg. Correa et al. (2015); Ludlow et al. (2016)) due to the analytic treatment of low-mass halo evolution and differences in simulation methodologies such as halo finder algorithm.

## 3.2 Numerical Simulation

### 3.2.1 Thermal History

To calculate the thermal history of IGM since recombination, I utilize the cosmological recombination code `CosmoRec` (Chluba and Thomas 2010) with modified dark matter annihilation power.

Firstly, I calculate the heating and ionization in the background IGM gas. As mentioned in Section 2.1, the annihilation energy deposited into the IGM gas is described by the deposited fraction $f_{\rm c}$. The DM annihilation emission power per baryon as $\epsilon_c^{\rm DM}$, where $c$ represents the deposition channel, which includes heating, HI and HeI ionization, and Ly-$\alpha$ photons. The additional temperature of IGM gas is given by $d\,T_{\rm K}/d\,t = d\,T_{\rm K}/d\,t + d\,T_{\rm K}/d\,t|_{\rm DM}$, where

$$\left.\frac{d\,T_K}{d\,z}\right|_{\rm DM} = \frac{d\,t}{d\,z}\frac{2}{3k_B(1+x_e)}\epsilon_{\rm heat}^{\rm DM}\,, \tag{3.9}$$

where $x_e$ is the electron fraction.

The ionization and Ly-$\alpha$ excitation by dark matter annihilation are

$$\Lambda_{\rm ion}|_{\rm DM} = f_{\rm H}\frac{\epsilon^{\rm DM}_{\rm HI}}{E_{\rm HI}} + f_{\rm He}\frac{\epsilon^{\rm DM}_{\rm HeI}}{E_{\rm HeI}} \tag{3.10}$$

$$J_{\alpha,\rm DM} = \frac{c\,n_b}{4\pi}\frac{\epsilon^{\rm DM}_{\rm Ly\alpha}}{h\,\nu_\alpha}\frac{1}{H(z)\nu_\alpha}\,, \tag{3.11}$$

where $E_{\rm HI,HeI}$ are the ionization energies for hydrogen and helium, $\mathfrak{f}_{\rm H,He}$ represent the number fractions of hydrogen and helium, $\nu_\alpha$ is the emission frequency of a Ly$\alpha$ photon.

Recall the energy deposition of dark matter annihilation, the deposited energy in channel $c$ can be written as

$$\begin{aligned}\epsilon_c^{\rm DM}(z) &= \frac{1}{n_{\rm B}} f_c(z)\left.\frac{dE}{dV\,dt}\right|_{\rm injected} \\ &= \frac{1}{n_{\rm B}} f_c(z)[1+B(z)]\left.\frac{dE}{dV\,dt}\right|_{\rm smooth}\,,\end{aligned} \tag{3.12}$$

We could denote the boosted deposit fraction $g_c(z) = f_c(z)[1+B(z)]$ to account for the contribution of structured halos. The energy deposition rate $\epsilon_c^{\rm DM}(z)$ can be calculated by Equation 3.2 and Equation 3.4, if we have the deposit fraction.

For the deposit fraction, I derived the $f_c(z)$ using the transfer functions from Slatyer (2016), which calculate these fractions for high-energy photons and $e^+e^-$ pairs resulting from DM annihilation. This gives us the deposit fraction for different masses. Fig. 3.1 shows the deposit fraction $f_c(z)$ calculated from the Table in Slatyer (2016) for the electron positron pair with initial energy 9 MeV, 130 MeV and 1.1 GeV. From top to bottom, panels illustrate the deposit rate in heating, Ly-$\alpha$ excitation, HI ionization, HeI ionization and total deposit fraction $f(z) = \sum f_c(z)$. The result indicates the different deposit fraction for different masses, due to the variation of interaction efficiency varies with energies and gas density, such as Inverse Compton scattering or photoionization.

It is worth noting that the total deposit fraction $f(z) = \sum f_c(z)$ is defined as the ratio of deposited energy from all DM annihilation history to injected energy at the same redshift. Therefore, the value of $f(z) > 1$ is possible if there is more energy deposited than the injected energy.

### 3.2.2 Jeans Mass

Dark matter annihilation heats the primordial gas, raising the gas temperature, and thereby increasinf the Jeans mass according to the Equation 1.21.

I denote $f_{\rm gas}$ for the gas fraction inside halos, which follows the equation (Gnedin 2000;

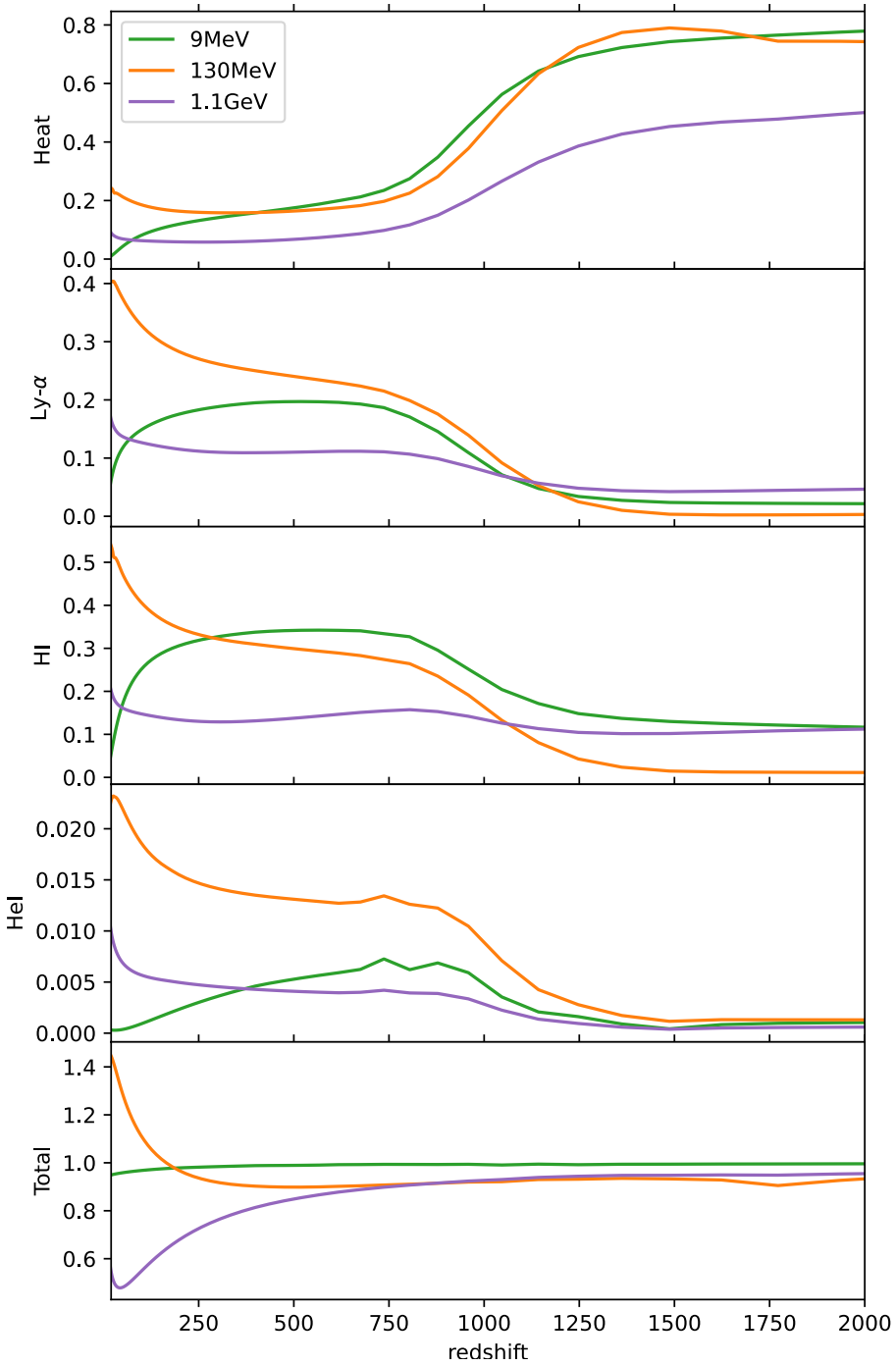


Figure 3.1: The deposit fraction $f_c(z)$ calculated from the Table in Slatyer (2016) for the electron positron pair with initial energy 9 MeV, 130 MeV and 1.1 GeV. From top to bottom, panels illustrate the deposit rate in heating, Ly-$\alpha$ excitation, HI ionization, HeI ionization and total deposit fraction $f(z) = \sum f_c(z)$.

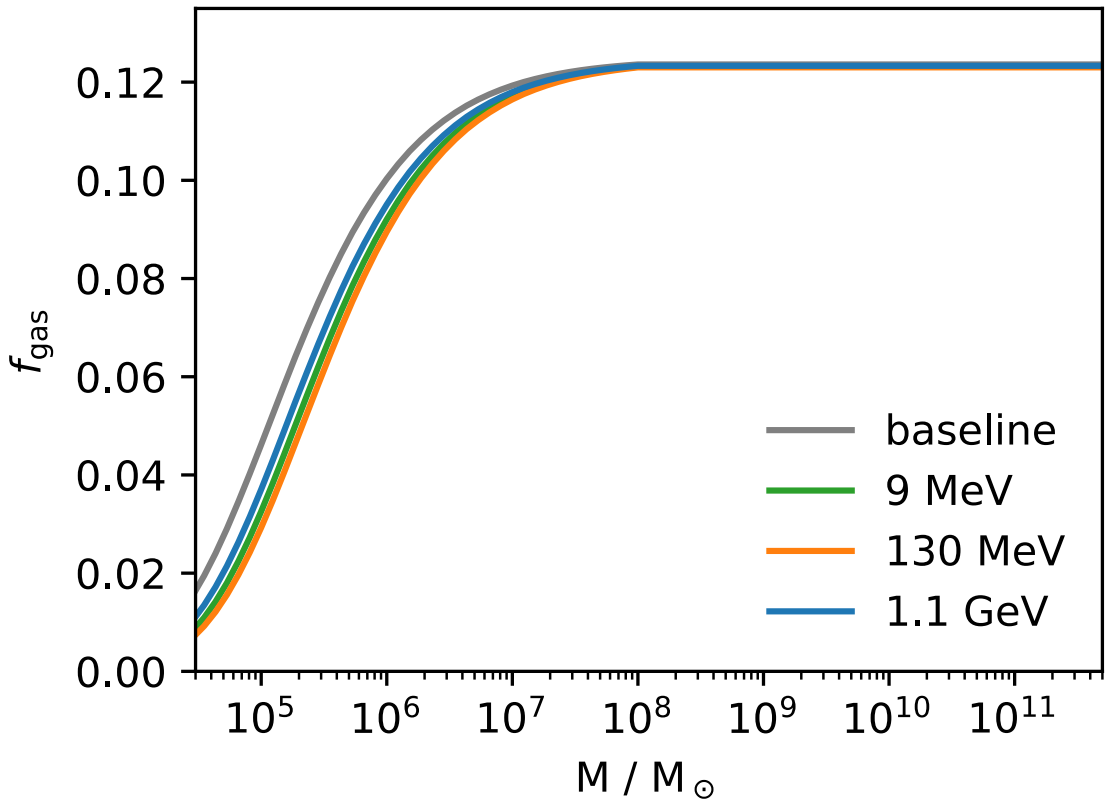


Figure 3.2: Gas fraction as a function of halo masses at redshift $z = 20$, with the impact of dark matter (DM) annihilation for DM masses of 9 MeV, 130 MeV and 1.1 GeV. The baseline (grey line) is given by Equation 3.13 without DM annihilation. Dark matter annihilation leads to suppression of the gas fraction within molecular cooling halos, but less in atomic cooling halos.

Naoz and Barkana 2007)

$$f_{\rm gas}(z,M) = f_{\rm b,0}\left[1+\left(2^{\alpha/3}-1\right)\left(\frac{M_{\rm F}}{M}\right)^{\alpha}\right]^{-3/\alpha}, \tag{3.13}$$

where $M_F$ is the filtering mass, $\alpha = 0.7$, and $f_{\rm b,0}$ is the cosmic baryon fraction

$$f_{\rm b,0}(z) = \frac{\Omega_b(z)}{\Omega_m(z)}(1+3.2\,r_{\rm LSS})\,. \tag{3.14}$$

In the dark matter halo, the distribution of gas is assumed to follow the dark matter density profile, that $\rho_{\rm gas}(r) = f_{\rm gas}\rho_{\rm DM}(r)$.

Fig. 3.2 shows the gas fraction as a function of halo mass at redshift $z = 20$, using the filtering mass defined in Equation 3.13. The gas thermal history is calculated using the recombination

code `cosmoRec`. I observe a significant suppression in the gas fraction, ranging from 10% to 40% at redshift $z = 20$, which varies with dark matter mass. The impact of dark matter annihilation on the gas fraction is notably less significant in halos of higher mass. For a halo of $10^6 M_\odot$, the reduction in gas fraction is only 5% to 10%.

### 3.2.3 Molecular Cooling

For the birth of the first stars, the gas within dark matter halos requires cooling for further collapse, and that cooling is primarily achieved through molecular hydrogen (Galli and Palla 1998; Glover and Savin 2006; Yoshida et al. 2007; Glover and Abel 2008; Glover and Savin 2009). Molecular cooling occurs only if the halo mass is larger than the specific value, denoted as the minimum cooling mass $M_{\rm cool}$. In this section, I build an analytical cooling model to calculate the influence of minimum cooling mass in the presence of dark matter annihilation.

#### Gas Density

To calculate gas cooling in molecular cooling halos, I must first estimate the gas profile, which can be approximated by following the distribution of the dark matter (DM) profile. In this approximation, the gas density in a halo of mass $M_h$, denoted as $\rho_{\rm gas}(M_h, r)$, is expressed as $\rho_{\rm gas}(M_h, r) = f_{\rm gas}(M_h)\rho_{\rm DM}(M_h, r)$, where $f_{\rm gas}(M_h)$ is the gas fraction.

I assume efficient gas cooling in the core region, defined as $R_{\rm core} = 0.1\, r_{\rm vir}$. Consequently, the gas density in the core of halo $M_h$ is given by

$$\rho^{\rm HM}_{\rm gas,core}(M_h) = f_{\rm gas}(z, M_h)\rho_{\rm DM}(M_h, 0.1\, r_{\rm vir})\,, \tag{3.15}$$

where the gas fraction $f_{\rm gas}(z, M_h)$ is derived from the filtering mass in Equation 3.13.

However, this assumption breaks down on small scales, particularly when $k \gtrsim k_J$, as the gas density cannot form a cusp-like central density like the dark matter in a standard NFW profile, due to thermal pressure. For these minihalos, I apply constraints from adiabatic compression and use the core density derived from hydrostatic equilibrium, given by Tegmark et al. (1997); Barkana and Loeb (2001b); Visbal et al. (2014)

$$\rho^{\rm LM}_{\rm gas,core}(M_h) = \bar{\rho}_b \left(1 + \frac{6}{5}\frac{T_{\rm vir}(M_h)}{T_{\rm IGM}}\right)^{3/2}\,, \tag{3.16}$$

where $\bar{\rho}_b$ represents the average baryonic density, and $T_{\rm IGM}$ denotes the background IGM temperature. Thus, the final core gas density of halo mass $M_h$ is given by the minimum of the two values: $\rho_{\rm gas,core}(M_h) = \min\{\rho^{\rm HM}_{\rm gas,core}, \rho^{\rm LM}_{\rm gas,core}\}$. In high-mass halos, $\rho^{\rm HM}_{\rm gas,core}$ dominates, while in low-mass halos, $\rho^{\rm LM}_{\rm gas,core}$ dominates. Importantly, the IGM temperature affects the gas density

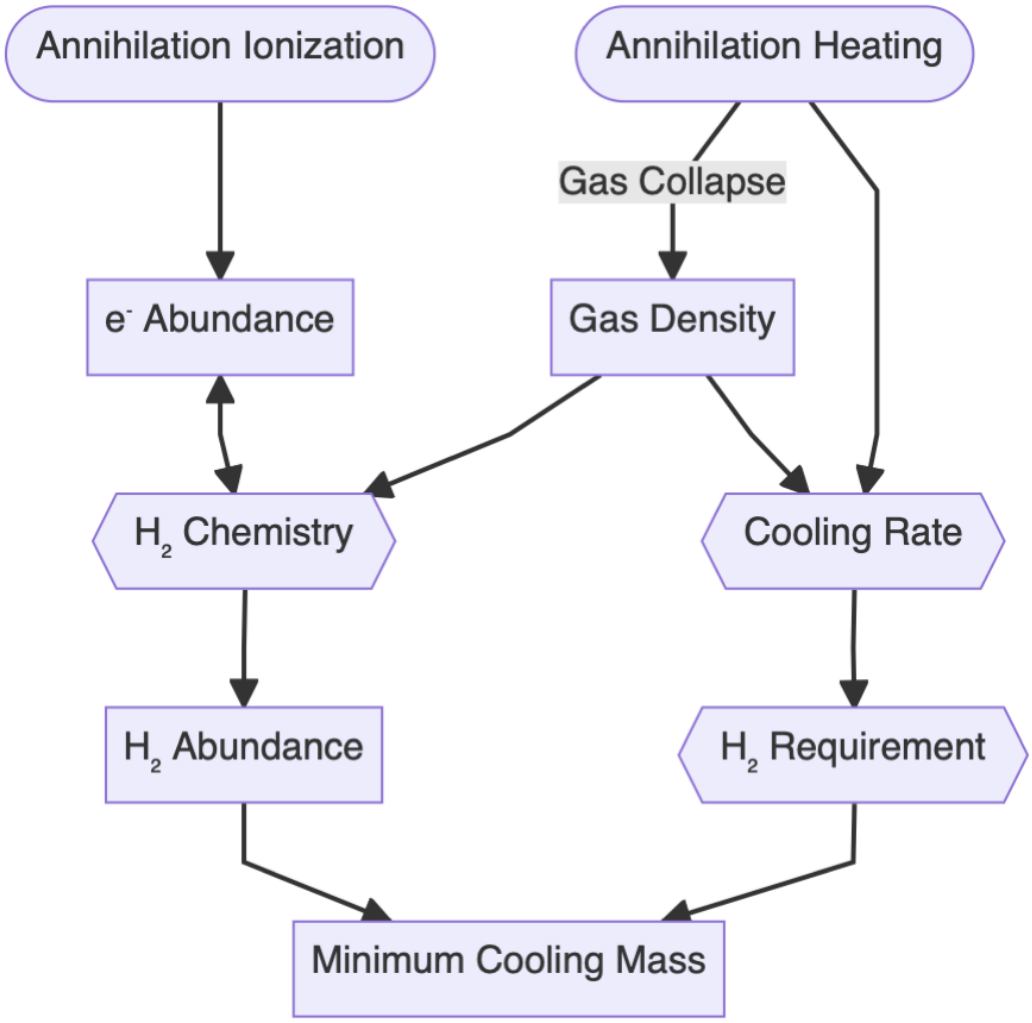


Figure 3.3: Diagram of dark matter annihilation in molecular cooling.

in both cases, and as a result, dark matter annihilation also influences gas cooling by altering the gas density.

### $H_2$ Production

Molecular hydrogen production in primordial gas is primarily through the $H^-$ mechanism:

$$H + e^- \rightarrow H^- + \gamma \qquad (\text{rate } k_1)\,, \tag{3.17}$$

$$H^- + H \rightarrow H_2 + e^- \qquad (\text{rate } k_2)\,. \tag{3.18}$$

I also consider the mutual neutralization and radiative recombination reactions:

$$H^+ + H^- \rightarrow H + H \qquad (\text{rate } k_3)\,. \tag{3.19}$$

$$H^+ + e^- \longrightarrow H \qquad (\text{rate } k_4)\,. \tag{3.20}$$

The corresponding reaction rates for Equations 3.17-3.20 are denoted as $k_1, k_2, k_3, k_4$, and they are functions of the gas temperature $T$. From reference Hutchins (1976), I have $k_1 = 1.83 \times 10^{-18}\, T^{0.8779}$ cm$^3$s$^{-1}$. The reaction rates $k_2$ and $k_3$ have relatively weak temperature dependences, and are calculated in Kreckel et al. (2010); Stenrup et al. (2009); I set $k_2/k_3 \approx 0.03$. For the recombination rate $k_4$, instead of using the coefficient adopted by Tegmark et al. (1997), $k_4 = 1.88 \times 10^{-10}\, T^{-0.644}$ cm$^3$s$^{-1}$, I follow Nebrin et al. (2023), and use the case-B recombination rate: $k_4 = 2.11 \times 10^{-10}\, T^{-0.72}$ cm$^3$s$^{-1}$.

In addition, I assume that $H^-$ reaches its equilibrium abundance, where $n_{H^-} = k_1 n_{e^-}/k_2$, and that the abundance of ionized hydrogen is equal to free electrons, $n_{e^-} = n_{H^+}$.

The abundance of electrons is written as

$$\frac{d\,x_e}{d\,t} = -k_4 n_H x_e^2\,. \tag{3.21}$$

The fraction of molecular hydrogen can be calculated via

$$\frac{d\,x_{H_2}}{d\,t} = k_1 x_e n_H \left(1 + \frac{k_3}{k_2} x_e\right)^{-1}\,. \tag{3.22}$$

It is possible to solve the above equations and obtain the abundance of $x_e$ and $H_2$ as a function of time $t$:

$$x_e = \frac{x_0}{1 + x_0 n_H k_4 t}\,, \tag{3.23}$$

$$x_{H_2} = x_{H_2,0} + \frac{k_1}{k_4} \ln\left(1 + \frac{k_4 n_H x_0 t}{1 + k_3/k_2 x_0}\right), \tag{3.24}$$

where $x_0$ and $x_{H_2,0}$ are the initial abundances of electrons and $H_2$. The logarithmic term implies that the abundance of $H_2$ is growing rapidly at the beginning, and then becomes slow.

Considering the impact of dark matter annihilation ionizing gas during the cooling process alters Equation. 3.21:

$$\frac{d\,x_e}{d\,t} = -k_4 n_H x_e^2 + \Lambda_{\text{ion}}|_{\text{DM}}\,, \tag{3.25}$$

where $\Lambda_{\text{ion}}|_{\text{DM}}$ is the ionization rate per hydrogen atom due to dark matter annihilation given by Equation 3.10. The first term on the right-hand side of the equation represents the re-

combination rate as a function of the electron fraction. When the electron fraction is high, recombination dominates over annihilation-induced ionization, causing the electron fraction to decrease. In contrast, if $\Lambda_{\rm ion}|_{\rm DM}$ exceeds the recombination rate, the electron fraction will increase over time.

The upper panel of Fig. 3.4 and 3.5 show the electron fraction calculated using Equation 3.25 in a $10^5 M_\odot$ halo at redshifts 40 and 20, respectively. For each specific dark matter mass, the initial electron fraction is provided by the public cosmological recombination code `CosmoRec` (Chluba and Thomas 2010). The black line represents the scenario without dark matter annihilation. Dashed lines assume the same initial electron fraction at $t = 0$ as the case without annihilation. The gas temperature is fixed at the virial temperature of the halo.

The production of molecular hydrogen is shown in the lower panel of Fig. 3.4 and 3.5. I set the initial molecular hydrogen fraction to $x_{\rm H_2,0} = 6 \times 10^{-7}$ (Galli et al. 2013). Indirect effects of dark matter annihilation alter the initial gas number density and associated reaction rates. In small halos, dark matter annihilation reduces gas density, leading to a suppression of the reaction rates, as discussed in the context of the gas fraction. However, I found that this effect is minimal; the production of $H_2$ is still dominated by the electron fraction. I found that the differences in molecular hydrogen fractions among the cases are primarily due to initial variations in the electron fraction. The molecular hydrogen fraction $x_{\rm H_2,0}$ has little impact on the results as long as it is small. Dashed lines represent scenarios in which the same initial fractions at $t = 0$ are assumed, with DM subsequently ionizing the gas.

**Cooling Criterion**

To find the minimum cooling mass inside halos via $H_2$ cooling, I take the criterion that cooling time must be less than 20% of the Hubble time, $t_{\rm cool} < 0.2\, t_H$, as adopted in Tegmark et al. (1997); Machacek et al. (2001), where the cooling time $t_{\rm cool}$ is given by

$$t_{\rm cool} = \frac{1}{\gamma - 1} \frac{n\, k_B\, T_{\rm vir}}{\Lambda_0\, n_{\rm H_2}}\,, \tag{3.26}$$

where $\gamma = 5/3$ for primordial gas, $n$ is the total number density of gas, $k_B$ is the Boltzmann constant, $n_{\rm H_2}$ is the number density of $H_2$, and $\Lambda_0$ is the total cooling rate of the gas per hydrogen molecule.

The total cooling rate per $H_2$ molecule is given by

$$\Lambda_0 = \sum_k \Lambda_{{\rm H_2},k}\, n_k\,, \tag{3.27}$$

where $\Lambda_{{\rm H_2},k}$ are the collisional excitation coefficients which are a function of temperature for

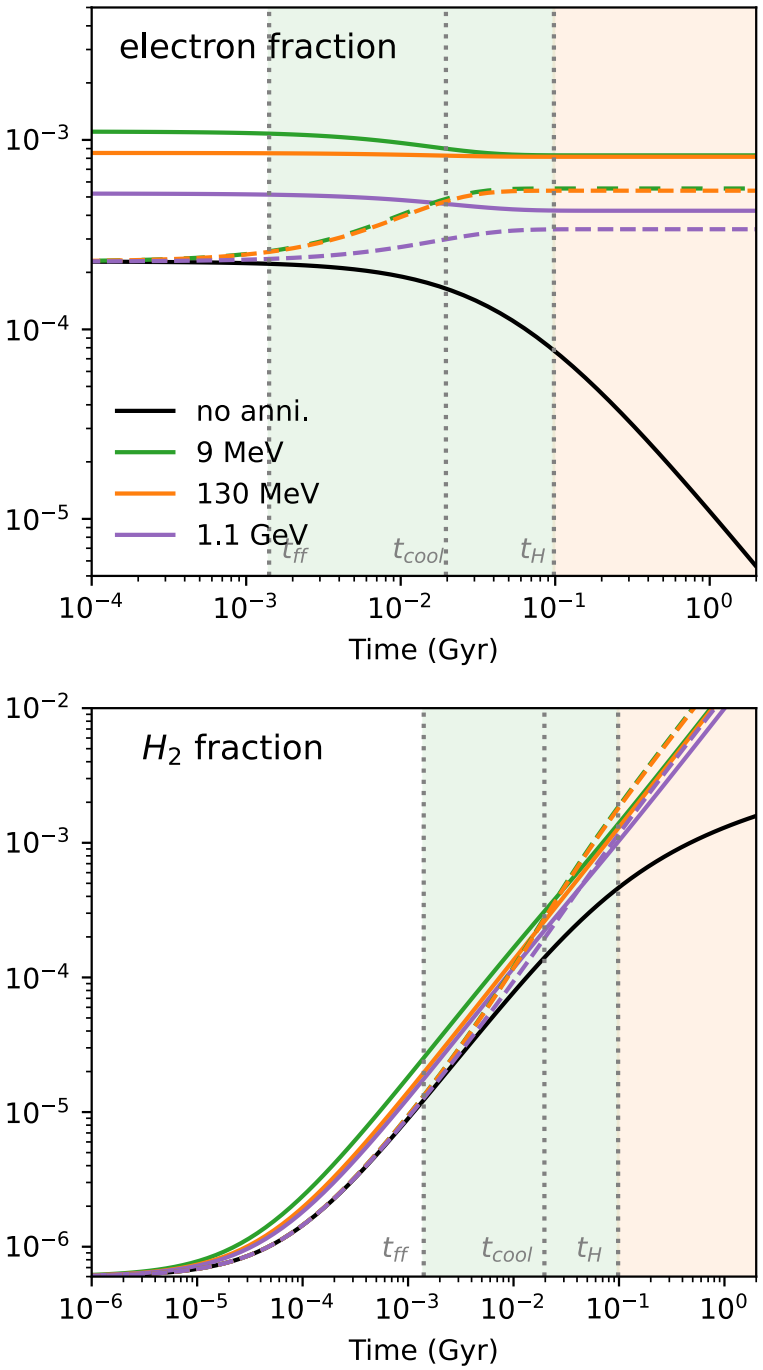


Figure 3.4: Fraction of electron and molecular hydrogen $H_2$ as a function of time during gas cooling. The halo has a mass $10^5 M_\odot$ at redshift $z = 40$. I present the case without annihilation (black), as well as cases with dark matter annihilation for different particle masses. Initial electron fractions are determined by the background thermal evolution, with the effects of corresponding dark matter annihilation. The free-fall time $t_{\rm ff}$ and the cooling time criterion $t_{\rm cool} = 0.2 t_H$ is presented in the figure. Dashes lines represent scenarios where the same initial condition of gas at $t = 0$ is assumed, with DM ionizing the gas thereafter.

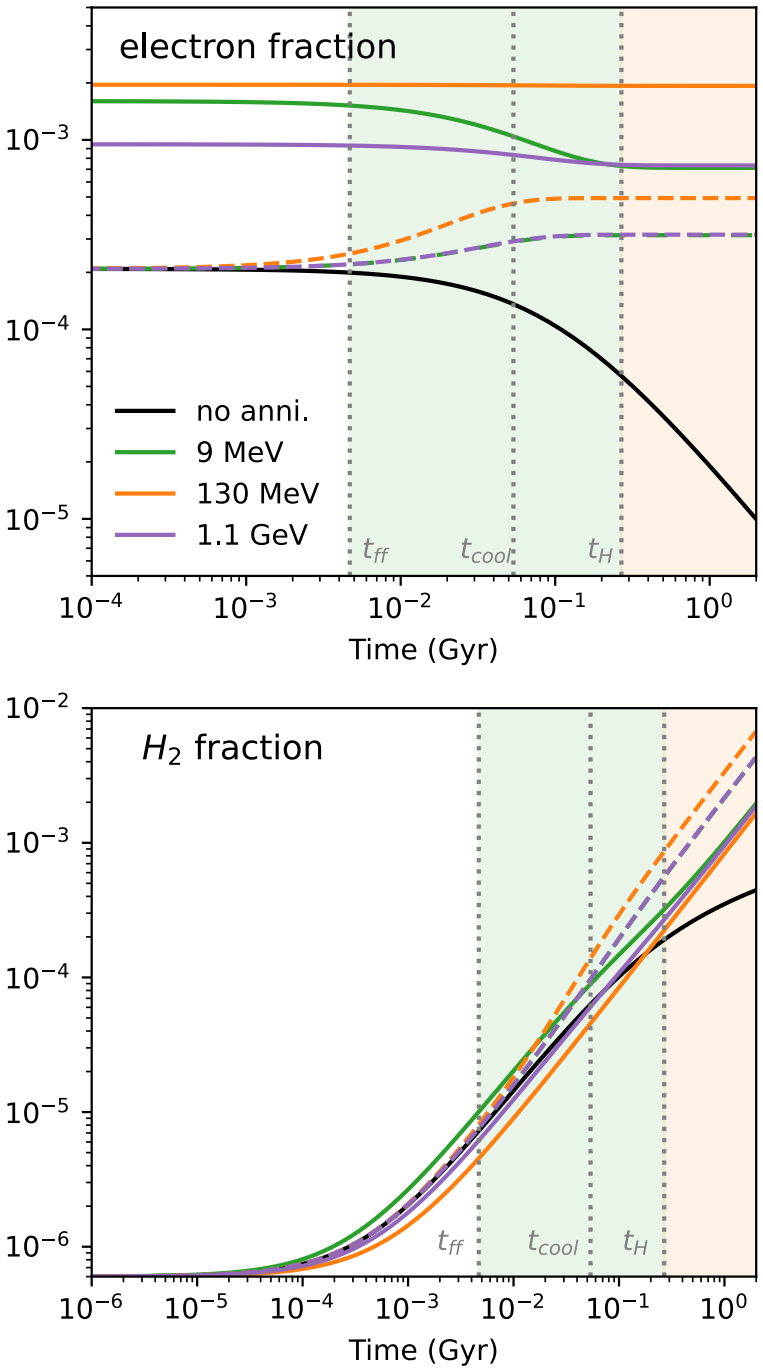


Figure 3.5: Fraction of electron and molecular hydrogen $H_2$ as a function of time during gas cooling. The halo has a mass $10^5 M_\odot$ at redshift $z = 20$. I present the case without annihilation (black), as well as cases with dark matter annihilation for different particle masses. Initial electron fractions are determined by the background thermal evolution, with the effects of corresponding dark matter annihilation. The free-fall time $t_{\rm ff}$ and the cooling time criterion $t_{\rm cool} = 0.2 t_H$ is presented in the figure. Dashes lines represent scenarios where the same initial condition of gas at $t = 0$ is assumed, with DM ionizing the gas thereafter.

each $k$, and $n_k$ is the number density of each species $k$, (such as H, He, $H_2$, $H^+$, and $e^-$).

The collisional excitation coefficients for $H_2$ are reviewed in Glover and Abel (2008), where the cooling rate has been calculated in several collisional processes involving H, $H_2$, He, $H^+$ and $e^-$. I adopt the cooling functions as calculated in that work, and maintain all the underlying assumptions of these functions. This includes adhering to the low-density environment and assuming an ortho-para ratio of 3:1. These assumptions are valid under the condition that the dark matter annihilation does not significantly alter the gas environment during the cooling process.

Dark matter annihilation has been implemented into our halo evolution model in the following two ways:

1. I use the gas number density $n$ and ionization fraction $x_e$ from our evolution results, which account for the effects of dark matter annihilation. The gas density is given by $n = f_{\rm gas}(z, M_h) n_{\rm DM}(0.1\, r_{\rm vir})$, where $f_{\rm gas}(z, M_h)$ represents the gas fraction, which is modified by dark matter annihilation. The initial ionization fraction of the gas, $x_e$, is determined using results from `CosmoRec`, which also include the impact of dark matter annihilation.

2. I modify the total cooling rate $\Lambda_0 n_{\rm H_2}$ to $n_{\rm H_2}\Lambda_0 - n_{\rm H}\epsilon^{\rm DM}_{\rm heat}(z)$ to account for dark matter annihilation heating during gas cooling. Here, $\epsilon^{\rm DM}_{\rm heat}(z)$ represents the energy deposited into the heating channel per unit time per baryon, as defined by Equation 3.5. I assume this value is solely a function of redshift.

In Fig. 3.6, I plot the fraction of molecular hydrogen, $H_2$, in a halo in the presence of a dark matter annihilation background, as a function of virial temperature, $T_{\rm vir}$. The plot compares the required $H_2$ fraction for cooling $x_{req}$ (dashed lines), determined by the criterion $t_{\rm cool} < 0.2\, t_{\rm H}$, with the produced $H_2$ fraction $x_{H_2}$ (solid lines), given by Equation 3.24. In the top panel, dark matter annihilation increases the produced $H_2$ fraction. Dark matter annihilation ionizes the IGM in the early universe, thereby providing higher initial ionization fraction compared to the baseline. This increase varies with the dark matter mass, with 9 MeV and 130 MeV dark matter producing higher $H_2$ fractions due to a larger energy deposition fraction in ionization. However, DM heating simultaneously suppresses the cooling rate by increasing the cooling time, $t_{\rm cool}$, which raises the required $H_2$ fraction for cooling. The dashed lines in the plot shift upward in the dark matter annihilation case, reflecting this increase in the required $H_2$ fraction.

The critical virial temperature, $T_{\rm crit}$, is defined as the point where the produced $H_2$ fraction equals the required fraction for cooling to occur. Since dark matter annihilation can alter both $x_{\rm H_2}$ and $x_{\rm req}$, the critical virial temperature is expected to change accordingly. However, in the top panel, both the produced and required $H_2$ fractions increase due to dark matter annihilation, resulting in only minor changes to the critical virial temperature.

In the bottom panel, I plot the fraction of $H_2$ at redshift $z = 20$. At this redshift, dark matter

annihilation has different effects on the produced $H_2$ fraction depending on the dark matter mass. The 9 MeV dark matter increases the $H_2$ fraction, while the 130 MeV dark matter decreases this fraction. The suppression of $H_2$ fraction is primarily driven by the strong DM heating. The intensity of DM annihilation is stronger at lower redshift because of a stronger boost from DM structure formation. The resulting heating reduces the gas density and makes $H_2$ production less efficient. This is also reflected in the dashed lines, where the required $H_2$ fraction increases more significantly compared to the case at higher redshift. As a result, the critical virial temperature shifts to higher values, even for 9 MeV dark matter. At this redshift, dark matter annihilation has a primarily negative effect on molecular cooling.

In Fig. 3.7, I predict the minimum cooling mass, $M_{\rm cool}$, in the presence of dark matter annihilation over redshifts ranging from $z = 20$ to $z = 50$. The solid black line in the top panel shows the minimum cooling mass in our baseline model without dark matter annihilation. I compare our results with those from several previous studies. The results from Fialkov et al. (2012); Kulkarni et al. (2021); Schauer et al. (2021) and Nebrin et al. (2023) are shown as dashed lines. I set the Lyman-Werner (LW) background and streaming velocity to zero in these models to match our baseline model. Our cooling threshold is close to that of Fialkov et al. (2012), but our slope is slightly lower. In Kulkarni et al. (2021), the halo mass above which 50% of halos host cool and dense gas is defined as $M_{\rm crit}$, while in Schauer et al. (2021), they define a minimal ($M_{\rm min}$) and an average ($M_{\rm ave}$) halo mass at collapse. Our minimum cooling mass is generally greater than the value $M_{\rm crit}(z)$ as reported in Kulkarni et al. (2021) but lower than the redshift-independent value $M_{\rm min}$ (shown in the plot) and $M_{\rm ave}$ (not shown in the plot) from Schauer et al. (2021). The grey dashed line represents the analytic model of Nebrin et al. (2023), which is similar to our model but uses a stricter cooling criterion, $t_{\rm cool} < 6t_{\rm ff}$, where $t_{\rm ff} = (3\pi/32G\bar{\rho}_{\rm core})^{1/2}$ is the free-fall timescale, and $\bar{\rho}_{\rm core}$ is the mean core density of the dark matter halo. This stricter criterion results in larger minimum cooling mass estimates than in our work, which uses the criterion $t_{\rm cool} < 0.2t_H$. Another key difference is that Nebrin et al. (2023) tailored the virial temperature $T_{\rm vir}$ by multiplying it by a factor of 0.75 relative to the formula given in Equation 1.30 to match simulation results. This results in a lower cored density for a halo of same mass, and thereby suppresses the molecular cooling. These factors may explain why our results are lower.

I acknowledge that a complete calculation would need to be more complex than our simplified model. For instance, I assumed that the gas density and temperature are fixed in order to obtain the cooling criterion for a halo. However, in reality, the gas temperature decreases as cooling proceeds, and the cooling rate, $\Lambda_0$, which depends on temperature, is not constant during this process. As a result, the calculation may slightly overestimate the cooling rate. I tested a method to incorporate the temperature evolution into our model and found that the

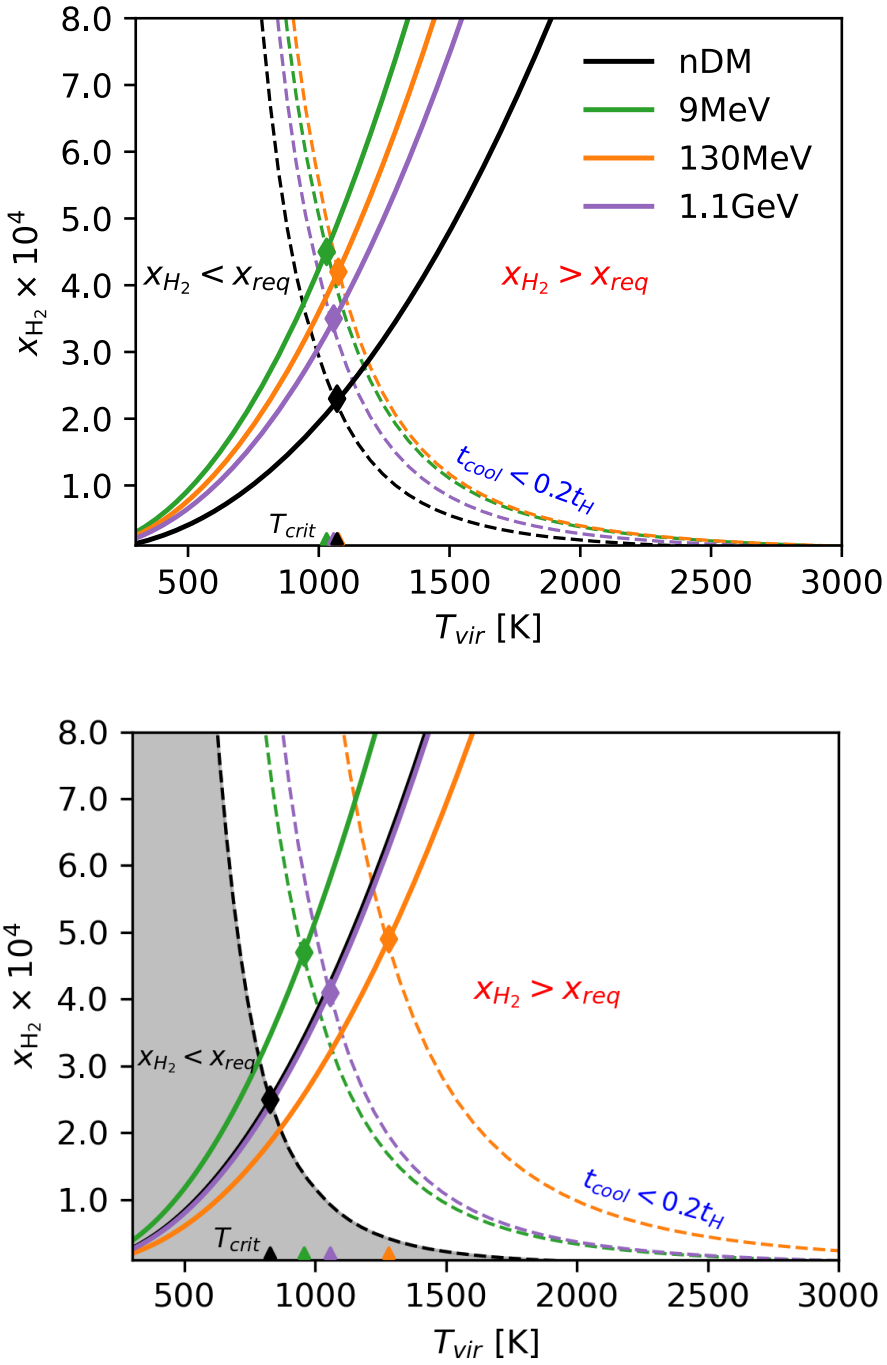


Figure 3.6: The molecular hydrogen fraction as a function of virial temperature at redshift $z = 40$ and $z = 20$. The dashed lines represent the required $H_2$ fraction, determined by the criterion $t_{\rm cool} < 0.2\,t_H$, while the solid lines correspond to the molecular hydrogen fraction at the same time. Cooling is not possible in the grey regions, where the produced $H_2$ fraction is lower than the required fraction. Dark matter annihilation alters both $x_{\rm H_2}$ and $x_{\rm req}$, as depicted by the different colored lines, each corresponding to a specific dark matter mass.

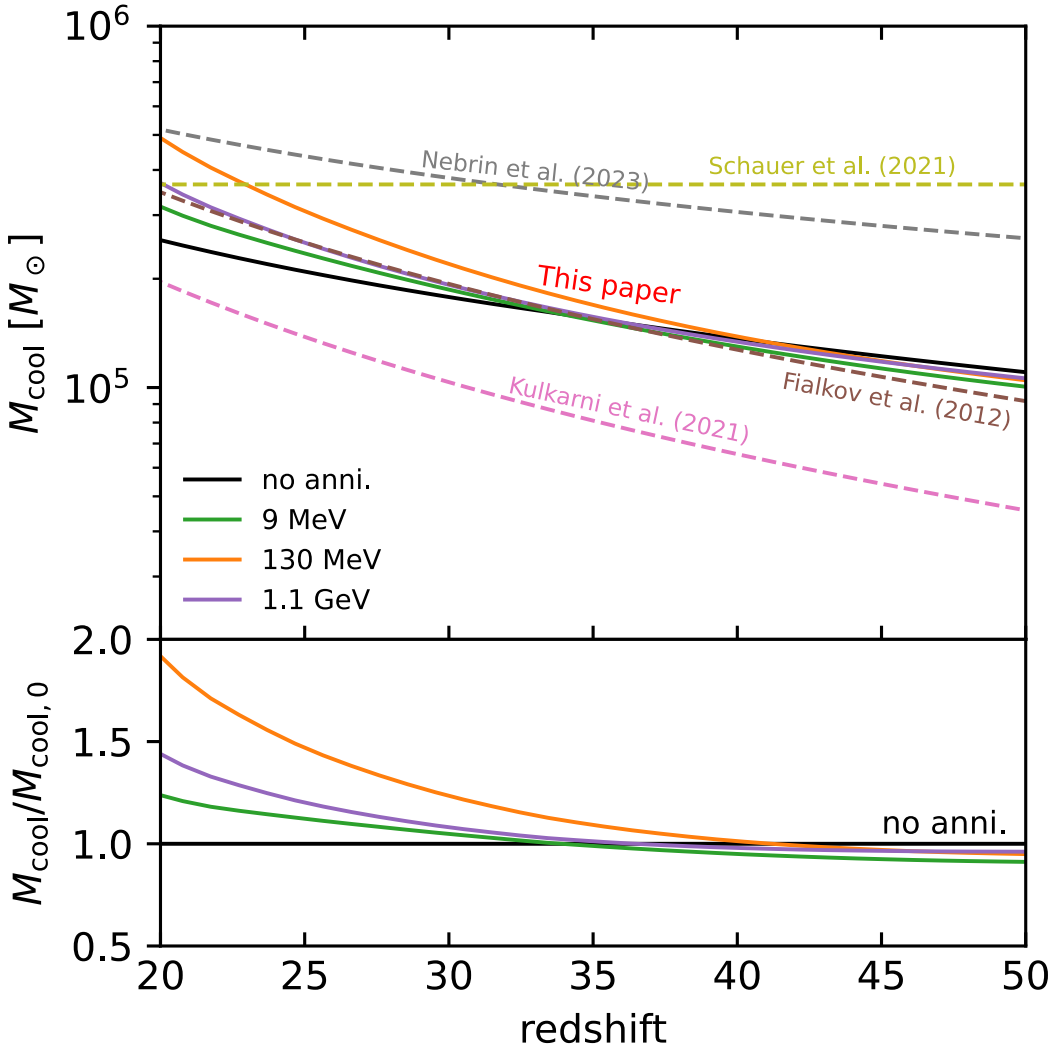


Figure 3.7: The minimum cooling mass, $M_{\rm cool}$, as a function of redshift with dark matter annihilation. In the top panel, the black line represents our baseline scenario without the effects of dark matter annihilation. The brown dashed line corresponds to the fit from simulations without a Lyman-Werner (LW) background and dark matter-baryon streaming, as detailed in (Fialkov et al. 2012). The pink dashed line is adopted from the fit in (Kulkarni et al. 2021). The grey dashed line shows the analytic model of (Nebrin et al. 2023), which assumes the criterion $t_{\rm cool} < 6t_{\rm ff}$. In the bottom panel, different lines represent the relative ratio of the minimum cooling mass to the baseline $M_{\rm cool,0}$ with different dark matter masses.

resulting changes were small for times $t < t_{\rm cool}$. Therefore, our approximation is likely sufficient in most cases.

Given the initial conditions of the gas, I calculate the cooling time-scale, $t_{\rm cool}$. The gas may undergo free-fall collapse if $t_{\rm cool} < t_{\rm ff}$ or experience collapse with an extended duration if $t_{\rm cool}$ is between $t_{\rm ff}$ and $t_H$. As shown in the green area of Fig. 3.4 and 3.5, the fraction of $H_2$ increases with time, while the required fraction decreases over time. This could lead to inaccuracies in the cooling mass estimation, as suggested by Nebrin et al. (2023). Some studies, such as Gurian et al. (2024), have also found that gas may collapse in halos that are excluded by the cooling criterion if the gas exhibits specific instabilities.

The bottom panel of Fig. 3.4 and 3.5 show the relative changes of minimum cooling mass with dark matter annihilation, $M_{\rm cool}/M_{\rm cool,0}$, where $M_{\rm cool,0}$ is the minimum cooling mass without dark matter annihilation, corresponding to the black line in the top panel. I found the dark matter annihilation impact increases with time. Dark matter annihilation slightly decreases the cooling mass at higher redshifts ($z > 40$) but increases it at lower redshifts ($z < 40$). At redshift $z = 20$, the DM could increase the minimum cooling mass by a factor of 2.

**LW Background**

In the presence of LW radiation, $H_2$ can be photo-dissociated. Although in this work I have not included the potential LW flux from dark matter annihilation, the LW flux from stellar feedback can lead to an increase in the minimum cooling mass (Trenti and Stiavelli 2009; Fialkov et al. 2013b; Visbal et al. 2014; Kulkarni et al. 2021; Schauer et al. 2021). I will consider molecular cooling with dark matter annihilation in presence of a stellar LW background. Here, the formation of $H_2$ in Equation 3.22 becomes

$$\frac{d\,x_{\rm H_2}}{d\,t} = k_1\,x_e\,n_H\left(1+\frac{k_3}{k_2}x_e\right)^{-1} - k_{\rm LW}\,x_{\rm H_2}\,, \tag{3.28}$$

where $k_{\rm LW}$ is the photo-dissociation rate of $H_2$, given by Wolcott-Green et al. (2017),

$$k_{\rm LW} = 1.38\times10^{-12}\,f_{sh}\,J_{\rm LW}\,, \tag{3.29}$$

where $J_{\rm LW}$ is the Lyman-Werner intensity in units of $10^{-21}\,{\rm erg\,s^{-1}\,cm^{-2}\,Hz^{-1}\,sr^{-1}}$ and $f_{sh}$ is the self-shielding parameter taken from Wolcott-Green and Haiman (2019), as a function of the gas density and temperature. The provided fitting function is:

$$
\begin{aligned}
f_{\rm sh}(N_{\rm H_2}, T) &= \frac{0.965}{(1+x/b_5)^{\alpha(n,T)}} + \frac{0.035}{(1+x)^{0.5}} \\
&\quad \times \exp\left[-8.5\times10^{-4}(1+x)^{0.5}\right], \\
\alpha(n,T) &= A_1(T) e^{-0.2856\log\left(\mathrm{n/cm^{-3}}\right)} + A_2(T), \\
A_1(T) &= 0.8711\log(T/K) - 1.928, \\
A_2(T) &= -0.9639\log(T/K) + 3.892,
\end{aligned}
\tag{3.30}
$$

where $b_5 = (2k_B T/m_{\rm H_2})^{1/2}/10^5$ cm$^2$ s$^{-1}$ and $x = N_{\rm H_2}/5\times10^{14}$ cm$^2$.

Fig. 3.8 shows the production of molecular hydrogen in a $10^5 M_\odot$ dark matter halo, influenced by both Lyman-Werner feedback and DM annihilation. The $H_2$ fraction is calculated using Equation 3.28 for a range of LW intensities: $J_{\rm LW} = 0$, 0.1, and 1.0. The initial fraction is $x_{\rm H_2} = 6\times10^{-7}$ for every case, as before. At each step, I estimate the $H_2$ column density $N_{\rm H_2} = 0.926 f_{\rm H_2} n_{\rm core} R_{\rm core}$ according to Nebrin et al. (2023), where $R_{\rm core} = 0.1 R_{\rm vir}$ and $n_{\rm core}$ is the core gas density, and I calculate $k_{\rm LW}$ using Equation 3.29.

In the top panel, at redshift $z = 40$, although the $H_2$ fraction has been suppressed by the LW photons, the effect of DM annihilation only slightly alters the $H_2$ formation before the cooling time, $t < t_{\rm cool}$. While I have included a full range of LW values, the expected intensity at $z = 40$ is very small, $J_{\rm LW} \approx 0.001$ (Fialkov et al. 2013b; Incatasciato et al. 2023), so the effect of LW radiation is likely not significant. In the bottom panel at redshift $z = 20$, where the LW intensity is expected to be stronger ($J_{\rm LW} \approx 1$), LW photons should efficiently dissociate $H_2$ molecules. The $H_2$ fraction decreases from $10^{-4}$ to $10^{-7}$ as $J_{\rm LW}$ rises during the cooling phase, consistent with the findings of Kulkarni et al. (2021). In the case with dark matter annihilation, the evolution is initially similar, but diverges from the baseline case after $t_{\rm cool}$, showing a larger $H_2$ fraction compared to the case with LW radiation alone.

To incorporate the stellar LW background in this study, I adopt the redshift-dependent LW intensity, $J_{\rm LW}(z)$, from Incatasciato et al. (2023). This function is fitted for the range $6 < z < 23$, and I extrapolate it to higher redshifts. I acknowledge that the PopIII star formation model used in that work differs from our model, which may lead to inconsistencies in the LW feedback. However, it still provides a good approximation for evaluating the effect of DM annihilation under varying LW radiation intensities.

Fig. 3.9 plots the minimum cooling mass with stellar LW feedback and dark matter annihilation. In the top panel, the solid black line represents the case with LW background alone. Compared to the case without LW radiation (as shown in Figure 3.7), I find that the LW background causes minor changes at high redshift, but significantly increases the minimum cooling mass at lower redshift ($z < 30$). I plot the result from previous studies in dashed lines. In our model, with LW feedback, the slope of $M_{\rm cool}$ at lower redshifts closely aligns with the analytic

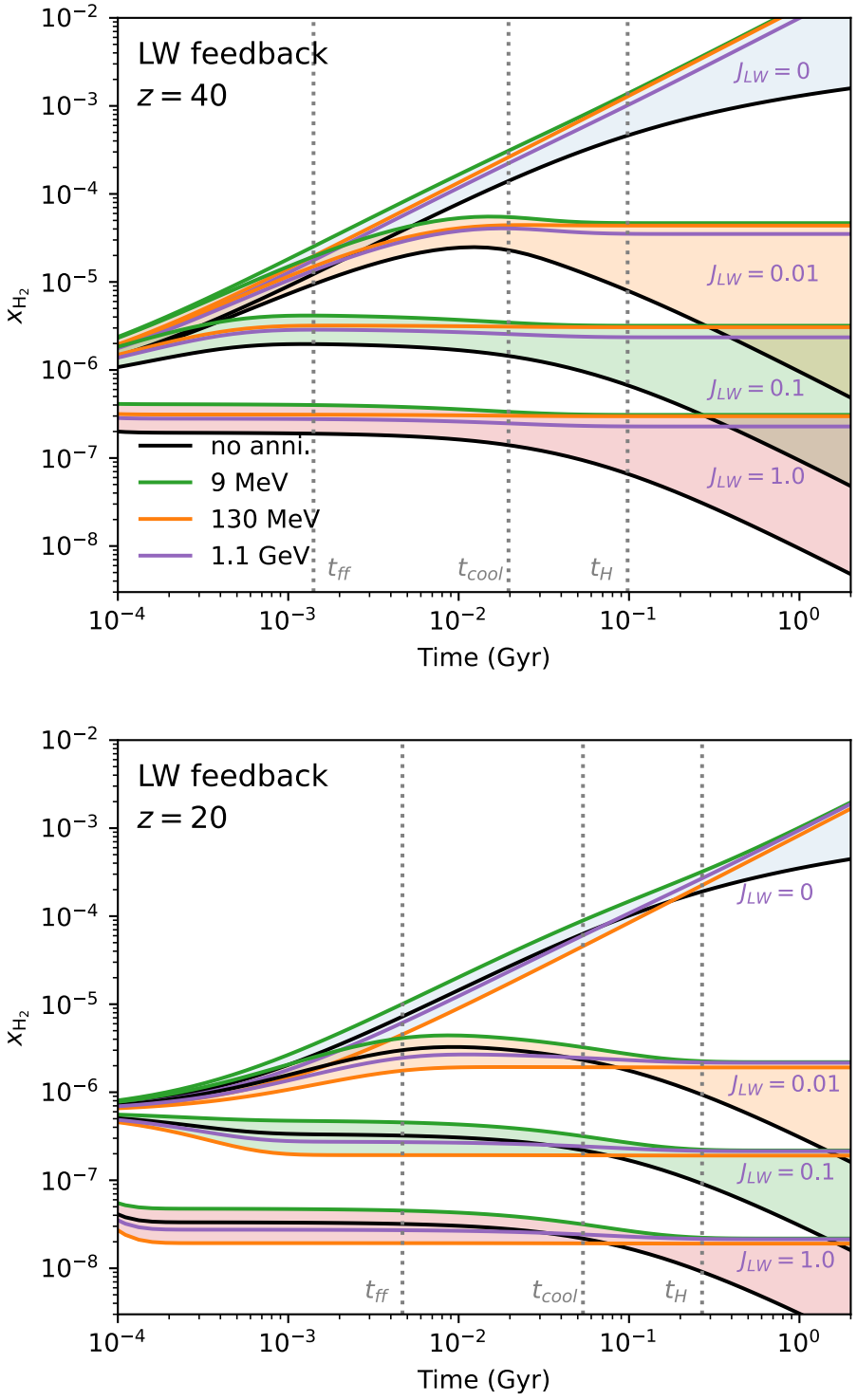


Figure 3.8: Molecular hydrogen fraction in a $10^5 M_\odot$ halo with both DM annihilation and Lyman-Werner (LW) feedback. The $H_2$ fractions at the redshift $z = 40$ (top panel) and $z = 20$ (bottom panel) are shown for different intensities of LW radiation (colored areas) and DM mass (colored lines). From top to bottom, the $H_2$ fractions was calculated with LW intensity values $J_{\rm LW} = 0$, 0.1, and 1.0.

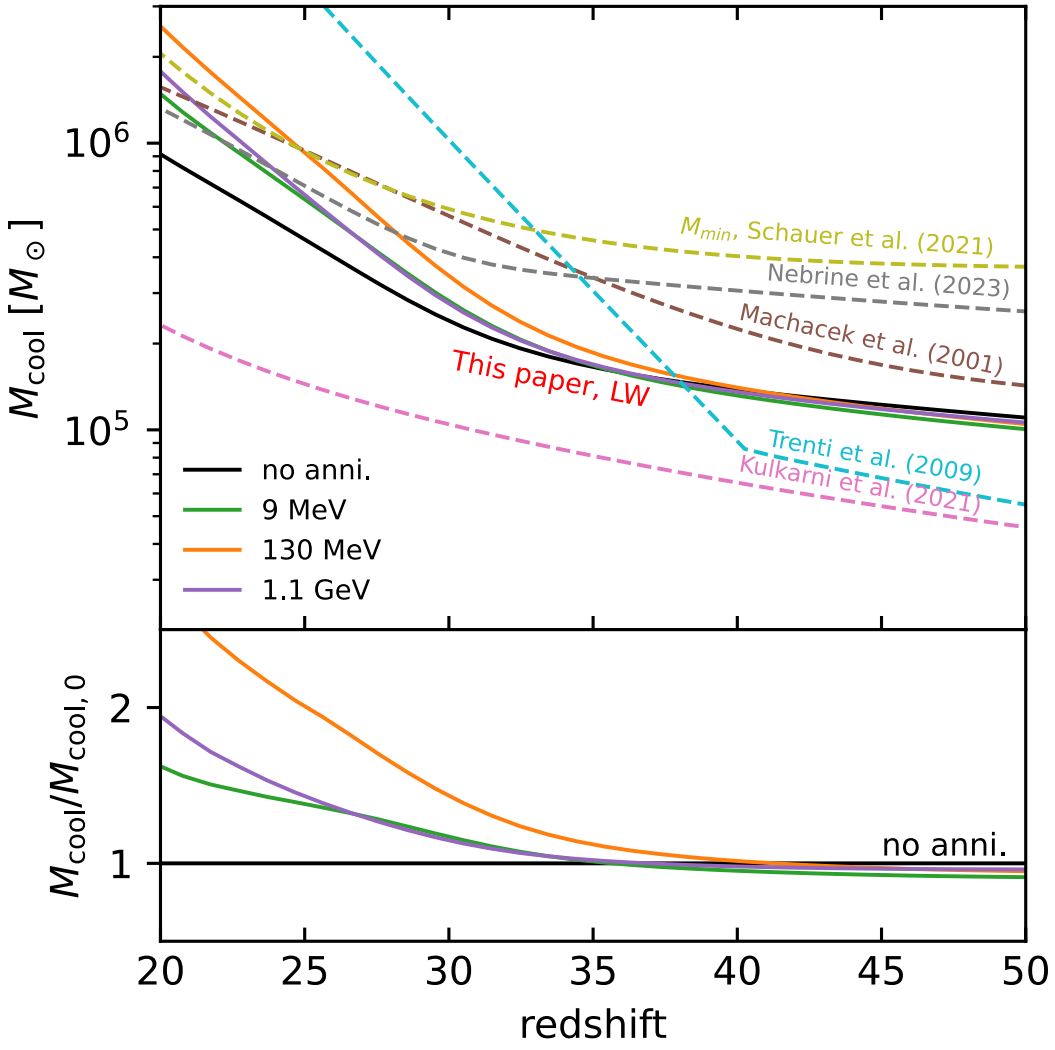


Figure 3.9: The minimum cooling mass $M_{\rm cool}$ as a function of redshift with both DM annihilation and LW feedback is included. Our results are compared to previous calculations from redshift $z = 20$ to 50. All cooling mass thresholds were calculated using the same LW background $J_{\rm LW}(z)$ as described in Incatasciato et al. (2023). The bottom panel shows the relative effect of DM annihilation on the minimum cooling mass. At high redshift, where LW feedback is weak, the effect of DM annihilation is similar to the case before, but it becomes stronger at lower redshift as LW feedback becomes more significant.

model of Trenti and Stiavelli (2009). I applied a self-shielding factor in Equation 3.28, resulting in a flatter slope that more closely matches simulation results at higher redshifts. The minimum cooling mass is sensitive to the choice of cooling time criterion (see Fig. 3.8), which may explain why our slope is steeper than that of the analytic model with a shorter time criterion (Nebrin et al. 2023) at low redshifts. I also include fitting functions from the simulations of Machacek et al. (2001) and Kulkarni et al. (2021), as well as the redshift-independent result from Schauer et al. (2021). Compared to our analytic results without DM annihilation (black line), the simulation results, particularly those of Kulkarni et al. (2021), suggest that LW feedback has a less pronounced effect at lower redshifts.

In the bottom panel, I show how the influence of dark matter annihilation in the presence of a LW background varies with DM mass. Generally, DM annihilation very slightly decreases $M_{\rm cool}$ at high redshift, similar to the behavior seen in the case without LW feedback (as shown in Figure 3.7). However, our result indicates that LW feedback magnifies the DM annihilation effect in molecular cooling, and the impact of DM annihilation increases over time, becoming slightly larger than in the case without LW feedback at lower redshifts.

I acknowledge that some radiative backgrounds, such as the cosmic X-ray background, are not included in this model. The cosmic X-ray background shares similar properties with DM annihilation, as both contribute to heating and ionizing primordial gas, which can either increase or decrease cooling. The transition between these two regimes occurs at gas densities between $n = 1$ and 100 cm$^{-3}$, depending on the strength of the X-ray background (Hummel et al. 2015). This effect has been included in recent molecular cooling studies and is expected to be important at lower redshifts ($z < 15$) (Hegde and Furlanetto 2023).

**Streaming Velocity**

Now, I can incorporate streaming into the molecular cooling model. First, I consider the effect of streaming on the gas density. I calculate the gas fraction, $f_{\rm gas}$, with streaming included. I modify the IGM temperature in the presence of streaming, following the prescription in McQuinn and O'Leary (2012):

$$T_{\rm IGM}(v_{bc}) = T_{\rm IGM}(1 + 5\mathscr{M}_{bc}^2/9)\,, \tag{3.31}$$

where $\mathscr{M}_{bc} = v_{bc}/c_{s,\rm IGM}$ and $c_{s,\rm IGM}$ is the sound speed in the IGM. The increase in temperature results in a suppression of the gas density according to Equation 3.16.

Subsequently, I recalculate the electron and molecular hydrogen fractions, and recalculate the cooling time. The minimum cooling mass $M_{\rm cool}$ is now expressed as $M_{\rm cool}(z, v_{bc})$ as a function of streaming velocity $v_{bc}$.

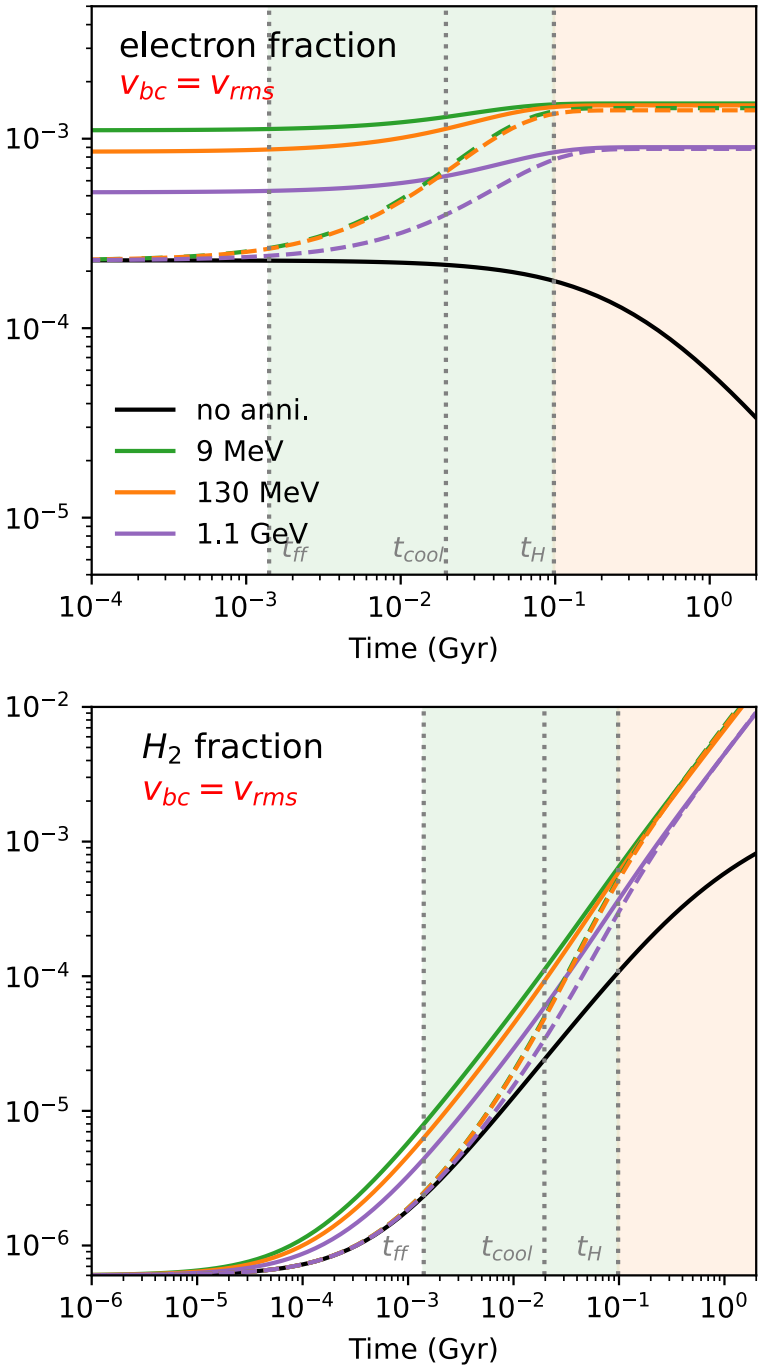


Figure 3.10: Fractions of electrons and molecular hydrogen in a $10^5 M_\odot$ halo at a redshift of $z = 40$. This figure accounts for both streaming velocity and dark matter annihilation, with the streaming velocity $v_{bc}$ set to the root-mean-squared value $v_{\rm rms}$, which leads to a decrease in gas density.

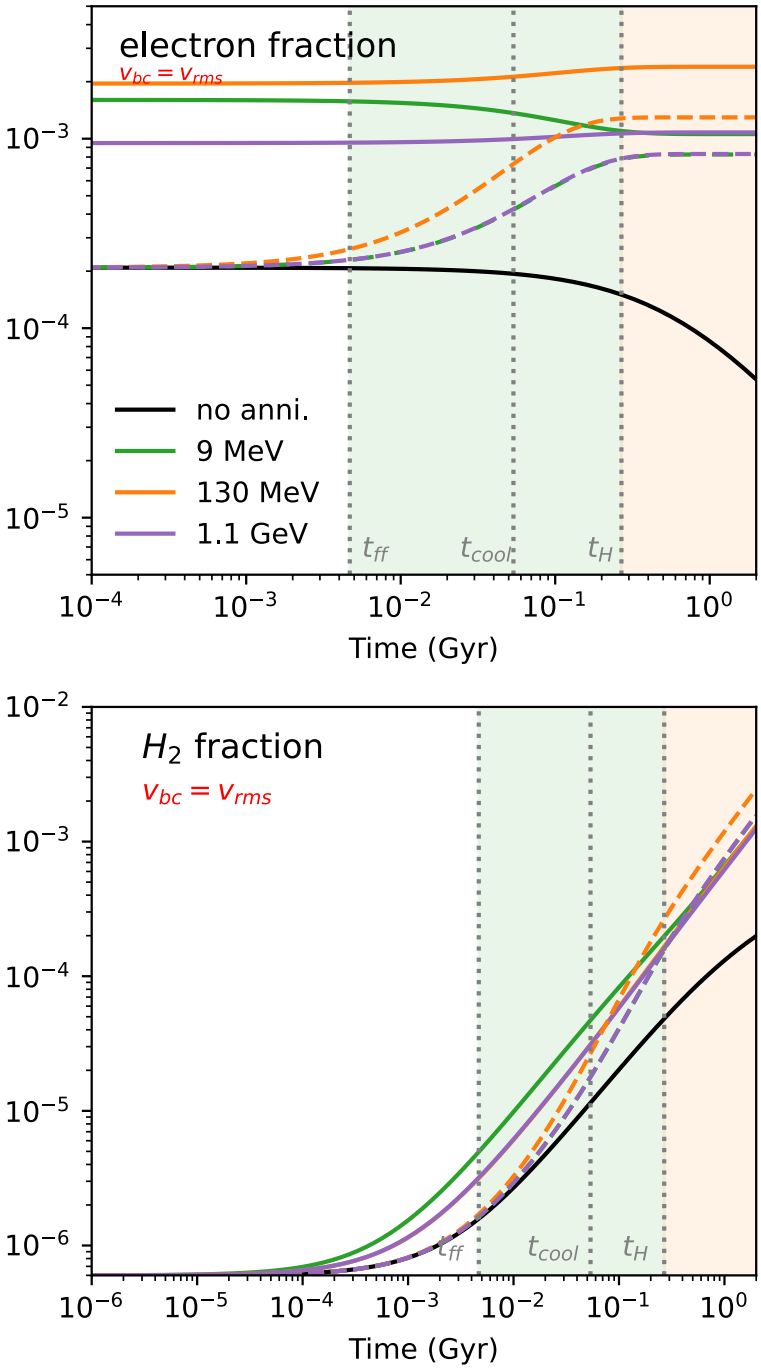


Figure 3.11: Fractions of electrons and molecular hydrogen in a $10^5 M_\odot$ halo at a redshift of $z = 20$. This figure accounts for both streaming velocity and dark matter annihilation, with the streaming velocity $v_{bc}$ set to the root-mean-squared value $v_{\rm rms}$, which leads to a decrease in gas density.

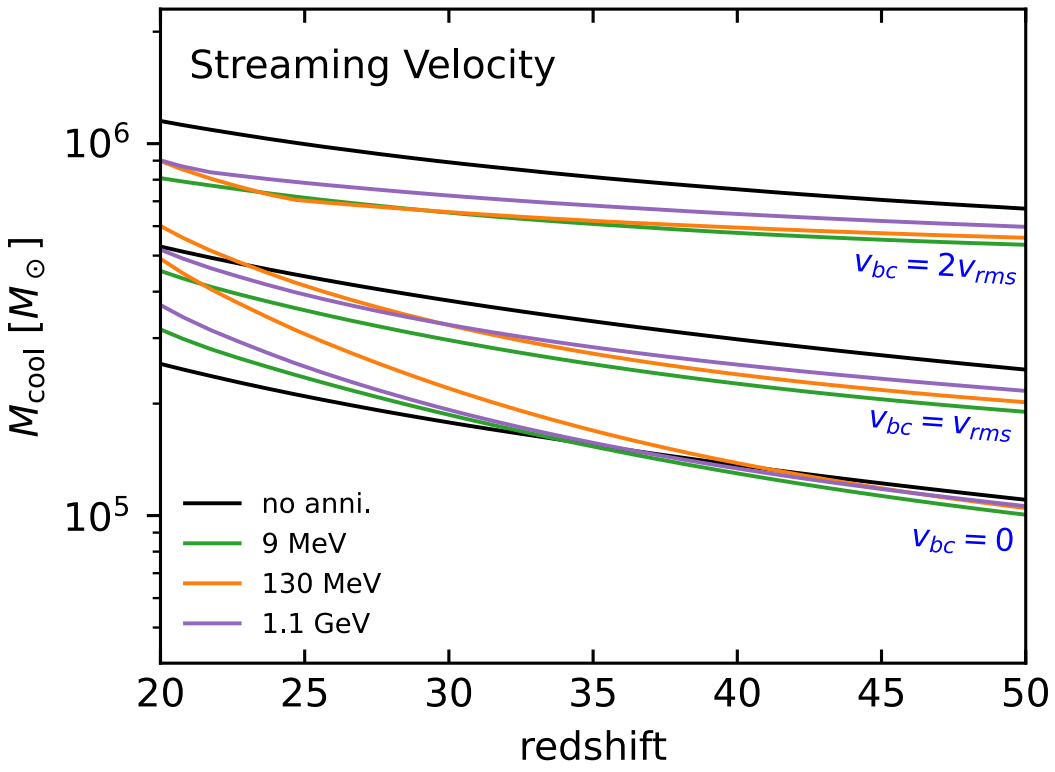


Figure 3.12: Minimum cooling mass as a function of redshift, considering the effects of dark matter annihilation and varying streaming velocities. The black lines (from top to bottom) represent the minimum cooling mass for streaming velocities of $v_{bc} = 2v_{\rm rms}$, $v_{bc} = v_{\rm rms}$, and $v_{bc} = 0$ in our model. The colored lines indicate the results with dark matter annihilation of mass 9 MeV, 130 MeV and 1.1 GeV incorporated at different streaming velocities.

Fig. 3.10 and 3.11 depict the fraction of free electrons $x_e$ and molecular hydrogen $x_{\rm H_2}$ in the presence of a streaming velocity $v_{bc} = v_{\rm rms}$. I observe that the electron fraction decreases more slowly compared to the case with $v_{bc} = 0$ (Fig. 3.4 and 3.5), since the recombination rate is higher in denser regions. Dark matter (DM) ionization becomes more efficient with streaming, resulting in the electron fraction being dominated by DM ionization. Consequently, $x_e$ becomes insensitive to the initial conditions after a sufficiently long time, $t > t_H$. The molecular hydrogen fraction, $x_{\rm H_2}$, is relatively lower than that in the absence of streaming. However, I observe that DM annihilation in this scenario accelerates $H_2$ production due to the increase in the electron fraction.

Fig. 3.12 shows the minimum cooling mass $M_{\rm cool}(z)$ in the presence of both streaming and DM annihilation. The reduction in the gas fraction decreases the efficiency of molecular hydrogen production, leading to an increase in the minimum cooling mass by a factor of

approximately 2. Dark matter annihilation shows a distinct effect in the case of streaming velocity. Without streaming, annihilation leads to a decrease in $M_{\rm cool}$ at high redshift, but an increase at low redshift. However, I found that annihilation primarily reduces $M_{\rm cool}$ in most cases when $v_{bc} = v_{\rm rms}$ and a reduction across nearly all redshifts at $v_{bc} = 2v_{\rm rms}$. This is primarily due to streaming suppressing the gas density and molecular cooling, while the $H_2$ production increases under DM-induced ionization. As a result, the effect of DM heating is not significant.

Without dark matter annihilation, our result indicates that the minimum cooling mass is increased by a factor of approximately $M_{\rm cool}(v_{\rm rms})/M_{\rm cool}(0) \approx 2.1$ when $v_{bc} = v_{\rm rms}$ at redshift $z = 20$. This factor is slightly higher than the fitting result of 1.7 given by Fialkov et al. (2012), but lower than the results from more recent simulations. For instance, Kulkarni et al. (2021) reports a factor of $M_{\rm crit}(v_{\rm rms})/M_{\rm crit}(0) \approx 3.5$, and Schauer et al. (2021) finds $M_{\rm min}(v_{\rm rms})/M_{\rm min}(0) \approx 4.1$.

Fig. 3.13 illustrates the complete scenario for the minimum cooling mass, including dark matter annihilation, stellar Lyman-Werner feedback, and streaming. Standard Lyman-Werner feedback, as described by Incatasciato et al. (2023), was applied in the calculation. Our minimum cooling mass is generally lower than the cooling threshold given by previous simulations, which may be due to our choice of cooling time, the use of a simplified molecular hydrogen chemistry model, or the need of a complete evolution of gas density profile during cooling in the model.

In the presence of stellar LW feedback, I use the recent self-shielding function described by Wolcott-Green and Haiman (2019), which leads to a flatter cooling mass at early times, when the gas is dense. Our analytic calculation indicates a relatively sharper slope at low redshift due to LW feedback compared to the slope from simulations (Kulkarni et al. 2021), though it shows a similar slope to that found in Schauer et al. (2021).

Regarding streaming, I point out that our model reveals two distinct impacts of dark matter annihilation, depending on whether streaming is present or absent. This is because the effects of dark matter heating and ionization depend on gas density, and the core gas density is significantly suppressed by streaming velocity. As shown in the bottom panel, dark matter annihilation has a suppression on molecular cooling, thereby increase the cooling mass without streaming at redshift $z \lesssim 30$, but this suppression is reduced with streaming, making the cooling mass remain lower than the case without annihilation. In our model, streaming velocity alters gas density by affecting the effective sound speed and filtering mass, a method also used in previous analyses such as Naoz et al. (2012). However, instead of estimating the impact of streaming on the minimum cooling mass through the halo of circular velocity $V_{\rm cool}$ fitted from simulations (Fialkov et al. 2012), I directly derive the minimum cooling mass with streaming in our analytic model by adjusting the gas density. This approach allows us to account for potential interactions between DM annihilation, LW feedback and streaming within

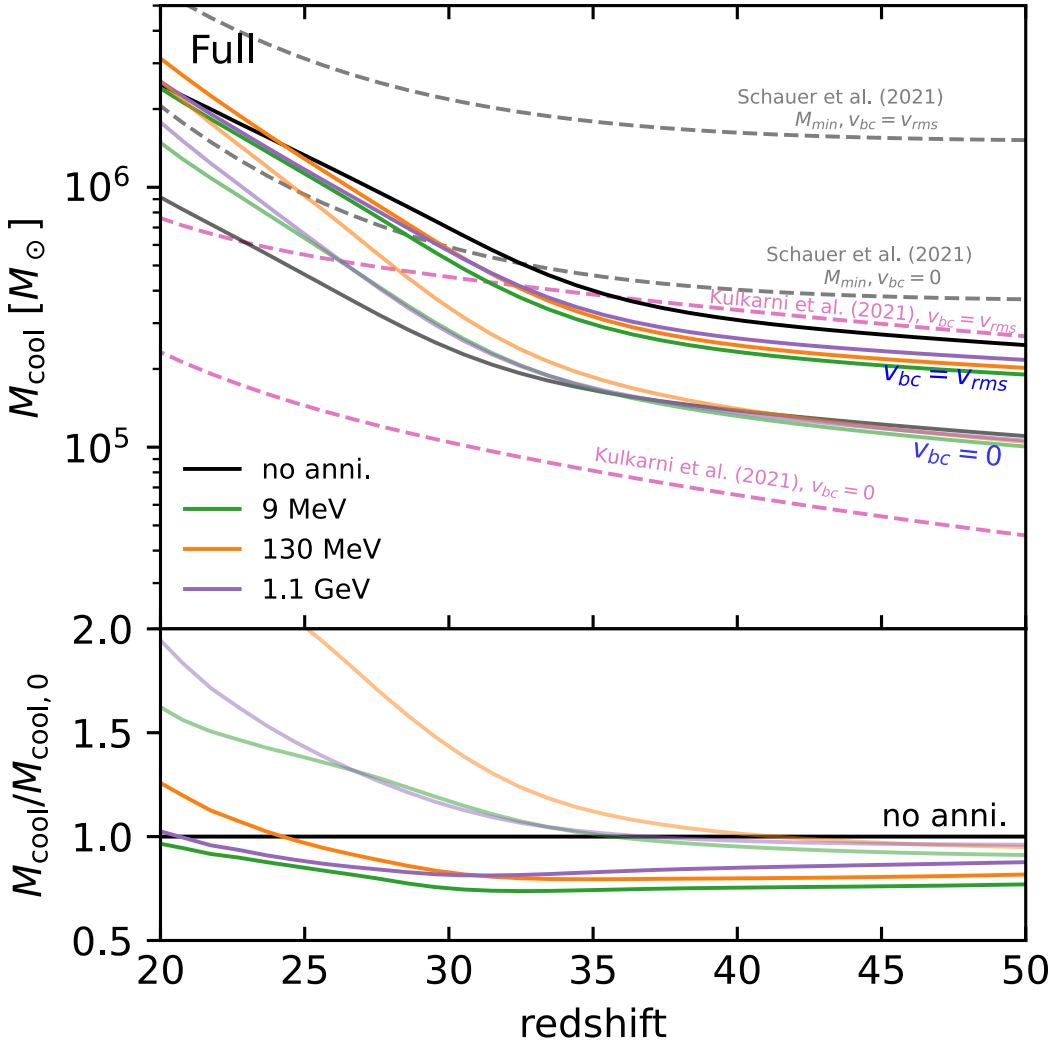


Figure 3.13: Minimal cooling mass in full scenario, include dark matter annihilation, Lyman-Werner feedback, and streaming velocity. The top panel plots $M_{\rm cool}$ as a function of redshift. The black line represents the scenario without dark matter annihilation. Different colors represent dark matter annihilation for various dark matter masses (9 MeV, 130 MeV, and 1.1 GeV). Two distinct scenarios are presented in the figure: one with streaming velocity ($v_{bc} = v_{\rm rms}$) and one without ($v_{bc} = 0$). These results are compared with those from previous simulations (Kulkarni et al. 2021; Schauer et al. 2021). The bottom panel plots the relative cooling mass compared to the scenario without dark matter annihilation as a function of redshift. Dark matter annihilation has a relatively greater impact in regions without streaming velocity than in those with streaming velocity.

a consistent framework.

### 3.2.4 Local Effect

While I have neglected the effects of dark matter (DM) annihilation local to DM halos in this work, the local DM has the potential to significantly influence the surrounding gas by depositing energy into it. This process can play a crucial role in various astrophysical phenomena, impacting the thermal and ionization states of the circumgalactic medium of early galaxies. Understanding the local effects of dark matter annihilation is essential for comprehending the behavior of gas, as well as the first stars and galaxies in the early universe. This section briefly summarizes the mechanisms through which dark matter annihilation contributes to energy deposition in the surrounding gas to estimate its importance in the context of gas cooling.

For a small halo, although a dense DM core can inject significant DM annihilation power, a large fraction, $f_{\rm esc}$, of dark matter annihilation energy is expected to escape from the local environment and boost the global DM annihilation background. The total deposited fraction in surrounding gas is $f_{\rm local} = 1 - f_{\rm esc}$. The energy deposition of dark matter annihilation products is determined by the interactions between the annihilation products from dark matter and the baryons or photons in the local environment and the Cosmic Microwave Background (CMB), via the process such as inverse Compton scattering, photo-ionization, etc. This has been studied in energy transfer simulations on large scales (Evoli et al. 2014; Schon et al. 2014), but only roughly on mini-halo scales (Schön et al. 2017). Therefore, I apply a parameterized semi-analytic model and provide a rough estimate of the local effects here.

It is worth noting that we have considered the boost factor $B(z)$ as a function of redshift in the cosmic dark matter annihilation power, as described in Sec. 3.1.1. This factor accounts for the contribution of dark matter annihilation from cosmic dark matter halos and provides a mean boost to the global dark matter annihilation power, depending solely on redshift. In contrast, the local dark matter annihilation arising from dark matter in the host halo introduces an additional boost to the local gas, which is strongly influenced by the specific dark matter distribution within the host halo.

First, I aim to estimate the intensity of local dark matter annihilation $\epsilon^{\rm DM}_{\rm c,local}$, and compare it with the global DM annihilation background $\epsilon^{\rm DM}_{\rm c,bg}$. The latter can be calculated using Equation 3.5. The parameter $\epsilon^{\rm DM}_{\rm c,local}$ reflects the energy transfer from the dark matter annihilation products produced by the local halo to the local baryonic environment. The calculation depends on the DM annihilation model and the gas profile, and requires detailed simulations for a fully rigorous treatment.

Recent small-scale energy transfer simulations suggest that an electron with an energy

of $10^8$ eV injected into a $10^6\,M_\odot$ halo at redshift $z = 40$ deposits approximately $0.1\,\mathrm{eV/pc^3}$ in the circumgalactic medium (CGM) (Schön et al. 2017). I adopt the CGM gas density profile $\rho \approx 20\bar{\rho}(r/R_{\rm vir})^{-1}$ (Dijkstra et al. 2007; Bruns Jr et al. 2012) and use it to calculate the total energy deposition $\epsilon^{\rm DM}_{\rm local}$, where $\bar{\rho}$ is the mean gas density of IGM. This results in $\log(\epsilon^{\rm DM}_{\rm local}/E_h) \sim -64$, where $E_h$ is the total dark matter annihilation power of the halo. For simplicity, I parameterize this dimensionless factor as $h = \log(\epsilon^{\rm DM}_{\rm local}/E_h)$, setting a baseline value of $h = -65$ and assuming it is independent of both halo mass and redshift. The local energy deposition in channel $c$ is given by $\epsilon^{\rm DM}_{\rm c,local} = f_c\,\epsilon^{\rm DM}_{\rm local}$, where $f_c$ represents the fraction of total energy deposited in channel $c$. I assign deposition fractions for heating and for the ionization of H and He as $f_{\rm heat} = [1+2x_e+f_{\rm He}(1+2Z_{\rm HeII})]/3[1+f_{\rm He}]$, $f_{\rm ion,H} = (1-x_e)/3$, and $f_{\rm ion,He} = (1-Z_{\rm HeII})/3$, respectively(Chen and Kamionkowski 2004; Chluba and Thomas 2010), where $Z_{\rm HeII}$ is the fraction of singly ionized helium atoms relative to the total number of helium nuclei.

To make a comparison between this effect and the DM background, I can write the local energy deposition in terms of the local boost factor $B_{\rm local}(z)$ and the DM annihilation power of a smooth background,

$$\epsilon^{\rm DM}_{\rm c,local} = \frac{1}{n_{\rm B}} f_c\, B_{\rm local}(z) \left.\frac{dE}{dV\,dt}\right|_{\rm smooth}, \tag{3.32}$$

where $n_{\rm B}$ is the local gas density, and $B_{\rm local}(z)$ is the local annihilation power as a fraction of the smooth background DM annihilation power, which is given by Equation 3.2.

The local boost factor, $B_{\rm local}(z)$, can be calculated by 3.32 with given value of efficiency $h$. Figure 3.14 illustrates the boost factor of dark matter annihilation near a $10^5\,M_\odot$ dark matter halo. The structure boost factor from external annihilation, following Equation 3.4, is shown with a solid line. The boost factor $B(z)$ in the global DM annihilation (as inEquation 3.4) assumes that dark matter annihilation products completely escape from the local environment and deposit all their energy into the IGM. To account for local energy deposition, the escape fraction $f_{\rm esc}$ should be considered in Equation 3.4. In this work, I set $f_{\rm esc} \approx 1$. The local boost factors, calculated at different values of the parameter 0.1, 1 and 10 times of base value $h = -65$, are represented by dot-dashed lines in Figure 3.14. The dashed lines indicate the total boost factor as a function of redshift. The structure boost factor from the background is very low at high redshifts due to the low abundance of halos. In contrast, the local boost factor for the halo is dominant at higher redshifts but decreases over time. After redshift $z = 40$, the structure boost factor from the background becomes more significant.

For the circumgalactic medium (CGM) gas, the gas temperature is represented by the IGM temperature, $T_{\rm IGM}$, and an additional component, $\Delta T$, from local DM heating. This heating leads to a scale-dependent collapse mass, because local DM energy deposition is a function

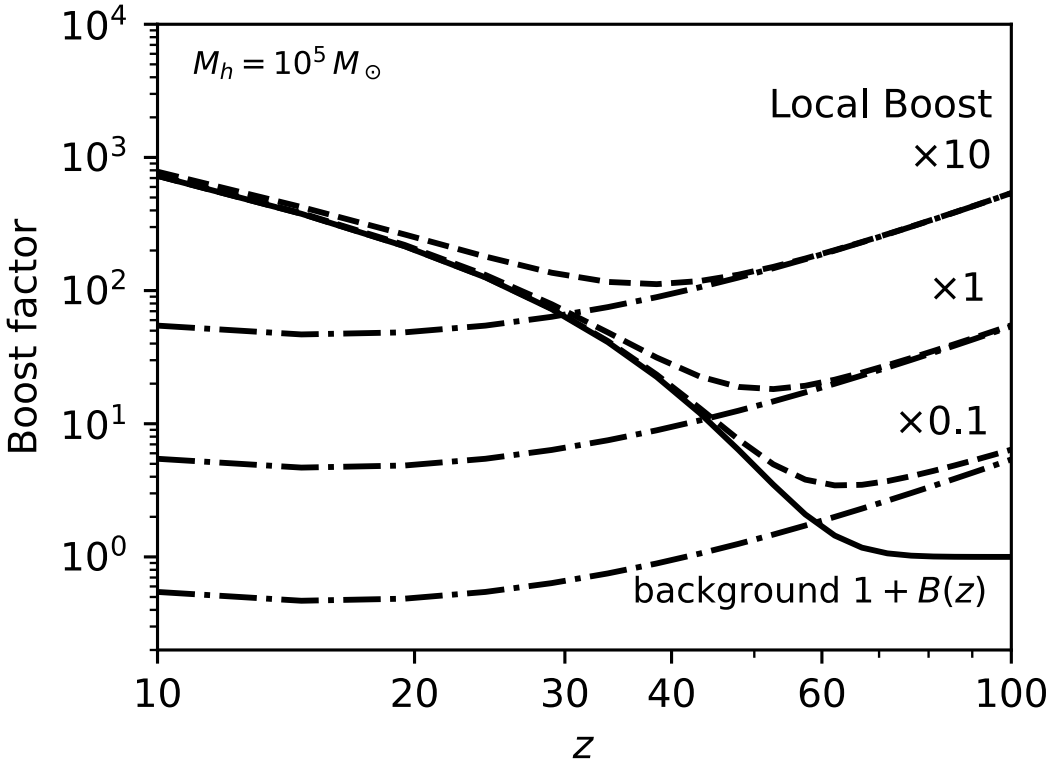


Figure 3.14: The local boost factor in dark matter (DM) annihilation around a $10^5 M_\odot$ dark matter halo at different redshift. The solid line represents the global boost factor $1 + B(z)$, the dot-dashed line indicates the contribution from the local $10^5 M_\odot$ halo with different local deposit efficiencies, and the dashed line shows the total boost factor.

of mass scale $M_h$. For massive halos, the DM heating is expected to be stronger, causing the surrounding gas temperature to increase. Therefore the Jeans mass is a function of mass scale, $M_{\rm J}(z, M_h)$. This can be approximated by following approach. As I fixed the local deposition efficiency, $h = \log(\epsilon^{\rm DM}_{\rm local}/E_h)$, the energy deposition per baryon is proportional to the total dark matter annihilation energy of the halo, $E_h$. As a result, the gas temperature raised by $\Delta T \propto E_h$, and the Jeans mass, as a function of gas temperature, follows the relation $M_{\rm J} \propto (T_{\rm IGM} + \Delta T)^{3/2}$.

To calculate the DM heating and ionization in local gas, I apply the local DM annihilation rate $\epsilon^{\rm DM}_{\rm c,local}$ into Equation 3.9, 3.10 and 3.11 to obtain the thermal evolution of local gas surrounding the halo.

Fig. 3.15 shows the gas temperature and ionized fraction surrounding a single $10^6 {\rm M}_\odot$ dark matter halo. I assume the halo formed at $z \approx 40$, with mass accretion following the power law $M = M_0(1+z)^\alpha e^{\beta z}$ (Correa et al. 2015), reaching $M = 10^6$ M$_\odot$ at redshift $z = 40$. Initially, the thermal history of the primordial gas is influenced solely by background dark matter annihilation (denoted by the black solid line). The impact of the local halo begins near the time of its formation. In the case of a low value of local deposit efficiency $h = -66$ and $-65$, the gas temperature and ionization fraction have almost no detectable change. However, once the energy deposition becomes significant ($h \gtrsim -64$), it can substantially increase the temperature and ionization fraction of the gas.

To summarize, dark matter annihilation from the halo can deposit energy into the surrounding gas before escaping the local environment. This energy deposition may enhance the total annihilation effects on small scales, such as increasing the gas temperature and ionization fraction. The impact of the local effect highly depends on the deposition efficiency. In our scenario, the local boost most significantly affects higher mass halos. While still preliminary, our calculation shows the importance of this avenue for probing the characteristics of dark matter annihilation, particularly in small halos, via its influence on gas and star formation. Further constraints require a more refined model for deposition efficiencies, for more robust galaxy formation simulations and comparison with observational data.

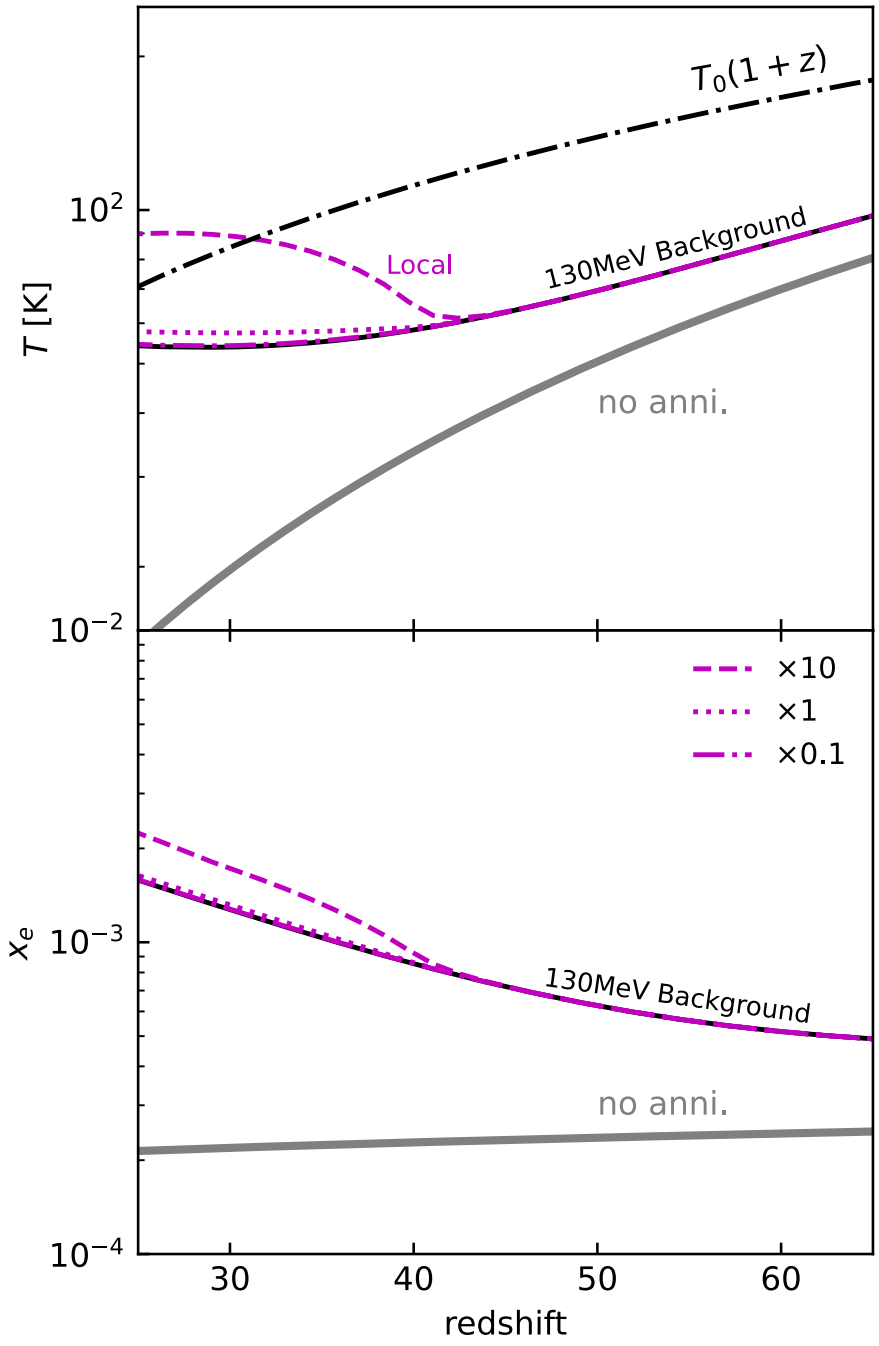


Figure 3.15: Kinetic temperature and ionization fraction of gas surrounding a $10^6 M_\odot$ dark matter halo, calculated using `CosmoRec`. The halo formation was assumed to occur at redshift $z_{\rm form} = 40$. The dotted-dashed line indicates the Cosmic Microwave Background (CMB) temperature. The gray solid line represents the baseline scenario without dark matter annihilation, and the solid black line represents the scenario with only 130 MeV background annihilation. The dotted and dashed lines corresponding to the gas property with both 130 MeV DM background and local annihilation power with value of 0.1, 1 and 10 times of base value.

CHAPTER

# 4

# IMPLICATIONS FOR HIGH-REDSHIFT 21CM ASTRONOMY

## 4.1 Model

The last chapter discussed the effect of dark matter annihilation in the early star formation within dark matter halos. Depending on the different dark matter models and gas environment, dark matter annihilation could either suppressed the gas cooling or accelerate the gas cooling within those halos.

This chapter will explore the further impact of the dark matter annihilation on the observable signal from the neutral hydrogen: the 21-cm signal. I will start with the result from our semi-analytic result in the last Chapter, and employ high-resolution numerical simulation to simulate the differential brightness temperature of the 21-cm signal at cosmic dawn.

### 4.1.1 Initial Condition

This section begins by calculating the corresponding energy injection rate from dark matter annihilation following Equation 3.5. This model includes both smooth background annihilation and enhanced annihilation resulting from structured halos. To determine the thermal history

of IGM, I solve the cosmic average thermal history in the cosmological recombination code `CosmoRec` with energy injected from dark matter annihilation. I updated the deposit fraction $f_c(z)$ of DM annihilation for different dark matter models using the pre-calculated table given by Slatyer (2016). I obtain the gas temperature $T_g$ and ionization fraction $x_e$ from redshift $z = 2700$ to $z = 35$ from the `CosmoRec` code.

I set the DM-dependent gas temperature $T_g$ and ionization fraction $x_e$ at redshift $z = 35$ as the initial parameters used in the public 21-cm simulation code `21cmvFAST`. To consider DM annihilation in the simulation, I modify the `21cmvFAST` to incorporate DM annihilation in the same way as in `CosmoRec`.

$$\left.\frac{dT_K}{dz}\right|_{\rm DM} = \frac{dt}{dz}\frac{2}{3k_B(1+x_e)}\epsilon^{\rm DM}_{\rm heat} \tag{4.1}$$

$$\Lambda_{\rm ion}|_{\rm DM} = f_{\rm H}\frac{\epsilon^{\rm DM}_{\rm HI}}{E_{\rm HI}} + f_{\rm He}\frac{\epsilon^{\rm DM}_{\rm HeI}}{E_{\rm HeI}} \tag{4.2}$$

$$J_{\alpha,\rm DM} = \frac{c\,n_b}{4\pi}\frac{\epsilon^{\rm DM}_{{\rm Ly}\alpha}}{h\,\nu_\alpha}\frac{1}{H(z)\nu_\alpha}\,. \tag{4.3}$$

Then I calculate the star-forming baryon collapsed fraction $f_{\rm coll}$ for the `21cmvFAST` simulation to estimate the star formation rate. In order to figure out $f_{\rm coll}$, I calculate the Jeans mass $M_J$ using the IGM temperature given by `cosmoRec`. By considering the effects of dark matter annihilation on thermal history, I figure out the Jeans mass with dark matter annihilation. Then, I obtain the gas fraction given by Equation 3.13 as a function of redshift and halo mass in the presence of dark matter annihilation.

### 4.1.2 Star-Forming Baryonic Fraction

For Pop III stars, I relate the star formation rate to the star-forming baryon collapsed fraction. The star-forming baryon collapsed fraction describes the cosmic total fraction of star-forming baryons, which can be written as

$$f_{\rm coll} = \int_{M_{\rm min}}^{\infty} M\frac{dn}{dM}\frac{f_{\rm gas}}{\rho_b}f_\star dM\,, \tag{4.4}$$

where $\rho_b$ is the comoving density of baryons and $f_{\rm gas}$ is the gas fraction within haloes.

$M_{\rm min}$ is the minimum star-forming halo mass. Since molecular cooling is essential for Pop III star formation at cosmic dawn, I enable star formation in halos where molecular cooling occurs and set the minimum star-forming halo mass at $M_{\rm min} = M_{\rm cool}$. This implies that only halos with a mass greater than $M_{\rm cool}$ can initiate star formation. Enabling star formation in

molecular cooling halos would significantly accelerate the onset of the 21-cm line compared to scenarios where only atomic cooling halos are considered.

The star formation efficiency, $f_\star$, is assumed to be a constant for halos with masses above the atomic cooling mass. However, for small molecular cooling halos, the $f_\star$ can be estimated in several different ways.

The first estimation is taken from Fialkov et al. (2013a). It is assumed to be constant for halos with masses above the atomic cooling mass and follows an exponential function for halos with masses between the molecular cooling mass and the atomic cooling mass.

$$f_*(M) = \begin{cases} f_* & \text{if } M \geqslant M_{\rm atomic} \\ f_* \frac{\log(M/M_{\rm cool})}{\log(M_{\rm atomic}/M_{\rm cool})} & \text{if } M_{\rm cool} < M < M_{\rm atomic} \\ 0 & \text{otherwise} \end{cases} , \tag{4.5}$$

where $M_{\rm atomic}$ is the mass threshold of atomic cooling halos, and $M_{\rm cool}$ is the minimal cooling mass defined in this work. $f_*$ is the star formation efficiency for atomic cooling halos, which is usually set by $f_* = 0.1$, as adopted in Muñoz (2019).

Another estimation is given by Muñoz (2023), which assumes the fraction of the gas that is accreted by a galaxy is converted into stars, follows $\dot{M}_* = f_* f_b \dot{M}_h$, and

$$f_*(M_h) = \frac{2\epsilon_*}{\left(M_h/M_{\rm pivot}\right)^{-\alpha_*} + \left(M_h/M_{\rm pivot}\right)^{-\beta_*}} f_{\rm duty} , \tag{4.6}$$

where $f_{\rm duty} = \exp(-M_{\rm turn}/M_h)$ is the duty fraction, with $M_{\rm turn}$ the turn-over mass below which gas does not cool into stars efficiently. The star formation in molecular cooling halos comes from an additional term, such as

$$\Delta f_\star(M_{\rm h}) = f_*^{\rm mol} e^{-M_{\rm cool}/M_{\rm h}} e^{-M_{\rm h}/M_{\rm atomic}} , \tag{4.7}$$

where $f_*^{\rm mol}$ is the star formation efficiency for molecular cooling halos, which is $f_*^{\rm mol} = 10^{-2.5}$ following current constraints to reionization (Qin et al. 2021; Muñoz et al. 2022), as adopted by Qin et al. (2023).

## 4.2 Results

### 4.2.1 Semi-Numerical Simulation

The `21cmFAST` code is a public semi-numerical simulation package (Mesinger et al. 2010) to calculate the evolution of cosmic neutral hydrogen during the Cosmic Dawn and the Epoch

of Reionization (EoR). It combines the excursion set formalism with perturbation theory to generate density, velocity, halo, and ionization, balancing computational speed and accuracy. The code provides a robust framework to simulate the 21 cm signal, and it is widely used for investigating the reionization history and structure formation in the early universe.

Muñoz (2019) improved the `21cmFAST` code, with emphasis on the first star formation in minihalos. They developed the `21cmvFAST` based on the original code, including a detailed implementation of Lyman-Werner (LW) feedback and dark matter-baryon relative velocity effects. These mechanisms successfully capture the suppression of star formation in molecular cooling halos.

I begin by calculating the corresponding energy injection rate from dark matter annihilation following Equation 3.5. This model includes both smooth background annihilation and the enhanced annihilation resulting from collapsed structures (halos). To determine the thermal history of the IGM, I model the cosmic average thermal history in the public cosmological recombination code `CosmoRec` (Chluba and Thomas 2010) with energy injected from dark matter annihilation. I update the energy deposition fraction $f_c(z)$ of DM annihilation for different dark matter models using the pre-calculated table given by Slatyer (2013) and calculate the gas temperature $T_g$ and ionization fraction $x_e$ from redshift $z = 2700$ to $z = 35$.

I calculate the star-forming baryon collapsed fraction $f_{\rm coll}$ in Equation 4.4, as input for the public `21cmvFAST` code to estimate the star formation rate. In order to determine $f_{\rm coll}$, I calculate the Jeans mass $M_J$ using the IGM temperature given by `CosmoRec`. By considering the effects of dark matter annihilation on the thermal history, I can calculate the Jeans mass with dark matter annihilation. Then, I can obtain the gas fraction given by Equation 3.13 as a function of redshift and halo mass in the presence of dark matter annihilation.

I use the public `21cmvFAST` semi-numerical code (Muñoz 2019) to calculate the spin temperature and sky-averaged 21cm brightness temperature. `21cmvFAST` modifies the `21cmFAST` code (Mesinger et al. 2010). It calculates star formation in molecular cooling halos and accounts for the effect of dark matter-baryon velocity offsets in the 21cm signal.

In this study, I modify `21cmvFAST` to implement dark matter annihilation at cosmic dawn. I assume the dark matter particles annihilate 100% into $e^+e^-$, and the energy is deposited into heating, ionization and Lyman-$\alpha$ photons. The thermal evolution in the simulation is modified as described by Equations 3.10 and 3.11. I employ the energy deposition fractions $f_c(z)$ as used in `CosmoRec`. However, for redshifts $z < 25$, I rescale the deposition fraction using $f_c(z < 25) = \frac{f(z')}{f(z)} f_c(z')$, where $z'$ corresponds to the redshift where the free electron fraction at $x_e(z) = x_e(z')$. For star formation, I update the baryon collapsed fraction from Equation 4.4 to account the effect of dark matter annihilation on gas cooling and star formation. Following (LH16), I set the X-ray efficiency in `21cmvFAST` to be $\zeta_X = 10^{56}$, corresponding to the number

of X-ray photons per solar mass in the simulation. I keep the default setting as described in Muñoz (2019) for all other options. The initial conditions $T_e, X_e$ were taken from `CosmoRec`.

In this paper, all cosmological parameters in the calculation and simulations were adopted from Planck 2018, with $h = 0.6766$, $\Omega_{m,0} = 0.3111$, and $\Omega_{b,0} = 0.049$ (Aghanim et al. 2020).

The differential brightness temperature of the 21-cm signal is given by

$$\delta T_b = \frac{T_S - T_\gamma}{1+z}(1 - \exp^{-\tau_{\nu_0}}), \tag{4.8}$$

where $T_\gamma$ is the CMB temperature, $\tau_{\nu_0}$ is the optical depth of the IGM for the 21cm signal, and $T_S$ is the spin temperature given by

$$T_S^{-1} = \frac{T_\gamma^{-1} + x_\alpha T_\alpha^{-1} + x_c T_k^{-1}}{1 + x_c + x_\alpha}, \tag{4.9}$$

where $T_k$ is the kinetic temperature of the gas, $T_\alpha$ is the color temperature, which is typically coupled to the kinetic temperature $T_\alpha \approx T_k$. $x_c$ is the collisional coupling coefficient, and $x_\alpha$ is the Wouthuysen-Field coupling coefficient.

The study by LH16 investigates the 21cm signal in the context of background dark matter annihilation using `21cmFAST`. Both LH16's study and ours calculate the thermal history of the IGM and the effect on the 21cm signal in the presence of the DM annihilation. However, LH16 does not account for molecular cooling, instead, setting the minimum virial temperature between $10^4$ and $10^5$ K. The atomic cooling-only model results in a significant delay in early galaxy formation relative to a model with molecular cooling, as evident in the position of the absorption trough in the 21cm signal.

Figure 4.1 presents our complete results with streaming velocity (solid lines) and without streaming velocity ($v_{bc} = 0$) (dot-dashed lines) compared to those from LH16 (dashed lines) with same parameter settings. For DM mass 9 MeV, 130 MeV and 1.1 GeV, our works find similar absorption troughs, primarily due to the same thermal history of IGM. With the molecular cooling halos included, our 21cm absorption trough appears at earlier redshifts ($\Delta z \approx 5$). I also study the DM annihilation in molecular cooling halos, and obtain a DM mass-dependent cooling mass. The increase of the minimum cooling mass due to dark matter annihilation results in a delay in star formation and therefore the 21cm signal. However, the effect is not significant in the global 21cm signal, as it is overshadowed by the effect in the IGM, which greatly boosts the differential brightness temperature. Additionally, the effect of streaming results in a slight offset in the brightness temperature as discussed. When both effects are combined, the redshift of the trough shifts by $\Delta z \approx 5$ for all dark matter masses compared to the previous results.

The study by Qin et al. (2023) examined the formation of the first stars under the influence

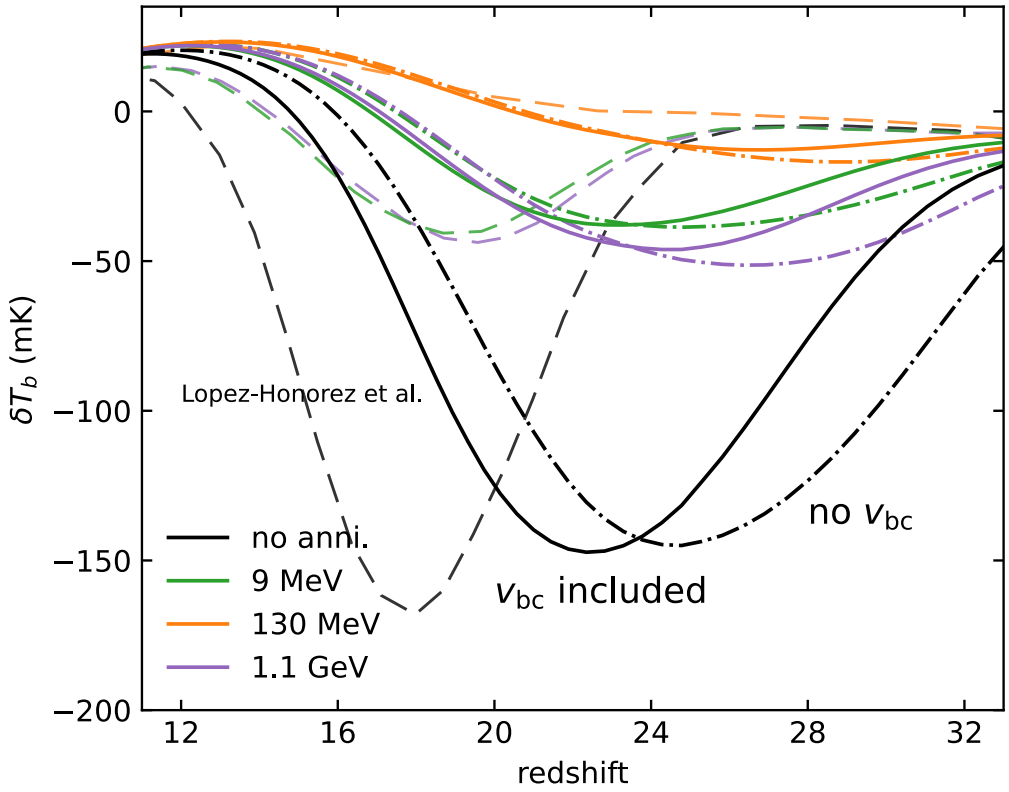


Figure 4.1: The global 21cm signal as a function of redshift for the no annihilation case and dark matter masses of 9 MeV, 130 MeV, and 1.1 GeV. Long dashed lines plot the previous results from Lopez-Honorez et al. (2016) without molecular cooling and LW feedback. Our results are depicted with solid lines, incorporating the effects of dark matter annihilation in molecular cooling halos and streaming velocity. Additionally, results without streaming velocity are represented by dot-dashed lines.

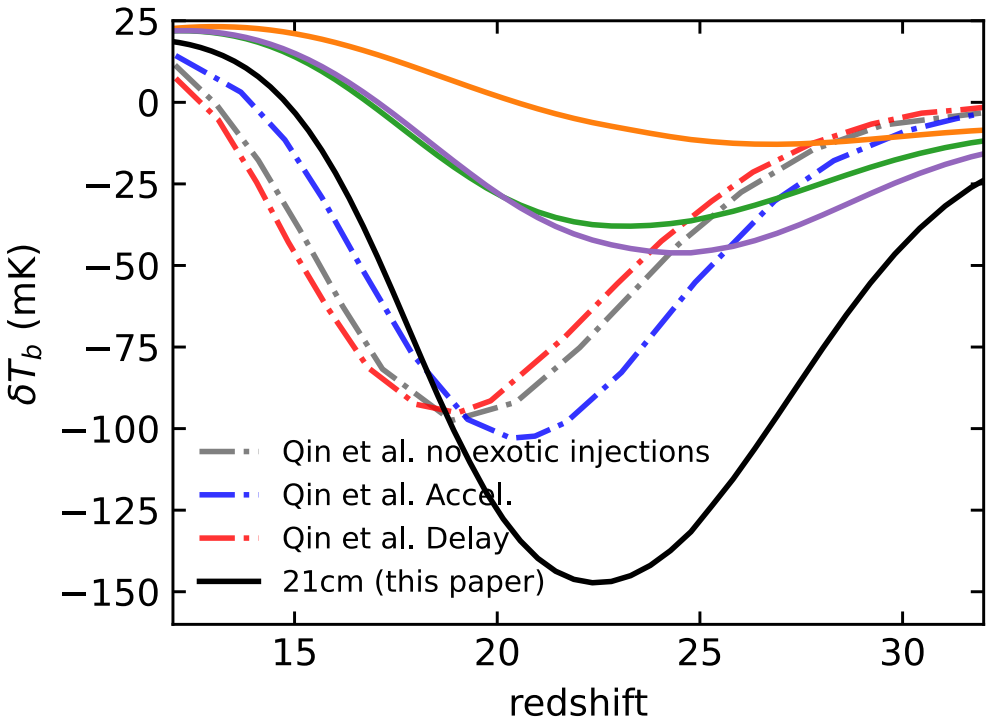


Figure 4.2: Comparison of the 21cm brightness temperature between our study and Qin et al. (2023). The figure shows the exotic energy accelerate (blue) and delay (red) the star formation. The baseline case, which excludes DM energy injections, exhibits a higher brightness temperature compared to ours.

of exotic energy injection from dark matter decay or annihilation, using the `DarkHistory` code (Liu et al. 2020). They employed the `Zeus21` code (Muñoz 2023) with a modified star formation model in molecular cooling halos to calculate the 21cm signal. A comparison of our results is presented in Fig. 4.2. Our findings indicate that, as in the study by Qin et al. (2023), molecular cooling in small halos shifts the 21cm absorption signal towards higher redshift. The authors of Qin et al. (2023) studied two dark matter models, each characterized by a particle mass of 185 MeV, decaying to $e^+e^-$ pairs. The model with lifetime $\tau = 25.6$ raises the mass threshold and the 21cm signal is slightly delayed, while the model with lifetime $\tau = 26.4$ accelerates the 21cm signal. Their work focused on the timing of cosmic dawn through the enhancement or suppression of $H_2$ from exotic energy injection. As such, they did not model other sources of feedback, e.g. stellar LW emission, DM-baryon relative velocities, or their combination, or IGM heating. In contrast, our study includes the effects of IGM heating and ionization, while considering regular stellar LW feedback (indirectly influenced by dark matter annihilation and streaming). However, I do not account for direct LW energy deposition from dark matter annihilation. Another notable difference in our work is the star formation efficiency $f_\star$ for molecular cooling halos. Their work adopts the model from Muñoz (2023), with star-formation efficiency $f_\star = 10^{-2.5}$ for molecular cooling halos; this star formation is lower than our model with star-formation efficiency $f_\star = 0.1$. Therefore, even with LW feedback and streaming considered, our 21cm signal still appears earlier than in their results.

### 4.2.2 Discussion

The primary aim of this work is to investigate the interactions between dark matter annihilation, dark matter-baryon velocity offsets, and molecular cooling, and their impact on early structure formation and the 21cm signal. This work attempts to bridge the gap between previous studies by incorporating multiple effects, offering a more comprehensive model of how these factors interplay.

I acknowledge that the modeling presented here is complex; however, it is essential to consider these interacting processes to achieve a more complete understanding of early cosmology. Dark matter annihilation can either enhance or suppress molecular cooling, leading to either an increase or decrease in the formation of the first stars. This effect can be further amplified by Lyman-Werner (LW) feedback and modified by the intensity of streaming velocities. Additionally, incorporating molecular cooling into the calculation of the 21cm signal can significantly shift the signal to earlier redshifts. The interplay among these effects is non-trivial, and understanding them together is crucial for making more accurate predictions.

One important avenue for future work is improving the estimates for energy deposition from

dark matter annihilation. On small scales, dark matter annihilation within halos can locally deposit energy into the gas, raising its temperature and increasing the ionization fraction. In the Chapter 4, I outline initial steps toward estimating these local effects. The gas temperature and ionization, which are raised by background dark matter annihilation power, can be further enhanced by local energy deposition within halos. Accurate estimates of the deposition fraction from specific annihilation products could be obtained through numerical simulations, which would include a detailed treatment of particle interactions with the primordial gas in profiled halos. We am currently developing such a program, which I expect will enable us to draw robust conclusions about the impact of dark-matter annihilation on structure formation.

Looking ahead, a key goal will be to trace the influence of dark matter annihilation and other small-scale factors through to observable galaxy formation. By doing so, I can apply redshift- and scale-dependent modifications to models of galaxy formation. Future studies should focus on connecting the detailed physics of small scales with observable large-scale phenomena, such as galaxy formation and evolution and the evolution of the IGM, which can provide testable predictions for current and near-future observations and potentially constrain the nature of dark matter.

This study investigates the impact of dark matter (DM) annihilation during the cosmic dawn, focusing on sub-GeV dark matter particles annihilating into $e^+e^-$. Our analysis shows that energy from DM annihilation impacts heat, ionization, and excitation in the cosmic gas, leading to an increase in both gas temperature and ionization fraction during this epoch.

I identified a strong dependence of baryon collapse on the thermal history, via the filtering mass. In mini-halos, where gravitational forces are weaker, heating from DM annihilation can increases the gas temperature and suppress gas collapse. Though the filtering mass is less affected due to weak annihilation effects at earlier times, I found a DM mass-dependent gas fraction of mini-halos at cosmic dawn.

I developed an analytic cooling model that incorporates DM annihilation. I calculate the production and the required fraction of molecular hydrogen for different redshifts and DM masses, showing both positive and negative impacts on molecular cooling. At high redshift $z > 30$, DM ionization increases the electron fraction, slightly lowering the minimum cooling mass. However, at lower redshifts ($z < 30$), DM heating dominates, raising the minimum cooling mass. The impact on the cooling mass with redshift is influenced by the DM mass, which determines the fraction of energy deposited in each channel.

I also account the influence of photo-dissociation from Lyman-Werner (LW) photons. In the presence of stellar LW feedback, the molecular hydrogen fraction is significantly reduced, which increases the minimum cooling mass at lower redshifts across all considered DM masses.

I extend our analysis to account for the effects of dark matter-baryon velocity offsets (stream-

ing) driven by baryon acoustic oscillations to better understand the 21cm signal and early star formation during cosmic dawn. Streaming suppresses small-scale halo formation, reducing the abundance of halos – particularly those near the Jeans scale. This reduction leads to a slight decrease in the DM annihilation boost factor.

Our study also examined the combined effect of DM annihilation and streaming on Population III star formation. The streaming significantly reduces the gas content in small halos, directly inhibiting star formation and altering the environment for molecular cooling. In our model, the minimum cooling mass increases as a function of the streaming velocity, and DM annihilation exhibits distinct features for different cases of streaming velocities. It shows the strongest suppression of molecular cooling in the absence of streaming, but may lead to an acceleration of cooling in the case of a large streaming velocity at the same redshift.

I calculated the 21cm signal using simulations from the `21cmvFAST` code, incorporating the cooling mass results from our molecular cooling model. The inclusion of star formation in molecular cooling halos shifts the global 21cm signal to earlier redshifts compared to previous studies. However, the precise shift in redshift is highly sensitive to the choice of parameters, such as the cooling criterion in the analytic model and the star formation efficiency of molecular cooling halos. When I include streaming in our calculations, I observe a slight delay in the global 21cm signal, due to the suppression of the gas fraction and molecular cooling.

CHAPTER

# 5

# REFINED MODEL OF ENERGY TRANSFER ON SMALL SCALES

## 5.1 Motivation

Understanding energy transfer processes on a small scale is critical for advancing our knowledge of cosmic structure formation. While DM annihilation is generally assumed to influence the remote cosmic backgrounds, recent studies suggest that it can also substantially impact the local gas environment. As outlined in previous chapters, DM annihilation plays a significant role in gas cooling and subsequent star formation processes. Therefore, evaluating the contribution and effect of DM annihilation on the local environment is crucial.

Despite its potential importance, energy deposition in local environments remains poorly understood owing to the limitations of current modeling approaches. Most existing simulations focus on homogeneous large-scale effects, often relying on assumptions that may not hold on smaller scales. These limitations are particularly evident in the interactions between high-energy particles produced by DM annihilation, such as electron–positron pairs, and the surrounding gas medium. Such interactions are complicated and dependent on model parameters, necessitating further detailed analysis.

This chapter aims to bridge these gaps by examining current energy transfer simulations

and identifying their limitations, particularly in the context of particle physics processes. By refining these models to better capture the interactions between high-energy electron–positron pairs and the local gas medium, this study seeks to offer a more accurate understanding of energy transfer processes on small scales. These improvements will facilitate more precise modeling of gas accretion, cooling, and star formation processes influenced by DM annihilation. Furthermore, the refined models may be valuable in generalized scenarios involving energy injection and deposition on small scales, extending beyond DM annihilation.

The chapter is structured as follows: In the next section, we provide a brief overview of a previous Monte Carlo code used for small-scale energy transfer simulations, focusing on its energy transfer iteration mechanisms and involved particle processes. Subsequently, we introduce refined models for specific processes, including ICS, photoionization, and pair production. Finally, we integrate the refined Monte Carlo code with standard energy deposition fractions and present a sample simulation result using the improved models.

## 5.2 Monte-Carlo Code

Numerical methods are widely employed to solve radiation transfer problems across various scales and approximation levels.

Slatyer et al. (2009) developed a code to map an energy injection history to an energy deposition history while accounting for the effects of electron and photon cooling, as detailed in Slatyer (2013). This code determines the fraction of energy deposited in the background IGM as a function of particle energy and redshift, making it a key tool for constraining DM annihilation based on CMB observations. Liu et al. (2020) expanded on this work by developing a new code to compute the evolution of ionization and temperature effects resulting from exotic energy injections, such as those from DM annihilation and decay. Qin et al. (2023) extended the application of this code to incorporate star formation processes.

Simulations of DM-annihilation-related physics, particularly focusing on particle cascades, were first introduced by Valdes et al. (2007b); Valdés et al. (2010). Their approach incorporated processes such as bremsstrahlung emissions, ICS, H/He collisional ionization and excitation, and electron–electron collisions. Evoli et al. (2012) further enhanced this methodology to include all relevant interactions of positrons and photons with their environment.

Schön et al. (2015) revised this model for application in the circumgalactic medium by excluding the assumption of a uniform spatial distribution of injected particles, which is not applicable on smaller scales, particularly within collapsed structures. This code utilizes the Monte Carlo sampling method from `MEDEAII` to model particle interactions and energy losses within halos. However, its accuracy diminishes in complex or relativistic regimes. As

discussed in the previous section, energy transfer processes vary substantially between low- and high-energy regimes, particularly for ICS, which is critical in the context of DM annihilation. Therefore, current high-energy transfer codes require improvements to handle diverse energy ranges. To this end, the detailed energy spectrum and cross-section must be refined.

**Particle Cascades Algorithm**

This section briefly reviews the particle cascade algorithm implemented in the code to examine the interactions and energy deposition processes involved in DM annihilation on smaller scales, particularly within DM halos.

The code revised by Schön et al. (2015) employs the Monte Carlo sampling method to model particle interactions. Each tracked particle is described by the parameters $\{\vec{x}_i, \vec{\theta}, E_i, \mathrm{id}\}$, corresponding to the position, orientation, energy, and particle type, respectively.

The particle evolves in a stepwise manner, and at each step, its position is updated according to

$$\begin{aligned} x_f &= x_i + S(r_i)\sin(\theta_i)\cos\left(\phi_i\right) \\ y_f &= y_i + S(r_i)\sin(\theta_i)\sin\left(\phi_i\right) \\ z_f &= z_i + S(r_i)\cos(\theta_i) \end{aligned} , \tag{5.1}$$

where $S(r_i)$ denotes the step size, determined by the parameter $\epsilon$ and the radial position of the particle, $r_i$, such that $S(r_i) = \epsilon\, r_i$.

The simulation domain is bounded by the maximum radius, $r_{\max}$. Any particles that move beyond this radius are considered to have escaped and are subsequently removed from the simulation. Interactions occurring outside the simulation domain are not modeled, even if such interactions could potentially scatter particles back into the simulation space.

At each step, the probability of an interaction is determined by the inverse of the mean free path, as follows:

$$\lambda_i^{-1} = n_i \sigma_i \,, \tag{5.2}$$

where $n_i$ denotes the density of the interacting particles, and $\sigma_i$ represents the interaction cross-section.

The probability $P$ of a particle travelling a distance $l$ without interacting follows the exponential decay law:

$$P(l) = e^{-\int_0^l \lambda_i^{-1}(l')dl'} \,. \tag{5.3}$$

This formula indicates that the probability decreases exponentially with increasing travel distance. The factor $\lambda_i^{-1}(l)$ varies with position $l$ as the density $n_i$ changes. For simplicity, the code randomly samples the density along the particle trajectory.

Hence, the probability of a particle interacting within a specific distance $l$ is defined as

$$P(\text{interaction}) = 1 - e^{-\int_0^l \lambda_i^{-1}(l')dl'} . \tag{5.4}$$

If an interaction occurs within the simulation domain, the behavior of the resulting particles is determined by the properties of the incoming particles and their interactions.

**Sampling Method**

To balance computational cost and efficiency, the program relies on Monte Carlo sampling methods. During each simulation run, the program tracks one or a pair of particles injected into the system, along with any secondary particles generated through subsequent interactions. Particle selection and interactions are governed by the probability distributions of the particles and their environment. For instance, the code samples CMB photons based on a black-body spectrum.

*Inverse transformation sampling* is a commonly used sampling technique for random variables $X$ with a probability density function (PDF) $p(x)$. The probability of $X < x$ is determined by its cumulative distribution function (CDF), defined as

$$F(x) = \int_{-\infty}^{x} p(x')dx' . \tag{5.5}$$

The CDF approaches one as $x \to \infty$, provided that the PDF is normalized. If the variable has an interval $x \in [a, b]$, the CDF becomes

$$F(x) = \int_{a}^{x} p(x')dx' . \tag{5.6}$$

The program uses a random number generator to produce a uniformly distributed value $y$ ranging from zero to one. The sampled value is then determined using the inverse function:

$$x = F^{-1}(y) . \tag{5.7}$$

Another widely used technique in Monte Carlo programs is *rejection sampling* (see Carter and Cashwell (1975) for further details). This method performs sampling based on the shape of a function, regardless of whether the function integrates to one. It is particularly useful for distributions where the PDF $p(x)$ is not normalized or the CDF is unknown.

The rejection sampling algorithm operates as follows: For an arbitrary PDF $p^*(x)$, where $x \in [a,b]$, the program generates pairs of random numbers $(\xi,\eta)$ uniformly distributed over $[0,1]$. Let $M$ denote the upper limit of the distribution $p^*(x)$, we compute the sample as $x' = a+(b-a)\xi$. If $p^*(x') > M\eta$, we accept $x'$ as a valid sample; otherwise, the program rejects this value and repeats the process.

## 5.3 Refined Model

### 5.3.1 Inverse Compton Scattering

Electrons and positrons produced from sub-gigaelectronvolt to gigaelectronvolt DM annihilation typically have very high energies, $E_e \gg m_e c^2 = 0.511$ MeV. These high-energy particles interact with background photons, such as those from the CMB, scattering these photons to much higher energies through a process known as **ICS**.

In the low-energy limit, known as the **Thomson regime**, the mean free path for Compton scattering, $\lambda$, is expressed as

$$\lambda = \frac{1}{\sigma_T n_\gamma} \,. \tag{5.8}$$

where $\sigma_T \approx 6.652 \times 10^{-25}$ cm$^2$ represents the Thomson cross-section, and $n_\gamma$ denotes the number density of CMB photons. The calculated mean free path is approximately $\lambda \simeq 4 \times 10^{17}[(1+z)/21]^{-3}$ cm.

The differential spectrum of scattered photons is determined by (see Fargion et al. (1997))

$$\left.\frac{dN_\gamma}{d\epsilon\, d\epsilon_1\, dt}\left(\beta, T, \epsilon, \epsilon_1\right)\right|_{\epsilon<\epsilon_1} = \frac{\pi r_0^2 c\, n(\epsilon, T)}{4\beta^6\gamma^2\epsilon} F\left(\beta, \epsilon, \epsilon_1\right) , \tag{5.9}$$

where $\epsilon$ denotes the incoming photon energy, while $\epsilon_1$ represents the outgoing photon energy. The parameter $r_0$ denotes the classical electron radius, and $n(\epsilon, T)$ represents the number density of photons with energy $\epsilon$. The function $F$ is defined as

$$\begin{aligned} F\left(\beta,\epsilon,\epsilon_1\right) = {} & \frac{1}{\gamma^4}\frac{\epsilon}{\epsilon_1} - \frac{1}{\gamma^4}\frac{\epsilon_1^2}{\epsilon^2} + (1+\beta)\left[\beta\left(\beta^2+3\right) + \frac{1}{\gamma^2}\left(9-4\beta^2\right)\right] \\ & + (1-\beta)\left[\beta\left(\beta^2+3\right) - \frac{1}{\gamma^2}\left(9-4\beta^2\right)\right]\frac{\epsilon_1}{\epsilon} \\ & - \frac{2}{\gamma^2}\left(3-\beta^2\right)\left(1+\frac{\epsilon_1}{\epsilon}\right)\log\left(\frac{1+\beta}{1-\beta}\frac{\epsilon}{\epsilon_1}\right) \end{aligned} \,. \tag{5.10}$$

This formula applies to the upscattering regime, where $(1-\beta)\epsilon_1/(1+\beta) < \epsilon < \epsilon_1$. For the

downscattering regime, the valid range is $\epsilon_1 < \epsilon < (1+\beta)\epsilon_1/(1-\beta)$.

$$\left.\frac{dN_\gamma}{d\epsilon d\epsilon_1 dt}(\beta, T, \epsilon, \epsilon_1)\right|_{\epsilon \geq \epsilon_1} = -\left.\frac{dN_\gamma}{d\epsilon d\epsilon_1 dt}(-\beta, T, \epsilon, \epsilon_1)\right|_{\epsilon < \epsilon_1} . \tag{5.11}$$

In the early Universe, once the gas decoupled from photons, its temperature decreased more rapidly than that of the CMB until reionization occurred. Under these circumstances, the thermal photons emitted by baryons were considered negligible, and CMB photons, following Planck's spectrum, were regarded as the sole photon source.

The number density of CMB photons as a function of energy, $n(\epsilon)$, follows the blackbody spectrum described by

$$n(\epsilon) = \frac{8\pi\epsilon^2}{(hc)^3}\frac{1}{e^{\frac{\epsilon}{k_B T}} - 1} , \tag{5.12}$$

where $h$ denotes Planck's constant, $k_B$ represents Boltzmann's constant, and $T$ denotes the CMB temperature.

The total number density of CMB photons with temperature $T$ is defined as

$$n_\gamma(T) = 16\pi\left(\frac{k_B T}{hc}\right)^3 \zeta(3) , \tag{5.13}$$

where $\zeta$ denotes the Riemann zeta function with an approximate value of $\zeta(3) \approx 1.20206$.

The total energy density is mathematically expressed as

$$U(T) = a T^4 , \tag{5.14}$$

where $a$ denotes the radiation constant, defined as

$$a = \frac{8\pi^5 k_B^4}{15 c^3 h^3} \approx 7.5657 \times 10^{-15} \text{erg cm}^{-3} \text{ K}^{-4} . \tag{5.15}$$

To analyze scattered photons from the CMB, one must integrate the differential energy spectrum defined by Equation. 5.9 across the photon distribution of the CMB detailed in Equation. 5.12. Although this integration is computationally complex, it may be feasible using numerical computational methods. Notably, the dependence of the spectrum on $\beta^{-6}$ can lead to highly unstable results as $\beta \to 0$.

Further integration of this spectrum over the scattered photon energies results in the total scattering rate:

$$\frac{dN_\gamma}{dt} = n_\gamma \sigma(E) c . \tag{5.16}$$

This yields the Thomson cross-section $\sigma(E) = \sigma_T$. The blue line in Fig. 5.2 illustrates the

ICS cross-section calculated using the above equations, which is independent of the incoming photon and electron energies.

The energy loss rate of electrons can be calculated using (see BLUMENTHAL and GOULD (1970))

$$\frac{dE_e}{dt} = -\frac{4}{3}\sigma_T c\gamma^2\beta^2 E_\gamma\,, \tag{5.17}$$

where $\gamma$ represents the Lorentz factor of the electrons, and $E_\gamma$ represents the energy density of the incoming photons (CMB photons in this context).

Electrons cool via ICS at the rate defined by the above equation. We can estimate the maximum lifetime of an electron until it reaches $E_{\rm min} \sim 10$ eV. At this point, other processes become dominant. For an electron with an initial energy $E_0$, we have the following:

$$\int_0^{t_c} \frac{dE_e}{dt} dt = E_0\,. \tag{5.18}$$

This yields $t_c \approx 10$ Myr for a wide range of initial electron energies. This timescale is considerably shorter than the conformal time, implying that the structure of the DM halo can be presumed to remain constant throughout this process.

Energy deposition within the DM halo can be roughly estimated under specific conditions. For an isotropic case with low electron energies, scattered electrons are emitted isotropically with no bias, and their step length remains constant. In this case, the electron path can be approximated as random walking within the DM halo. The average number of electron scattering events before they escape from the halo is $N_{\rm esc} \approx (\frac{r_{\rm vir}}{\lambda})^2$. Electrons lose all their energy if the number of escape scatterings exceeds the number of cooling scatterings, $N_{\rm esc} > N_{\rm cool}$. During each scattering, the energy loss is $\Delta E \approx (4/3)\gamma^2\epsilon \sim 300(E_e/100{\rm MeV})^2[(1+z)/21]$ eV. The number of electron cooling scattering events is $N_{\rm cool} \approx E_e/\Delta E \sim 3\times10^5(E_e/100{\rm MeV})^{-1}[(1+z)/21]^{-1}$. In this case, down-scattered photons are negligible, and the energy of the scattered photons equals the energy lost by the electrons. For a $10^5 M_\odot$ halo at redshift 20, this yields $E_e > 19.6$ MeV.

Fig. 5.1 illustrates a halo with mass $M = 10^6\,{\rm M}_\odot/h$. The scale in this figure is expressed in units of virial radius, $r_{\rm vir}$. As depicted in the figure, an electron is injected at the center of the halo, and its step size is determined by the mean free path of ICS, as defined in Equation 5.8. For this case, the step size remains constant because both the cross-section $\sigma_T$ and CMB photon density $n_\gamma$ are invariant with respect to position and energy.

However, when the incident electron energy is high, the scattering becomes anisotropic. This anisotropy reduces the number of escape scatterings, making it easier for electrons to escape the halo before losing their energy. In the relativistic limit, also known as the Klein–Nishina limit, the Compton spectrum is described by BLUMENTHAL and GOULD (1970):

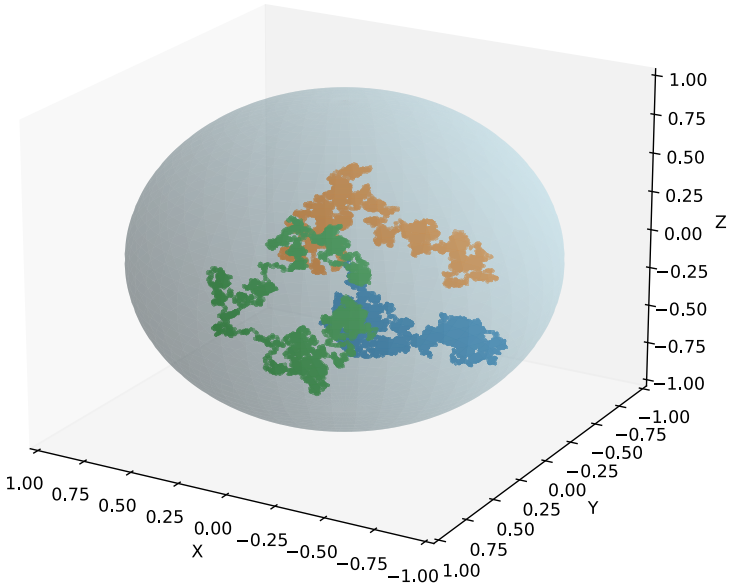


Figure 5.1: Trajectory of a randomly walking electron injected at the center of a $10^6 M_\odot/h$ halo. The diagram illustrates three different trails of particles in different colors.

$$\frac{dN_{\gamma,\epsilon}}{dt\,dE_1} = \frac{2\pi r_0^2 m_e c^3}{\gamma}\frac{n(\epsilon)d\epsilon}{\epsilon} \times \left[2q\ln q + (1+2q)(1-q) + \frac{1}{2}\frac{(\Gamma_\epsilon q)^2}{1+\Gamma_\epsilon q}(1-q)\right], \tag{5.19}$$

where

$$\Gamma_\epsilon = 4\epsilon\gamma/m_e c^2, \quad q = E_1/\Gamma_\epsilon(1-E_1)\,. \tag{5.20}$$

In the above equation, $r_0$ denotes the classical electron radius, $\epsilon$ represents the energy of the incident photon, $\gamma$ denotes the Lorentz factor for electrons, and $E_1$ represents the energy of the scattered photon.

Fig. 5.2 illustrates the differential energy spectrum of ICS in the relativistic regime from Equation 5.19. The energy spectrum in this case depends on both the density of incoming CMB photons and the energy of the electron. The green lines in the figure represent the cross-section of ICS calculated using Equation 5.19. This cross-section aligns with the Thomson scattering

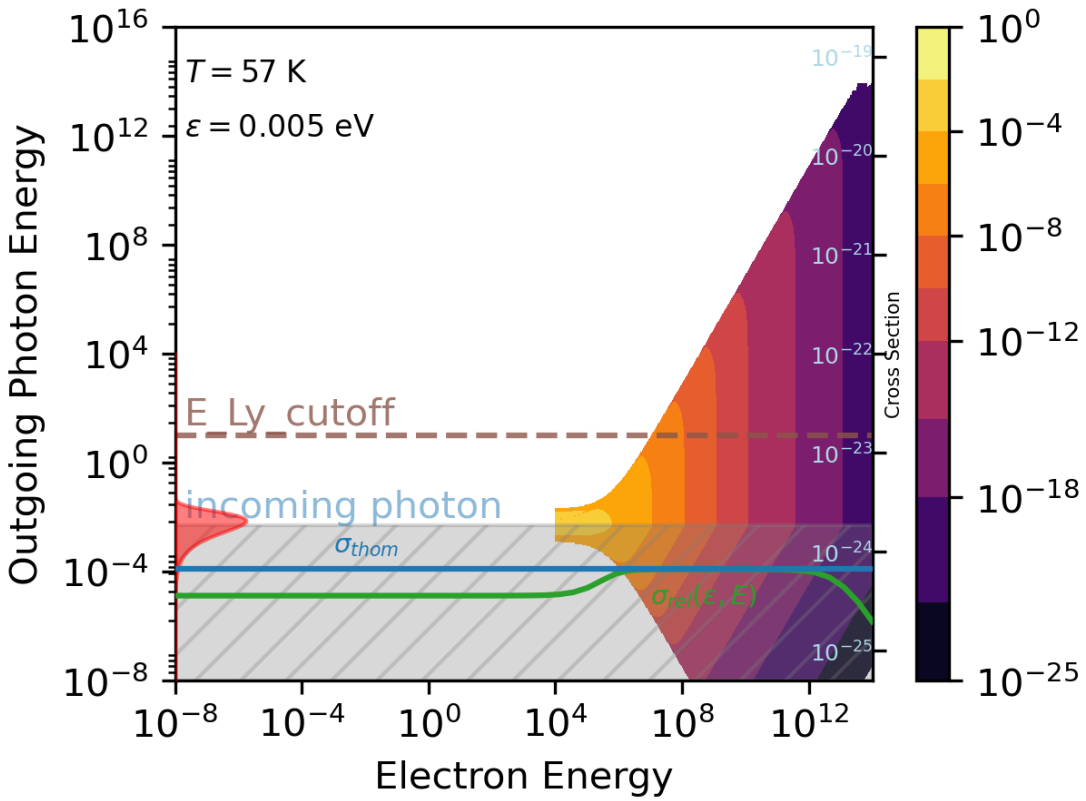


Figure 5.2: Relativistic energy spectrum of ICS for an incoming photon energy of $\epsilon = 0.005\,\text{eV}$, with a CMB temperature of $T = 57\,\text{K}$. The dashed purple line represents the Lyman-alpha cutoff at a photon energy of $E = 10.2\,\text{eV}$.

cross-section at electron energies ranging from megaelectronvolt to gigaelectronvolt. However, it falls below the Thomson scattering cross-section at both lower and higher electron energies. The electron energy thresholds for these reduced cross-sections depend on the energy of incoming photons.

Fig. 5.3 illustrates the differential energy spectrum of ICS within the CMB. This spectrum is obtained by integrating Equation 5.19 over the blackbody spectrum of the CMB. At lower energies, the spectrum is derived using the differential energy spectrum in the Thomson regime, while at higher energies, the relativistic regime is applied.

As detailed previously, low-energy electrons can entirely cool down through the ICS process before escaping the halo. However, the energy of the scattered photons, given as $E_1 \approx (4/3)\gamma^2\epsilon$, falls below the photoionization threshold ($E < 13.6$ eV). Consequently, these low-energy electrons do not contribute to the subsequent heating and ionization processes via ICS. Instead, other interactions, such as collisional ionization and excitation, dominate in the low-energy regime.

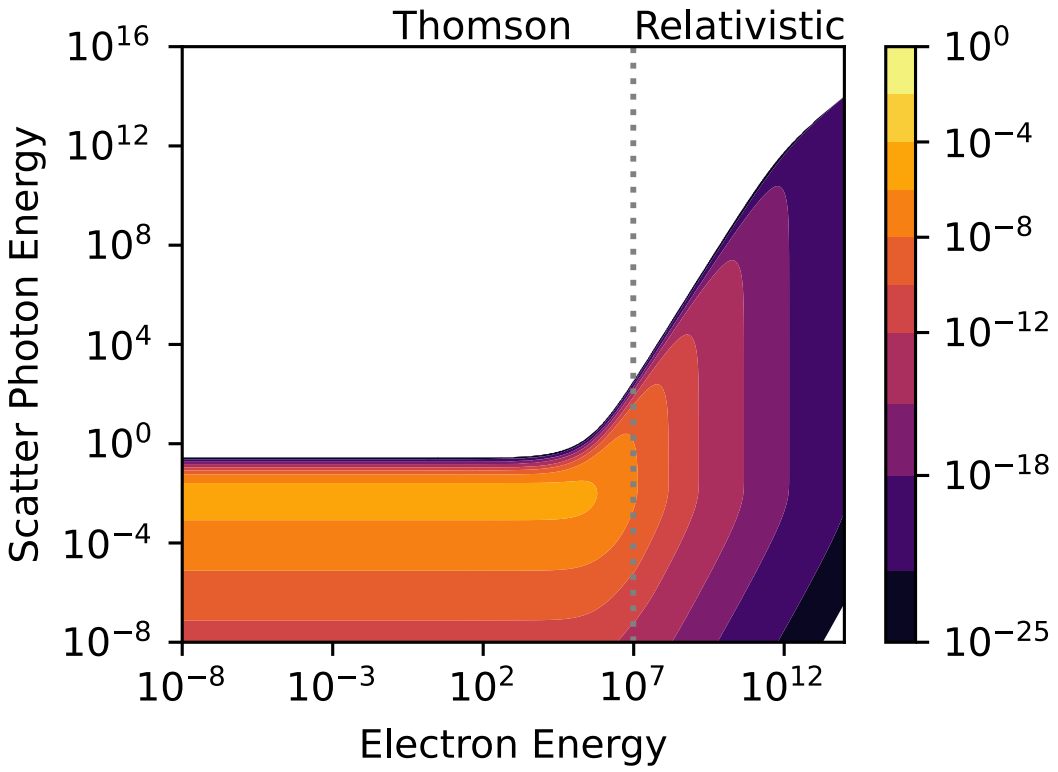


Figure 5.3: Energy spectrum of photons scattered through ICS. The CMB background is modeled as a blackbody spectrum. At lower energies, the spectrum is computed using the differential energy spectrum in the Thomson regime, while at higher energies, it is computed in the relativistic regime.

### 5.3.2 Photoionization

Following the ICS of electrons produced by DM annihilation, photons emerge as the dominant secondary particles. However, not all upscattered photons completely deposit their energy into the gas within the halo. For instance, photons with energies $E < 10.2$ eV, which are insufficient to effectively heat or excite the medium, are often considered negligible in related studies. Conversely, photons with very high energies exhibit reduced effective deposition fractions owing to the decrease in the photoionization cross-section of neutral hydrogen as photon energy increases. In these scenarios, Compton scattering becomes the predominant secondary mechanism, producing low-energy electrons. The subsequent ICS of these electrons usually generates low-energy photons $E < 10.2$ eV, which have minimal impact on the medium and are typically excluded from calculations.

Scattered photons can photoionize neutral hydrogen at energies exceeding $E_{i,\mathrm{H}} = 13.6$ eV and neutral helium at energies surpassing $E_{i,\mathrm{He}} = 24.6$ eV. The photoionization cross-section per helium atom in a cosmological mixture containing hydrogen and helium atoms (with helium atoms comprising 25% of the mass fraction) is defined as (Zdziarski and Svensson 1989)

$$\sigma_{\mathrm{He+H}} \simeq 5.1 \times 10^{-20} \left( \frac{E}{250\mathrm{eV}} \right)^{-p} \ \mathrm{cm}^2 \,, \tag{5.21}$$

where

$$p = \begin{cases} 2.65, & 25\mathrm{eV} \leq E \leq 250\mathrm{eV}, \\ 3.30, & E \geq 250\mathrm{eV} \end{cases} . \tag{5.22}$$

A more precise calculation of photoionization cross-sections is provided by Verner et al. (1996),

$$\sigma(E) = 10^{-18} \sigma_0 F(y) \mathrm{cm}^2 \,, \tag{5.23}$$

where

$$F(y) = [(x-1)^2 + y_w^2] y^{0.5P-5.5} (1 + \sqrt{y/y_a})^{-P} \,. \tag{5.24}$$

In the above equations, $x = E/E_0 - y_0$, and $y = \sqrt{x^2 + y_1^2}$. Notably, the parameters $\{\sigma_0, y_0, y_1, E_0, P\}$ vary depending on the element, such as HI, HeI, and HeII.

If photons are injected at the center of the halo, their escape fraction can be determined from the absorption cross-section detailed in Equation 5.21 by integrating along their paths. However, gas density within the DM halo is not uniform, with most of the gas mass being

concentrated near the center. To calculate the escape fraction of photons without relying on computationally expensive simulations, absorption must be evaluated at each radial bin.

Although accurate results require detailed halo simulations to calculate the energy deposition fraction, the process can be conceptualized similarly to the method used for electrons in the previous sections. At a given radial bin around $r$, the energy loss fraction relative to the initial photon energy is

$$\frac{\Delta E}{E} \propto \frac{\sigma(E)^2 n(r)^2}{E} \sim E^{-7.60} r^{-2} (1+r)^{-4} \,. \tag{5.25}$$

This calculation produces a sharp transition in the energy escape fraction curve. For sufficiently high photon energies ($E > E_{\rm esc}$), the energy loss fraction is minimal ($\Delta E/E \ll 1$), allowing photons to escape the halo while experiencing minimal interactions with the surrounding gas. The photon energy threshold $E_{\rm esc}$ depends on the halo model and ranges from $10^3$ to $10^6$ eV.

Conversely, photons with energies $E < E_{i,\rm H} = 13.6$ eV are assumed to exert no direct effect on the gas. Although photons with $E > 10.2$ eV (LW photons) can influence gas cooling and star formation processes, such effects are not considered in this discussion of photoionization. The energy range of photons $E_{i,\rm H} < E < E_{\rm esc}$ provides an effective window wherein electron energy or DM mass significantly contributes to gas heating and ionization within the DM halo.

The optical depth of photoionization within the DM halo can be expressed as

$$\left.\frac{d\tau_v(r)}{ds}\right|_{\rm photoion} = \sum_i \sigma_i(E) n_i(r) \,, \tag{5.26}$$

where $\sigma_i$ denotes the photoionization cross-section for element $i$, and $n_i$ represents the number density of element $i$ at radius $r$. The left panel of Fig. 5.4 illustrates the dimensionless quantity $R_{\rm vir} d\tau/ds$ within a $10^6$ $M_\odot$ DM halo at a redshift of $z = 20$ as a function of the virial radius and photon energy. The results indicate a notable decrease in the photoionization cross-section with increasing photon energy and a slight decrease with increasing radius. Meanwhile, the right panel of Fig. 5.4 presents the optical depth integrated from the center to the virial radius $r_{\rm vir}$ as a function of photon energy. This demonstrates that photon energy can be deposited in the halo gas via photoionization at high optical depths.

The characteristic photoionization radius for a DM halo, analogous to the *photosphere* in stellar physics, can be defined by setting $\tau_v(r_p) = 1$. This radius represents the distance photons can travel before losing a significant amount of their energy, making it particularly useful in rapidly changing environments. In situations with a homogeneous background, this characteristic radius can be expressed as $r_p = 1/(\sigma n)$, further reducing to the mean free path $r_p(E) = \lambda(E)$. For a simple top-hat model where $\rho_{\rm DM} = \Delta_c \rho_{\rm crit}$ and $\Delta_c = 200$, the characteristic

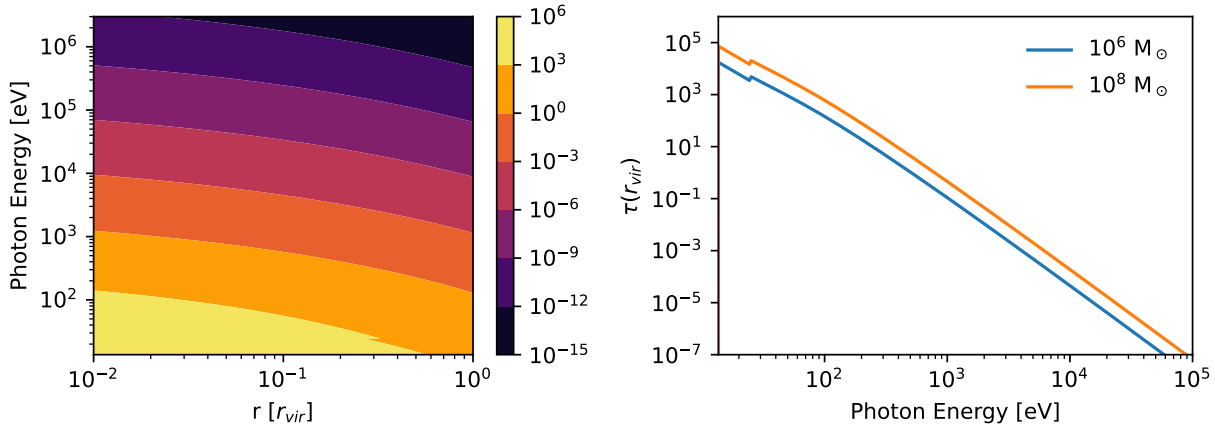


Figure 5.4: Optical depth of photoionization within an Einasto DM halo at a redshift of $z = 20$. The left panel presents the dimensionless quantity $r_{\rm vir} d\tau/ds$ at different radii $r$ and photon energies. The right panel presents the optical depth from the center to the virial radius $r_{\rm vir}$ as a function of the photon energy. Colored lines represent optical depths within DM halos with masses $10^6$ M$_\odot$ and $10^8$ M$_\odot$.

radius $r_p$ can be approximated as $r_p \approx 0.6\left(\frac{E}{250\,\mathrm{eV}}\right)^p (1+z)^{-3}$ Mpc using the cross-section detailed in Equation 5.21. Precise numerical results for an Einasto DM halo are illustrated in Fig. 5.5. For a halo with mass $10^6 M_\odot$, the characteristic radius $r_p$ is smaller than $r_{\rm vir}$, requiring different photon energies at different redshifts. This result aligns with the previously discussed escape energy $E_{\rm esc}$.

To obtain a straightforward result for DM annihilation, combining the ICS and photoionization processes for an approximate estimation can prove valuable. In this scenario, ICS serves as the dominant process for transferring energy from electrons or positrons, produced via DM annihilation, into scattered photons. These photons subsequently deposit their energy into the gas through photoionization. For effective energy deposition, electrons undergoing ICS must generate sufficient photons with energies lying within the photoionization window.

As illustrated in Fig. 5.5, for a DM halo with mass $10^6\,\mathrm{M}_\odot$ at redshift $z = 20$, an optical photoionization depth of $\tau(r_{\rm vir}) \leq 1$ requires photon energies in the range $10.2\,\mathrm{eV} < E < 500\,\mathrm{eV}$, with the minimum value defined by the Lyman-alpha cutoff. This constraint applies to ICS. If all scattered photons are assumed to originate from ICS and all primary photons are assumed to undergo photoionization, we can relate the threshold for electron energy to the photon energy. The limitation on electron energy is approximately $E_e > 10^6\,\mathrm{eV}$. For $E_e > 10^8\,\mathrm{eV}$, higher-energy photons can easily escape the halo in a photoionization-only scenario.

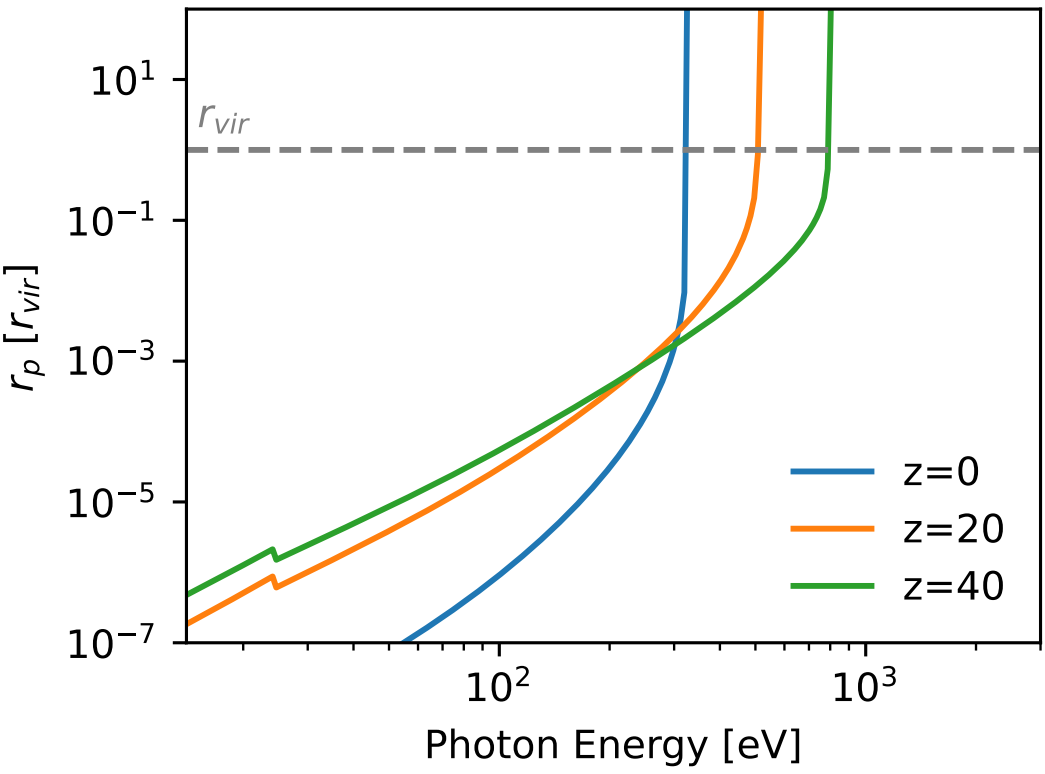


Figure 5.5: Characteristic radius of photoionization within a DM halo with an Einasto profile and a mass of $10^6$ $M_\odot$ at different redshifts.

### 5.3.3 Pair Production

For photon energies exceeding the threshold of approximately 1 MeV ($2m_e c^2 \approx 1.022$ MeV), electron–positron pair production becomes possible. During this process, a photon interacts with the strong electromagnetic field of a nucleus (or, less commonly, an electron) to create an electron–positron pair. This interaction converts the photon's energy into the mass and kinetic energy of the pair, along with any secondary particles. This phenomenon was first experimentally observed in the 1930s and has been widely documented in the literature MOTZ et al. (1969); Hubbell et al. (1980); Hubbell (2006).

In previous implementations, photon energies exceeding the threshold of $E_p > 2m_e c^2$ were typically distributed equally between the electron and positron pair, with each particle receiving an energy of $E_+ = E_- = E_p/2$. The total cross-section for this process was calculated using the Bethe–Heitler formula. Simulations often modeled pair production in two simplified steps: First, a photon scatters off a nucleus, creating an electron–positron pair. Second, the electron and positron are each assigned half of the photon's energy. The Bethe –Heitler formula determines the total cross-section. However, this approach is valid only for high-energy photons and high-$Z$ atoms. For photons produced by DM annihilation within the energy range of megaelectronvolts to gigaelectronvolts in primordial gas, a more detailed treatment is necessary.

The energy and momentum conservation equations in the laboratory system for pair production are as follows:

$$\gamma + Z \rightarrow e^+ + e^- + Z\,, \tag{5.27}$$

$$E_p = E_+ + E_- + E_r\,, \tag{5.28}$$

$$\vec{p} = \vec{e_+} + \vec{e_-} + \vec{q}\,, \tag{5.29}$$

The threshold energy in the laboratory or halo system is given as

$$E_p = 2(1 + m_0/m_r)\,. \tag{5.30}$$

The minimum and maximum recoil momentum $q$ are expressed as

$$q_{\min} = k - (k^2 - 4)^{1/2}\,. \tag{5.31}$$

$$q_{\max} = \frac{k + (m_r/m_0)}{2k + (m_r/m_0)}[k + (k^2 - 4)^{1/2}]\,. \tag{5.32}$$

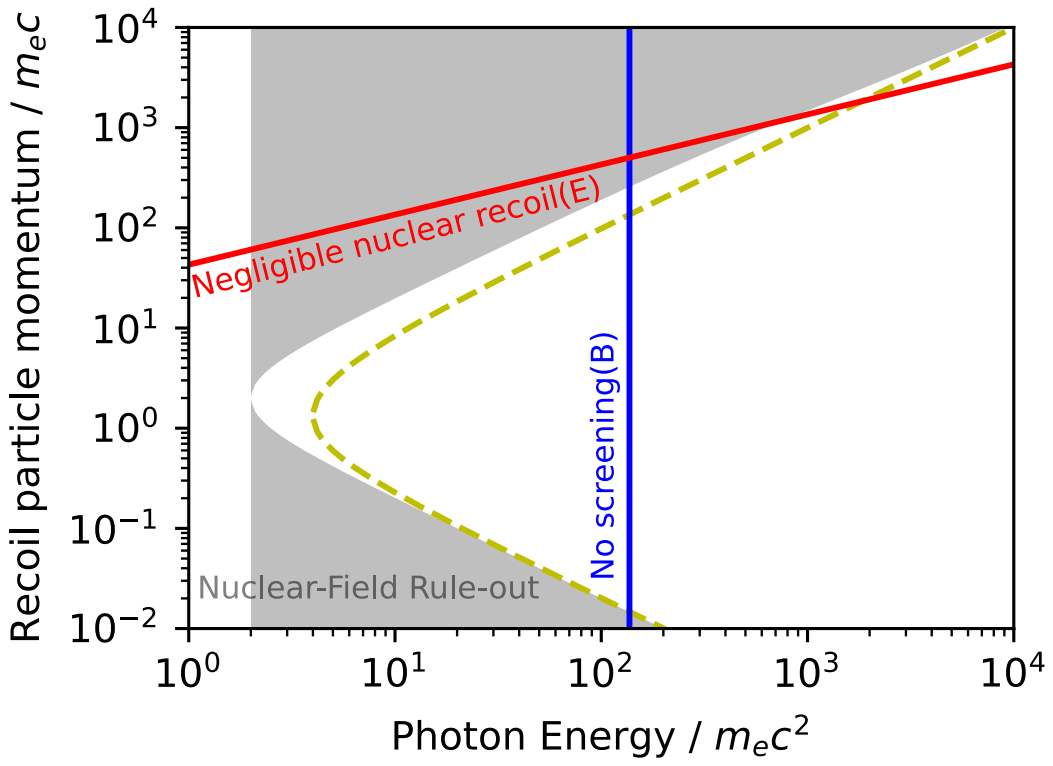


Figure 5.6: Validity of pair production within the nuclear field, as presented in MOTZ et al. 1969. The shaded gray region represents constraints on the recoil momentum, calculated using energy and momentum conservation.

The differential pair production cross-section depends on factors such as atomic number, photon energy, and nucleus recoil. Figure 5.6 illustrates the validity of pair production across a range of particle momenta and photon energies for a hydrogen nucleus. The applied constraints correspond to those detailed in Table 6.01 of MOTZ et al. 1969. The shaded gray region indicates the exclusion zone determined by the minimum and maximum possible recoil momenta of the particles (calculated using Equations 5.31 and 5.32). Meanwhile, the dashed yellow line represents the same the exclusion zone in an electron field, where the energy threshold is $E > 4m_e c^2$. Finally, the red line corresponds to conditions under which nuclear recoil is negligible, specifically at $q^2 \ll k m_r / m_0$. In most cases, the energy of nuclear recoil is negligible, and the energy of the electron–positron pair is $E_0 = E_+ + E_+$. The blue line delineates the boundary between complete and no screening, based on $k = 1/(\alpha Z^{1/3})$.

Pair production in an atomic field can occur either without (elastic or coherent) or with (inelastic or incoherent) atomic excitation. The differential pair production cross-section, including both elastic and inelastic scattering cross-sections, is given by Tsai (1974):

$$\begin{aligned}\frac{d\sigma}{dx} =& \alpha r_0^2 \left\{ \left( \frac{4}{3}x^2 - \frac{4}{3}x + 1 \right) \right. \\ & \times \left[ Z^2 \left( \Phi_1 - \frac{4}{3}\ln Z - 4f \right) + Z \left( \Psi_1 - \frac{8}{3}\ln Z \right) \right], \\ & \left. -\frac{2}{3}x(1-x)\left[ Z^2(\Phi_1 - \Phi_2) + Z(\Psi_1 - \Psi_2) \right] \right\}\end{aligned} \tag{5.33}$$

where $x = E\_/k$ denotes the reduced energy, and $\Phi$ and $\Psi$ describe elastic and inelastic scattering under various conditions. The function $f$ represents the Coulomb correction, calculated using Davies et al. (1954)

$$\begin{aligned}f(Z) &= a^2 \sum_{n=1}^{\infty} \frac{1}{n(n^2 + a^2)} \\ &\approx a^2[(1+a^2)^{-1} + 0.202059 - 0.03693a^2]\end{aligned} \quad . \tag{5.34}$$

where $a = \alpha Z$ and $\alpha = 1/137$ denote fine structure constants. For hydrogen, the Coulomb correction, as detailed in Equation (5.34), is $f(Z = 1) \approx 6.4 \times 10^{-5}$, while for helium, it is $f(Z = 2) \approx 2.6 \times 10^{-4}$.

For high-$Z$ atoms ($Z \gg 1$), the first-order terms in $Z$ become negligible, causing all inelastic term ($\Psi_1$ and $\Psi_2$) to vanish. In this regime, the ross-section simplifies to the Bethe–Heitler form:

$$\frac{\mathrm{d}\sigma_{\mathrm{pp}}^{(\mathrm{BH})}}{\mathrm{d}x} = \alpha r_{\mathrm{e}}^2 Z^2 \left\{ \left[ x^2 + (1-x)^2 \right] \left( \Phi_1 - 4f \right) + \frac{2}{3}x(1-x)\left( \Phi_2 - 4f \right) \right\} . \tag{5.35}$$

However, for hydrogen and helium, inelastic scattering cannot be ignored. Salvat et al. (1996) incorporated the inelastic scattering effects into factor $\eta$, as follows:

$$\frac{\mathrm{d}\sigma_{\mathrm{pp}}}{\mathrm{d}x} = \alpha r_{\mathrm{e}}^2 Z(Z+\eta) \left\{ \left[ x^2 + (1-x)^2 \right] \left( \Phi_1 - 4f \right) + \frac{2}{3}x(1-x)\left( \Phi_2 - 4f \right) \right\} , \tag{5.36}$$

where $\eta$ varies with photon energy and approaches $\eta_\infty$ in the high-energy limit. The empirical expression for $\eta$ is

$$\eta = \left[ 1 - \exp^{-\nu} \right] \eta_\infty . \tag{5.37}$$

The corresponding values for $\eta_\infty$ can be obtained from the tables in Hubbell et al. (1980). For hydrogen, $\eta_\infty = 1.157$, while for helium, $\eta_\infty = 1.169$. The function $\nu$ is defined as

$$\begin{aligned}\nu =& (0.2840 - 0.1909a)\ln(4/k) + (0.1095 + 0.2206a)\ln^2(4/k) \\ & + (0.02888 - 0.04269a)\ln^3(4/k) + (0.002527 + 0.002623a)\ln^4(4/k) .\end{aligned} \tag{5.38}$$

where $\kappa = E/mc^2$ represents the photon energy in units of the electron rest energy.

In pair production simulations, triplet production is often neglected because the recoiling electron has a range that is much smaller than the mean free path of the incident photon in cases where pair production is dominant (Salvat et al. 1996; Romano et al. 2015).

Notably, the symmetric energy distribution ($E_- = E_+$) derived from the Bethe–Heilter formula is valid only under certain conditions. For instance, as the atomic number Z increases and the photon energy decreases ($k > 10$), the energy distribution becomes asymmetric (Øverbø et al. 1973). For more general cases, energy sampling from the cross-section can be handled using rejection sampling techniques, as implemented in `GEANT4` (Brun et al. 1993; Collaboration et al. 2020).

We define two functions:

$$F_1(\delta) = 3\Phi_1(\delta) - \Phi_2(\delta) - F(Z)$$
$$F_2(\delta) = \frac{3}{2}\Phi_1(\delta) - \frac{1}{2}\Phi_2(\delta) - F(Z)$$

where $F(Z)$ is the Coulomb correction function. Notably, the above functions $F_1(\delta)$ and $F_2(\delta)$ are decreasing functions of $\delta$ and are valid for $\forall\delta \in [\delta_{\min}, \delta_{\max}]$. These functions attain their maximum values when $\delta_{\min} = \delta(\epsilon = 1/2)$.

$$F_{10} = \max F_1(\delta) = F_1(\delta_{\min})$$
$$F_{20} = \max F_2(\delta) = F_2(\delta_{\min})$$

Following algebraic manipulations, the formula can be expressed as

$$\frac{d\sigma(Z,\epsilon)}{d\epsilon} = \alpha r_e^2 Z[Z + \xi(Z)]\frac{2}{9}\left[\frac{1}{2} - \epsilon_{\min}\right]\left[N_1 f_1(\epsilon) g_1(\epsilon) + N_2 f_2(\epsilon) g_2(\epsilon)\right] \tag{5.39}$$

$$\begin{aligned}
N_1 &= \left[\tfrac{1}{2} - \epsilon_{\min}\right]^2 F_{10} \\
f_1(\epsilon) &= \frac{3}{\left[\frac{1}{2} - \epsilon_{\min}\right]^3}\left[\tfrac{1}{2} - \epsilon\right]^2 \\
g_1(\epsilon) &= \frac{F_1(\epsilon)}{F_{10}} \\
N_2 &= \tfrac{3}{2} F_{20} \\
f_2(\epsilon) &= \text{const} = \frac{1}{\left[\frac{1}{2} - \epsilon_{\min}\right]} \\
g_2(\epsilon) &= \frac{F_2(\epsilon)}{F_{20}}
\end{aligned}$$

The functions $f_1(\epsilon)$ and $f_2(\epsilon)$ denote PDFs over the interval $\epsilon \in [\epsilon_{\min}, 1/2]$, satisfying the following:

$$\int_{\epsilon_{\min}}^{1/2} f_i(\epsilon)\, d\epsilon = 1$$

Additionally, $g_1(\epsilon)$ and $g_2(\epsilon)$ represent valid rejection functions, ensuring $0 < g_i(\epsilon) \leq 1$.

Given a triplet of uniformly distributed random numbers $(r_a, r_b, r_c)$, we follow the given steps to sample values:

1. Use $r_a$ to select the decomposition term to be used:

$$\text{if } r_a < \frac{N_1}{N_1 + N_2} \rightarrow f_1(\epsilon) g_1(\epsilon)$$
$$\text{otherwise } \rightarrow f_2(\epsilon) g_2(\epsilon)$$

2. sample $\epsilon$ from $f_1(\epsilon)$ or $f_2(\epsilon)$ with $r_b$:

$$\epsilon = \frac{1}{2} - \left(\frac{1}{2} - \epsilon_{\min}\right) r_b^{1/3} \quad \text{or} \quad \epsilon = \epsilon_{\min} + \left(\frac{1}{2} - \epsilon_{\min}\right) r_b$$

3. reject $\epsilon$ if $g_1(\epsilon)$ or $g_2(\epsilon) < r_c$

In pair production, the polar angle of the electron (or positron) is defined relative to the direction of the parent photon. Tsai (1974) proposed sampling the angular distribution from the full cross-section $\frac{d\sigma}{d\Omega dp}$ for hydrogen and helium. However, this approach is complex and can be approximated using the density function suggested by Brun et al. (1993).

$$f(u) = C\left(u e^{-a u} + d\, u e^{-3a u}\right) \tag{5.40}$$

where $C = \frac{9a^2}{9+d}$, $a = 0.625$, and $d = 27.0$. The azimuthal angle is generated isotropically within the range of $(0, 2\pi)$.

When a recoil particle is involved in the emission, the emission angle of the pairs cannot be directly determined based on their energies. In this case, the angular distribution of the electron and positron can be derived from the leading terms in the Bethe–Heitler differential cross-section (Salvat et al. 1996):

$$p(\cos\theta_\pm) = a(1 - \beta_\pm \cos\theta_\pm)^{-2}\,, \tag{5.41}$$

where $a$ denotes a normalized constant, and $\beta_\pm$ represents the velocities of the electron and positron.

The total pair production cross-section, including both coherent and incoherent contributions, has been calculated by Knasel 1968 for $k \gg 2$.

For hydrogen, a simple fit with 5% accuracy was obtained by Zdziarski and Svensson (1989):

$$\sigma_{\mathrm{H}} = 5.4\alpha_f r_0^2 \ln\left(\frac{513\epsilon}{\epsilon+825}\right). \tag{5.42}$$

For helium, the equivalent expression is

$$\sigma_{\mathrm{He}} = 8.76\alpha_f r_0^2 \ln\left(\frac{513\epsilon}{\epsilon+825}\right), \tag{5.43}$$

where $\alpha_f$ denotes the fine structure constant, $r_0$ denotes the classical electron radius, and $\epsilon$ denotes the photon energy in units of the electron rest mass.

## 5.4 Simulation Results

### 5.4.1 Establishing the Relationship with Deposition Fraction

In the energy-transfer Monte Carlo code, particles are injected at fixed positions, and the program monitors their trajectories and interactions with other particles in the environment. When a particle transfers energy to other particles, these particles are added to the tracking pool. If a particle deposits its energy into predefined channels (such as heating or ionization channels), the program records the corresponding energy as the deposited energy at the given radius.

However, accurately determining the complete energy deposition fraction for DM annihilation is challenging. For DM annihilation into electron–positron pairs, the program provides the radial distribution of deposited energy at specific injection points, rather than the total energy deposited fraction. While the total DM annihilation energy in the halo can be theoretically calculated by accounting for all electron–positron pairs injected at every point, this approach is computationally expensive, even if the halo is spherically symmetric.

To improve computational efficiency, the simulation divides the DM halo into $n$ radial bins, ranging from $r_1$ to $r_n$, with radii spanning from the core (e.g., $0.01\,r_{\mathrm{vir}}$) to the maximum radius (e.g., $1.0\,r_{\mathrm{vir}}$). This division applies solely to energy deposition calculations, while particle dynamics, interactions, and density profiles are computed using a more precise radial profile to maintain accuracy.

We focus on general energy transport within the simulation domain. Let $E_i^{\mathrm{inj}}$ represent the total energy injection rate in radial bin $r_i$ and $E_j^{\mathrm{dep,c}}$ denote the total energy deposition rate for channel $c$ in radial bin $r_j$. The energy transport fraction, $\hat{f}_{ij}$, is defined as the fraction of

energy deposited in radial bin $r_j$ originating from injections in radial bin $r_i$:

$$\hat{f}^{\mathrm{c}}_{ij} = \frac{E^{\mathrm{dep,c}}_{ij}}{E^{\mathrm{inj}}_{i}} \,. \tag{5.44}$$

The total energy deposition rate in channel $c$ within radial bin $r_j$ is expressed as

$$E^{\mathrm{dep,c}}_{j} = \sum_{i=1}^{n} E^{\mathrm{dep,c}}_{ij} \,. \tag{5.45}$$

Assuming that the deposited energy follows the same distribution as the injected energy within a radial bin, the deposited fraction remains constant within that bin. Consequently, the total energy deposition fraction within radial bin $r_j$ in channel $c$ from all DM annihilations events within the halo is defined as

$$f^{\mathrm{c}}_{j} = \frac{E^{\mathrm{dep,c}}_{j}}{E^{\mathrm{inj}}_{j}} = \frac{\sum_{i=1}^{n} E^{\mathrm{inj}}_{i} \hat{f}^{c}_{ij}}{E^{\mathrm{inj}}_{j}} \,. \tag{5.46}$$

The energy injection rate $E^{\mathrm{inj}}_{i}$ is related to the DM annihilation power $p_{\mathrm{ann}}$ as

$$E^{\mathrm{inj}}_{i} = \int_{r_i}^{r_{i+1}} p_{\mathrm{ann}}(r') 4\pi r'^2 dr' \,, \tag{5.47}$$

where the annihilation rate is

$$p_{\mathrm{ann}}(r) = \frac{\langle \sigma v \rangle}{m_{\mathrm{DM}}} \rho^2(r) \,. \tag{5.48}$$

Here, $\rho(r)$ represents the DM density profile.

The simulation output provides the energy distribution $f_j$ along the radial bin $r_j$ for a single particle injection event with an initial energy of $E_p$ at position $r$. By denoting the energy deposited for this single event as $\epsilon^{\mathrm{c}}_{j}(r)$, the overall energy deposition can be expressed as

$$E^{\mathrm{dep,c}}_{ij} = \int_{r_i}^{r_{i+1}} N_{\mathrm{ann}}(r') \epsilon^{1}_{j}(r') 4\pi r'^2 dr' \,, \tag{5.49}$$

where $N_{\mathrm{ann}}(r)$ denotes the frequency of DM annihilation events per unit volume at radius $r$:

$$N_{\mathrm{ann}}(r) = \frac{p_{\mathrm{ann}}(r)}{2 m_{\mathrm{DM}} c^2} \,. \tag{5.50}$$

The output energy distribution fraction can be related to the energy deposited in radial bin $r_j$ and initial particle energy $E_p$ as

$$\tilde{f}_j^{\mathrm{c}}(r) = \frac{\epsilon_j^{\mathrm{c}}(r)}{E_p}\,. \tag{5.51}$$

In scenarios wherein a DM annihilation event leads to the conversion of 100% of the initial energy into an electron–positron pair, the initial energy of the pair is $E_p = 2m_{\mathrm{DM}}c^2$. Thus, the output energy distribution can be transformed into the deposited fraction using Equations 5.46 and 5.51, canceling out the terms $E_j^{\mathrm{inj}}$ and $E_j^{\mathrm{dep,c}}$:

$$\begin{aligned} f_j^c &= \frac{\sum_{i=1}^{n}\int_{r_i}^{r_{i+1}} N_{\mathrm{ann}}(r')\epsilon_j^{\mathrm{c}}(r')4\pi r'^2 dr'}{E_j^{\mathrm{inj}}} \\ &= \frac{\sum_{i=1}^{n}\int_{r_i}^{r_{i+1}} N_{\mathrm{ann}}(r')E_p\tilde{f}_j(r')4\pi r'^2 dr'}{\int_{r_j}^{r_{j+1}} p_{\mathrm{ann}}(r')4\pi r'^2 dr'}\,. \\ &= \frac{\sum_{i=1}^{n}\int_{r_i}^{r_{i+1}} \rho(r')^2\tilde{f}_j^{\mathrm{c}}(r')r'^2 dr'}{\int_{r_j}^{r_{j+1}} \rho(r')^2 r'^2 dr'} \end{aligned} \tag{5.52}$$

In practice, $\tilde{f}_j^{\mathrm{c}}(r)$ can be approximated as a constant $\tilde{f}_j^{\mathrm{c}}(r) \equiv \tilde{f}_{ij}^{\mathrm{c}}$ within radial bin $r_i$, provided that this bin is adequately small. This simplifies Equation 5.52 to

$$f_j^c = \frac{\sum_{i=1}^{n}\tilde{f}_{ij}^{\mathrm{c}}\int_{r_i}^{r_{i+1}} \rho(r')^2 r'^2 dr'}{\int_{r_j}^{r_{j+1}} \rho(r')^2 r'^2 dr'}\,. \tag{5.53}$$

The weighted factor $w_i$ of the DM halo is defined as

$$w_i = \int_{r_i}^{r_{i+1}} \rho(r')^2 r'^2 dr'\,. \tag{5.54}$$

Given the DM density profile, the value of $w_i$ can be easily calculated. This allows the relation to be expressed in a simpler form:

$$f_j^{\mathrm{c}} = \frac{\sum_{i=1}^{n}\tilde{f}_{ij}^{\mathrm{c}} w_i}{w_j}\,. \tag{5.55}$$

The deposited fraction can be determined once the energy distribution fraction is obtained from the simulation program.

### 5.4.2 Monte-Carlo Visualization Tool

`Chimera` simulates Monte Carlo iterations and cascades based on user-defined profiles, outputting detailed energy distributions. To enable deeper exploration of the patterns and interactions in these simulations, I developed a visualization tool called `xChimera`.

`xChimera` is a web-based single-page application (SPA) that visualizes simulation outputs from `Chimera`. Its accessible design caters to both academic researchers and the wider public. The tool integrates with `Chimera` via three main components:

- **Chimera Debug Mode Integration**: The tool utilizes `Chimera`'s debug mode to extract comprehensive data on simulation processes. This includes details on incoming particles (type, position, energy), outgoing particles (type, position, energy), and the types of interactions occurring at each step. These data points are stored in an optional compressed file format, allowing users to trace individual particle trajectories and analyze specific cascades in depth.
- **Data-Interface Backend**: The backend processes debug mode outputs into structured, analyzable datasets through the following steps:
  - **Parsing Log Data**: Converts raw logs into a structured format, identifying cascades, iterations, and individual interactions.
  - **Statistical Computation**: Derives numerical insights at multiple levels:
    - *Cascade-Level*: Duration, total iterations, interaction counts, and particle statistics.
    - *Iteration-Level*: Energy losses and interaction details per iteration.
    - *Interaction-Specific*: Frequencies and energy losses for distinct interaction types.
  - **Integration and Results Generation**: Combines parsed data with computed statistics, creating enriched datasets for visualization and further analysis.
- **Web Frontend**: The intuitive web interface enables users to upload data files via drag-and-drop or traditional input. Built with modern web technologies, the frontend uses:
  - *Astro Framework*: For SPA development.
  - *React with TypeScript*: To manage dynamic user interactions with strong type checking and maintainable code.
  - *D3.js*: For rendering interactive, data-driven visualizations.

By transforming raw simulation data into statistical insights, `xChimera` facilitates advanced research in particle physics and beyond. The following section demonstrates the tool's capabilities through sample outputs from `Chimera` simulations.

### 5.4.3 Example Simulation Results

We consider a scenario in which particles with an initial energy $E_{p,i}$ are injected at a radius $r_i$ from the center of the halo. The DM and baryonic profiles are modeled as follows.

For DM halos with mass $M_h$, we employ the Navarro–Frenk–White profile:

$$\rho_{\rm DM}(r) = \frac{\rho_0}{\frac{r}{r_s}(1+\frac{r}{r_s})^2}\,,$$

where $r_s = R_{\rm vir}/c$, and $c$ denotes a concentration parameter. The virial radius of the halo is defined as $R_{\rm vir} = \left(\frac{3M_h}{4\pi\Delta\rho_c}\right)^{1/3}$. Meanwhile, density normalization is expressed as $\rho_0 = \frac{M_h}{4\pi r_s^3 c_h}$, where $c_h = \log(1+c) - c/(1+c)$.

For simplicity, we assume that the baryonic density follows the DM density profile within the DM halo:

$$\rho_{\rm gas,i}(r) = f_{\rm gas,i} f_B \rho_{\rm DM}(r)\,,$$

where $f_B$ represents the cosmic baryonic fraction, and $f_{\rm gas,i}$ denotes the baryonic fraction for species $i$ (e.g., HI, HeI, HII, and HeII). The number density of each species is determined by $n_i(r) = \rho_{\rm gas,i}(r)/m_i$, where $m_i$ denotes the mass of the species.

The fraction of free electrons within the halo is defined as $n_{\rm ele}(r) = f_{\rm ele} n_{\rm H}(r)$, where $f_{\rm ele}$ represents the electron fraction, and $n_{\rm H}$ denotes the total number density of atomic hydrogen. To account for background photons, the number density of CMB photons is calculated as a function of redshift $z$ as follows: $n_\gamma(z) = n_{\gamma,0}(1+z)^3$, where $n_{\gamma,0}$ represents the present-day density of CMB photons.

Owing to differences in initial energy, DM annihilation interacts with and deposits energy into the gas through various processes. For instance, high-energy electrons produce high-energy photons through ICS. These photons photoionize the atoms in the surrounding medium. Conversely, at lower energies, interactions such as Coulomb scattering or electron excitation become dominant.

We performed simulations with 10 cascades in our Monte-Carlo code. Each electron and positron had an initial energy of $E_{p,i}$. The baryonic mass fraction was set to $f_B = 0.15$, with $f_{\rm gas,HI} = 0.75$ and $f_{\rm gas,HeI} = 0.25$. The electron fraction relative to total atomic hydrogen was $f_{\rm ele} = f_{\rm gas,HII} = 10^{-4}$. Fig. 5.7 illustrates the number of interaction events for $E_{p,i} = 100$ keV, while

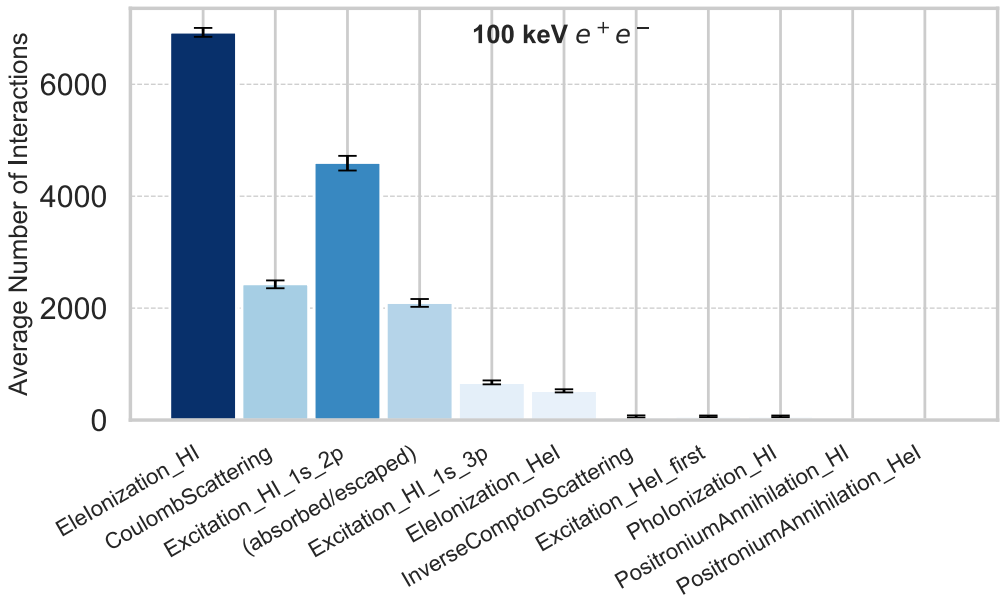


Figure 5.7: Average interaction events for different types of particle interactions. Error bars represent the minimum and maximum values across different cascades. The electron–positron pair has an initial energy $E_{p,i} = 10^5$ eV. Particles are injected at a radius of $r = 0.005 R_{\rm vir}$ within a $10^6 M_\odot$ halo at a redshift of $z = 40$.

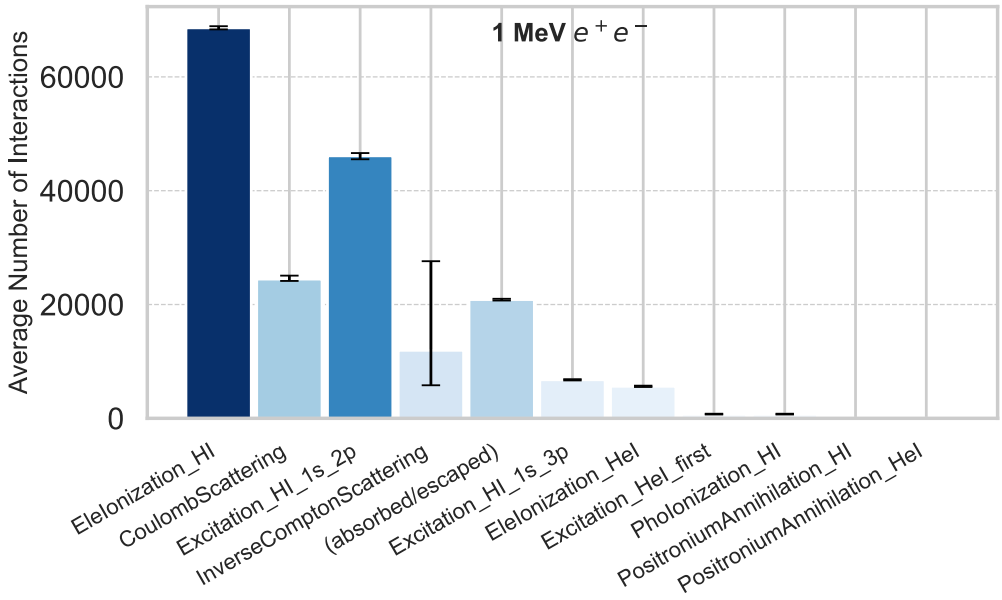


Figure 5.8: Average interaction events for different types of particle interactions. Error bars denote the minimum and maximum values across different cascades. The electron–positron pair has an initial energy of $E_{p,i} = 10^6$ eV. Particles are injected at a radius of $r = 0.005 R_{\rm vir}$ within a $10^6 M_\odot$ halo at a redshift of $z = 40$.

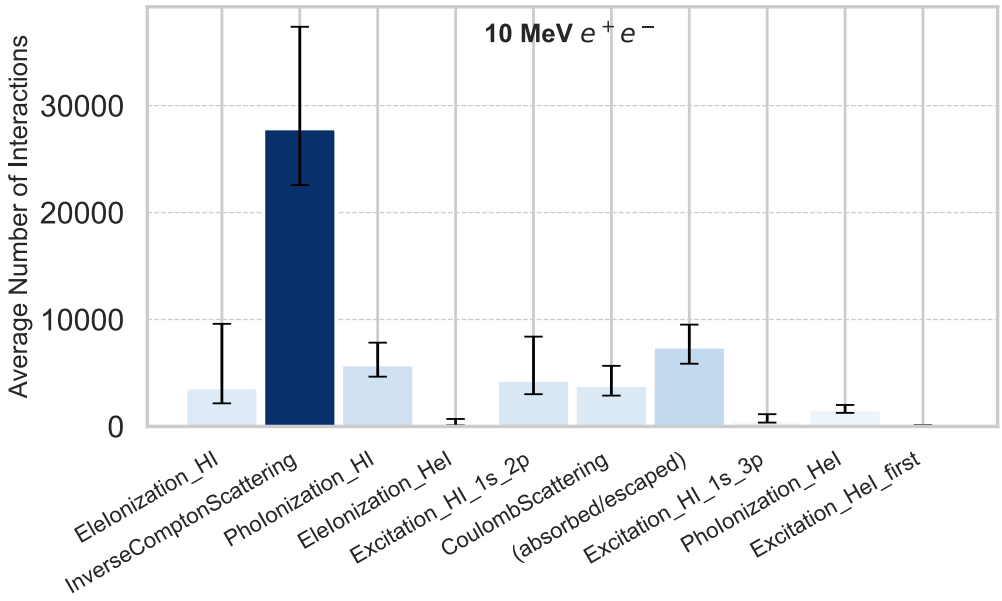


Figure 5.9: Average interaction events for different types of particle interactions. Error bars represent the minimum and maximum values across different cascades. The electron–positron pair has an initial energy of $E_{p,i} = 10^7$ eV. Particles are injected at a radius of $r = 0.005 R_{\rm vir}$ within a $10^6 M_\odot$ halo at a redshift of $z = 40$.

Fig. 5.9 illustrates the number of interaction events for $E_{p,i} = 10$ MeV. Owing to the stochastic nature of Monte Carlo simulations, different cascades yield varying probabilities for particle interactions. This variability is reflected in the error bars, which represent the minimum and maximum values across different cascades. During the simulations, particles were injected at a radius of $r = 0.005 R_{\rm vir}$ from the center of a $10^6 M_\odot$ halo at a redshift of $z = 40$. For each simulation, the program continued until all tracked particles either lost their energy or escaped the halo.

As depicted in Fig. 5.7, 100 keV electrons and positrons exhibit the highest rate of electron ionization of HI (EleIonization_HI). This process occurs approximately 1.5 times more frequently than the electron excitation of HI from the 1s to 2p state (Excitation_HI_1s_2p). Coulomb scattering (CoulombScattering) also contributes to the observed trends. Electrons with energies below the Lyman-alpha threshold ($E < 12$ eV) are directly absorbed in the medium. Combined with the escaped particles, these processes constitute the fourth most frequent processes for 100 keV $e^+e^-$ pairs.

As illustrated in Fig. 5.8, the behavior of 1 MeV positrons and electrons is qualitatively similar to the 100 keV case. Electron ionization and excitation remain the dominant interactions. However, the 1 MeV particles undergo a significantly higher number of interactions before

losing their energy. At this energy, ICS becomes more prominent, as photons are scattered by high-energy electrons, gaining additional energy.

For higher-energy electron–positron pairs (10 MeV), as illustrated in Fig. 5.9, the interaction dynamics differ markedly. ICS emerges as the most prominent process. Electrons and positrons upscatter low-energy photons, producing high-energy photons. While most of these high-energy photons escape the local environment, some still ionize hydrogen (Phoionization_HI) and helium (Phoionization_HeI).

For injection at position $r_i$, the simulation calculates the energy deposition fraction across radial bins ranging from $r_1$ to $r_n$. As detailed in Sec. 5.4.1, the energy distribution fraction in radial bin $r_j$ within channel $c$, originating from DM annihilation within halo $\tilde{f}_j^c$, is defined by the ratio of deposited energy $\epsilon_j^c$ to the total initial energy $E_{\rm tot} = 2m_{\rm DM}c^2$. The energy distribution fractions for DM annihilation are illustrated in Fig. 5.10 and Fig. 5.11 for initial particle energies of $E_{p,i} = 10^6$ and $10^7$ eV, respectively. In both cases, particles with an initial energy of $E_{p,i} = 1$ MeV are injected at a radius of $r = 0.005R_{\rm vir}$ from the center of a $10^6 {\rm M}_\odot$ halo at a redshift of $z = 40$.

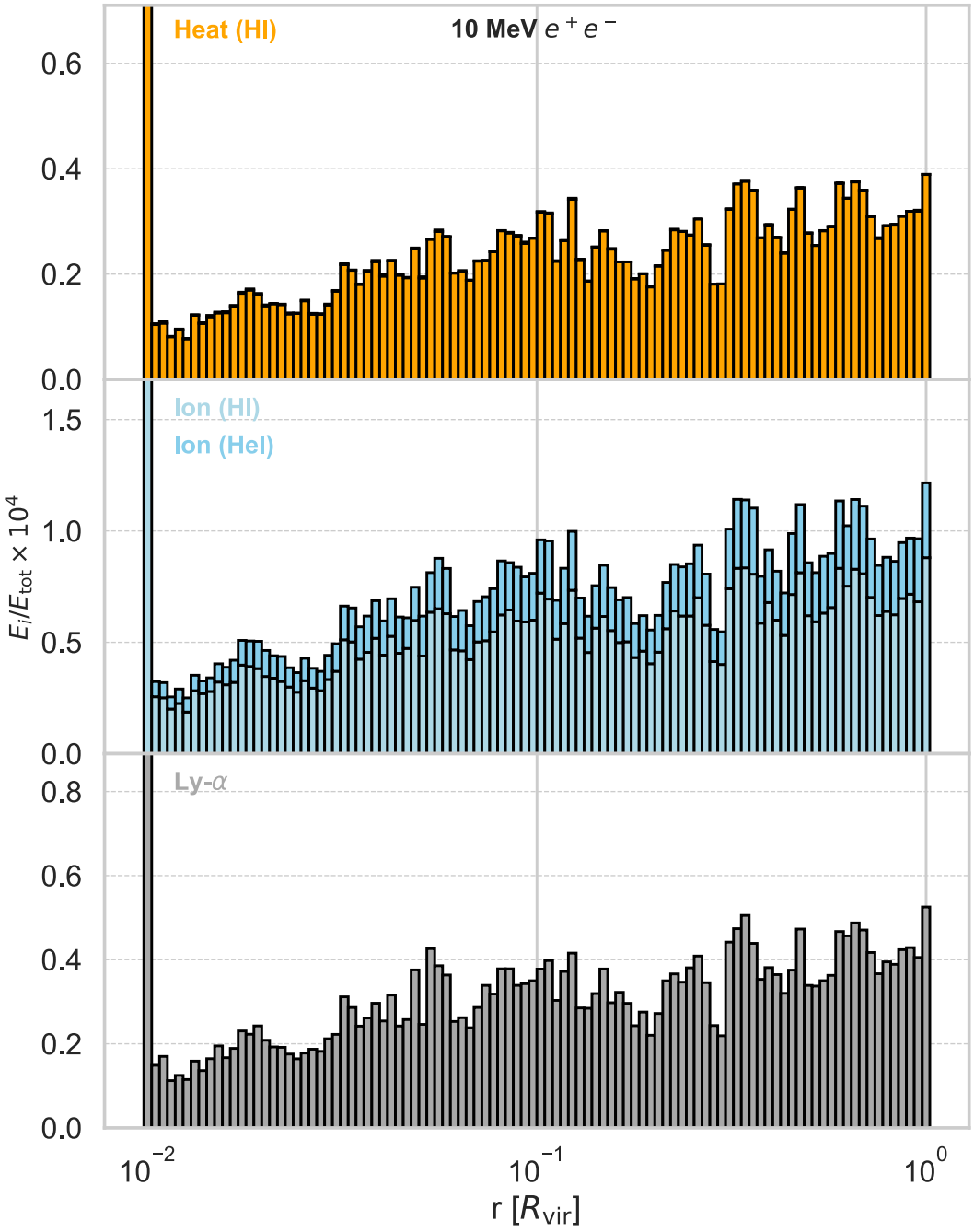


Figure 5.10: Fraction of energy deposited in each radial bin $E_i$ for an electron–positron pair with an initial total energy of $E_{\rm tot} = 2 \times 10$ MeV. During this simulation, particles are injected at a radius of $r = 0.005 R_{\rm vir}$ from the center of a $10^6 M_\odot$ halo at a redshift $z = 40$. The top panel presents the fraction of deposited energy contributing to the heating of hydrogen (HI) across different radial bins. The middle panel presents the fraction of deposited energy contributing to the ionization of hydrogen (HI) and helium (HeI). The bottom panel illustrates the fraction of deposited energy contributing to Lyman-$\alpha$ (Ly-$\alpha$) emission.

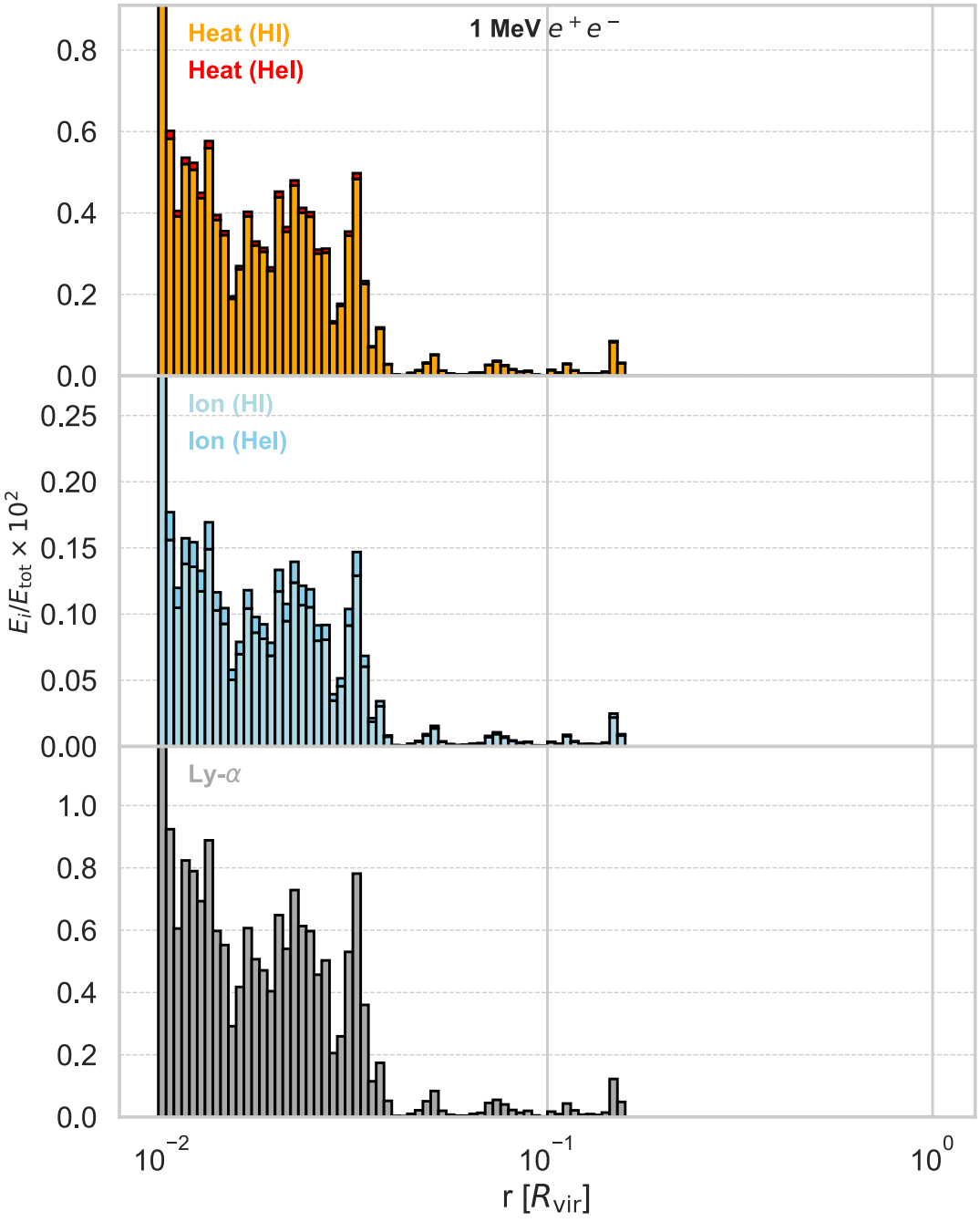


Figure 5.11: Fraction of energy deposited in each radial bins $E_i$ for an electron–positron pair with an initial total energy of $E_{\rm tot} = 2 \times 1$ MeV. During this simulation, particles are injected at a radius of $r = 0.005 R_{\rm vir}$ from the center of a $10^6 M_\odot$ halo at a redshift of $z = 40$. The top panel illustrates the fraction of deposited energy contributing to the heating of hydrogen (HI) and helium (HeI) across different radial bins. The middle panel illustrates the fraction of deposited energy contributing to the ionization of hydrogen (HI) and helium (HeI). The bottom panel illustrates the fraction of deposited energy contributing to Lyman-$\alpha$ (Ly-$\alpha$) emission.

CHAPTER

# 6

# CONCLUSIONS

## 6.1 Summary of Results

This dissertation explores the effects of DM particle physics on early cosmic structure formation, focusing on DM annihilation and its influence on small-scale structures. Detailed calculations were performed to investigate the manner in which early DM annihilation influenced the thermal history of the Universe and the formation of the first stars and galaxies. In summary, I review the related background in first two chapters and present my research in the following chapters.

Chapter 1 introduces the framework of cosmic structure formation within the context of the ΛCDM model. This chapter details the HMF, the influence of streaming velocities on early cosmic structures, and the formation of the first stars. Constraints on DM properties derived from both direct and indirect detection methods are also explored.

Chapter 2 examines DM annihilation models and discusses the cross-sections and energy deposition processes relevant to DM annihilation. This chapter also introduces the 21-cm signal and evaluates the impact of DM annihilation on this signal.

Chapter 3 presents a detailed model of DM annihilation within halos. Our discussion focuses on the annihilation power, structure of DM halos, and thermal history of the IGM, emphasizing impacts on gas collapse. Molecular cooling processes, crucial for Pop III star

formation, are also examined. Additionally, numerical simulations are employed to model the local effects of DM annihilation on small scales.

Chapter 4 discusses the implications of DM annihilation for the high-redshift global 21-cm signal. A model integrating the latest star formation prescriptions is developed, yielding simulated predictions for the 21-cm signal. These predictions are compared with the results of previous and ongoing research on the 21-cm signal.

Chapter 5 refines the current energy transfer model on small scales by analyzing detailed processes such as ICS, photoionization, and pair production. The chapter highlights the importance of considering small-scale energy transfer and high-energy particle interactions in the context of DM annihilation, addressing discrepancies between previous assumptions and the actual conditions of DM annihilation in the primordial gas. It presents example results for energy deposition obtained from a Monte Carlo code using the refined model, linking these findings to the broader context of DM annihilation.

Throughout this dissertation, the observational signatures of DM annihilation are a central focus, particularly in the context of the formation of the first stars and the 21-cm signal. By simulating the effects of DM annihilation, this research aims to advance the current understanding of the influence of DM on small scales and during the early developmental stages of the Universe.

### 6.1.1 DM Halos

We investigated DM annihilation in collapsed halos by employing models of baryon collapse, gas cooling, and early star formation.

We first examined DM annihilation power derived from both a smooth background and small-scale structures. Our results revealed that inhomogeneities could significantly boost global DM annihilation, and this increase became more pronounced with increasing redshift owing to the growing abundance of halos. This amplification, quantified as the boost factor, was calculated using the given HMF and halo density profile. Simulations of the thermal history, conducted using the program code, revealed that boosted DM annihilation redefined the gas temperature and ionization histories during Cosmic Dawn. These changes can impact cosmic structure formation and star formation in subsequent stages.

Next, we analyzed gas cooling using Jeans and molecular hydrogen analyses. Jeans analysis links the thermal history to baryonic collapse within DM halos. We found that the filtering mass provides an estimate of the gas fraction within low-mass halos with DM annihilation. Depending on the specific DM model, the gas fraction within low-mass halos can be suppressed owing to the heating effects of DM annihilation. Our analysis focused on DM annihilation in

the range of megaelectronvolts to gigaelectronvolts, which has been demonstrated to produce the strongest signals during electron–positron pair production. The annihilation of DM with a mass of approximately 100 MeV led to the most pronounced effects on the thermal history and gas fraction within low-mass halos.

Finally, molecular hydrogen was essential for the formation of the first stars within low-mass halos, where atomic cooling is generally inefficient, and gas cooling primarily relies on molecular cooling. We developed an analytical model of molecular cooling to assess the effects of DM annihilation. Molecular hydrogen chemistry was studied in a simplified manner, considering only the most critical processes during early $H_2$ formation. We analyzed the production of molecular hydrogen and its required amount based on the cooling time. The results of this model aligned with those of previous simulations. We also examined the impact of DM annihilation on heating and ionization.

After analyzing the effects of DM annihilation on gas properties such as temperature, density, cooling rate, and ionization fraction, we observed that the impact of annihilation on the fraction of molecular hydrogen depends on the interplay between heating and ionization. Our results revealed that DM annihilation exerts a redshift-dependent effect on the minimum cooling mass. At high redshifts ($z \gtrsim 40$), where DM heating is less pronounced, the minimum cooling mass decreases slightly in the presence of DM annihilation, thereby accelerating star formation within low-mass halos. Conversely, at low redshifts ($z < 35$), DM annihilation suppresses gas cooling and increases the minimum cooling mass.

We also examined the interplay between DM annihilation, LW feedback, and streaming velocity, all of which substantially influence early star formation. For LW feedback, we observed substantial photo-dissociation of molecular hydrogen, consistent with previous simulations. Both DM annihilation and LW feedback increased the minimum cooling mass at lower redshifts, with the effects of DM annihilation becoming slightly more prominent in the presence of LW feedback. Regarding streaming velocity, we incorporated suppressed gas fractions into our model and observed that streaming velocity significantly reduces the gas fraction within low-mass halos as expected. The resulting lower gas density decreases the recombination rate of electrons and reduces the production rate of molecular hydrogen, increasing the minimum cooling mass. While our findings are consistent with those of previous simulations, the impact of streaming velocity in our model appears less pronounced than that in other simulations. Notably, in the presence of streaming velocity, DM annihilation becomes sub-dominant, causing the increase in the minimum cooling mass at lower redshifts to become negligible or even producing the opposite effect.

Additionally, we explored the local effects of DM annihilation, which deposits energy not only in the cosmic background but also within its local environment. Although the intensity of

these local effects remains unclear, they are expected to significantly influence galaxy and star formation processes within low-mass halos. We examined three regimes of local effects, ranging from weak to strong. In the strongest regime of DM annihilation, gas temperature and ionization history were significantly higher compared to those in scenarios without annihilation. This increase in energy raised the Jeans mass of the affected halos, expelling gas and suppressing molecular cooling to some extent.

### 6.1.2 Global 21-cm Signal

We also examined the global 21-cm signal, a key observable for probing the early Universe. By integrating the effects of DM annihilation and streaming velocity into the `21cmvFAST` simulation code, we analyzed the effects of these factors on the 21-cm signal. Our findings revealed distinct signatures in the signal indicative of DM annihilation processes. The interaction between streaming velocity and DM annihilation reduces the abundance of low-mass halos and influences the gas fraction and molecular cooling. These effects, in turn, delay the global 21-cm signal, offering a potential observational signature of DM properties.

First, we reviewed early studies examining the effect of DM annihilation on the 21-cm signal. Although these studies provided valuable insights, we identified a lack of detailed discussions on gas cooling processes, streaming velocity effects, and updated calculations of deposited energy fractions.

Second, we evaluated the spin temperature history of the Universe using our DM annihilation models. By modifying the recombination code `CosmoRec` to incorporate energy injection from DM annihilation and the latest deposited energy fractions, we found that DM annihilation raised the global spin temperature at Cosmic Dawn, mirroring the gas temperature history. Subsequently, we calculated the differential brightness temperature as an observational signal. To this end, we simulated the 21-cm signal using the public cosmological code `21cmvFAST`.

Third, we discussed the effect of the DM–baryon relative velocity. This effect plays a significant role in structural formation at high redshifts and on small scales. Streaming velocity impacts the amplification factor of DM annihilation, resulting in a suppression of approximately 10% to 17%, depending on the redshift, DM model, and streaming velocity. We observe that streaming velocity influences the filtering mass of DM halos in a manner similar to DM annihilation. However, when considering both annihilation and streaming velocity, DM annihilation results in less than a 10% increase in the filtering mass compared to the 40% increase in the absence of streaming velocity. Additionally, streaming velocity impacts molecular cooling, thereby suppressing the formation of the first stars.

Finally, we integrated star formation models with the effects of DM annihilation on molecu-

lar cooling and analyzed the resulting global 21-cm signal, as depicted in Fig. 4.2. As illustrated, DM annihilation in this model can significantly increase the differential brightness temperature, depending on the DM mass. A comparison of our results with those of a previous study revealed a significant acceleration in the processes. However, when considering streaming velocity, the 21-cm signal appeared delayed but still occurred earlier than predicted by previous studies.

### 6.1.3 Energy Transfer

An important conclusion derived from Chapter 3 is the potential local effect of DM annihilation. Energy deposited into the surrounding environment by DM annihilation can alter the gas content, leading to a modified star-formation history. However, detailed calculations of the local energy deposition efficiency of DM annihilation are still lacking.

In Chapter 5, we reviewed energy transport calculations and examined the current stage of the Monte Carlo energy-transfer simulation program `Chimera`. Our study of the program's detailed algorithm revealed an approach for connecting the results of the single-particle Monte Carlo energy-transfer simulation program to the general deposited fraction. Following this, we discussed some of the most important processes related to DM annihilation in a local environment, including ICS, photoionization, and pair production. Notably, the particle physics involved is relatively complex owing to the wide variety of energy scales considered.

For DM annihilation into electron and positron pairs, we identified ICS as the key process. In the Thomson regime, where electron energy is relatively low, ICS was modeled using the Thomson scattering cross-section, allowing for a rough estimation of the energy escape fraction. Our findings revealed that low-energy electrons cannot escape the DM halo because most of their energy is deposited through ICS. Electrons require sufficient initial energy—implying greater DM masses—to escape the halo. However, in the relativistic regime, the behavior of ICS differs and must be described by the Klein–Nishina formula. We numerically calculated the differential cross-section for ICS in this context.

Next, we studied the process of photoionization, wherein photons ionize neutral hydrogen and neutral helium atoms when their energies exceed the respective thresholds. Our findings reveal that the energy-loss fraction of photons during photoionization rapidly decreases with increasing photon energy and halo radius. We also defined the characteristic radius of photoionization within DM halos, observing that this radius increases sharply as photon energy rises from $E \sim 10^2$ eV to $E \sim 10^3$ eV. By considering scattered photons originate from ICS and subsequently undergo photoionization, we linked this threshold to the electron energy. For instance, electrons participating in ICS must have energies between $10^3$ eV and $10^6$ eV to

generate photons capable of easily escaping the halo.

Additionally, we examined the pair production process of photons in atomic gases, which occurs when photon energy exceeds the threshold of approximately $2m_e c^2$, resulting in electron–positron pair production. Our results revealed that incoherent scattering, which is significant for low-Z atoms, played an important role in our context owing to the primordial gas components.

## 6.2 Future Research

The findings of this study on the effects of DM annihilation during the Cosmic Dawn period have notable implications for both theoretical astrophysics and observational cosmology. Our findings reveal that sub-gigaelectronvolt mass DM particles can substantially alter the thermal history of the Universe and the formation of the first galaxies, particularly through $e^+e^-$ pair production. This research paves the way for several future applications and investigations.

One immediate application is the integration of DM annihilation effects into large-scale cosmological simulations. By incorporating the heating, ionization, and excitation effects observed in this study, future simulations can more precisely model the thermal history of the early Universe and the evolution of cosmic structures. These enhanced simulations will enable more precise predictions of the CMB and the 21-cm signal, providing critical insights into the epoch of reionization and the formation of the first stars and galaxies.

Our findings regarding the suppression of stellar formation owing to DM annihilation highlight the need for refined models of early star formation. Future research can expand on this one by exploring a wider range of DM particle masses and annihilation channels. Additionally, the impacts of varying environmental conditions, such as various streaming velocities and halo masses, can be further investigated. This will help develop more comprehensive models that accurately predict star formation rates and the initial mass function in the early Universe.

The distinct patterns in the 21-cm signal caused by interactions between DM annihilation and streaming velocity present a promising avenue for future observational studies. Upcoming radio telescopes, such as the SKA, will have the sensitivity required to detect these subtle imprints. Our results suggest that careful analysis of the 21-cm signal can provide indirect evidence of DM properties and their effects on early cosmic structures. Future observational endeavors should focus on identifying these signatures, which could serve as a novel probe for DM physics.

The relationship between DM annihilation and cosmic gas properties offers a promising means for constraining DM properties. By comparing our theoretical predictions with future observational data, researchers can impose stringent constraints on the annihilation cross-

section, particle mass, and other properties of DM. This approach complements traditional DM detection methods and enables independent verification of DM models.

Understanding the feedback mechanisms between DM annihilation and baryonic matter is crucial for acquiring a holistic view of cosmic evolution. This study highlights the importance of local thermal history and gas dynamics in DM halos. Future research should aim to explore these feedback processes in greater detail, particularly using high-resolution simulations capable of capturing the complex interplay between DM and baryonic matter on small scales.

Looking ahead, the refined energy-transfer code (`Chimera`) is poised to become a versatile tool for examining the impacts of exotic energy injections, such as through DM annihilation and decay, in primordial halos. Its ability to model complex processes, including ICS, photoionization, and pair production, will enable a more accurate and detailed understanding of the manner in which these energy sources influence the thermal and ionization histories of the IGM and the formation of early cosmic structures. Integrating `Chimera` into larger numerical simulations will provide crucial subgrid physics for galaxy formation and IGM evolution, bridging the gap between small-scale processes and large-scale cosmological phenomena. The public release of `Chimera` will serve as a powerful tool for exploring the role of exotic energy sources in shaping the early Universe, contributing substantially to future research in cosmology and astrophysics.

# REFERENCES

Aalbers, J., Akerib, D., Akerlof, C., Al Musalhi, A., Alder, F., Alqahtani, A., Alsum, S., Amarasinghe, C., Ames, A., Anderson, T., Angelides, N., Araújo, H., Armstrong, J., Arthurs, M., Azadi, S., Bailey, A., Baker, A., Balajthy, J., Balashov, S., Bang, J., Bargemann, J., Barry, M., Barthel, J., Bauer, D., Baxter, A., Beattie, K., Belle, J., Beltrame, P., Bensinger, J., Benson, T., Bernard, E., Bhatti, A., Biekert, A., Biesiadzinski, T., Birch, H., Birrittella, B., Blockinger, G., Boast, K., Boxer, B., Bramante, R., Brew, C., Brás, P., Buckley, J., Bugaev, V., Burdin, S., Busenitz, J., Buuck, M., Cabrita, R., Carels, C., Carlsmith, D., Carlson, B., Carmona-Benitez, M., Cascella, M., Chan, C., Chawla, A., Chen, H., Cherwinka, J., Chott, N., Cole, A., Coleman, J., Converse, M., Cottle, A., Cox, G., Craddock, W., Creaner, O., Curran, D., Currie, A., Cutter, J., Dahl, C., David, A., Davis, J., Davison, T., Delgaudio, J., Dey, S., de Viveiros, L., Dobi, A., Dobson, J., Druszkiewicz, E., Dushkin, A., Edberg, T., Edwards, W., Elnimr, M., Emmet, W., Eriksen, S., Faham, C., Fan, A., Fayer, S., Fearon, N., Fiorucci, S., Flaecher, H., Ford, P., Francis, V., Fraser, E., Fruth, T., Gaitskell, R., Gantos, N., Garcia, D., Geffre, A., Gehman, V., Genovesi, J., Ghag, C., Gibbons, R., Gibson, E., Gilchriese, M., Gokhale, S., Gomber, B., Green, J., Greenall, A., Greenwood, S., van der Grinten, M., Gwilliam, C., Hall, C., Hans, S., Hanzel, K., Harrison, A., Hartigan-O'Connor, E., Haselschwardt, S., Hernandez, M., Hertel, S., Heuermann, G., Hjemfelt, C., Hoff, M., Holtom, E., Hor, J.-K., Horn, M., Huang, D., Hunt, D., Ignarra, C., Jacobsen, R., Jahangir, O., James, R., Jeffery, S., Ji, W., Johnson, J., Kaboth, A., Kamaha, A., Kamdin, K., Kasey, V., Kazkaz, K., Keefner, J., Khaitan, D., Khaleeq, M., Khazov, A., Khurana, I., Kim, Y., Kocher, C., Kodroff, D., Korley, L., Korolkova, E., Kras, J., Kraus, H., Kravitz, S., Krebs, H., Kreczko, L., Krikler, B., Kudryavtsev, V., Kyre, S., Landerud, B., Leason, E., Lee, C., Lee, J., Leonard, D., Leonard, R., Lesko, K., Levy, C., Li, J., Liao, F.-T., Liao, J., Lin, J., Lindote, A., Linehan, R., Lippincott, W., Liu, R., Liu, X., Liu, Y., Loniewski, C., Lopes, M., Lopez Asamar, E., López Paredes, B., Lorenzon, W., Lucero, D., Luitz, S., Lyle, J., Majewski, P., Makkinje, J., Malling, D., Manalaysay, A., Manenti, L., Mannino, R., Marangou, N., Marzioni, M., Maupin, C., McCarthy, M., McConnell, C., McKinsey, D., McLaughlin, J., Meng, Y., Migneault, J., Miller, E., Mizrachi, E., Mock, J., Monte, A., Monzani, M., Morad, J., Morales Mendoza, J., Morrison, E., Mount, B., Murdy, M., Murphy, A., Naim, D., Naylor, A., Nedlik, C., Nehrkorn, C., Neves, F., Nguyen, A., Nikoleyczik, J., Nilima, A., O'Dell, J., O'Neill, F., O'Sullivan, K., Olcina, I., Olevitch, M., Oliver-Mallory, K., Orpwood, J., Pagenkopf, D., Pal, S., Palladino, K., Palmer, J., Pangilinan, M., Parveen, N., Patton, S., Pease, E., Penning, B., Pereira, C., Pereira, G., Perry, E., Pershing, T., Peterson, I., Piepke, A., Podczerwinski, J., Porzio, D., Powell, S., Preece, R., Pushkin, K., Qie, Y., Ratcliff, B., Reichenbacher, J., Reichhart, L., Rhyne, C., Richards, A., Riffard, Q., Rischbieter, G., Rodrigues, J., Rodriguez, A., Rose, H., Rosero, R., Rossiter, P., Rushton, T., Rutherford, G., Rynders, D., Saba, J., Santone, D., Sazzad, A., Schnee, R., Scovell, P., Seymour, D., Shaw, S., Shutt, T., Silk, J., Silva, C., Sinev, G., Skarpaas, K., Skulski, W., Smith, R., Solmaz, M., Solovov, V., Sorensen, P., Soria, J., Stancu, I., Stark, M., Stevens, A., Stiegler, T., Stifter, K., Studley, R., Suerfu, B., Sumner, T., Sutcliffe, P., Swanson, N., Szydagis, M., Tan, M., Taylor, D., Taylor, R., Taylor, W., Temples, D., Tennyson, B., Terman, P., Thomas, K., Tiedt, D., Timalsina, M., To, W., Tomás, A., Tong, Z., Tovey, D., Tranter, J., Trask, M., Tripathi, M., Tronstad, D., Tull, C., Turner, W., Tvrznikova, L., Utku, U., Va'vra, J., Vacheret, A., Vaitkus, A., Verbus, J., Voirin, E., Waldron, W., Wang, A., Wang, B., Wang, J., Wang, W., Wang, Y., Watson, J., Webb, R., White, A., White,

D., White, J., White, R., Whitis, T., Williams, M., Wisniewski, W., Witherell, M., Wolfs, F., Wolfs, J., Woodford, S., Woodward, D., Worm, S., Wright, C., Xia, Q., Xiang, X., Xiao, Q., Xu, J., Yeh, M., Yin, J., Young, I., Zarzhitsky, P., Zuckerman, A., and Zweig, E. (2023). First dark matter search results from the lux-zeplin (lz) experiment. *Physical Review Letters*, 131(4).

Aartsen, M. G., Abbasi, R., Ackermann, M., Adams, J., Aguilar, J., Ahlers, M., Ahrens, M., Alispach, C., Allison, P., Amin, N., et al. (2021). Icecube-gen2: the window to the extreme universe. *Journal of Physics G: Nuclear and Particle Physics*, 48(6):060501.

Abbasi, R., Ackermann, M., Adams, J., Aguilar, J., Ahlers, M., Ahrens, M., Alameddine, J., Alves Jr, A., Amin, N., Andeen, K., et al. (2023). Searches for connections between dark matter and high-energy neutrinos with icecube. *Journal of Cosmology and Astroparticle Physics*, 2023(10):003.

Abdallah, H., Abramowski, A., Aharonian, F., Ait Benkhali, F., Angüner, E., Arakawa, M., Arrieta, M., Aubert, P., Backes, M., Balzer, A., Barnard, M., Becherini, Y., Becker Tjus, J., Berge, D., Bernhard, S., Bernlöhr, K., Blackwell, R., Böttcher, M., Boisson, C., Bolmont, J., Bonnefoy, S., Bordas, P., Bregeon, J., Brun, F., Brun, P., Bryan, M., Büchele, M., Bulik, T., Capasso, M., Caroff, S., Carosi, A., Carr, J., Casanova, S., Cerruti, M., Chakraborty, N., Chaves, R., Chen, A., Chevalier, J., Colafrancesco, S., Condon, B., Conrad, J., Davids, I., Decock, J., Deil, C., Devin, J., deWilt, P., Dirson, L., Djannati-Ataï, A., Domainko, W., Donath, A., Drury, L., Dutson, K., Dyks, J., Edwards, T., Egberts, K., Eger, P., Emery, G., Ernenwein, J.-P., Eschbach, S., Farnier, C., Fegan, S., Fernandes, M., Fiasson, A., Fontaine, G., Förster, A., Funk, S., Füßling, M., Gabici, S., Gallant, Y., Garrigoux, T., Gaté, F., Giavitto, G., Giebels, B., Glawion, D., Glicenstein, J., Gottschall, D., Grondin, M.-H., Hahn, J., Haupt, M., Hawkes, J., Heinzelmann, G., Henri, G., Hermann, G., Hinton, J., Hofmann, W., Hoischen, C., Holch, T., Holler, M., Horns, D., Ivascenko, A., Iwasaki, H., Jacholkowska, A., Jamrozy, M., Janiak, M., Jankowsky, D., Jankowsky, F., Jingo, M., Jouvin, L., Jung-Richardt, I., Kastendieck, M., Katarzyński, K., Katsuragawa, M., Katz, U., Kerszberg, D., Khangulyan, D., Khélifi, B., King, J., Klepser, S., Klochkov, D., Kluźniak, W., Komin, N., Kosack, K., Krakau, S., Kraus, M., Krüger, P., Laffon, H., Lamanna, G., Lau, J., Lees, J.-P., Lefaucheur, J., Lemière, A., Lemoine-Goumard, M., Lenain, J.-P., Leser, E., Liu, R., Lohse, T., Lorentz, M., López-Coto, R., Lypova, I., Malyshev, D., Marandon, V., Marcowith, A., Mariaud, C., Marx, R., Maurin, G., Maxted, N., Mayer, M., Meintjes, P., Meyer, M., Mitchell, A., Moderski, R., Mohamed, M., Mohrmann, L., Morå, K., Moulin, E., Murach, T., Nakashima, S., de Naurois, M., Ndiyavala, H., Niederwanger, F., Niemiec, J., Oakes, L., O'Brien, P., Odaka, H., Ohm, S., Ostrowski, M., Oya, I., Padovani, M., Panter, M., Parsons, R., Pekeur, N., Pelletier, G., Perennes, C., Petrucci, P.-O., Peyaud, B., Piel, Q., Pita, S., Poireau, V., Poon, H., Prokhorov, D., Prokoph, H., Pühlhofer, G., Punch, M., Quirrenbach, A., Raab, S., Rauth, R., Reimer, A., Reimer, O., Renaud, M., de los Reyes, R., Rieger, F., Rinchiuso, L., Romoli, C., Rowell, G., Rudak, B., Rulten, C., Sahakian, V., Saito, S., Sanchez, D., Santangelo, A., Sasaki, M., Schandri, M., Schlickeiser, R., Schüssler, F., Schulz, A., Schwanke, U., Schwemmer, S., Seglar-Arroyo, M., Settimo, M., Seyffert, A., Shafi, N., Shilon, I., Shiningayamwe, K., Simoni, R., Sol, H., Spanier, F., Spir-Jacob, M., Stawarz, , Steenkamp, R., Stegmann, C., Steppa, C., Sushch, I., Takahashi, T., Tavernet, J.-P., Tavernier, T., Taylor, A., Terrier, R., Tibaldo, L., Tiziani, D., Tluczykont, M., Trichard, C., Tsirou, M., Tsuji, N., Tuffs, R., Uchiyama, Y., van der Walt, J., van Eldik, C., van Rensburg, C., van Soelen, B., Vasileiadis, G., Veh, J., Venter, C., Viana, A., Vincent, P., Vink, J., Voisin, F., Völk, H., Vuillaume, T., Wadiasingh, Z., Wagner, S., Wagner, P., Wagner, R.,

White, R., Wierzcholska, A., Willmann, P., Wörnlein, A., Wouters, D., Yang, R., Zaborov, D., Zacharias, M., Zanin, R., Zdziarski, A., Zech, A., Zefi, F., Ziegler, A., Zorn, J., and Żywucka, N. (2018). Search for <mml:math xmlns:mml="http://www.w3.org/1998/math/mathml" display="inline"><mml:mi></mml:mi></mml:math> -ray line signals from dark matter annihilations in the inner galactic halo from 10 years of observations with h.e.s.s. *Physical Review Letters*, 120(20).

Abdelhameed, A. H., Angloher, G., Bauer, P., Bento, A., Bertoldo, E., Bucci, C., Canonica, L., D'Addabbo, A., Defay, X., Di Lorenzo, S., et al. (2019). First results from the cresst-iii low-mass dark matter program. *Physical Review D*, 100(10):102002.

Abe, H., Abe, S., Acciari, V., Aniello, T., Ansoldi, S., Antonelli, L., Arbet Engels, A., Arcaro, C., Artero, M., Asano, K., et al. (2023). Search for gamma-ray spectral lines from dark matter annihilation up to 100 tev toward the galactic center with magic. *Physical review letters*, 130(6):061002.

Abramoff, O., Barak, L., Bloch, I. M., Chaplinsky, L., Crisler, M., Dawa, Drlica-Wagner, A., Essig, R., Estrada, J., Etzion, E., et al. (2019). Sensei: Direct-detection constraints on sub-gev dark matter from a shallow underground run using a prototype skipper ccd. *Physical review letters*, 122(16):161801.

Acciari, V. A., Ansoldi, S., Antonelli, L. A., Engels, A. A., Artero, M., Asano, K., Baack, D., Babić, A., Baquero, A., de Almeida, U. B., et al. (2022). Combined searches for dark matter in dwarf spheroidal galaxies observed with the magic telescopes, including new data from coma berenices and draco. *Physics of the Dark Universe*, 35:100912.

Acharyya, A., Adams, C., Bangale, P., Bartkoske, J., Batista, P., Benbow, W., Christiansen, J., Chromey, A., Duerr, A., Errando, M., et al. (2024). An indirect search for dark matter with a combined analysis of dwarf spheroidal galaxies from veritas. *arXiv preprint arXiv:2407.16518*.

Adhikari, G., Adhikari, P., de Souza, E. B., Carlin, N., Choi, S., Djamal, M., Ezeribe, A., Ha, C., Hahn, I., Jeon, E., Jo, J., Joo, H., Kang, W., Kang, W., Kauer, M., Kim, G., Kim, H., Kim, H., Kim, K., Kim, N., Kim, S., Kim, Y., Kim, Y., Ko, Y., Kudryavtsev, V., Lee, H., Lee, J., Lee, J., Lee, M., Leonard, D., Lynch, W., Maruyama, R., Mouton, F., Olsen, S., Park, B., Park, H., Park, H., Park, K., Pitta, R., Prihtiadi, H., Ra, S., Rott, C., Shin, K., Scarff, A., Spooner, N., Thompson, W., Yang, L., and Yu, G. (2019). Search for a dark matter-induced annual modulation signal in nai(tl) with the cosine-100 experiment. *Physical Review Letters*, 123(3).

Aghanim, N., Akrami, Y., Ashdown, M., Aumont, J., Baccigalupi, C., Ballardini, M., Banday, A., Barreiro, R., Bartolo, N., Basak, S., et al. (2020). Planck 2018 results-vi. cosmological parameters. *Astronomy & Astrophysics*, 641:A6.

Agnes, P., Albuquerque, I., Alexander, T., Alton, A., Ave, M., Back, H., Batignani, G., Biery, K., Bocci, V., Bonivento, W., et al. (2023). Search for low-mass dark matter wimps with 12 ton-day exposure of darkside-50. *Physical Review D*, 107(6):063001.

Agnese, R., Aralis, T., Aramaki, T., Arnquist, I., Azadbakht, E., Baker, W., Banik, S., Barker, D., Bauer, D., Binder, T., et al. (2018). First dark matter constraints from a supercdms single-charge sensitive detector. *Physical review letters*, 121(5):051301.

Agostini, M., Böhmer, M., Bosma, J., Clark, K., Danninger, M., Fruck, C., Gernhäuser, R., Gärtner, A., Grant, D., Henningsen, F., et al. (2020). The pacific ocean neutrino experiment. *Nature Astronomy*, 4(10):913–915.

Aguilar-Arevalo, A., Amidei, D., Baxter, D., Cancelo, G., Vergara, B. C., Chavarria, A., D'Olivo, J., Estrada, J., Favela-Perez, F., Gaïor, R., Guardincerri, Y., Hoppe, E., Hossbach, T., Kilminster, B., Lawson, I., Lee, S., Letessier-Selvon, A., Matalon, A., Mitra, P., Overman, C., Piers, A., Privitera, P., Ramanathan, K., Da Rocha, J., Sarkis, Y., Settimo, M., Smida, R., Thomas, R., Tiffenberg, J., Traina, M., Vilar, R., and Virto, A. (2020). Results on low-mass weakly interacting massive particles from an 11 kgd target exposure of damic at snolab. *Physical Review Letters*, 125(24).

Ajaj, R., Amaudruz, P.-A., Araujo, G., Baldwin, M., Batygov, M., Beltran, B., Bina, C., Bonatt, J., Boulay, M., Broerman, B., Bueno, J., Burghardt, P., Butcher, A., Cai, B., Cavuoti, S., Chen, M., Chen, Y., Cleveland, B., Cranshaw, D., Dering, K., DiGioseffo, J., Doria, L., Duncan, F., Dunford, M., Erlandson, A., Fatemighomi, N., Fiorillo, G., Florian, S., Flower, A., Ford, R., Gagnon, R., Gallacher, D., Garcés, E., Garg, S., Giampa, P., Goeldi, D., Golovko, V., Gorel, P., Graham, K., Grant, D., Hallin, A., Hamstra, M., Harvey, P., Hearns, C., Joy, A., Jillings, C., Kamaev, O., Kaur, G., Kemp, A., Kochanek, I., Kuźniak, M., Langrock, S., La Zia, F., Lehnert, B., Li, X., Lidgard, J., Lindner, T., Litvinov, O., Lock, J., Longo, G., Majewski, P., McDonald, A., McElroy, T., McGinn, T., McLaughlin, J., Mehdiyev, R., Mielnichuk, C., Monroe, J., Nadeau, P., Nantais, C., Ng, C., Noble, A., O'Dwyer, E., Ouellet, C., Pasuthip, P., Peeters, S., Piro, M.-C., Pollmann, T., Rand, E., Rethmeier, C., Retière, F., Seeburn, N., Singhrao, K., Skensved, P., Smith, B., Smith, N., Sonley, T., Soukup, J., Stainforth, R., Stone, C., Strickland, V., Sur, B., Tang, J., Vázquez-Jáuregui, E., Veloce, L., Viel, S., Walding, J., Waqar, M., Ward, M., Westerdale, S., Willis, J., and Zuñiga-Reyes, A. (2019). Search for dark matter with a 231-day exposure of liquid argon using deap-3600 at snolab. *Physical Review D*, 100(2).

Albert, A., Alfaro, R., Alvarez, C., Álvarez, J. D., Arceo, R., Arteaga-Velázquez, J. C., Rojas, D. A., Solares, H. A. A., Bautista-Elivar, N., Becerril, A., Belmont-Moreno, E., BenZvi, S. Y., Bernal, A., Braun, J., Brisbois, C., Caballero-Mora, K. S., Capistrán, T., Carramiñana, A., Casanova, S., Castillo, M., Cotti, U., Cotzomi, J., León, S. C. d., León, C. D., Fuente, E. D. l., Hernandez, R. D., Dingus, B. L., DuVernois, M. A., Díaz-Vélez, J. C., Ellsworth, R. W., Engel, K., Fiorino, D. W., Fraija, N., García-González, J. A., Garfias, F., González, M. M., Goodman, J. A., Hampel-Arias, Z., Harding, J. P., Hernandez, S., Hernandez-Almada, A., Hona, B., Hüntemeyer, P., Iriarte, A., Jardin-Blicq, A., Joshi, V., Kaufmann, S., Kieda, D., Lauer, R. J., Lennarz, D., Vargas, H. L., Linnemann, J. T., Longinotti, A. L., Proper, M. L., Raya, G. L., Luna-García, R., López-Coto, R., Malone, K., Marinelli, S. S., Martinez-Castellanos, I., Martínez-Castro, J., Martínez-Huerta, H., Matthews, J. A., Miranda-Romagnoli, P., Moreno, E., Mostafá, M., Nellen, L., Newbold, M., Nisa, M. U., Noriega-Papaqui, R., Pelayo, R., Pretz, J., Pérez-Pérez, E. G., Ren, Z., Rho, C. D., Rivière, C., Rosa-González, D., Rosenberg, M., Ruiz-Velasco, E., Greus, F. S., Sandoval, A., Schneider, M., Schoorlemmer, H., Sinnis, G., Smith, A. J., Springer, R. W., Surajbali, P., Taboada, I., Tibolla, O., Tollefson, K., Torres, I., Vianello, G., Weisgarber, T., Westerhoff, S., Wood, J.,

Yapici, T., Younk, P. W., and Zhou, H. (2018). Dark matter limits from dwarf spheroidal galaxies with the hawc gamma-ray observatory. *The Astrophysical Journal*, 853(2):154.

Amaré, J., Cebrián, S., Cintas, D., Coarasa, I., García, E., Martínez, M., Oliván, M., Ortigoza, Y., de Solórzano, A. O., Puimedón, J., et al. (2021). Annual modulation results from three-year exposure of anais-112. *Physical Review D*, 103(10):102005.

Aprile, E., Abe, K., Agostini, F., Ahmed Maouloud, S., Althueser, L., Andrieu, B., Angelino, E., Angevaare, J., Antochi, V., Antón Martin, D., Arneodo, F., Baudis, L., Baxter, A., Bazyk, M., Bellagamba, L., Biondi, R., Bismark, A., Brookes, E., Brown, A., Bruenner, S., Bruno, G., Budnik, R., Bui, T., Cai, C., Cardoso, J., Cichon, D., Cimental Chavez, A., Colijn, A., Conrad, J., Cuenca-García, J., Cussonneau, J., D'Andrea, V., Decowski, M., Di Gangi, P., Di Pede, S., Diglio, S., Eitel, K., Elykov, A., Farrell, S., Ferella, A., Ferrari, C., Fischer, H., Flierman, M., Fulgione, W., Fuselli, C., Gaemers, P., Gaior, R., Gallo Rosso, A., Galloway, M., Gao, F., Glade-Beucke, R., Grandi, L., Grigat, J., Guan, H., Guida, M., Hammann, R., Higuera, A., Hils, C., Hoetzsch, L., Hood, N., Howlett, J., Iacovacci, M., Itow, Y., Jakob, J., Joerg, F., Joy, A., Kato, N., Kara, M., Kavrigin, P., Kazama, S., Kobayashi, M., Koltman, G., Kopec, A., Kuger, F., Landsman, H., Lang, R., Levinson, L., Li, I., Li, S., Liang, S., Lindemann, S., Lindner, M., Liu, K., Loizeau, J., Lombardi, F., Long, J., Lopes, J., Ma, Y., Macolino, C., Mahlstedt, J., Mancuso, A., Manenti, L., Marignetti, F., Marrodán Undagoitia, T., Martens, K., Masbou, J., Masson, D., Masson, E., Mastroianni, S., Messina, M., Miuchi, K., Mizukoshi, K., Molinario, A., Moriyama, S., Morå, K., Mosbacher, Y., Murra, M., Müller, J., Ni, K., Oberlack, U., Paetsch, B., Palacio, J., Peres, R., Peters, C., Pienaar, J., Pierre, M., Pizzella, V., Plante, G., Qi, J., Qin, J., Ramírez García, D., Singh, R., Sanchez, L., dos Santos, J., Sarnoff, I., Sartorelli, G., Schreiner, J., Schulte, D., Schulte, P., Schulze Eißing, H., Schumann, M., Scotto Lavina, L., Selvi, M., Semeria, F., Shagin, P., Shi, S., Shockley, E., Silva, M., Simgen, H., Takeda, A., Tan, P.-L., Terliuk, A., Thers, D., Toschi, F., Trinchero, G., Tunnell, C., Tönnies, F., Valerius, K., Volta, G., Weinheimer, C., Weiss, M., Wenz, D., Wittweg, C., Wolf, T., Wu, V., Xing, Y., Xu, D., Xu, Z., Yamashita, M., Yang, L., Ye, J., Yuan, L., Zavattini, G., Zhong, M., and Zhu, T. (2023). First dark matter search with nuclear recoils from the xenonnt experiment. *Physical Review Letters*, 131(4).

Arnaud, Q., Asner, D., Bard, J.-P., Brossard, A., Cai, B., Chapellier, M., Clark, M., Corcoran, E., Dandl, T., Dastgheibi-Fard, A., et al. (2018). First results from the news-g direct dark matter search experiment at the lsm. *Astroparticle Physics*, 97:54–62.

Barkana, R. (2016). The rise of the first stars: Supersonic streaming, radiative feedback, and 21-cm cosmology. *Physics Reports*, 645:1–59.

Barkana, R. (2018). Possible interaction between baryons and dark-matter particles revealed by the first stars. *Nature*, 555(7694):71–74.

Barkana, R. and Loeb, A. (2001a). In the beginning: the first sources of light and the reionization of the universe. *Physics reports*, 349(2):125–238.

Barkana, R. and Loeb, A. (2001b). In the beginning: the first sources of light and the reionization of the universe. *Physics Reports*, 349(2):125–238.

Barkana, R. and Loeb, A. (2011). Scale-dependent bias of galaxies from baryonic acoustic oscillations. *Monthly Notices of the Royal Astronomical Society*, 415(4):3113–3118.

Basu, R., Banerjee, S., Pandey, M., and Majumdar, D. (2020). Lower bounds on dark matter annihilation cross-sections by studying the fluctuations of 21-cm line with dark matter candidate in inert doublet model (idm) with the combined effects of dark matter scattering and annihilation. *arXiv preprint arXiv:2010.11007*.

Battat, J. B., Ezeribe, A., Gauvreau, J.-L., Harton, J., Lafler, R., Law, E., Lee, E., Loomba, D., Lumnah, A., Miller, E., et al. (2017). Low threshold results and limits from the drift directional dark matter detector. *Astroparticle Physics*, 91:65–74.

Bennett, C. L., Larson, D., Weiland, J. L., Jarosik, N., Hinshaw, G., Odegard, N., Smith, K. M., Hill, R. S., Gold, B., Halpern, M., Komatsu, E., Nolta, M. R., Page, L., Spergel, D. N., Wollack, E., Dunkley, J., Kogut, A., Limon, M., Meyer, S. S., Tucker, G. S., and Wright, E. L. (2013). Nine-year wilkinson microwave anisotropy probe ( wmap ) observations: Final maps and results. *The Astrophysical Journal Supplement Series*, 208(2):20.

Bernabei, R., Belli, P., Bussolotti, A., Cappella, F., Caracciolo, V., Cerulli, R., Dai, C.-J., d'Angelo, A., Di Marco, A., He, H.-L., et al. (2018). First model independent results from dama/libra–phase2. *Universe*, 4(11):116.

Bernabei, R., Belli, P., Cappella, F., Cerulli, R., Dai, C., d'Angelo, A., He, H., Incicchitti, A., Kuang, H., Ma, X., et al. (2010). New results from dama/libra. *The European Physical Journal C*, 67:39–49.

Bernardi, G., Zwart, J., Price, D., Greenhill, L., Mesinger, A., Dowell, J., Eftekhari, T., Ellingson, S., Kocz, J., and Schinzel, F. (2016). Bayesian constraints on the global 21-cm signal from the cosmic dawn. *Monthly Notices of the Royal Astronomical Society*, 461(3):2847–2855.

BLUMENTHAL, G. R. and GOULD, R. J. (1970). Bremsstrahlung, synchrotron radiation, and compton scattering of high-energy electrons traversing dilute gases. *Reviews of Modern Physics*, 42(2):237–270.

Bouta, M., Brunner, J., Moussa, A., Păvălaş, G., and Tayalati, Y. (2021). Nuclearite search with antares. *Journal of Instrumentation*, 16(09):C09010.

Bowman, J. D., Rogers, A. E., Monsalve, R. A., Mozdzen, T. J., and Mahesh, N. (2018). An absorption profile centred at 78 megahertz in the sky-averaged spectrum. *Nature*, 555(7694):67–70.

Boylan-Kolchin, M., Bullock, J. S., and Kaplinghat, M. (2011). Too big to fail? the puzzling darkness of massive milky way subhaloes. *Monthly Notices of the Royal Astronomical Society: Letters*, 415(1):L40–L44.

Bromm, V. (2013a). Formation of the first stars. *Reports on Progress in Physics*, 76(11):112901.

Bromm, V. (2013b). Formation of the first stars. *Reports on Progress in Physics*, 76(11):112901.

Bromm, V., Coppi, P. S., and Larson, R. B. (2002). The formation of the first stars. i. the primordial star-forming cloud. *The Astrophysical Journal*, 564(1):23–51.

Brooks, A. M., Kuhlen, M., Zolotov, A., and Hooper, D. (2013). A baryonic solution to the missing satellites problem. *The Astrophysical Journal*, 765(1):22.

Brooks, A. M. and Zolotov, A. (2014). Why baryons matter: the kinematics of dwarf spheroidal satellites. *The Astrophysical Journal*, 786(2):87.

Brun, R., Urban, L., Carminati, F., Giani, S., Maire, M., McPherson, A., Bruyant, F., and Patrick, G. (1993). Geant: detector description and simulation tool. Technical report, CERN.

Bruns Jr, L. R., Wyithe, J. S. B., Bland-Hawthorn, J., and Dijkstra, M. (2012). Clustering of ly$\alpha$ emitters around luminous quasars at z= 2–3: an alternative probe of reionization on galaxy formation. *Monthly Notices of the Royal Astronomical Society*, 421(3):2543–2552.

Buck, T., Macciò, A. V., Dutton, A. A., Obreja, A., and Frings, J. (2019). Nihao xv: the environmental impact of the host galaxy on galactic satellite and field dwarf galaxies. *Monthly Notices of the Royal Astronomical Society*, 483(1):1314–1341.

Bullock, J. S. and Boylan-Kolchin, M. (2017). Small-scale challenges to the cdm paradigm. *Annual Review of Astronomy and Astrophysics*, 55(1):343–387.

Cang, J., Gao, Y., and Ma, Y.-Z. (2023). Signatures of inhomogeneous dark matter annihilation on 21-cm.

Carilli, C., Gnedin, N. Y., and Owen, F. (2002). Hi 21 centimeter absorption beyond the epoch of reionization. *The Astrophysical Journal*, 577(1):22.

Carter, L. L. and Cashwell, E. D. (1975). Particle-transport simulation with the monte carlo method. Technical report, Los Alamos National Lab.(LANL), Los Alamos, NM (United States).

Chen, X. and Kamionkowski, M. (2004). Particle decays during the cosmic dark ages. *Physical Review D*, 70(4):043502.

Chen, X. and Tye, S.-H. H. (2006). Heating in brane inflation and hidden dark matter. *Journal of Cosmology and Astroparticle Physics*, 2006(06):011–011.

Cheung, K., Kuo, J.-L., Ng, K.-W., and Tsai, Y.-L. S. (2019). The impact of edges 21-cm data on dark matter interactions. *Physics Letters B*, 789:137–144.

Chluba, J. and Thomas, R. M. (2010). Towards a complete treatment of the cosmological recombination problem. *Monthly Notices of the Royal Astronomical Society*, pages no–no.

Ciardi, B., Inoue, S., Mack, K. J., Xu, Y., and Bernardi, G. (2015). 21cm forest with the ska. *arXiv preprint arXiv:1501.04425*.

Cirelli, M., Iocco, F., and Panci, P. (2009). Constraints on dark matter annihilations from reionization and heating of the intergalactic gas. *Journal of Cosmology and Astroparticle Physics*, 2009(10):009–009.

Clark, H. A., Iwanus, N., Elahi, P. J., Lewis, G. F., and Scott, P. (2017). Heating of galactic gas by dark matter annihilation in ultracompact minihalos. *Journal of Cosmology and Astroparticle Physics*, 2017(05):048–048.

Clark, P. C., Glover, S. C. O., and Klessen, R. S. (2011). Treecol: a novel approach to estimating column densities in astrophysical simulations: Column densities in astrophysical simulations. *Monthly Notices of the Royal Astronomical Society*, 420(1):745–756.

Clowe, D., Gonzalez, A., and Markevitch, M. (2004). Weak-lensing mass reconstruction of the interacting cluster 1e 0657–558: Direct evidence for the existence of dark matter. *The Astrophysical Journal*, 604(2):596.

Collaboration, G. et al. (2020). Physics reference manual. *Version: geant4*, 9(0).

Collaboration, P., Ade, P., Aghanim, N., Armitage-Caplan, C., Arnaud, M., Ashdown, M., Atrio-Barandela, F., Aumont, J., Baccigalupi, C., Banday, A., et al. (2014). Planck 2013 results. xvi. cosmological parameters. *A&A*, 571:A16.

Correa, C. A., Wyithe, J. S. B., Schaye, J., and Duffy, A. R. (2015). The accretion history of dark matter haloes – ii. the connections with the mass power spectrum and the density profile. *Monthly Notices of the Royal Astronomical Society*, 450(2):1521–1537.

Cui, M.-Y., Yuan, Q., Tsai, Y.-L. S., and Fan, Y.-Z. (2017). Possible dark matter annihilation signal in the ams-02 antiproton data. *Physical Review Letters*, 118(19):191101.

Dalal, N., Pen, U.-L., and Seljak, U. (2010). Large-scale BAO signatures of the smallest galaxies. *Journal of Cosmology and Astroparticle Physics*, 2010(11):007–007.

Davies, H., Bethe, H., and Maximon, L. (1954). Theory of bremsstrahlung and pair production. ii. integral cross section for pair production. *Physical Review*, 93(4):788.

Daylan, T., Finkbeiner, D. P., Hooper, D., Linden, T., Portillo, S. K., Rodd, N. L., and Slatyer, T. R. (2016). The characterization of the gamma-ray signal from the central milky way: A case for annihilating dark matter. *Physics of the Dark Universe*, 12:1–23.

DeBoer, D. R., Parsons, A. R., Aguirre, J. E., Alexander, P., Ali, Z. S., Beardsley, A. P., Bernardi, G., Bowman, J. D., Bradley, R. F., Carilli, C. L., et al. (2017). Hydrogen epoch of reionization array (hera). *Publications of the Astronomical Society of the Pacific*, 129(974):045001.

Di Mauro, M., Pérez-Romero, J., Sánchez-Conde, M. A., and Fornengo, N. (2023). Constraining the dark matter contribution of $\gamma$ rays in clusters of galaxies using fermi-lat data. *Physical Review D*, 107(8):083030.

Diemer, B. and Joyce, M. (2019). An accurate physical model for halo concentrations. *The Astrophysical Journal*, 871(2):168.

Diemer, B. and Kravtsov, A. V. (2015). A universal model for halo concentrations. *The Astrophysical Journal*, 799(1):108.

Dijkstra, M., Lidz, A., and Wyithe, J. S. B. (2007). The impact of the igm on high-redshift ly$\alpha$ emission lines. *Monthly Notices of the Royal Astronomical Society*, 377(3):1175–1186.

Dodelson, S. (2011). The real problem with mond. *International Journal of Modern Physics D*, 20(14):2749–2753.

Donato, F., Maurin, D., Brun, P., Delahaye, T., and Salati, P. (2009). Constraints on wimp dark matter from the high energy pamela p/p data. *Physical review letters*, 102(7):071301.

Draine, B. T. and Bertoldi, F. (1996). Structure of stationary photodissociation fronts. *The Astrophysical Journal*, 468:269.

Einasto, J. (1965). On the Construction of a Composite Model for the Galaxy and on the Determination of the System of Galactic Parameters. *Trudy Astrofizicheskogo Instituta Alma-Ata*, 5:87–100.

Ellis, R. and Silk, J. (2008). *New frontiers in cosmology and galaxy formation: challenges for the future*. Cambridge University Press.

Evoli, C., Mesinger, A., and Ferrara, A. (2014). Unveiling the nature of dark matter with high redshift 21 cm line experiments. *Journal of Cosmology and Astroparticle Physics*, 2014(11):024–024.

Evoli, C., Valdés, M., Ferrara, A., and Yoshida, N. (2012). Energy deposition by weakly interacting massive particles: a comprehensive study: Energy deposition by wimps. *Monthly Notices of the Royal Astronomical Society*, 422(1):420–433.

Fargion, D., Konoplich, R. V., and Salis, A. (1997). Inverse compton scattering on laser beam and monochromatic isotropic radiation. *Zeitschrift für Physik C Particles and Fields*, 74:571–576.

Fialkov, A., Barkana, R., Tseliakhovich, D., and Hirata, C. M. (2012). Impact of the relative motion between the dark matter and baryons on the first stars: semi-analytical modelling. *Monthly Notices of the Royal Astronomical Society*, 424(2):1335–1345.

Fialkov, A., Barkana, R., Visbal, E., Tseliakhovich, D., and Hirata, C. M. (2013a). The 21-cm signature of the first stars during the lyman–werner feedback era. *Monthly Notices of the Royal Astronomical Society*, 432(4):2909–2916.

Fialkov, A., Barkana, R., Visbal, E., Tseliakhovich, D., and Hirata, C. M. (2013b). The 21-cm signature of the first stars during the lyman–werner feedback era. *Monthly Notices of the Royal Astronomical Society*, 432(4):2909–2916.

Field, G. B. (1958). Excitation of the hydrogen 21-cm line. *Proceedings of the IRE*, 46(1):240–250.

Foster, J. W., Park, Y., Safdi, B. R., Soreq, Y., and Xu, W. L. (2023). Search for dark matter lines at the galactic center with 14 years of fermi data. *Physical Review D*, 107(10):103047.

Furlanetto, S. R. and Loeb, A. (2005). Is double reionization physically plausible? *The Astrophysical Journal*, 634(1):1.

Furlanetto, S. R., Oh, S. P., and Pierpaoli, E. (2006). Effects of dark matter decay and annihilation on the high-redshift 21 cm background. *Physical Review D*, 74(10).

Galli, D. and Palla, F. (1998). The chemistry of the early universe.

Galli, S., Slatyer, T. R., Valdes, M., and Iocco, F. (2013). Systematic uncertainties in constraining dark matter annihilation from the cosmic microwave background. *Physical Review D*, 88(6).

Gao, L., Navarro, J. F., Cole, S., Frenk, C. S., White, S. D., Springel, V., Jenkins, A., and Neto, A. F. (2008). The redshift dependence of the structure of massive $\lambda$ cold dark matter haloes. *Monthly Notices of the Royal Astronomical Society*, 387(2):536–544.

Garrison-Kimmel, S., Hopkins, P. F., Wetzel, A., Bullock, J. S., Boylan-Kolchin, M., Kereš, D., Faucher-Giguère, C.-A., El-Badry, K., Lamberts, A., Quataert, E., et al. (2019). The local group on fire: dwarf galaxy populations across a suite of hydrodynamic simulations. *Monthly Notices of the Royal Astronomical Society*, 487(1):1380–1399.

Gessey-Jones, T., Sartorio, N., Fialkov, A., Mirouh, G., Magg, M., Izzard, R., de Lera Acedo, E., Handley, W., and Barkana, R. (2022). Impact of the primordial stellar initial mass function on the 21-cm signal. *Monthly Notices of the Royal Astronomical Society*, 516(1):841–860.

Glover, S. and Savin, D. W. (2006). cooling in primordial gas. *Philosophical Transactions of the Royal Society A: Mathematical, Physical and Engineering Sciences*, 364(1848):3107–3112.

Glover, S. C. O. (2015). Simulating the formation of massive seed black holes in the early universe – i. an improved chemical model. *Monthly Notices of the Royal Astronomical Society*, 451(2):2082–2096.

Glover, S. C. O. and Abel, T. (2008). Uncertainties in hsub2/suband HD chemistry and cooling and their role in early structure formation. *Monthly Notices of the Royal Astronomical Society*, 388(4):1627–1651.

Glover, S. C. O. and Savin, D. W. (2009). Is hsup/supsub3/subcooling ever important in primordial gas? *Monthly Notices of the Royal Astronomical Society*, 393(3):911–948.

Gnedin, N. Y. (2000). Effect of reionization on structure formation in the universe. *The Astrophysical Journal*, 542(2):535–541.

Gnedin, N. Y. and Ostriker, J. P. (1997). Reionization of the universe and the early production of metals. *The Astrophysical Journal*, 486(2):581.

Greif, T. H., Glover, S. C., Bromm, V., and Klessen, R. S. (2010). The first galaxies: chemical enrichment, mixing, and star formation. *The Astrophysical Journal*, 716(1):510.

Greif, T. H., Johnson, J. L., Bromm, V., and Klessen, R. S. (2007). The first supernova explosions: Energetics, feedback, and chemical enrichment. *The Astrophysical Journal*, 670(1):1.

Greif, T. H., White, S. D. M., Klessen, R. S., and Springel, V. (2011). THE DELAY OF POPULATION III STAR FORMATION BY SUPERSONIC STREAMING VELOCITIES. *The Astrophysical Journal*, 736(2):147.

Gurian, J., Liu, B., Jeong, D., Hosokawa, T., Hirano, S., and Yoshida, N. (2024). An analytic model of gravitational collapse induced by radiative cooling: Instability scale, infall velocity, and accretion rate. *arXiv preprint arXiv:2408.12940*.

Hegde, S. and Furlanetto, S. R. (2023). A self-consistent semi-analytic model for population iii star formation in minihaloes. *Monthly Notices of the Royal Astronomical Society*, 525(1):428–447.

Hehn, L., Armengaud, E., Arnaud, Q., Augier, C., Benoît, A., Bergé, L., Billard, J., Blümer, J., De Boissiere, T., Broniatowski, A., et al. (2016). Improved edelweiss-iii sensitivity for low-mass wimps using a profile likelihood approach. *The European Physical Journal C*, 76:1–10.

Hektor, A., Hütsi, G., Marzola, L., Raidal, M., Vaskonen, V., and Veermäe, H. (2018). Constraining primordial black holes with the edges 21-cm absorption signal. *Physical Review D*, 98(2).

Hirano, S., Hosokawa, T., Yoshida, N., Omukai, K., and Yorke, H. W. (2015). Primordial star formation under the influence of far ultraviolet radiation: 1540 cosmological haloes and the stellar mass distribution. *Monthly Notices of the Royal Astronomical Society*, 448(1):568–587.

Hiroshima, N., Hayashida, M., and Kohri, K. (2019). Dependence of accessible dark matter annihilation cross sections on the density profiles of dwarf spheroidal galaxies with the cherenkov telescope array. *Physical Review D*, 99(12):123017.

Hubbell, J. H. (2006). Electron–positron pair production by photons: A historical overview. *Radiation Physics and Chemistry*, 75(6):614–623.

Hubbell, J. H., Gimm, H. A., and O/verbo/, I. (1980). Pair, triplet, and total atomic cross sections (and mass attenuation coefficients) for 1 mev-100 gev photons in elements z= 1 to 100. *Journal of physical and chemical reference data*, 9(4):1023–1148.

Hui, L., Ostriker, J. P., Tremaine, S., and Witten, E. (2017). Ultralight scalars as cosmological dark matter. *Physical Review D*, 95(4):043541.

Hummel, J. A., Stacy, A., Jeon, M., Oliveri, A., and Bromm, V. (2015). The first stars: formation under x-ray feedback. *Monthly Notices of the Royal Astronomical Society*, 453(4):4137–4148.

Hutchins, J. B. (1976). The thermal effects of h2 molecules in rotating and collapsing spheroidal gas clouds. *Astrophysical Journal, vol. 205, Apr. 1, 1976, pt. 1, p. 103-121.*, 205:103–121.

Incatasciato, A., Khochfar, S., and Oñorbe, J. (2023). Modelling the cosmological lyman–werner background radiation field in the early universe. *Monthly Notices of the Royal Astronomical Society*, 522(1):330–349.

Kadota, K., Mao, Y., Ichiki, K., and Silk, J. (2014). Cosmologically probing ultra-light particle dark matter using 21 cm signals. *Journal of Cosmology and Astroparticle Physics*, 2014(06):011.

Katz, H., Kimm, T., Ellis, R. S., Devriendt, J., and Slyz, A. (2023). The challenges of identifying population iii stars in the early universe. *Monthly Notices of the Royal Astronomical Society*, 524(1):351–360.

Khlopov, M. Y., Malomed, B., and Zeldovich, Y. B. (1985). Gravitational instability of scalar fields and formation of primordial black holes. *Monthly Notices of the Royal Astronomical Society*, 215(4):575–589.

Kim, S. Y., Peter, A. H., and Hargis, J. R. (2018). Missing satellites problem: Completeness corrections to the number of satellite galaxies in the milky way are consistent with cold dark matter predictions. *Physical Review Letters*, 121(21).

Kitayama, T., Yoshida, N., Susa, H., and Umemura, M. (2004). The structure and evolution of early cosmological h ii regions. *The Astrophysical Journal*, 613(2):631.

Klessen, R. S. and Glover, S. C. (2023). The first stars: formation, properties, and impact. *Annual Review of Astronomy and Astrophysics*, 61(1):65–130.

Klypin, A., Kravtsov, A. V., Valenzuela, O., and Prada, F. (1999). Where are the missing galactic satellites? *The Astrophysical Journal*, 522(1):82.

Knasel, T. M. (1968). Incoherent-scattering function, total pair-production cross section, and pair-production length for helium. *Physical Review*, 171(5):1643–1647.

Kreckel, H., Bruhns, H., Čížek, M., Glover, S., Miller, K., Urbain, X., and Savin, D. W. (2010). Experimental results for h2 formation from h- and h and implications for first star formation. *Science*, 329(5987):69–71.

Krommydas, I. and Cholis, I. (2023). Revisiting gev-scale annihilating dark matter with the ams-02 positron fraction. *Physical Review D*, 107(2):023003.

Kuhlen, M., Madau, P., and Montgomery, R. (2006). The spin temperature and 21 cm brightness of the intergalactic medium in the pre-reionization era. *The Astrophysical Journal*, 637(1):L1.

Kulkarni, M. and Ostriker, J. P. (2022). What is the halo mass function in a fuzzy dark matter cosmology? *Monthly Notices of the Royal Astronomical Society*, 510(1):1425–1430.

Kulkarni, M., Visbal, E., and Bryan, G. L. (2021). The critical dark matter halo mass for population III star formation: Dependence on lyman–werner radiation, baryon-dark matter streaming velocity, and redshift. *The Astrophysical Journal*, 917(1):40.

Kuzio de Naray, R., Martinez, G. D., Bullock, J. S., and Kaplinghat, M. (2010). The case against warm or self-interacting dark matter as explanations for cores in low surface brightness galaxies. *The Astrophysical Journal*, 710(2):L161–L166.

Lewis, A. and Challinor, A. (2011). Camb: Code for anisotropies in the microwave background. *Astrophysics source code library*, pages ascl–1102.

Lin, W., Chen, X., Ganjoo, H., Hou, L., and Mack, K. J. (2023). Cosmology of single species hidden dark matter. *arXiv preprint arXiv:2305.08943*.

Lin, W., Mack, K. J., and Hou, L. (2020). Investigating the hubble constant tension: Two numbers in the standard cosmological model. *The Astrophysical Journal Letters*, 904(2):L22.

Liszt, H. (2001). The spin temperature of warm interstellar hi. *Astronomy & Astrophysics*, 371(2):698–707.

Liu, H., Ridgway, G. W., and Slatyer, T. R. (2020). Code package for calculating modified cosmic ionization and thermal histories with dark matter and other exotic energy injections. *Physical Review D*, 101(2).

Liu, H., Slatyer, T. R., and Zavala, J. (2016). Contributions to cosmic reionization from dark matter annihilation and decay. *Physical Review D*, 94(6).

Liu, Z., Yue, Q., Yang, L., Kang, K., Li, Y., Wong, H., Agartioglu, M., An, H., Chang, J., Chen, J., et al. (2019). Constraints on spin-independent nucleus scattering with sub-gev weakly interacting massive particle dark matter from the cdex-1b experiment at the china jinping underground laboratory. *Physical review letters*, 123(16):161301.

Loeb, A. and Barkana, R. (2001). The reionization of the universe by the first stars and quasars. *Annual review of astronomy and astrophysics*, 39(1):19–66.

Loeb, A., Ferrara, A., and Ellis, R. S. (2008). *First light in the universe*. Springer.

Loeb, A. and Wyithe, J. S. B. (2008). Possibility of precise measurement of the cosmological power spectrum with a dedicated survey of 21 cm emission after reionization. *Physical Review Letters*, 100(16):161301.

Loeb, A. and Zaldarriaga, M. (2004). Measuring the small-scale power spectrum of cosmic density fluctuations<? format?> through 21 cm tomography prior to the epoch of structure formation. *Physical Review Letters*, 92(21):211301.

Lopez-Honorez, L., Mena, O., Moliné, Á., Palomares-Ruiz, S., and Vincent, A. C. (2016). The 21 cm signal and the interplay between dark matter annihilations and astrophysical processes. *Journal of Cosmology and Astroparticle Physics*, 2016(08):004–004.

Lovell, M. R., Frenk, C. S., Eke, V. R., Jenkins, A., Gao, L., and Theuns, T. (2014). The properties of warm dark matter haloes. *Monthly Notices of the Royal Astronomical Society*, 439(1):300–317.

Ludlow, A. D., Bose, S., Angulo, R. E., Wang, L., Hellwing, W. A., Navarro, J. F., Cole, S., and Frenk, C. S. (2016). The mass–concentration–redshift relation of cold and warm dark matter haloes. *Monthly Notices of the Royal Astronomical Society*, 460(2):1214–1232.

Machacek, M. E., Bryan, G. L., and Abel, T. (2001). Simulations of pregalactic structure formation with radiative feedback. *The Astrophysical Journal*, 548(2):509–521.

Mack, K. J. (2014a). Known unknowns of dark matter annihilation over cosmic time. *Monthly Notices of the Royal Astronomical Society*, 439(3):2728–2735.

Mack, K. J. (2014b). Known unknowns of dark matter annihilation over cosmic time. *Monthly Notices of the Royal Astronomical Society*, 439(3):2728–2735.

Marsh, D. J. and Silk, J. (2014). A model for halo formation with axion mixed dark matter. *Monthly Notices of the Royal Astronomical Society*, 437(3):2652–2663.

May, S. and Springel, V. (2023). The halo mass function and filaments in full cosmological simulations with fuzzy dark matter. *Monthly Notices of the Royal Astronomical Society*, 524(3):4256–4274.

McGaugh, S. S. (2015). A tale of two paradigms: the mutual incommensurability of cdm and mond. *Canadian Journal of Physics*, 93(2):250–259.

McGaugh, S. S., Rubin, V. C., and de Blok, W. J. G. (2001). High-resolution rotation curves of low surface brightness galaxies. i. data. *The Astronomical Journal*, 122(5):2381–2395.

McQuinn, M. and O'Leary, R. M. (2012). The impact of the supersonic baryon–dark matter velocity difference on the z  20 21 cm background. *The Astrophysical Journal*, 760(1):3.

Mena, O., Palomares-Ruiz, S., Villanueva-Domingo, P., and Witte, S. J. (2019). Constraining the primordial black hole abundance with 21-cm cosmology. *Physical Review D*, 100(4):043540.

Meng, Y., Wang, Z., Tao, Y., Abdukerim, A., Bo, Z., Chen, W., Chen, X., Chen, Y., Cheng, C., Cheng, Y., et al. (2021). Dark matter search results from the pandax-4t commissioning run. *Physical Review Letters*, 127(26):261802.

Mesinger, A., Furlanetto, S., and Cen, R. (2010). 21cmfast: a fast, seminumerical simulation of the high-redshift 21-cm signal. *Monthly Notices of the Royal Astronomical Society*, 411(2):955–972.

Moore, B., Ghigna, S., Governato, F., Lake, G., Quinn, T., Stadel, J., and Tozzi, P. (1999). Dark matter substructure within galactic halos. *The Astrophysical Journal*, 524(1):L19.

MOTZ, J. W., OLSEN, H. A., and KOCH, H. W. (1969). Pair production by photons. *Reviews of Modern Physics*, 41(4):581–639.

Muñoz, J. B. (2019). Robust velocity-induced acoustic oscillations at cosmic dawn. *Physical Review D*, 100(6).

Muñoz, J. B. (2023). An effective model for the cosmic-dawn 21-cm signal. *Monthly Notices of the Royal Astronomical Society*, 523(2):2587–2607.

Muñoz, J. B., Qin, Y., Mesinger, A., Murray, S. G., Greig, B., and Mason, C. (2022). The impact of the first galaxies on cosmic dawn and reionization. *Monthly Notices of the Royal Astronomical Society*, 511(3):3657–3681.

Naoz, S. and Barkana, R. (2007). The formation and gas content of high-redshift galaxies and minihaloes. *Monthly Notices of the Royal Astronomical Society*, 377(2):667–676.

Naoz, S., Yoshida, N., and Gnedin, N. Y. (2012). SIMULATIONS OF EARLY BARYONIC STRUCTURE FORMATION WITH STREAM VELOCITY. i. HALO ABUNDANCE. *The Astrophysical Journal*, 747(2):128.

Narayanan, V. K., Spergel, D. N., Davé, R., and Ma, C.-P. (2000). Constraints on the mass of warm dark matter particles and the shape of the linear power spectrum from the l[clc]y[/clc] forest. *The Astrophysical Journal*, 543(2):L103–L106.

Natarajan, A. and Schwarz, D. J. (2009). Dark matter annihilation and its effect on cmb and hydrogen 21 cm observations. *Physical Review D*, 80(4).

Navarro, J. F., Eke, V. R., and Frenk, C. S. (1996). The cores of dwarf galaxy haloes. *Monthly Notices of the Royal Astronomical Society*, 283(3):L72–L78.

Navarro, J. F., Frenk, C. S., and White, S. D. (1997). A universal density profile from hierarchical clustering. *The Astrophysical Journal*, 490(2):493.

Navas, S., Amsler, C., Gutsche, T., Hanhart, C., Hernández-Rey, J., Lourenço, C., Masoni, A., Mikhasenko, M., Mitchell, R., Patrignani, C., Schwanda, C., Spanier, S., Venanzoni, G., Yuan, C., Agashe, K., Aielli, G., Allanach, B., Alvarez-Muñiz, J., Antonelli, M., Aschenauer, E., Asner, D., Assamagan, K., Baer, H., Banerjee, S., Barnett, R., Baudis, L., Bauer, C., Beatty, J., Beringer, J., Bettini, A., Biebel, O., Black, K., Blucher, E., Bonventre, R., Briere, R., Buckley, A., Burkert, V., Bychkov, M., Cahn, R., Cao, Z., Carena, M., Casarosa, G., Ceccucci, A., Cerri, A., Chivukula, R., Cowan, G., Cranmer, K., Crede, V., Cremonesi, O., D'Ambrosio, G., Damour, T., de Florian, D., de Gouvêa, A., DeGrand, T., Demers, S., Demiragli, Z., Dobrescu, B., D'Onofrio, M., Doser, M., Dreiner, H., Eerola, P., Egede, U., Eidelman, S., El-Khadra, A., Ellis, J., Eno, S., Erler, J., Ezhela, V., Fava, A., Fetscher, W., Fields, B., Freitas, A., Gallagher, H., Gershon, T., Gershtein, Y., Gherghetta, T., Gonzalez-Garcia, M., Goodman, M., Grab, C., Gritsan, A., Grojean, C., Groom, D., Grünewald, M., Gurtu, A., Haber, H., Hamel, M., Hashimoto, S., Hayato, Y., Hebecker, A., Heinemeyer, S., Hikasa, K., Hisano, J., Höcker, A., Holder, J., Hsu, L., Huston, J., Hyodo, T., Ianni, A., Kado, M., Karliner, M., Katz, U., Kenzie, M., Khoze, V., Klein, S., Krauss, F., Kreps, M., Križan, P., Krusche, B., Kwon, Y., Lahav, O., Lellouch, L., Lesgourgues, J., Liddle, A., Ligeti, Z., Lin, C.-J., Lippmann, C., Liss, T., Lister, A., Littenberg, L., Lugovsky, K., Lugovsky, S., Lusiani, A., Makida, Y., Maltoni, F., Manohar, A., Marciano, W., Matthews, J., Meißner, U.-G., Melzer-Pellmann, I.-A., Mertsch, P., Miller, D., Milstead, D., Mönig, K., Molaro, P., Moortgat, F., Moskovic, M., Nagata, N., Nakamura, K., Narain, M., Nason, P., Nelles, A., Neubert, M., Nir, Y., O'Connell, H., O'Hare, C., Olive, K., Peacock, J., Pianori, E., Pich, A., Piepke, A., Pietropaolo, F., Pomarol, A., Pordes, S., Profumo, S., Quadt, A., Rabbertz, K., Rademacker, J., Raffelt, G., Ramsey-Musolf, M., Richardson, P., Ringwald, A., Robinson, D., Roesler, S., Rolli, S., Romaniouk, A., Rosenberg, L., Rosner, J., Rybka, G., Ryskin, M., Ryutin, R., Safdi, B., Sakai, Y., Sarkar, S., Sauli, F., Schneider, O., Schönert, S., Scholberg, K., Schwartz, A., Schwiening, J., Scott, D., Sefkow, F., Seljak, U., Sharma, V., Sharpe, S., Shiltsev, V., Signorelli, G., Silari, M., Simon, F., Sjöstrand, T., Skands, P., Skwarnicki, T., Smoot, G., Soffer, A., Sozzi, M., Spiering, C., Stahl, A., Sumino, Y., Takahashi, F., Tanabashi, M., Tanaka, J., Taševský, M., Terao, K., Terashi, K., Terning, J., Thoma, U., Thorne, R., Tiator, L., Titov, M., Tovey, D., Trabelsi, K., Urquijo, P., Valencia, G., Van de Water, R., Varelas, N., Verde, L., Vivarelli, I., Vogel, P., Vogelsang, W., Vorobyev, V., Wakely, S., Walkowiak, W., Walter, C., Wands, D., Weinberg, D., Weinberg, E., Wermes, N., White, M., Wiencke, L., Willocq, S., Woody, C., Workman, R., Yao, W.-M., Yokoyama, M., Yoshida, R., Zanderighi, G., Zeller, G., Zhu, R.-Y., Zhu, S.-L., Zimmermann, F., Zyla, P., Anderson, J., Kramer, M., Schaffner, P., and Zheng, W. (2024). Review of particle physics. *Physical Review D*, 110(3).

Nebrin, O., Giri, S. K., and Mellema, G. (2023). Starbursts in low-mass haloes at cosmic dawn. i.

the critical halo mass for star formation. *Monthly Notices of the Royal Astronomical Society*, 524(2):2290–2311.

Nussbaumer, H. and Bieri, L. (2011). Who discovered the expanding universe? *arXiv preprint arXiv:1107.2281*.

O'Shea, B. W. and Norman, M. L. (2008). Population III star formation in a {$upLambda$CDM universe. II. effects of a photodissociating background. *The Astrophysical Journal*, 673(1):14–33.

Park, J., Ricotti, M., and Sugimura, K. (2021). Population iii star formation in an x-ray background – i. critical halo mass of formation and total mass in stars. *Monthly Notices of the Royal Astronomical Society*, 508(4):6176–6192.

Patil, A., Yatawatta, S., Koopmans, L., De Bruyn, A., Brentjens, M., Zaroubi, S., Asad, K., Hatef, M., Jelić, V., Mevius, M., et al. (2017). Upper limits on the 21 cm epoch of reionization power spectrum from one night with lofar. *The Astrophysical Journal*, 838(1):65.

Perlmutter, S., Aldering, G., Goldhaber, G., Knop, R. A., Nugent, P., Castro, P. G., Deustua, S., Fabbro, S., Goobar, A., Groom, D. E., et al. (1999). Measurements of $\omega$ and $\lambda$ from 42 high-redshift supernovae. *The Astrophysical Journal*, 517(2):565.

Press, W. H. and Schechter, P. (1974). Formation of galaxies and clusters of galaxies by self-similar gravitational condensation. *Astrophysical Journal, Vol. 187, pp. 425-438 (1974)*, 187:425–438.

Pritchard, J. R. and Loeb, A. (2008). Evolution of the 21 cm signal throughout cosmic history. *Physical Review D*, 78(10).

Pritchard, J. R. and Loeb, A. (2012). 21 cm cosmology in the 21st century. *Reports on Progress in Physics*, 75(8):086901.

Pérez de los Heros, C. (2017). *The Quest for Dark Matter with Neutrino Telescopes*, page 155–171. WORLD SCIENTIFIC.

Qin, W., Munoz, J. B., Liu, H., and Slatyer, T. R. (2023). Birth of the first stars amidst decaying and annihilating dark matter.

Qin, Y., Mesinger, A., Bosman, S. E. I., and Viel, M. (2021). Reionization and galaxy inference from the high-redshift ly forest. *Monthly Notices of the Royal Astronomical Society*, 506(2):2390–2407.

Reed, D., Gardner, J., Quinn, T., Stadel, J., Fardal, M., Lake, G., and Governato, F. (2003). Evolution of the mass function of dark matter haloes: Evolution of the mass function. *Monthly Notices of the Royal Astronomical Society*, 346(2):565–572.

Ricotti, M. (2016). X-ray twinkles and population iii stars. *Monthly Notices of the Royal Astronomical Society*, 462(1):601–609.

Riess, A. G., Casertano, S., Yuan, W., Macri, L. M., and Scolnic, D. (2019). Large magellanic cloud cepheid standards provide a 1% foundation for the determination of the hubble constant and stronger evidence for physics beyond $\lambda$cdm. *The Astrophysical Journal*, 876(1):85.

Riess, A. G., Filippenko, A. V., Challis, P., Clocchiatti, A., Diercks, A., Garnavich, P. M., Gilliland, R. L., Hogan, C. J., Jha, S., Kirshner, R. P., et al. (1998). Observational evidence from supernovae for an accelerating universe and a cosmological constant. *The astronomical journal*, 116(3):1009.

Riess, A. G., Yuan, W., Macri, L. M., Scolnic, D., Brout, D., Casertano, S., Jones, D. O., Murakami, Y., Anand, G. S., Breuval, L., et al. (2022). A comprehensive measurement of the local value of the hubble constant with 1 km s- 1 mpc- 1 uncertainty from the hubble space telescope and the sh0es team. *The Astrophysical journal letters*, 934(1):L7.

Romano, P. K., Horelik, N. E., Herman, B. R., Nelson, A. G., Forget, B., and Smith, K. (2015). Openmc: A state-of-the-art monte carlo code for research and development. *Annals of Nuclear Energy*, 82:90–97.

Rubin, V. C., Thonnard, N., and Ford, W. K., J. (1980). Rotational properties of 21 sc galaxies with a large range of luminosities and radii, from ngc 4605 /r = 4kpc/ to ugc 2885 /r = 122 kpc/. *The Astrophysical Journal*, 238:471.

Ryan, J. L. (2023). Search for dark matter annihilation signals in the galactic center halo with veritas. *arXiv preprint arXiv:2309.12403*.

Rydberg, C.-E., Zackrisson, E., Lundqvist, P., and Scott, P. (2013). Detection of isolated population iii stars with the james webb space telescope. *Monthly Notices of the Royal Astronomical Society*, 429(4):3658–3664.

Safranek-Shrader, C., Agarwal, M., Federrath, C., Dubey, A., Milosavljević, M., and Bromm, V. (2012). Star formation in the first galaxies–i. collapse delayed by lyman–werner radiation. *Monthly Notices of the Royal Astronomical Society*, 426(2):1159–1177.

Šaina, A., Gutiérrez, M., Gozzini, S. R., and de Dios, J. (2023). Indirect search for dark matter with the km3net neutrino telescope. *Contributions of KM3NeT to ICRC2023*, page 224.

Salvat, F., Fernandez-Varea, J., Baro, J., and Sempau, J. (1996). Penelope, and algorithm and computer code for monte carlo simulation of electron-photon showers.

Santos, D., Billard, J., Bosson, G., Bouly, J., Bourrion, O., Fourel, C., Grignon, C., Guillaudin, O., Mayet, F., Richer, J., et al. (2011). Mimac: A micro-tpc matrix for directional detection of dark matter. In *Journal of Physics: Conference Series*, volume 309, page 012014. IOP Publishing.

Schauer, A. T., Boylan-Kolchin, M., Colston, K., Sameie, O., Bromm, V., Bullock, J. S., and Wetzel, A. (2022). Dwarf galaxy formation with and without dark matter-baryon streaming velocities. *arXiv preprint arXiv:2210.12815*.

Schauer, A. T., Drory, N., and Bromm, V. (2020). The ultimately large telescope: what kind of facility do we need to detect population iii stars? *The Astrophysical Journal*, 904(2):145.

Schauer, A. T., Liu, B., and Bromm, V. (2019a). Constraining first star formation with 21 cm cosmology. *The Astrophysical Journal Letters*, 877(1):L5.

Schauer, A. T. P., Glover, S. C. O., Klessen, R. S., and Ceverino, D. (2019b). The influence of streaming velocities on the formation of the first stars. *Monthly Notices of the Royal Astronomical Society*, 484(3):3510–3521.

Schauer, A. T. P., Glover, S. C. O., Klessen, R. S., and Clark, P. (2021). The influence of streaming velocities and lyman–werner radiation on the formation of the first stars. *Monthly Notices of the Royal Astronomical Society*, 507(2):1775–1787.

Schive, H.-Y., Chiueh, T., Broadhurst, T., and Huang, K.-W. (2016). Contrasting galaxy formation from quantum wave dark matter, $\psi$dm, with $\lambda$cdm, using planck and hubble data. *The Astrophysical Journal*, 818(1):89.

Schneider, A. (2018). Constraining noncold dark matter models with the global 21-cm signal. *Physical Review D*, 98(6):063021.

Schneider, A., Anderhalden, D., Macciò, A. V., and Diemand, J. (2014). Warm dark matter does not do better than cold dark matter in solving small-scale inconsistencies. *Monthly Notices of the Royal Astronomical Society: Letters*, 441(1):L6–L10.

Schneider, A., Smith, R. E., and Reed, D. (2013). Halo mass function and the free streaming scale. *Monthly Notices of the Royal Astronomical Society*, 433(2):1573–1587.

Schon, S., Mack, K. J., Avram, C. A., Wyithe, J. S. B., and Barberio, E. (2014). Dark matter annihilation in the first galaxy halos. *arXiv preprint arXiv:1411.3783*.

Schön, S., Mack, K. J., Avram, C. A., Wyithe, J. S. B., and Barberio, E. (2015). Dark matter annihilation in the first galaxy haloes. *Monthly Notices of the Royal Astronomical Society*, 451(3):2840–2850.

Schön, S., Mack, K. J., and Wyithe, J. S. B. (2017). Dark matter annihilation in the circumgalactic medium at high redshifts. *Monthly Notices of the Royal Astronomical Society*, 474(3):3067–3079.

Sekiguchi, T. and Tashiro, H. (2014). Constraining warm dark matter with 21 cm line fluctuations due to minihalos. *Journal of Cosmology and Astroparticle Physics*, 2014(08):007.

Sheth, R. K., Mo, H. J., and Tormen, G. (2001). Ellipsoidal collapse and an improved model for the number and spatial distribution of dark matter haloes. *Monthly Notices of the Royal Astronomical Society*, 323(1):1–12.

Shimabukuro, H., Ichiki, K., and Kadota, K. (2020). Constraining the nature of ultra light dark matter particles with the 21 cm forest. *Physical Review D*, 101(4):043516.

Shull, J. M. and van Steenberg, M. E. (1985). X-ray secondary heating and ionization in quasar emission-line clouds. *The Astrophysical Journal*, 298:268.

Singh, S., Nambissan T, J., Subrahmanyan, R., Udaya Shankar, N., Girish, B., Raghunathan, A., Somashekar, R., Srivani, K., and Sathyanarayana Rao, M. (2022). On the detection of a cosmic dawn signal in the radio background. *Nature Astronomy*, 6(5):607–617.

Singh, S., Subrahmanyan, R., Shankar, N. U., Rao, M. S., Fialkov, A., Cohen, A., Barkana, R., Girish, B. S., Raghunathan, A., Somashekar, R., and Srivani, K. S. (2017). First results on the epoch of reionization from first light with SARAS 2. *The Astrophysical Journal*, 845(2):L12.

Sitwell, M., Mesinger, A., Ma, Y.-Z., and Sigurdson, K. (2014). The imprint of warm dark matter on the cosmological 21-cm signal. *Monthly Notices of the Royal Astronomical Society*, 438(3):2664–2671.

Slatyer, T. R. (2013). Energy injection and absorption in the cosmic dark ages. *Physical Review D*, 87(12).

Slatyer, T. R. (2016). Indirect dark matter signatures in the cosmic dark ages. i. generalizing the bound on s-wave dark matter annihilation from planck results. *Physical Review D*, 93(2):023527.

Slatyer, T. R., Padmanabhan, N., and Finkbeiner, D. P. (2009). Cmb constraints on wimp annihilation: Energy absorption during the recombination epoch. *Physical Review D*, 80(4).

Stacy, A., Bromm, V., and Loeb, A. (2011). EFFECT OF STREAMING MOTION OF BARYONS RELATIVE TO DARK MATTER ON THE FORMATION OF THE FIRST STARS. *The Astrophysical Journal*, 730(1):L1.

Stenrup, M., Larson, Å., and Elander, N. (2009). Mutual neutralization in low-energy h++ h- collisions: A quantum ab initio study. *Physical Review A—Atomic, Molecular, and Optical Physics*, 79(1):012713.

Taoso, M., Bertone, G., and Masiero, A. (2008). Dark matter candidates: a ten-point test. *Journal of Cosmology and Astroparticle Physics*, 2008(03):022.

Tegmark, M., Silk, J., Rees, M. J., Blanchard, A., Abel, T., and Palla, F. (1997). How small were the first cosmological objects? *The Astrophysical Journal*, 474(1):1–12.

Tinker, J., Kravtsov, A. V., Klypin, A., Abazajian, K., Warren, M., Yepes, G., Gottlöber, S., and Holz, D. E. (2008). Toward a halo mass function for precision cosmology: The limits of universality. *The Astrophysical Journal*, 688(2):709–728.

Trenti, M. and Stiavelli, M. (2009). Formation rates of population iii stars and chemical enrichment of halos during the reionization era. *The Astrophysical Journal*, 694(2):879.

Trussler, J. A., Conselice, C. J., Adams, N. J., Maiolino, R., Nakajima, K., Zackrisson, E., Austin, D., Ferreira, L., and Harvey, T. (2023). On the observability and identification of population iii galaxies with jwst. *Monthly Notices of the Royal Astronomical Society*, 525(4):5328–5352.

Tsai, Y.-S. (1974). Pair production and bremsstrahlung of charged leptons. *Reviews of Modern Physics*, 46(4):815–851.

Tseliakhovich, D., Barkana, R., and Hirata, C. M. (2011). Suppression and spatial variation of early galaxies and minihaloes. *Monthly Notices of the Royal Astronomical Society*, 418(2):906–915.

Tseliakhovich, D. and Hirata, C. (2010). Relative velocity of dark matter and baryonic fluids and the formation of the first structures. *Physical Review D*, 82(8):083520.

Undagoitia, T. M. and Rauch, L. (2015). Dark matter direct-detection experiments. *Journal of Physics G: Nuclear and Particle Physics*, 43(1):013001.

Valdes, M., Ferrara, A., Mapelli, M., and Ripamonti, E. (2007a). Constraining dark matter through 21-cm observations. *Monthly Notices of the Royal Astronomical Society*, 377(1):245–252.

Valdes, M., Ferrara, A., Mapelli, M., and Ripamonti, E. (2007b). Constraining dark matter through 21-cm observations. *Monthly Notices of the Royal Astronomical Society*, 377(1):245–252.

Valdés, M., Evoli, C., and Ferrara, A. (2010). Particle energy cascade in the intergalactic medium. *Monthly Notices of the Royal Astronomical Society*.

Verner, D., Ferland, G. J., Korista, K., and Yakovlev, D. (1996). Atomic data for astrophysics. ii. new analytic fits for photoionization cross sections of atoms and ions. *arXiv preprint astro-ph/9601009*.

Visbal, E., Haiman, Z., Terrazas, B., Bryan, G. L., and Barkana, R. (2014). High-redshift star formation in a time-dependent lyman–werner background. *Monthly Notices of the Royal Astronomical Society*, 445(1):107–114.

Watson, W. A., Iliev, I. T., D'Aloisio, A., Knebe, A., Shapiro, P. R., and Yepes, G. (2013). The halo mass function through the cosmic ages. *Monthly Notices of the Royal Astronomical Society*, 433(2):1230–1245.

Weinberg, S. (2003). Scientist: Four golden lessons. *Nature*, 426(389):27.

Wetzel, A. R., Hopkins, P. F., Kim, J.-h., Faucher-Giguère, C.-A., Kereš, D., and Quataert, E. (2016). Reconciling dwarf galaxies with $\lambda$cdm cosmology: simulating a realistic population of satellites around a milky way–mass galaxy. *The Astrophysical Journal Letters*, 827(2):L23.

Wise, J. H. (2019). An introductory review on cosmic reionization. *arXiv preprint arXiv:1907.06653*.

Wise, J. H. and Abel, T. (2008). Resolving the formation of protogalaxies. III. feedback from the first stars. *The Astrophysical Journal*, 685(1):40–56.

Wise, J. H., Turk, M. J., Norman, M. L., and Abel, T. (2011). The birth of a galaxy: primordial metal enrichment and stellar populations. *The Astrophysical Journal*, 745(1):50.

Wolcott-Green, J. and Haiman, Z. (2019). H2self-shielding with non-lte rovibrational populations: implications for cooling in protogalaxies. *Monthly Notices of the Royal Astronomical Society*, 484(2):2467–2473.

Wolcott-Green, J., Haiman, Z., and Bryan, G. L. (2017). Beyond ij/i subcrit/sub : a critical curve for suppression of h sub2/sub –cooling in protogalaxies. *Monthly Notices of the Royal Astronomical Society*, page stx167.

Wouthuysen, S. (1952). On the excitation mechanism of the 21-cm (radio-frequency) interstellar hydrogen emission line. *The Astronomical Journal*, 57:31–32.

Wu, X. and Kroupa, P. (2014). Galactic rotation curves, the baryon-to-dark-halo-mass relation and space–time scale invariance. *Monthly Notices of the Royal Astronomical Society*, 446(1):330–344.

Wyithe, J. S. B., Loeb, A., and Geil, P. M. (2008). Baryonic acoustic oscillations in 21-cm emission: a probe of dark energy out to high redshifts. *Monthly Notices of the Royal Astronomical Society*, 383(3):1195–1209.

Yoshida, N., Oh, S. P., Kitayama, T., and Hernquist, L. (2007). Early cosmological hscpii/scp/hescpiii/scpregions and their impact on second-generation star formation. *The Astrophysical Journal*, 663(2):687–707.

Zdziarski, A. A. and Svensson, R. (1989). Absorption of x-rays and gamma rays at cosmological distances. *The Astrophysical Journal*, 344:551.

Zolotov, A., Brooks, A. M., Willman, B., Governato, F., Pontzen, A., Christensen, C., Dekel, A., Quinn, T., Shen, S., and Wadsley, J. (2012). Baryons matter: why luminous satellite galaxies have reduced central masses. *The Astrophysical Journal*, 761(1):71.

Øverbø, I., Mork, K. J., and Olsen, H. A. (1973). Pair production by photons: Exact calculation for unscreened atomic field. *Physical Review A*, 8(2):668–685.

# APPENDICES

APPENDIX

# A

# ACRONYMS

A summary of all acronyms is documented in Table A.1.

Table A.1: A summary of acronyms used in alphabetical order.

| Acronym | Abbreviation |
|---|---|
| Axion-Like Particle | ALP |
| Big Bang Nucleosynthesis | BBN |
| Cold Dark Matter | CDM |
| Compton Scattering | CS |
| Cosmic Microwave Background | CMB |
| Circumgalactic Medium | CGM |
| Dark Matter | DM |
| Dark Matter Annihilation | DMA |
| Fuzzy Dark Matter | FDM |
| Halo Mass Function | HMF |
| Hidden Dark Matter | HiDM |
| Hubble Space Telescope | HST |
| Inverse Compton Scattering | ICS |
| Intergalactic Medium | IGM |

| | |
|---|---|
| Interstellar Medium | ISM |
| Luminosity Function | LF |
| Lambda($\Lambda$) Cold Dark Matter | LCDM |
| Modified Newtonian Dynamics | MOND |
| National Science Foundation | NSF |
| Planck Space Observatory | PLANCK |
| Self-Interacting Dark Matter | SIDM |
| Sloan Digital Sky Survey | SDSS |
| Strongly Interacting Massive Particles | SIMPs |
| Star Formation Rate | SFR |
| Standard Model | SM |
| Supermassive Black Hole | SMBH |
| Too-Big-To-Fail | TBTF |
| Warm Dark Matter | WDM |
| Weakly Interacting Massive Particles | WIMPs |
| Wilkinson Microwave Anisotropy Probe | WMAP |
| Ultralight Dark Matter | UDM |
| Ultraviolet | UV |

APPENDIX

# B

# VARIABLES

A summary of all variables is documented in Table B.1.

Table B.1: A summary of common astrophysics variables and their abbreviations in alphabetical order.

| Variable | Abbreviation |
|---|---|
| Arbitrary variable | $X$ |
| Boost factor | $B$ |
| Cross section | $\sigma$ |
| Density | $\rho$ |
| Energy | $E$ |
| Hubble constant | $H$ |
| Speed of light | $c$ |
| Overdensity | $\delta$ |
| Pressure | $p$ |
| Planck's constant | $h$ |
| Redshift | $z$ |
| Scale factor | $a$ |
| Lorentz factor | $\gamma$ |

| | |
|---|---|
| Mass | $m$ |
| Mean free path | $\lambda$ |
| Temperature | $T$ |
| Time | $t$ |
| Velocity divided by the speed of light | $\beta$ |
| Wavenumber | $k$ |